Some Practical Aspects of the Photoelastic Stressmeter in Concrete

by

Howard Rose

Thesis submitted in fulfilment of the requirements for the Degree of Doctor of Philosophy, Department of Civil and Structural Engineering, University of Sheffield.

July, 1970.

SYNOPSIS

Further investigations are described in the development of a biaxial glass inclusion gauge as a practical instrument for internal stress determinations in concrete. With this technique the magnitudes and directions of the required host stresses are interpreted from the induced stresses in the gauge by photoelastic methods.

Before discussing the new work the concepts and principal features of earlier stress gauges are described and existing knowledge of the photoelastic stressmeter is summarised.

Some elementary aspects of concrete shrinkage effects on the gauge readings are then discussed; the experimental evidence includes the problem of inclusion stresses produced by shrinkage and superposed external loads.

The discussion continues with an assessment of stressmeter behaviour under the action of two-dimensional stresses of opposite sign. Experimental evidence is compared with a theoretical solution and other indirect stress measurements using conventional strain gauge techniques.

The experimental results from both the shrinkage and compression-tension tests reveal significant anomalies in the inclusion stress distribution when comparisons are made with calculated conditions. This feature, which has not been considered by previous investigators, is discussed with reference to the assumptions implicit in the theoretical solutions. An explanation is proposed for the observed behaviour.

Finally a practical application of the stressmeter in a buttress dam is described and the readings are compared with calculated stress conditions for the buttress. Recommendations are made for the benefit of similar applications in the future.

The thesis concludes by discussing the implications of the present results to the photoelastic stressmeter method of determining stresses in concrete and suggestions are made for topics of further study.

CONTENTS

Appendices

Appendix 1 - Data for Chapter 3

Appendix 2 - Data for Chapter 4

Appendix 3 - Theoretical Isochromatic Fringe Patterns in the Annular Stressmeter

Appendix 4 - Mechanical Loading of Inclusions in Thin Plates

(A) Solid Inclusion with "Weldad" Interface.
(B) Annular Inclusion with an "Exact-Fit" Interface.

Appendix 5 - Data for Chapter 5

Appendix 6 - Data for Chapter 6

NOTATION

a,b	:	outer and inner radii, annular stressmeter.
A,B,C,A',B',C'	:	constants, axi-symmetric stress function.
A_o,A_2,B_o,B_2,C_2,D_2	:	Hiramatsu inclusion constants.
A_n	:	cross-section area, dam buttress.
C	:	stress optic coefficient.
d	:	diameter of a disc or cylinder.
d_1	:	position of section centroid from dam axis.
d_2	:	position of W_c from dam axis.
d_u	:	length of buttress section exposed to uplift.
D,H	:	Coutinho inclusion constants.
e	:	base for Napierian logarithms.
e_n	:	eccentricity of resultant force through dam section.
e_u	:	eccentricity of resultant force with uplift.
E,μ	:	Young's Modulus and Poisson's Ratio, host material.
E',μ'	:	Young's Modulus and Poisson's Ratio, inclusion.
E_f	:	Young's Modulus, dam foundation.
E_c, μ_c	:	Young's Modulus, Poisson's Ratio in compression.
E_T, μ_T	:	Young's Modulus, Poisson's Ratio in tension.
f_g	:	material fringe value.
G	:	shear modulus.
H_W	:	total horizontal water load on dam buttress.
k_1,k_2,k_3,k_4	:	annular inclusion constants.
k_n	:	stressmeter sensitivity parameter.
k_s, k_t	:	shrinkage and thermal constants, annular inclusion.
K_1,K_2	:	Coutinho's rigid inclusion constants.
l	:	axial length or thickness of a disc or cylinder.
l_g	:	axial length of glass inclusion

L'	:	axial length of uniaxial stress gauge.
$N_{(r,\theta)}$	:	isochromatic fringe order at point (r,θ).
N_s	:	shrinkage fringe order.
N_t	:	thermal fringe order.
N_T	:	resultant fringe order.
(p,q)	:	principal stresses being measured in host material.
P_s, P_t	:	radial boundary tractions due to shrinkage and thermal effects.
P_r	:	radial compressive stress on loading arc of a disc.
P'	:	diametrical force on a cylinder or disc.
(r,θ)	:	polar co-ordinates.
r_1, r_2	:	radial distance from diametrical loading points.
$R(=\frac{d}{2})$	:	radius of a disc or cylinder.
R'	:	radius of uniaxial stress gauge.
$R_W = \sqrt{V_W^2 + H_W^2}$	:	resultant water load on dam buttress.
$R_W' = \sqrt{V_R^2 + H_W^2}$	:	resultant water load with uplift
S_n	:	photoelastic stressmeter sensitivity factor.
t	:	change in temperature.
u_r, u_θ	:	radial and tangential displacements in host material.
u_r', u_θ'	:	radial and tangential displacements in inclusion.
U_p	:	maximum uplift pressure.
U_T	:	total uplift force on buttress.
$V_R = (V_W - U_T)$	:	resultant vertical water load with uplift.
V_W	:	vertical water load on buttress.
W_c	:	weight of buttress cap.
W_s	:	width of disc loading arc.
$x,y,z,$	:	rectangular co-ordinates.
$\bar{x}_n$	:	position of buttress section centroid.
x_s	:	distance along buttress section from centroid.

x_u	:	position of uplift force U_T.
x_R'	:	position of resultant force R'.
$\bar{x}_w, \bar{y}_w$	:	co-ordinates of centre of gravity of water load prism.
y_w	:	position of horizontal force H_W.
α, α'	:	coefficients of linear expansion, host material and inclusion.
β	:	Rhines' exponential decay factor.
δ	:	unrestrained primary shrinkage.
$\varepsilon_1, \varepsilon_2$	:	principal strains in host material.
$\varepsilon_r, \varepsilon_\theta, \gamma r_\theta$	:	radial, tangential and shear strain components in host material.
$\varepsilon_{G_1}, \varepsilon_{G_2}$, etc.	:	measured normal strains from gauge G1 etc.
σ_1', σ_2'	:	principal stresses in inclusion.
$\sigma_x, \sigma_y, \tau_{xy}$	:	normal and shear stress components in host material.
$\sigma_r, \sigma_\theta, \tau_{r\theta}$	:	radial, tangential andshear stress components in host material.
$\sigma_r', \sigma_\theta', \tau_{r\theta}'$	:	radial, tangential and shear stress components in inclusion.
suffix 's'	:	stress components due to shrinkage.
suffix 't'	:	stress components due to thermal effects.
suffix 'L'	:	stress components due to applied loads.
$\sigma_v, \sigma_h, \tau_{vh}$	:	normal and shear stresses on vertical and horizontal planes in dam buttress.
σ_z, σ_z'	:	normal stresses in z direction, host material and inclusion.
σ_{G_1}, σ_{G_2}, etc.	:	measured stresses in gauge G1, etc.
σ_{tens}	:	nominal tensile strength.
$\eta (= \frac{q}{p})$	:	applied principal stress ratio.
θ	:	angular position from direction of p.
θ_B	:	angular position of p in dam buttress.
θ_D	:	angular position of p in diametrically loaded disc.
ψ	:	half angle subtended at disc centre by loading arc.
ϕ, ϕ'	:	Airey stress functions.
λ	:	wavelength of light in polariscope.

Notes on Units Employed

Throughout this text the f.p.s. system of units is employed; in particular the units of stress, strain and angle are pounds per square inch (abbreviated to "p.s.i."), microstrains (abbreviated to "με"), and degrees, respectively. Temperatures are referred to the Fahrenheit scale.

If necessary the imperial units of the text may be converted to the International System of Units (SI units) by means of the following equalities:

Length	:	1 in.	= 25.4 mm.
		1 ft.	= 304.8 mm.
Area	:	1 $in.^2$	= 645.16 $mm.^2$
		1 $ft.^2$	= 0.0929 $m.^2$
Volume	:	1 $in.^3$	= 16387.1 $mm.^3$
		1 $ft.^3$	= 0.0283 $m.^3$
Mass	:	1 lb.	= 0.4536 kg.
Density	:	1 lb/ft^3	= 16.0185 $kg/m.^3$
Force	:	1 lb.f.	= 4.4482 N.
Pressure or Stress	:	1 $lb.f/in^2$	= 6.8948 KN/m^2
Moment	:	1 lb.ft.	= 1.3558 Nm.
Moment of Inertia of an Area	:	1 $ft.^4$	= 0.00863 $m.^4$
Temperature	:	$1^\circ F$	= $\frac{5}{9}$ of Kelvin unit. ($32^\circ F = 0^\circ C = 273.15^\circ K$)
Plane Angle	:	1°	= $\frac{\pi}{180}$ radians

It should also be noted that compressive effects are given positive signs when discussing forces, stresses and displacements.

ACKNOWLEDGEMENTS

This thesis has been made possible by facilities and helpful criticism offered by Professor W. Eastwood, Head of Department, and Dr. F.T. Williams, Senior Lecturer, of the Department of Civil and Structural Engineering, University of Sheffield.

The stressmeter application in the buttress dam has been assessed with the co-operation of Sir William Halcrow and Partners, Consultant Engineers to the Clywedog Reservoir Joint Authority. The stressmeters were installed during a programme of field investigations supervised by Dr. A. Roberts, Director of the former Postgraduate School of Mining, University of Sheffield, and sponsored by the U.S. Army Research and Development Group, European Research Office. Dr. I. Hawkes also acted as an advisor to the stressmeter investigations at that time.

The computer programme referred to in Chapter 5 was prepared by Dr. M.S. Atkinson. Valuable assistance has also been received from the technical and secretarial staff of the University of Sheffield. Much of the photoelastic instrumentation was provided by Horstman Limited of Bath, England.

CHAPTER 1

Measuring Stresses in Concrete: Preliminary Considerations

1.1. Introduction

In recent years the universal application of concrete as a structural material has prompted attention to the experimental determination of the stresses produced by external and internal forces. In this context the stresses of interest are generally those average values which act over an area of finite size in relation to the size of the matrix constituents, i.e. allowance is made for the heterogeneous structure and the fundamental definition of stress is not extended to the limit of an infinitely small area of action. It is these average stresses which are related to existing engineering methods of analysis rather than those which occur on a microscopic scale at discrete points in the mixture.

Conventional experimental methods of determining the average stresses rely on measurements of deformation which are subsequently converted to stresses via an independent knowledge of the relationship between stress and strain. With modern strain measurement techniques this indirect method is satisfactory if the deformation is elastic but difficulties arise if the elastic constants are not accurately known or when non-elastic strains occur.

Concrete may or may not be considered as an elastic material according to its age, the stress magnitudes involved and the time during which loads are applied. In short term loading tests it is usually unnecessary to take inelastic effects into account, notably if the concrete is considered to be mature. On the other hand in the computation of stresses due to gravity or live loads which are applied very slowly, it is generally necessary to consider the non-elastic increments of the deformation measurements. Methods have been developed to take these increments into

account (see for example [1]), but they involve extensive reiterative computations supported by a large number of experimental observations and independent laboratory tests. Furthermore, Hooke's Law is ultimately involved and like the short-term tests, the accuracy of the full stress determination will largely be a function of the Young's Modulus and Poisson's Ratio values applied to the experimental data.

More direct experimental methods are attractive and in recent years several instruments have been developed which avoid an accurate knowledge of the elastic constants and a direct response to strains not associated with changes in stress. These instruments are generally called "stressmeters" or "stress gauges", the name implying theirpreferential dependence upon changes in stress rather than deformation in the surrounding material.

Some of the difficulties associated with an ideal stressmeter are immediately obvious; for clarity, they may be enumerated as follows:

1. The device must always give readings which can be interpreted solely in terms of host material stress components which would otherwise exist in its absence. Thus the response produced by shrinkage, swelling, thermal or creep displacements must either be negligible or capable of systematic correction.
2. A well-defined directional response is required and the readings should not include unknown effects from orthogonal stresses. With this characteristic the stressmeter is amenable to a rosette application which allows the complete state of stress to be determined at a point. (In practice the "point" will have small but finite dimensions, depending upon the space occupied by the component gauges of the rosette. Ideally a sufficient number of individual stress components would be indicated by one gauge but at the present time a full three-dimensional device has yet to be developed.)

3. The device should respond to tension as well as compression, bearing in mind that tensile stresses in concrete generally have smaller orders of magnitude than compressive stresses.

4. For practical applications there are the additional requirements of long-term and economic reliability, including the ancillary equipment, which should allow remote observations so that the device can be applied to internal locations within the concrete mass.

Although the first attempts at the more direct method of stress measurement were made about forty years ago, none of the existing stress gauges satisfy all the above requirements and this includes the photoelastic stressmeter which is the subject of the following discussion. Nevertheless, there is sufficient evidence to encourage further study and development of the general method. The photoelastic stressmeter in particular has several potential advantages which are distinctly attractive but before summarising the existing knowledge of the device and the outstanding problems, it will be useful to trace the background of the general method.

1.2. Existing Devices

Existing stressmeters can be classified into "active" and "passive" gauges[2] according to the principle of the measurement technique.

In an "active" measurement the measuring apparatus must be actively adjusted from an external source in order to achieve a balance. The Glotzl cell is the best known example of a stressmeter working on this principle.

In a "passive" measurement the apparatus is influenced only by the object of the measurement which may be recorded as a deflection against a graduated scale. Most existing stressmeters use this principle; the first attempts appear to have been made by Hast[3] in Sweden and Carlson[4] in the U.S.A., about 1930.

1.2.1. The Glotzl Cell

The cell is shown in Figure 1.1; a small space between two flat plates is pressurised from an external supply and a relief valve opens immediately after the condition of force balance is achieved with the host material stresses applied perpendicular to the plates. The maximum pressure gauge reading is then very nearly equal to the applied compressive stress in the direction of reference.

Tensile stresses cannot be measured and theoretically small corrections are required for concrete shrinkage and mismatched thermal effects. The device is used for measurements in soils as well as concrete.

1.2.2. The Hast Stressmeter

Hast used a small nickel alloy cylindrical inclusion which could be cast into a concrete mix. A magnetostriction method was used to measure the subsequent axial stress condition in the spool-shaped inclusion when the matured concrete was subjected to load. The diameter and axial length of the inclusion were approximately the same and it was designed to have an effective modulus closely similar to that of the surrounding concrete. A paper sleeve prevented a direct response to orthogonal stresses and end caps could be fitted for tensile stress conditions. The construction of the stressmeter is shown in Figure 1.2.

The experimental behaviour of the device was found to be in reasonable agreement with an approximate theoretical analysis (given in[3] and[11]). It was found to be sensitive to shrinkage which would necessitate systematic corrections in general applications. The effects of creep on the gauge readings were not investigated. It is interesting to note that the gauge was used to investigate differential shrinkage stresses in concrete prisms but there appears to have been no further development of the device as a practical instrument for general use.

1.2.3. The Carlson Stressmeter

In contrast to Hast's device, the Carlson stressmeter is designed in the form of a thin plate; to preserve equilibrium through the thickness the induced stress must then always be approximately the same as the compressive stress in the surrounding concrete. The stressmeter is shown in Figure 1.3; the deflection of the internal plate is measured by a resistance strain wire and the mercury filled diaphragm is designed to give an effective gauge modulus similar to the concrete.

Theoretical analyses have revealed the spurious response to mismatched elastic modulii, shrinkage and creep under constant stress. Carlson called these phenomena "extraneous deformations" and showed that they could be allowed for systematically together with the temperature corrections necessary in long term investigations. Later independent tests[5] which included creep investigations, generally confirmed the designer's remarks. Like the Glotzl stressmeter, the device cannot be used to measure tensile stresses.

The theoretical analysis also revealed the important feature that the effective modulus of the plate can be much larger than the concrete modulus without causing any significant change in stressmeter response. Conversely, serious errors can be produced if the plate is less rigid than the surrounding concrete. Carlson also realised the importance of the height-radius ratio of the diaghragm and pointed out that a long slender stress gauge is acutely sensitive to extraneous deformations.

The influence of gauge shape was subsequently discussed by Loh [6] and Rocha[7]. Figure 1.4, shows the variation of stress in the gauge with modular ratio and shape; the remarks made by Hast and Carlson are consistent with Loh's analysis. In Figure 1.4, E' represents the effective modulus of the inclusion gauge.

The size of the Carlson gauge limits its applications to mass concrete; as a result, it is mainly used for measurement in dams. Installation calls for careful technique [8, 9] and its high cost appears to prevent comprehensive rosette arrangements.

1.2.4. The Coutinho Stressmeter

The Hast and Carlson stressmeters are limited to a unidirectional response and a need for installation at the time of concrete pouring. In 1948 Coutinho[10] described a small biaxial surface gauge which could be applied to concrete of any age and by virtue of the measurement method the readings could be interpreted immediately in terms of principal stresses and directions in the surrounding concrete.

The gauge consisted of a circular glass mirror bonded around its circumference in the surface of the concrete test piece; the back face of the mirror was also in direct contact with the concrete. The induced stresses in the plane of the glass disc produced by subsequent concrete stress changes were identified by a photoelastic technique. Coutinho showed that the magnitudes of the inclusion stresses are approximately constant for all systems involving a high modular ratio between the gauge and host concrete, an important feature which was subsequently discussed in more detail (see below).

Although the experimental evidence did not conclusively demonstrate the desired small effects of shrinkage and creep on the gauge response, the device represents a significant step in the development of the direct stress determination method and it was used in several structural investigations. The glass disc was either positioned in the formwork during pouring or grouted into a prepared hole on the surface of the mature concrete. Despite an observation instrument which appears to have been inconvenient for field use, it is claimed that the technique was used successfully to identify both compressive and tensile stresses in magnitude and direction.

1.3. The Rigid Inclusion Principle

After his experimental observations Coutinho went on to discuss[11] the fundamental relationships between the induced stresses in spherical and disc shaped inclusions and the stresses in the surrounding material. This second

paper was based on existing two and three-dimensional analyses for elastic inclusionsin elastic bodies [12, 13, 14].

Of particular interest is the two-dimensional solution for a disc shaped inclusion in a thin plate, the interface between the two being continuously connected. For example, from Sezawa and Nishimura's solution[13] the principal stresses in the disc can be written:

$$\sigma_1' = \frac{p}{2}(D + H) + \frac{q}{2}(D - H)$$

$$\sigma_2' = \frac{p}{2}(D - H) + \frac{q}{2}(D + H) \qquad (1.1)$$

where: σ_1', σ_2' are the principal stresses in the disc

p, q are the principal stresses being measured in the host material, i.e. those stresses which would exist in the plate in the absence of the inclusion.

D, H are constants defined by Countinho.

Since D and H do not involve position co-ordinates, equations(1.1) show that a homogeneous state of stress exists in the disc inclusion. (Equations are also given for the stresses at any point in the disturbed area around the inclusion; for practical purposes the stress disturbance in the plate due to the presence of the disc can be considered to extend over a distance from its centre equal to three times the radius of the disc.)

For the required principal stresses in the host material, equations (1.1) can be rewritten:

$$p = K_1.\sigma_1' + K_2.\sigma_2'$$

$$q = K_1.\sigma_2' + K_2.\sigma_1' \qquad (1.2.)$$

where K_1 and K_2 are further constants given by:

$$K_1 = \tfrac{1}{2}\left(\frac{1}{D} + \frac{1}{H}\right)$$

$$K_2 = \tfrac{1}{2}\left(\frac{1}{D} - \frac{1}{H}\right) \qquad (1.3.)$$

These relationships allow the host stresses to be calculated from the measured principal stresses in the inclusion.

The variations of K_1 and K_2 with modular ratio are shown in Figure 1.5. It can be seen that:

(a) Only small changes occur in K_1 and K_2 when $\frac{E'}{E} > 3$.

(b) The influence of Poisson's Ratio on K_1 is very small.

(c) Values of K_2 are approximately one-tenth of the corresponding K_1 values.

An important conclusion which is frequently referred to as the "rigid inclusion principle" can be drawn from these observations, namely that the stresses developed in a high modulus inclusion are practically independent of the modular ratio and if the inclusion is used as a stress transducer, the sensitivity will be unchanged in a variety of low modulus host materials.

In the case of a solid glass inclusion, the Young's Modulus will be of the order of $E' = 10 \times 10^6$ p.s.i., and therefore to a satisfactory degree of approximation, it should function as a stressmeter in materials with Young's Modulus $E < 3.5 \times 10^6$ p.s.i., assuming that some means can be provided to measure the induced stresses in the inclusion. This modulus criterion can frequently be satisfied by concrete.

Coutinho extended the conclusion to consider a system in which the modulus of the host material changed during the observation period; such a system could represent a high modulus inclusion in concrete under sustained loading. An example is shown in Figure 1.6, which indicates in conditions of various initial modular ratios the small changes produced in an inclusion when the host modulus changes by a factor of 50 per cent.

Thus an unexpected situation is apparent which demonstrates the attraction of the direct method of stress measurement; an elastic analysis of the problem reveals that a carefully selected inclusion gauge can be used for stress determinations in a range of materials whose Young's Modulus is generally difficult to define.

Referring again to Figure 1.5, it can be seen that K_1 is less than unity in "rigid inclusion conditions" and therefore the major principal stress in the inclusion is higher than the corresponding stress being measured in the host material. Despite the higher stress in the inclusion, the technique still requires the determination of small deformations; in practice, the inclusion strains are approximately one-third of the elastic strains which would otherwise exist at that point in the host material. The measurements in the inclusion must therefore be made with considerable accuracy and this requires careful technique for practical long-term applications. As an example, the vibrating wire method has been used satisfactorily in a hollow cylindrical stressmeter developed in Portugal[7]. In the special case of a glass inclusion, photoelastic methods present a simpler alternative, an advantage utilised in the stressmeter which provides the subject for the following discussion.

CHAPTER 2

The Photoelastic Stressmeter

2.1. Introduction

The preceding remarks have referred to some of the principles which are involved with the rigid inclusion method of direct stress determination. In recent years another photoelastic inclusion has been developed by Roberts et al[15] and although it is based on Coutinho's observations there are several significant features which have prompted its independent development.

Since the stressmeter has already been the subject of considerable study it will be worthwhile to summarise existing knowledge before outlining the outstanding problems, some of which will be considered in later sections of this thesis. The scope of the present work will be explained at the end of this Chapter.

The design and calibration characteristics of the stressmeter have been studied by Williams[16] and Dhir[17]. Their results have been included in the more widely known publication[15] which also describes the method of taking readings. The stress-optical principles and terminology involved with the photoelastic technique will not be described since these details are readily available in standard texts[26, 33]. Alternatively, reviews of the basic principles are given in a more concise form in [34, 35]. A description of the glass from which the stressmeters are made is included with the following summary.

It is interesting to note that an annular photoelastic inclusion has also been described by Hiramatsu et al [36, 37] but their method of interpretation appears to ignore Coutinho's principle. The photoelastic measurements are compared directly with theoretical elastic analyses of the inclusion stresses and thus the accuracy of the device depends on an accurate

knowledge of elastic constants and the realism of the calculated stresses in the inclusion.

In the sense of the present discussion, Hiramatsu's device cannot strictly be called a stressmeter. Although there are circumstances when the Sheffield gauges also cannot be considered to be true stressmeters, the terms "annular and solid stressmeters" in the following discussion refer to the inclusions developed by Roberts et al.

2.2. Description of the Instrument

The annular stressmeter consists of a thick walled glass cylinder (ratio of outer to inner diameters 5:1) which is bonded around its periphery into the host material. The bonding agent is generally a thin layer of epoxy resin adhesive. Normal and shear stresses are therebye transmitted to the glass element and if circular polarised light is passed in an axial direction through the annulus perpendicular to the plane of the applied stresses an isochromatic fringe pattern can be observed. Inspection of this pattern can give the following information:

(i) The directions of the principal stresses in the host material, i.e. the principal stresses which would exist at the same point in the absence of the device. (In the general three-dimensional problem the indicated stress components will be secondary principal stresses[31] since the axis of the annulus will not necessarily be aligned with a principal direction in the host material. Additionally, the indicated stresses will not be absolute values unless the stressmeter has experienced the total loading history of the host material.)

(ii) The ratio between the magnitudes of these major and minor principal stresses.

(iii) The magnitude of the major principal stress and, since their ratio is known, the magnitude of the minor principal stress.

(iv) The signs of the principal stresses.

The above information can be obtained without the observation of isoclinics. Since circular polarised light is used, the gauge and polarising filter do not require special orientation to identify the applied principal stress directions and the gauge is thus a self-orientating biaxial device, the stress components in the direction of light propogation being excluded from the photoelastic response. (Some of the effects of inclusion stresses in an axial direction are discussed in Chapter 5).

The polarising filter is usually incorporated in the instrument with a reflector unit, whilst the probe light source and hand-held analyser are carried by the observer. Fractional fringe orders are measured by Tardy goniometriccompensation. The polariser and analyser form a crossed circular polariscope which displays full order isochromatics.

Hiramatsu (loc.cit.) and Williams (loc.cit.) have described reflection polariscopes for use with glass stressmeters, in which case it is not necessary to include polarising filters in position with the inclusion.

A diffused white light source without collimation is generally used for illumination and the isochromatics then appear as coloured zones in accordance with the scale of interference colours. If monochromatic light is used then the pattern consists of a background of monochromatic colour with the integral fringe orders shown as dark lines. The fringe patterns shown in Figures 2.1-2.5 have been photographed with a diffused monochromatic sodium light source.

2.2.1. Inclusion Principal Stress Differences

The average through-the-thickness principal stress difference at any point in the glass can be readily identified from the isochromatic fringe order using the stress optic law which may be written:

$$N_{(r,\theta)} = \frac{C.lg}{\lambda} (\sigma_1' - \sigma_2') \qquad (2.1.)$$

where $N_{(r,\theta)}$ is the observed fringe order in light of wavelength λ

σ_1', σ_2' are the principal stresses in the glass at the point of interest in a plane perpendicular to the axis of the annulus

lg is the length of the light path

C is the stress optic coefficient for the glass and wavelength employed.

Hiramatsu showed that the orientation of the applied principal stresses perpendicular to the inclusion axis is given by the two axes of symmetry of the isochromatic pattern. Barron[38] extended Hiramatsu's generalised plane stress solution and gave equations for the principal stress difference at any point in terms of the applied principal stresses in the host material. In the general case:

$$(\sigma_1' - \sigma_2') = \{\left[k_1(p+q) + k_2(p-q)\cos 2\theta\right]^2 + k_3^2(p-q)^2\sin^2 2\theta\}^{\frac{1}{2}} \qquad (2.2)$$

where σ_1', σ_2', p and q are defined as before,

θ is an angular position in the inclusion (see Figure 1.7)

k_1, k_2, k_3 are constants which vary with radial position; definitions are given in Barron's analysis.

The fringe order N at any position in the glass is thus a function of the required principal stresses. For transducer purposes the fringe order at a particular point (see below) in the isochromatic pattern is related to the applied major principal stress in the surrounding material.

2.2.2. Stressmeter Sensitivity

The sensitivity of the stressmeter can be defined as:

$$S_n = \frac{p}{N_{(r,\theta)}} \qquad (2.3.)$$

The units (f.p.s.) are generally expressed in terms of pounds per square inch per fringe (p.s.i./fr.). The point (r,θ) at which the fringe orders are measured depends upon the applied stress system.

In the uniaxial case an easily identified datum point is used near the centre of each of the four sectors in the isochromatic pattern. These points have co-ordinates ($\frac{r}{b}$ = 1.60, θ = 45°, 135°, 225°, 315°) and Barron showed that they are the optimum points for instrument sensitivity. They are commonly referred to as the "45° points" of the stressmeter pattern in uniaxial loading.

In biaxial stress conditions different points are used; the co-ordiuates are ($\frac{r}{b}$ = 1.40, θ = 90°, 270°). The radial positions of the isochromatics along the minor axis of pattern symmetry (θ = 90°-270°) are referred to the edge of a circular opaque collar (radius 1.40b) held in the axial hole of the stressmeter by the light source probe. The reasons for the choice of these datum points have been discussed by Barron and Dhir (loc.cit.).

Substituting the above radial positions into the constant terms k_1, k_2, k_3, the stressmeter sensitivity can be expressed in terms of the inclusion properties by reference to equations (2.1)-(2.3).

For θ = 45° etc:

$$S_n = \frac{f_g}{l_g\sqrt{k_1^2(1+\eta)^2+k_3^2(1-\eta)^2}} \tag{2.4}$$

For θ = 90°, 270°:

$$S_n = \frac{f_g}{l_g\left[(k_1 + k_2)+\eta(k_1-k_2)\right]} \tag{2.5}$$

where $$f_g = \frac{\lambda}{c} \tag{2.6}$$

and $$\eta = \frac{q}{p} \tag{2.7}$$

The variation of stressmeter sensitivity in uniaxial loading with modulus of the host material is shown in Figure 2.6; experimental values given by Dhir (with a small difference in notation) are shown as squared points. In this presentation the sensitivity is expressed by the parameter k_n where:

$$k_n = \frac{S_n \times l_g}{f_g} \qquad (2.8)$$

The difference which is apparent between the observed and theoretical results for the materials of particular interest in the rigid inclusion technique (i.e. when $E < 4 \times 10^6$ p.s.i.) has been attributed by Dhir to the difficulty of defining a satisfactory value of Young's Modulus for low strength rocks and cementitious materials. This possible reason does not explain the discrepancies with the two observations in high modulus materials (i.e. the points in Figure 2.6 which correspond to $E = 15 \times 10^6$ p.s.i. and $E = 30 \times 10^6$ p.s.i.).

The sensitivity decreases in biaxial stress conditions, the calibration factor varying with the ratio of the applied principal stresses; values for rigid inclusion conditions are shown in Figure 2.7. So far no explanation has been offered for the difference between the theoretical and observed values given in Figure 2.7.

2.3. Interpretation of Stressmeter Patterns

2.3.1. Stressmeter Fringe Patterns

Fringe patterns characteristic of various biaxial loading conditions are shown in Figures 2.1-2.5. The conventional interpretation of a typical annular stressmeter fringe pattern in rigid inclusion conditions is illustrated by Figure 2.8.

The patterns shown in the illustrations have two axes of symmetry, which as mentioned before, are aligned with the principal stress directions in the surrounding material. In the examples shown here the axes are vertical and

in each case the major axis, corresponding to the direction of the major principal stress, is vertical. The principal stresses are compressive although the same patterns would be produced by two tensile stresses if the host material, the interface bond and the inclusion had sufficient strength to withstand the tensile stresses.

Combinations of compressive and tensile principal stresses produce very different fringe order profiles unless the ratio of the magnitudes approaches the uniaxial condition.

Figure 2.1 shows the patterns in a uniaxial stress condition with increasing applied stress.

Figures 2.2-2.5, show the same fringe orders with increasing values of minor principal stress. In the extreme case of equal principal stresses the fringe pattern appears as a series of concentric circles around the axial hole. In Figure 2.4, the black points seen on the major axis of symmetry near the axial hole are isotropic points and should not be confused with the first integral fringe order at high stress levels. It can be shown[22] that their radial positions are independent of the stress level but proportional to the ratio of the principal stresses in the surrounding material. Isotropic points are not seen in uniaxial or hydrostatic fringe patterns.

2.3.2. The Sign of the Major Principal Stress

Depending on the optical alignment of the polariscope components with respect to the axes of symmetry of the fringe pattern, the direction of displacement of the fringe pattern during goniometric compensation enables the sign of the major principal stress in the host material to be determined. The fringes either move towards or away from the datum point on the stressmeter pattern as the compensator is operated.

If the transmission plane of the polarising plate in the conventional hand-held analyser used with photoelastic stressmeters is first aligned with the major axis of symmetry of the fringe pattern, a major principal compressive

stress is indicated when the lower fringe orders move towards the datum points during goniometric compensation. Tensile stresses are indicated by higher fringe orders moving towards the datum points.

The alignment of the polarising plate presents no difficulty since the analyser is so constructed that the transmission plane is parallel to the handle of the analyser when the compensation pointer is set to zero.

2.3.3. The Minor Principal Stress

The simplest method of determining the magnitude of the minor principal stress, but one which is clearly subject to some inaccuracy, is to compare the observed pattern with the standard forms illustrated in Figures 2.1-2.5. The minor stress is then estimated as a fraction of the major principal stress. Since more refined methods were not available in the circumstances, this method was used in the field investigations described in Chapter 6.

Alternative methods involve radial measurements of isochromatic positions, or the consideration of fringe order ratios at different points in the pattern[37]. There are practical difficulties associated with these methods and considerable errors are still possible. In particular, the methods depend on the accuracy of the theoretical solution for the stresses in the glass and it will be apparent from the discussion in Chapter 5 that there is experimental evidence to question the validity of the existing theoretical solution for the inclusion stresses with current methods of applying the device.

Another method of determining the minor principal stress uses a solid stressmeter in conjunction with the annular instrument.

2.4 The Solid Stressmeter

Reference has been made earlier to Coutinho's solid inclusion in which a homogeneous state of stress is induced by the applied principal stresses in the host material.

If the optical system used with the annular stressmeter is applied to a solid inclusion, the limited information so given is sufficient to identify the principal stress difference in the inclusion and hence the difference between the applied principal stresses in the host material. (It should be noted that Coutinho used a more elaborate observation system[10] to give a full interpretation of the in-plane stresses within the inclusion. Directions and individual magnitudes cannot be deduced by using circular polarised light alone in the solid stressmeter.)

If an annular and solid stressmeter are exposed to the same stressfield then the annular instrument will give the magnitude and direction of the major principal stress. The solid instrument will give the difference between the two stresses and hence the minor principal stress is known. The value so found should correspond to the magnitude indicated by the profile of the fringe pattern observed in the annular instrument.

With the exception of a narrow zone near the boundary, the isochromatic pattern seen in a solid instrument is one of uniform colour; the exact colour will be a function of the average through-the-thickness principal stresses in the glass.

Calibration characteristics were included in Dhir's investigations; the results are included in Figure 2.6, and the theoretical behaviour is included for comparison purposes. (In this instance the theoretical solution was conveniently obtained from the Muskhelishvili equation[39]). Again, an explanation has yet to be given for the considerable divergence between the experimental and theoretical sensitivities in high modulus materials.

Readings are taken from the solid stressmeter in a similar manner to that used with the annular stressmeter. The analyser is aligned with the major stress direction in the inclusion and the uniform fringe pattern is compensated at the centre of the inclusion ($r = 0$) to the tint of passage as the datum point between integral fringe orders.

In general, without the use of plane polarised light the direction of the major stress in the inclusion is not readily apparent. The directions indicated by the neighbouring annular instrument and the behaviour of the fringe pattern during compensation have to provide this information.

Care has to be taken during the compensation process to avoid miscounting the integral fringe order. The Tardy method enables observed fringe orders to be compensated to the nearest integral value, which in turn has to be identified by inspection of the colour sequence during compensation. When a uniform state of principal stress difference exists in the test piece, the duplication of colours in the interference colour scale can produce ambiguous interpretations of the integral fringe orders but this can be avoided by using additional filters in the manner suggested by Pant[40].

It may be noted that Dhir called the solid stressmeter a "shear stressmeter" by virtue of the relationship between the maximum shear stress and principal stress difference, viz:

$$\tau_{max} = \frac{p-q}{2} \qquad (2.9)$$

2.5. The Stressmeter Glass

Glass is a relatively strong material with good time-dependent properties and it behaves as an almost perfectly linear elastic solid up to stresses very near to its breaking strength at normal temperatures.

Although it is now rarely used in conventional photoelasticity, its birefringent properties were originally recognised by Brewster[41] and many of the early investigators used glass models, notably Mesnager[42] and Coker and Filon[33]. It was Mesnager who first proposed the use of glass in force and stress transducers; more recently transducer applications have been developed by Roberts et al[43] and Hooper[44]. Although for rigid inclusion measurements it would be desirable for glass to have a higher elastic modulus, its easily observed birefringent properties compensate for this small disadvantage.

The physical properties of glass vary widely with chemical composition. With some exceptions in early studies, photoelastic stressmeters are prepared from a soda-lime plate glass which can be obtained and worked without difficulty. The manufacturers give the following approximate composition by weight:

SiO_2	NaO	CaO	MgO	Al_2O3	K_2O	SO_3
73.3%	12.6%	9.2%	3.2%	0.8%	0.3%	0.3%

The thermal softening temperature and coefficient of linear expansion are similarly given as 1360°F (739°C) and $\alpha' = 4\text{-}5 \times 10^{-6}$ per °F (8.0×10^{-6} per °C) respectively. The static Young's Modulus and Poisson's Ratio have been measured in compression by the present writer as 10.4×10^6 p.s.i. and 0.22 respectively.

2.5.1. The Stress Optic Coefficient

For glass of a given chemical composition the stress optic coefficient C can vary with wavelength, age and temperature. Referring to the work of Harris[45] and Van Zee and Noritake[46], Hooper (loc.cit.) has pointed out that C can be considered to be constant for soda-lime plate glass in normal temperature ranges (i.e. 32°F-200°F). Age effects would also appear to be of little consequence unless observations are carried out over several decades or unless the glass is freshly cast. Experience so far has been gained from stressmeters that have been prepared from glass already several years old.

In the present circumstances C is more conveniently incorporated in another constant, f_g, which may be called the material fringe value[27] where:

$$f_g = \frac{\lambda}{C} \qquad (2.6)$$

Thus equation (2.1) may be rewritten:

$$N_{(r,\theta)} = \frac{(\sigma_1' - \sigma_2')}{f_g} \lg \qquad (2.1a)$$

It can be seen that f_g has units of stress per fringe per unit thickness; with present notation these units could also be written in terms of "pounds per fringe inch" (lbs./fr.in.). The material fringe value can be defined in terms of maximum shear stress or principal shear difference, the latter being preferred in the present discussion.

Since the constants C and f_g vary with chemical composition, calibration tests have been carried out throughout the development period of the photo-elastic stressmeter. For the investigations to be described a specimen from each batch of stressmeter glass has been tested according to the method shown in Figure 2.9.

The diametrically loaded cylindrical test piece is particularly convenient to use since it can be prepared with the same diamond drill as the usual stressmeter element. The compressive loads have been provided by a laboratory universal testing machine through two rigid steel platens; the silicone rubber encapsulant in Figure 2.9 is of very low strength and gives stability to the platens and test pieces for handling purposes.

The principal stress difference at the centre of the cylinder is given by conventional calculation (see Chapter 4). and values have been compared with incremental fringe orders observed with a diffused light source of known wave length; in this case sodium and white light sources have been used. (Although the fringe orders of Figure 2.9 refer to sodium light it has been experimentally verified that the same results are given in white light within the limits of experimental error. This is to be expected since the tint of passage in white light closely corresponds to the extinction of the sodium yellow region of the spectrum.)

The results shown in Figure 2.9, are representative of all the present tests and no significant differences were observed in any of the many calibration specimens, including examples tested before and after the four year field applicaton to be described in Chapter 6.

The material fringe value so determined (f_g = 1220 p.s.i./fr./in. ± 20 p.s.i./fr./in.) has been independently confirmed by Hooper and Atkinson[47] with glass supplied to the same specification. This f_g value is equivalent to a stress optic coefficient of approximately 2.70 brewsters which compares favourably with values of 2.62 brewsters given by Waxler[48] and 2.68 brewsters determined by Van Zee and Noritake (loc.cit.) for similar plate glasses. On the other hand, Dhir[18] gives a fringe value of f_g = 1050 p.s.i./fr./in. (C ≈ 3.20 brewsters) for his stressmeter investigations and this significantly different figure has to be allowed for if comparisons are made in the following discussion.

It is also interesting to note from Figure 2.9 that doubling the length of the test-piece has no effect on the observed fringe orders in the glass. This is a requirement of the stress optic law as long as the diametrical loads remain the same. In this case the double length specimen has been prepared by cementing two normal test-pieces (length 1.5 in.) together with a thin layer of polyurethane adhesive and the experimental result shows that this process has no significant effect on the birefringence of the system. Double length stressmeter elements prepared in this manner have been included in the investigations to be described.

2.6. Existing Experience in Concrete

After discussing the stressmeter interpretation procedure Dhir went on to consider some of the particular problems which occur when the device is applied to concrete. Because of the scope of the subject his conclusions were restricted to general remarks about the response of the annular stressmeter in relation to aggregate size and extraneous deformations.

For example, as a general rule it was found that the stressmeter pattern was not disturbed by aggregate effects so long as the inclusion was larger than the nominal maximum aggregate size. Experimental evidence also suggested that the stressmeter readingswere only affected to a very

small degree by creep, shrinkage and temperature changes, but none of these problems were investigated in sufficient detail to allow a systematic assessment of the effects in a given practical application of the technique.

The necessity for a comprehensive knowledge of these effects has been emphasised by the results from a limited number of field applications. For example, stressmeter installations in a pre-stressed concrete bridge[49] and an arch dam[49] have demonstrated the ability of the device to give well defined photoelastic signals over long periods of time, but it has not been possible to draw firm conclusions about the behaviour of the stressmeters or the stresses in the structures because of the unknown quantitative effects of the extraneous deformations.

For this reason, some of the effects of creep and temperature changes on the stressmeter response were studied separately[50, 51], soon after Dhir's original observations. Preliminary results[50] from the creep tests have tended to confirm earlier impressions (also supported by Hawkes[52] with photoelastic stressmeter tests in frozen sand) but at the present time the full investigation has not been reported in detail. Similarly the results of the temperature investigations cannot yet be interpreted in general terms. These results will clearly be of fundamental importance to the technique if it is to be applied to long-term measurements in concrete.

Another point which has only received brief attention so far concerns the effects of stresses which act in an axial direction around the inclusion. As far as the stressmeter readings are concerned, no photoelastic response should be produced by stress components which act in the direction of propagation[32]. Some disturbance might be expected near the boundary with the host material but it is presumed that this does not extend into the locality of the reading points on the stressmeter pattern. It would be desirable to confirm the assumption experimentally and this will be left as a suggestion for future study.

2.7. Scope of the Present Work

The effects of shrinkage have not yet been considered beyond Dhir's remarks. In a mechanical sense, shrinkage and temperature changes present the same problem and although it is possible that the temperature investigations might give results which can be referred to the shrinkage response, it is clearly desirable to make independent experimental studies of the effects.

A detailed shrinkage study has been beyond the scope of the present work but some elementary aspects of the problem will be discussed in Chapter 3. The further effects of superposing stresses from an external load onto a stressmeter already subjected to shrinkage stresses will also be discussed for the first time with experimental evidence. The practical difficulties which have appeared in the tests will be of interest to any comprehensive study planned in the future.

Another feature which will be discussed for the first time concerns the response of the annular stressmeter to biaxial stresses of opposite sign. This is relevant because in some circumstances the stressmeter may be required to measure a stress condition consisting of a major compressive principal stress in combination with a smaller minor tensile principal stress, e.g. in the arch dam investigations mentioned previously.

For a given condition the fringe pattern produced in the stressmeter may be calculated using the Hiramatsu-Barron equation (2.2) and the stress optic law equation (2.1a) but it is desirable to check the behaviour experimentally because tensile stresses are involved both in the inclusion and over a portion of the interface with the surrounding material.

Again, it has not been possible to carry out comprehensive tests which provide for all circumstances, but with the aid of a disc-shaped calibration specimen one particular combination of compression and tension has been considered. The stressmeter results are discussed in Chapter 4 in comparison with the calculated stress conditions and other indirect measurements using electrical resistance strain gauges and a demountable mechanical strain gauge.

In both series of tests it will be seen that the observed stressmeter sensitivity factor S_n does not agree with the theoretical value, the measured fringe orders being significantly higher than calculation predicts. The same general observation is apparent from Dhir's earlier experimental data. This important feature of the results will be discussed separately in Chapter 5.

In the final chapter a description is given of a stressmeter application in a large buttress dam. In so far as the results allow, an assessment is made of stressmeter behaviour from the basis of existing knowledge and recommendations are given for the benefit of any similar applications in the future. It may be noted here that it has not been possible to discuss applications of the photoelastic stressmeter to reinforced and prestressed concrete in this account.

The thesis concludes by discussing the implications of the most important results obtained from the present work and suggestions for further study are put forward.

CHAPTER 3

The Effects of Shrinkage on the Photoelastic Stressmeter

3.1. Introduction

Since it is not possible to match the physical properties of the stressmeter and host concrete it is to be expected that shrinkage, thermal and creep deformations will produce spurious stresses in and around the inclusion. The preliminary results already referred to have indicated that there is only a small response to each of these effects but more quantitative evidence is clearly required.

Some aspects of the shirnkage problem have been referred to by Dhir[25] who gives results from reinforced concrete columns involving differential shrinkage. In this case the gradients of deformation produce internal concrete stresses and as far as an inclusion is concerned the stress system is the same as that caused by an external load.

The problem of differential or "secondary" shrinkage is different to the other case involving "primary" shrinkage. In this sense, primary shrinkage defines the isotropic physical contractions associated with unrestrained shrinkage. It is the primary shrinkage component which will cause a spurious stressmeter reading and this can clearly occur with or without the presence of an external load. This shrinkage increment of the total stressmeter reading must be identified if the device is to be used for measuring true internal stresses, i.e. those stresses which would exist in the absence of the inclusion.

In practice it is difficult to isolate primary and secondary effects since shrinkage gradients will always occur as drying proceeds through the thickness of the concrete structure or test-piece. In the later stages of drying these gradients will be reduced and the differential shrinkage effects will become less significant.

In the absence of an external load the expected stressmeter response to primary shrinkage will be as follows. Since the shrinkage deformations are the same in all directions they will induce a symmetrical distribution of radial and hoop stresses in the circular inclusion. To maintain equilibrium a similar distribution of stress will occur in the surrounding matrix. In the annular stressmeter this form of stress distribution produces concentric isochromatic fringes around the central hole, a pattern which is ambiguous with a two-dimensional hydrostatic stress condition produced by external loads. (As far as the solid stressmeter is concerned no readings will be produced in these circumstances; the fringe pattern will not change from zero since a homogeneous state of compression and hence zero principal stress difference will exist in the glass inclusion.)

If an external load is also present (and this might include a component due to differential shrinkage) then the annular stressmeter pattern will be produced by the resultant of two superposed stress systems. The individual increments will be difficult to separate at any arbitrary point in the stressmeter pattern; in general the principal stresses in the glass due to external loading will differ in direction to the stresses produced by primary shrinkage.

The only exceptions will be along the axes of symmetry of the pattern where the fringe order increments will be directly additive. (Along the axes of symmetry, the shear stress $\tau_{r\theta}'$ is zero; the radial and hoop stress components σ_r', σ_θ' respectively then take principal values). This property suggests a method of separating the stress components but the magnitude of the shrinkage stress increment must still be known before p, the required major principal stress due to external load, can be found. In addition the problem of identifying the minor principal stress q will still remain.

The comments made so far have not taken into account the effects of localised creep or relaxation which may occur simultaneously with the development of shrinkage; its effect will be to relieve the stresses in the concrete and inclusion. Creep will thus oppose the generation of significant

shrinkage stresses in the stressmeter, and although in some cases this may be beneficial, the effect in general only complicates the problem.

It is clear that the identification of shrinkage fringe order increments in a baded stressmeter will present several difficulties. It would appear that the problem cannot be generalised and in principle each installation will have to be considered in terms of the appropriate shrinkage changes, applied stresses and creep deformations. Since so little is known, it would seem reasonable to begin an investigation of shrinkage effects with an assessment of the orders of magnitude involved in a stressmeter before it is subject to stresses from external loads. It is possible to calculate a "worst condition" by a simple elastic analysis of the deformations and stresses which would occur in the absence of creep or relaxation and this condition can be compared with practice by observing the growth of shrinkage fringe orders in laboratory specimens. A more rigorous study of what is essentially a time-dependent phenomenum is beyond the scope of the present discussion.

Subsequently it should be possible to consider the additional problem produced by superposing stresses from an external load. If the shrinkage fringe order distribution is known the resultant fringe pattern produced by a controlled external load can be investigated and referred to the appropriate theoretical solution available from the Hiramatsu-Barron equation (2.2). In the examples discussed below the external loading has been restricted to a simple uniaxial compressive stress applied to a rectangular section element or slab.

3.2. An Elastic Analysis of the Shrinkage Problem

In the simplest analysis of shrinkage stresses the host material is assumed to be elastic, homogeneous and isotropic throughout the time of the shrinkage change. It will be appreciated that this assumption is necessarily unrealistic in concrete but non-elastic effects will tend to oppose the growth of shrinkage stresses and the elastic analysis will therefore describe

the worst possible condition as far as the inclusion is concerned. The method of calculation is essentially the familiar "shrink-fit" problem of two concentric cylinders; as before, compressive stresses will be given positive signs.

Consider the annular stressmeter outer radius a, inner radius b, elastic properties E', μ', surrounded by an infinite host material, elastic properties E, μ, experiencing a uniform primary shrinkage strain δ.

Because of the mismatched elastic properties and the absence of shrinkage in the inclusion a localised boundary pressure, or radial compressive stress, is set-up at the interface between the two materials. (The effect of the out-of-plane restraint at the interface is assumed to be negligible.) This radial stress is designated p_s and it produces a radial displacement u_r' at the outer perimeter of the inclusion. Associated with the displacement are inclusion stress components σ_r', σ_θ' ($\tau_{r\theta}' = 0$, because of geometrical and stress symmetry). The system is shown diagrammatically in Figure 3.1.

At the same time the free shrinkage of the concrete is restrained by the inclusion; the stress p_s only allows the limited interface displacement u_r and localised stresses σ_r, σ_θ, ($\tau_{r\theta} = 0$) are produced in the concrete. Thus for the host material:

$$u_r = \int_{r=(a-\delta a)}^{r=\infty} \varepsilon_r \, dr = \frac{1}{E} \int_a^\infty (\sigma_r - \mu\sigma_\theta) d\theta \qquad (3.1)$$

For the inclusion:

$$u_r' = \int_{r=0}^{r=a} \varepsilon_r' \, dr = \frac{1}{E'} \int_o^a (\sigma_r' - \mu'\sigma_\theta') d\theta \qquad (3.2)$$

For compatibility:

$$\delta a = u_r + u_r'$$

therefore:

$$\delta a = \frac{1}{E} \int_a^\infty (\sigma_r - \mu\sigma_\theta) d\theta + \frac{1}{E'} \int_o^a (\sigma_r' - \mu'\sigma_\theta') d\theta \qquad (3.3)$$

The stresses σ_r, σ_θ, σ_r', σ_θ' can be found from the general axi-symmetric stress function[53]:

$$\sigma_r = \frac{A}{r^2} + B(1 + 2 \log r) + 2C \tag{3.4}$$

$$\sigma_\theta = -\frac{A}{r^2} + B(3 + 2 \log r) + 2C \tag{3.5}$$

The same equations can be used for σ_r', σ_θ'. The constants A, B, C, A', B', C', remain to be found from the boundary conditions for each material.

In the host material: $\sigma_r = \sigma_\theta = 0$ when $r = \infty$

$\sigma_r = p_s$ when $r = a$

therefore $A = p_s.a^2$, $B = C = 0$

So $\sigma_r = +\frac{p_s a^2}{r^2}$, $\sigma_\theta = -\frac{p_s a^2}{r^2}$ (3.6)

For the inclusion: $\sigma_r' = p_s$ when $r = a$

$\sigma_r' = 0$ when $r = b$

therefore $A' = -\frac{p_s.a^2b^2}{(a^2-b^2)}$, $C' = +\frac{p_s a^2}{2(a^2-b^2)}$

$B' = 0$

(The zero value for B' follows from an independent consideration of the displacements in the general axi-symmetric stress problem[53]).

Therefore $\sigma_r' = -\frac{p_s a^2}{(a^2-b^2)}\left[\frac{b^2}{r^2} - 1\right]$ (3.7)

$\sigma_\theta' = +\frac{p_s.a}{(a^2-b^2)}\left[\frac{b^2}{r^2} + 1\right]$ (3.8)

Substituting equations (3.6)-(3.8) into equation (3.3), integrating and rearranging terms gives:

$$p_s = \frac{\delta . E . E' (a^2 - b^2)}{E\left[(a^2+b^2)+\mu'(b^2-a^2)\right] + E'\left[(a^2-b^2)(1+\mu)\right]} \qquad (3.9)$$

The interface stress p_s produced by a given shrinkage change δ can thus be found; the concrete and inclusion stresses follow directly. The resulting stress distribution through the inclusion and the surrounding concrete is shown in Figure 3.2. The tensile values of σ_θ given by equation (3.6) are clearly apparent. It can be seen that the localised stresses in the host material decrease parabolically with distance from the inclusion and the disturbance level of stress falls to less than 5 per cent of the peak value at a distance of 4a.

The stresses σ_r', σ_θ' produce a fringe order distribution in the glass inclusion which can be expressed by the modified stress optic law:

$$N_s = (\sigma_1' - \sigma_2') \frac{l_g}{f_g} = (\sigma_\theta' - \sigma_r') \frac{l_g}{f_g}$$

where N_s = the fringe order due to shrinkage

l_g = the optical path length through the inclusion (in a transmitted polarised light system the optical path length is equal to the axial length of the inclusion)

f_g = material fringe value defined in Section 2.5.1.

From equations (3.7)(3.8):

$$(\sigma_\theta' - \sigma_r') = \frac{2 . p_s . a^2 . b^2}{r^2 (a^2 - b^2)} \qquad (3.10)$$

therefore: $$N_s = k_s \cdot \frac{b^2}{r^2} \qquad (3.11)$$

where $$k_s = \frac{2 . a^2 . l_g . p_s}{f_g (a^2 - b^2)} = 2.08 \frac{l_g}{f_g} \cdot p_s .$$

The fringe order distribution is thus parabolic with the peak value occurring at the edge of the axial hole where $\frac{r}{b} = 1.0$. The distribution is shown in Figure 3.3.

For arithmetical convenience equation (3.9) can be rewritten;

$$\frac{p_s}{\delta} = \frac{12.E.E'}{E\left[13-12\mu'\right] + 12E'\left[1+\mu\right]} \qquad (3.9a)$$

Using this expression the relationship between $\frac{p_s}{\delta}$ and the modular ratio $\frac{E'}{E}$ can easily be drawn for various Poisson's Ratio conditions, as shown in Figure 3.4. The values of $\frac{p_s}{\delta}$ are not significantly affected by small variations in the combinations of Poisson's Ratio.

The master curves of Figures 3.4 enable the shrinkage fringe order to be determined at any point in the stressmeter for a known condition of primary shrinkage change and elasticity. Consider for example two cases, representing reasonable extremes for concrete, where:

(a) $E = 2.0 \times 10^6$ p.s.i. $\qquad \mu = 0.20$

(b) $E = 6.0 \times 10^6$ p.s.i. $\qquad \mu = 0.20$

The shrinkage change in both cases is 400 με.

In (a) the modular ratio becomes $\frac{E'}{E} = 5.0$. From the curve for $\mu = \mu' = 0.20$ (no significant error will be introduced by taking $\mu' = 0.20$ in comparison with $\mu' = 0.22$) the value of $\frac{p_s}{\delta} = 1.45 \times 10^6$ (in stress units) is obtained. Thus:

$$p_s = + 400 \times 10^{-6} \times 1.45 \times 10^6 = + 580 \text{ p.s.i.}$$

If the annular stressmeter constants are $l_g = 1.5$ in., $f_g = 1220$ p.s.i./fr./in. Then:

$$k_s = + \frac{2.08 \times 1.5 \times 580}{1220} = +1.48$$

From Figure 3.3, the maximum fringe order occurs at $\frac{r}{b} = 1.0$ where $\frac{N_s}{k_s} = +1.0$. Therefore $N_s = +1.48$ fringes.

(The fringe order at any other point in the glass can be obtained in a similar manner. The two significant identification points recommended by Dhir are marked in Figure 3.3.)

In case (b) the same process gives $\frac{E'}{E} = 1.67$, $\frac{p_s}{\delta} = 3.425 \times 10^6$ p.s.i., $k_s = +3.50$

$$N_{s\ max} = +3.50 \text{ fringes}$$

The concrete with the highest E value clearly produces a greater response in the stressmeter for a given shrinkage change; this could be expected from an initial qualitative assessment of the problem. In both cases the fringe orders are by no means insignificant.

It is also possible to consider the lower limit of shrinkage which might be detected photoelastically in the annular stressmeter. Beginning with a uniform condition of zero stress throughout the glass inclusion the smallest shrinkage fringe order at the inner edge ($\frac{r}{b} = 1.0$) which can be measured with confidence will be approximately +0.5 fringe. In practice a small negative residual fringe order usually exists at this point; its magnitude is approximately 0.25 fringe (deduced from observations with a double sensitivity element - see Section 3.6.3.). The smallest effective shrinkage fringe order; will therefore be (0.5 + 0.25) = + 0.75 fringe.

In the standard stressmeter element (length 1.5 in.) the corresponding stress increment will be:

$$\text{At } \frac{r}{b} = 1.0,\ \sigma_\theta' = + \frac{N_s}{l_g} \cdot fg = + \frac{0.75 \times 1220}{1.5}$$

The required interface stress p_s can be found by rearranging equation (3.8) for the point $\frac{r}{b} = 1.0$:

$$p_s = + \frac{\sigma_\theta'(a^2-b^2)}{2a^2}$$

Since $\frac{a}{b} = 5.0$, $p_s = \frac{+610 \times 24}{2 \times 25} = 292$ p.s.i.

Figure 3.4 enables the shrinkage change δ associated with this interface stress level to be determined.

For a low modulus concrete, e.g. $E = 2.0 \times 10^6$ p.s.i.,

$$\frac{p_s}{\delta} = 1.45 \times 10^6 \text{ p.s.i.}$$

therefore $$\delta_{min} = \frac{292 \times 10^{-6}}{1.45} \approx 200 \ \mu\varepsilon$$

For a high modulus concrete e.g. $E = 6.0 \times 10^6$ p.s.i.

$$\frac{p_s}{\delta} = 3.425 \times 10^6 \text{ p.s.i.}$$

therefore $$\delta_{min} \approx 80 \ \mu\varepsilon$$

The standard stressmeter will therefore be relatively insensitive to shrinkage in low modulus concretes but the lower limit of shrinkage response will decrease as the host modulus increases.

The analysis and numerical examples have been discussed without any reference to creep effects. Considered as an elastic problem, the actual shrinkage response of the stressmeter will be exaggerated, but with no quantitative knowledge of the relaxation produced by creep it is not possible to estimate the degree of exaggeration involved.

3.3. The Thermal Mismatch Problem

The shrinkage problem is directly analogous to the condition produced by a change of environment temperature. The coefficients of expansion and the elastic constants of the inclusion will not be matched to the properties of the concrete and the restraints involved during thermal expansions or contractions will also produce spurious stresses in both materials.

In the steady state condition, i.e. no temperature gradients through the inclusion-concrete system, the interface stress p_t is given by:

$$p_t = \frac{t(\alpha-\alpha')EE'(a^2-b^2)}{E\left[(a^2+b^2)+\mu'(b^2-a^2)\right]+E'\left[(a^2-b^2)(1+\mu)\right]} \qquad (3.12)$$

where t = the change in temperature

α, α' = the coefficients of linear expansion for the concrete and inclusion respectively

Equation (3.12) can be derived in an exactly similar manner to equation (3.9); in the thermal equation the sign of the term $t(\alpha-\alpha')$ may or may not take the sign of the earlier shrinkage term δ.

Comparing equations (3.9) and (3.12) for similar conditions of elasticity and geometry it is apparent that:

$$\frac{p_s}{\delta} = \frac{p_t}{t(\alpha-\alpha')} \qquad (3.13)$$

The relationship between $\frac{p_t}{t(\alpha-\alpha')}$ and modular ratio $\frac{E'}{E}$ is therefore expressed by the curves already given in Figure 3.4. Similarly the fringe order distribution in the inclusion takes the same form as before but attention must be paid to the sign of p_t. If a temperature rise is involved and $\alpha>\alpha'$ then p_t will occur as a tensile interface stress producing corresponding tensile values of σ_r' and σ_θ'. (For consistency of sign convention the temperature rise t would require a negative sign in this discussion). Assuming that the boundary adhesive around the stressmeter can withstand tensile stresses, a state of tension in the glass would be revealed by the photoelastic identification technique. A decrease in temperature would clearly involve a state of compression in the inclusion.

It is worth considering the orders of magnitude involved. The coefficient of expansion for the stressmeter (soda-lime glass $\alpha' = 5 \times 10^{-6}/^{\circ}F$) is at the lower end of the coefficient range published for concrete[55], the

highest values being of the order of $\alpha \simeq 8 \times 10^{-6}/^{\circ}F$. Suppose a temperature rise of $50^{\circ}F$ occurs (which would not be unreasonable in an outdoor location in the British Isles) and the appropriate elastic, geometric and optical parameters are the same as the shrinkage examples previously considered. The terms become:

$$t(\alpha-\alpha') = -50 \times (8-5) \times 10^{-6} = -150\ \mu\varepsilon$$

Case (a): $E = 2.0 \times 10^{6}$ p.s.i., $\mu = 0.20$

$$\frac{E'}{E} = 5.0, \quad \frac{p_t}{t(\alpha-\alpha')} = +1.45 \times 10^{-6} \text{ p.s.i.}$$

therefore $p_t = -218$ p.s.i.

(This tensile stress could be tolerated by most concretes and the adhesive bond around the stressmeters).

From Figure 3.3,

$$N_{t_{max}} = -\frac{2.08 \times 1.50 \times 218}{1220}$$

$$= -0.56 \text{ fringe}$$

Case (b): $E = 6.0 \times 10^{6}$ p.s.i. $\mu = 0.20$

$$\frac{E'}{E} = 1.67, \quad \frac{p_t}{t(\alpha-\alpha')} = +3.425 \times 10^{6} \text{ p.s.i.}$$

$$p_t = -515 \text{ p.s.i.}$$

This tensile stress is of the same order as the tensile strengths quoted for various concretes[56] but assuming cracking does not occur the maximum fringe order becomes:

$$N_{t_{max}} = -1.32 \text{ fringe.}$$

Although the result in case (a) is unlikely to be significant, bearing in mind the parabolic distribution with radius, case (b) clearly involves an appreciable fringe order.

As with the shrinkage problem, non-elastic behaviour will oppose the growth of thermal fringe orders, but in some cases the second steady state temperature condition may be achieved in a short period of time. The effects of creep and the degree of exaggeration involved in the elastic analysis will then be reduced and the magnitude of the tensile σ_r stress component may become critical. It should be remembered that the arithmetical examples quoted here consider liberal circumstances which may not occur in practice. In many cases the temperature change is unlikely to be as large as $50^{\circ}F$, the coefficient of expansion of the concrete may also be more close to that of the glass.

Further discussion of the thermal problems will be reserved since it is currently included in another project[51].

3.4. Superposition of Shrinkage and External Load Stresses

In general the distribution of stress in the stressmeter will be the result of superposed systems from shrinkage, thermal and external load effects. The resultant fringe pattern will be defined by:

$$N_T = (\sigma_1' - \sigma_2')_T \cdot \frac{l_g}{f_g} \qquad (3.14)$$

where N_T = the resultant fringe order at a given point

$(\sigma_1' - \sigma_2')_T$ = the resultant principal stress difference at the same point.

l_g, f_g are defined as before.

The term $(\sigma_1' - \sigma_2')_T$ can be found by superposing the stress components due to shrinkage and thermal effects $(\sigma_r'_s, \sigma_\theta'_s, \tau_{r\theta}'_s)$, $(\sigma_{r_t}', \sigma_\theta't, \tau_{r\theta}'t)$ respectively, on the stress components $\sigma_r'_L$, $\sigma_\theta'_L$, $\tau_{r\theta}'_L$ due to external load. From Sections 3.2, 3.3:

$$\sigma_r'_s, \sigma_{r_t}' = -(p_s, p_t) \frac{a^2}{(a^2-b^2)} \left[\frac{b^2}{r^2} - 1\right] \qquad (3.7)$$

$$\sigma_\theta{}'_s,\ \sigma_\theta{}'_t = +(p_s,\ p_t)\ \frac{a^2}{(a^2-b^2)}\ \left[\frac{b^2}{r^2}+1\right] \qquad (3.8)$$

$$\tau_{r\theta}{}'_s = \tau_{r\theta}{}'_t = 0$$

For external stresses p, q, produced by the applied load, the stress components are:

$$\sigma_{r_L}{}' = (p+q)\left[2A'_o + \frac{B'_o}{r^2}\right] - (p-q)\left[\frac{6B'_2}{r^4} + 2C'_2 + \frac{4D'_2}{r^2}\right]\cos 2\theta \qquad (3.15)$$

$$\sigma_\theta{}'_L = (p+q)\left[2A'_o - \frac{B'_o}{r^2}\right] + (p-q)\left[12A'_2 r^2 + \frac{6B'_2}{r^4} + 2C'_2\right]\cos 2\theta \qquad (3.16)$$

$$\tau_{r\theta}{}'_L = (p-q)\left[6A'_2 r^2 - 6B'_2 r^{-4} + 2C'_2 - \frac{2D'_2}{r^2}\right]\sin 2\theta \qquad (3.17)$$

The constants A_o', A_2', B_o', B_2', C_2', D_2' are written here with Barron's[38] modified notation of the original Hiramatsu[36] definitions. Thus the resultant stress components are given by:

$$\sigma_r{}'_T = \sigma_{r_s}{}' + \sigma_{r_t}{}' + \sigma_r{}'_L \qquad (3.18)$$

$$\sigma_\theta{}'_T = \sigma_\theta{}'_s + \sigma_\theta{}'_t + \sigma_\theta{}'_L \qquad (3.19)$$

$$\tau_{r\theta}{}'_T = \tau_{r\theta}{}'_L \qquad (3.20)$$

The principal stresses $\sigma_1{}'_T$, $\sigma_2{}'_T$ at the point (r,θ) can now be found:

$$\sigma_1{}'_T,\ \sigma_2{}'_T = \frac{(\sigma_r{}' + \sigma_\theta{}')}{2}_T \pm \tfrac{1}{2}\left[(\sigma_r{}' - \sigma_\theta{}')^2_T + 4\tau_{r\theta_T}{}'^2\right]^{\frac{1}{2}} \qquad (3.21)$$

Hence the principal stress difference at the point is:

$$(\sigma_1{}' - \sigma_2{}')_T = \left[(\sigma_r{}' - \sigma_\theta{}')_T^2 + 4\,\tau_{r\theta}{}'^2_T\right]^{\frac{1}{2}} \qquad (3.22)$$

Using equations (3.7)-(3.8) (3.15)-(3.20) and simplifying terms:

$$(\sigma_r{}' - \sigma_\theta{}')_T = k_1(p+q) - k_2(p-q)\cos 2\theta - k_4\,(p_s+p_t) \qquad (3.23)$$

$$2\tau_{r\theta}{}'_T = k_3 (p-q) \sin 2\theta \qquad (3.24)$$

where
$$k_1 = 2\frac{B_c}{r^2}$$
$$k_2 = 4\left[3A_2 r^2 + 3\frac{B_2}{r^4} + C_2 + \frac{D_2}{r^2}\right]$$
$$k_3 = 4\left[3A_2 r^2 - 3\frac{B_2}{r^4} + C_2 - \frac{D_2}{r^2}\right] \qquad (3.24a)$$
$$k_4 = \frac{2a^2b^2}{r^2(a^2-b^2)}$$

Thus:

$$(\sigma_1{}'-\sigma_2{}')_T = \left[\{k_1(p+q)-k_2(p-q)\cos 2\theta - k_4(p_s+p_t)\}^2+k_3{}^2(p-q)^2\sin^2 2\theta\right]^{\frac{1}{2}} \qquad (3.25)$$

Equation (3.25) is the same as equation (2.2) for stresses due to p and q only except for the modification term $k_4(p_s+p_t)$.

The interpretation technique used by Dhir[21] relies on the (p,q) fringe pattern profile to evaluate the ratio $\frac{q}{p}$; in addition, the stressmeter sensitivity factor, S_n varies with fringe pattern profile. The term $k_4(p_s+p_t)$ clearly modifies the required (p,q) fringe pattern; an infinite number of profiles can be derived from equations (3.25)(3.14) for all possible combinations of p, q, p_s, p_t. It follows that the profile identification technique will give erroneous results when significant shrinkage and thermal stresses are present in the annular glass inclusion.

Equation (3.25) shows that the individual applied stresses p,q, can only be found from one measurement on the fringe pattern if the ratio $\frac{q}{p}$, and the term (p_s+p_t) are known independently. (This statement is demonstrated in Section 3.6.4. below). If only (p_s+p_t) is known then two measurements at different points on the fringe pattern will be required before p and q can be found separately.

It may be noted at this point that the above solution of the superposition problem is not exact as far as the inclusion stresses are concerned because equations (3.7) (3.8) (3.15) - (3.17) do not take into account othereffects which will be discussed in Chapter 5.

3.5. Primary Shrinkage Tests

A simple laboratory test has been carried out to consider the shrinkage fringe orders which might occur in practical circumstances. From the preceding discussion, the worst effects are to be expected in high modulus, and therefore high strength, concrete mixes which show rapid shrinkage; three such mixes have been considered for test purposes.

The first problem is to create a test-piece which approximates to an infinite plate shrinking onto the stressmeter element without significant differential effects occurring through the thickness. Thus a circular slab or disc with a thickness to match the axial length of the stressmeter element should be least affected by differential shrinkage. (The photoelastic pattern in the stressmeter gives an integrated response to stress components in planes perpendicular to the stressmeter axis.) The diameter of the disc needs to be consistent with the extent of the stress disturbance revealed in Figure 3.2.

In addition, the maximum aggregate size used in the mix will be limited by the thickness of the disc; it is general practice to restrict the aggregate size to a maximum of one-quarter of the smallest dimension of the concrete member. This presents no problem with a disc thickness equal to the standard stressmeter length (1.5 in.) since a $\frac{3}{8}$ in. aggregate can be used and this size is frequently employed in high strength mixes. It is also apparent from Dhir's practical observations in loaded concrete specimens[24] that a $\frac{3}{8}$ in. aggregate will not produce any significant localised disturbances in the stress distribution of the inclusion.

Considering these points, a series of discs were prepared for the high strength mixes specified in Tables 3.1 and 3.2 (mixes A, B, C). River sand and river gravel aggregates were used. Disc details are shown in Figure 3.5.

To eliminate the effects of early plastic shrinkage the stressmeters were not applied until the specimens were eight days old. (The discs were polythene wrapped for seven days after casting before instrumentation and subsequent shrinkage in a known laboratory environment.) The stressmeters (length 1.5 in., diameter 1.25 in.) were bonded in position in the usual manner with a filled epoxy adhesive available commercially for this purpose*; a constant radial thickness of resin was used ($\frac{1}{16}$ in., equivalent to $\frac{a}{10}$ for these stressmeters).

Shrinkage was measured with an 8 in. Demec gauge on both sides of each disc along four diametrical gauge lengths. According to the elastic analysis the stress disturbance caused by the inclusion does not extend far enough to affect strains measured on the Demec gauge length. (This feature was subsequently confirmed by shrinkage measurements on identical discs without stressmeters.)

3.5.1. Results

The observed shrinkage changes from discs with stressmeters are summarised in Figure 3.6. Laboratory temperatures and relative humidities were measured with a whirling hygrometer and hygrometric charts[83]. For brevity, only the results from four representative gauge lengths on each disc are shown in Figure 3.6. An example of a laboratory data sheet is given in Appendix 1 (Table A.1.1)

It can be seen that the shrinkage varied between 300 με and 500 με after 65 days; in each case shrinkage proceeded at a slow rate after forty days. In general the readings showed the expected radial symmetry although an appreciable scatter occurred in the results from mix A.

---

*Horstman "Twin Pack" Adhesive.

Although well-defined shrinkage changes were thus successfully produced no significant changes occurred in the stressmeter fringe patterns. From the elastic calculation a change of at least +2.30 fringes would be expected at the inner edge ($\frac{r}{b} = 1.0$) assuming that the elastic modulus of each mix was approximately $E = 5.0 \times 10^6$ p.s.i. In two cases (mixes A and B), the zero condition in the stressmeter was maintained throughout the observation period.

An unidentifiable disturbance was produced in the stressmeter pattern of mix C after approximately twenty days but the change could not be related to any internal or external system of stress. The isoclinics (indicating stress directions) were discontinuous, and the low order isochromatics (indicating stress magnitudes) were erratically distributed. Such behaviour is consistent with stress variations in magnitude and direction through the thickness of the photoelastic test-piece, (Frocht[28]). It is not known how the disturbance would affect the response of this stressmeter to an external load but similar experiences with other rock and concrete specimens have shown that systematic behaviour is soon achieved once the stresses due to external load dominate the initial low order disturbances.

These results have shown that the stress distribution predicted by the elastic analysis bears no resemblance to the practical circumstances involved in these tests, a conclusion which is consistent with comments made by previous users. If the stresses are absent from the inclusion the associated stresses in the concrete must also be absent. Furthermore, it would seem reasonable to expect that no significant response will be produced in more general conditions involving stressmeters applied in a similar manner to concrete mixes of lower strength.

The test circumstances in this instance do not allow any explanation for the observed results but they serve to emphasise that the time-dependent properties of the combined concrete-epoxy system around the stressmeter probably dominate the shrinkage stress process.

3.6. Test-Pieces for the Superposition of Shrinkage and Loading Stresses

Considering the absence of a shrinkage response in the disc tests it might be expected that the superposition problem will not exist in similar practical circumstances and the stressmeter fringe patterns generated by external loads of short duration should be independent of preceding shrinkage changes in the host material. This point was verified in additional tests on rectangular specimens which were prepared before the results from the disc tests became apparent. The response to shrinkage was again negligible despite using double sensitivity stressmeter elements, but the rectangular specimens revealed two important subsidiary features concerning:

(a) the uniaxial stress sensitivity factor of the annular stressmeter in an elastic low modulus material.

(b) the behaviour of the epoxy resin adhesive at temperatures above 80°F.

The first feature will be discussed separately in Chapter 5; the second feature may be relevant to future shrinkage investigations and the test observations will therefore be described below. Clearly the performance of the epoxy adhesive is fundamental to any stressmeter application and the implications of these observations will not be restricted to shrinkage problems.

3.6.1. Specimen Details and Observations

A family of six identical specimens was prepared from a fine aggregate mix intended to show large rapid shrinkage strains. In this instance coarse aggregate was omitted from the mix to simplify the experimental conditions. Mix details are included in Tables 3.1 and 3.3 (mix F); specimen dimensions are indicated in Figure 3.7

All specimens were polythene wrapped for the first seven days before applying Demec gauge points to the two wide faces. At this stage access holes for the later stressmeters were diamond drilled and sealed off to restrict

drying from the hole bore. The specimens were then transferred to an automatically controlled test room maintained at 80°F, 50 per cent relative humidity. Before transfer one specimen was coated with a thick layer of bees wax to retard shrinkage. The wax contained a resin additive to improve handling properties.

The subsequent shrinkage characteristics are shown in Figure 3.10. The open square points in this graph refer to the mean strain changes from one of the fully exposed specimens (F1-2); no significant differences were observed in the other five test-pieces.

It was originally intended to apply annular stressmeters at intervals in the shrinkage process so that consideration could also be given to age effects in the stressmeter response to shrinkage and external load. The wax coated specimen was intended to provide a comparison base for age effects independent of significant shrinkage changes. The first stressmeter was therefore applied to one of the exposed specimens (F1-1) after a steady state temperature condition had been achieved in the controlled test chamber. An identical stressmeter was applied to the wax coated specimen (F1-6) soon afterwards.

A low fringe order disturbance similar to that already described for the mix C specimen in Section 3.5, was observed in the F1-1 stressmeter after approximately fifteen days exposure to shrinkage. As before, the disturbance could not be related to any uniform stress distribution along the length of the glass element. During a similar time interval no change was observed in the F1-6 stressmeter; it was apparent by this time that the wax coating was suppressing most, but not all, of the shrinkage in this specimen. (Throughout the test period the shrinkage of the wax coated specimen was 20-25 per cent of the exposed specimens).

A stressmeter was then applied to exposed specimen F1-2 and after forty-eight hours a compression load test was carried out in the rig shown in Figures 3.7, 3.8. This rig had previously been calibrated against a 0-20 tons proving ring (Figure 3.9). It was immediately apparent that the

induced stress condition in the inclusion was unstable; the stressmeter fringe pattern relaxed continuously as the applied load was increased or maintained. The effect was conspicuous at an applied stress level as low as 200 p.s.i. The same behaviour was observed in specimens F1-1 and F1-6. After considering the load applied by the rig, the deformation measurements on the concrete specimen and the known stability of the glass at this temperature, it was concluded that the epoxy adhesive was incapable of withstanding the interface stresses caused by the applied load.

All specimens were therefore withdrawn from the test chamber and returned to the lower temperature environment considered for the disc shrinkage tests. (Specimen F1-1 was damaged during this operation and was eliminated from further load tests). Specimens F1-2 and F1-6 were reloaded forty-eight hours after transfer and the response was found to be entirely consistent with later results from this series where the epoxy adhesive had not been exposed to temperatures above 72°F.

In all tests at the lower temperature the inclusion fringe orders were observed to be stable and reproducible over the duration of loading. It is concluded therefore that a significant change of rigidity occurred in the adhesive within the temperature range 72-82°F. (This may or may not be a particular property of the resin under consideration, but it seems likely that epoxy adhesives in general will show similar behaviour.)

Since the adhesive is unstable in short-term loading at temperatures above 80°F the question of its long-term stability at lower temperatures must be raised. The limited evidence available from the field investigation (see Chapter 6) suggests that the epoxy adhesives can maintain stressmeter boundary loadings for several months at temperatures below 72°F but more conclusive information will presumably be included in the full results of the independent creep investigations begun in reference[50].

As a result of the adhesive problem the effective shrinkage of the F1 series specimens must be restricted to the period after transfer from the controlled test room. The observed shrinkage during this time was approximately 350 με (see Figure 3.10), and it is to be expected from the disc test results that this change would be insufficient to produce a response in the stressmeter of specimen F1-2 (this was the only inclusion exposed to the full change). Although the stressmeter sensitivity was doubled for the F1 tests (achieved by doubling the axial length of the inclusion) no shrinkage response was produced in any of the stressmeters during a total observation period of one hundred and twenty days.

Uniaxial compression tests carried out throughout this time revealed a reproducible linear response to applied stress. A typical result is shown in Figure 3.11. Longitudinal deformations measured with the Demec gauges were also linear over the stress range considered (0-900 p.s.i.). It is shown in Chapter 4 that the 8 in. gauge length used on these specimens is not significantly affected by end conditions and the strain readings have therefore been accepted for the determination of Young's Modulus.

(The elastic modulus of the wax coated specimen F1-6 was approximately 10 per cent in excess of the observed values for the exposed specimens but the increase was not associated with a significant change in stressmeter response. The observed Young's Modulus for the exposed specimens was $E = 3.4 \times 10^6$ p.s.i. $\pm$ 6 per cent; the stressmeter sensitivity factor was S_n = 185 p.s.i./fringe $\pm$ 2 per cent (white light illumination, l_g = 3.0 in., f_g = 1220 p.s.i./fr./in). These values did not change over the effective eighty five days of the observation period. Fringe order and deformation data is detailed in Appendix 5.)

3.6.2. Thermal Strain Corrections

One extra feature of interest in the results concerns the thermal strain increments of the apparent shrinkage deformations.

The thermal expansions and contractions were clearly shown at transfer to and from the controlled test room. The initial expansion of the exposed specimens was masked by the very fast rate of shrinkage and the net expansion was restricted to approximately 50 με (14°F temperature rise).

The effect of shrinkage on the initial expansion of the wax coated specimen F1-6 can be considered to be negligible and the coefficient of thermal expansion for this mix can therefore be deduced from the observed increase in strain (95με for 11.5°F temperature rise)

$$\alpha_{F1-6} = \frac{95 \times 10^{-6}}{11.5} /^{\circ}F = 8.3 \times 10^{-6}/^{\circ}F.$$

The corresponding contraction observed on transfer to the lower temperature environment gave:

$$\alpha_{F1-6} = \frac{100 \times 10^{-6}}{17} /^{\circ}F = 5.9 \times 10^{-6}/^{\circ}F$$

Shrinkage was not dominant in the contractions of the exposed specimens at the second transfer, the mean contraction from five specimens, including the damaged F1-1, was 117 με. Thus:

$$\alpha_{F1-1 - F1-5} = \frac{117 \times 10^{-6}}{17} /^{\circ}F = 6.9 \times 10^{-6}/^{\circ}F$$

It would therefore seem reasonable to consider a value of $\alpha = 7.0 \times 10^{-6}/^{\circ}F$ for this fine aggregate mix throughout the considered test period. This figure has been used to correct the apparent shrinkage strain readings to a common temperature base of 70°F. The corrected points for the exposed and wax coated specimens show a good fit with the full line curves given in Figure 3.10. Observed strains, corrections and net strains for specimens F1-2 and F1-6 are given in Appendix Tables A.1.2., A.1.3.

3.6.3. An Example of Experimental Shrinkage Stresses

The evidence so far shows that primary shrinkage of up to 350 με produces no significant response even in the double sensitivity stressmeter when the

device is bonded in position in the customary manner. This range will cover most of the shrinkage from many concrete mixes and it might, therefore, be concluded that there is little chance of a significant response ever being produced in practical circumstances. Such a conclusion would be incorrect because significant fringe orders have since been observed for a shrinkage change of less than 500 με in a specimen originally prepared for another investigation (see Chapter 4). This specimen (F3-4) was never exposed to the higher temperature of the controlled test room but it was identical in all other details, except age, to the F1 series rectangular slabs described above.

The shrinkage history of specimen F3-4 is shown in Figure 3.12. A double sensitivity stressmeter (i.e. nominal length 3.0 in.) was applied thirty two days after casting and for the following twenty three days the specimen was involved in the loading tests described in Chapter 4. Subsequently a fringe order distribution similar to that predicted by the elastic analysis was generated around the axial hole of the inclusion; the fringe orders were observed at regular intervals with a telemicroscope and diffused light crossed circular polariscope. A plane polariscope combination was also used on several occasions to verify the radial display of isoclinics.

The development of fringe order with time at two positions at the edge of the axial hole is shown in Figure 3.12. The same fringe orders plotted with respect to shrinkage subsequent to the application of the stressmeter are shown in Figure 3.13. Experimental data is given in Appendix Tables A.1.4 and A.1.5.

The radial distribution of fringe order is illustrated by Figures 3.14, and 3.15 which refer to the four radii of the inclusion parallel and perpendicular to the long axis of the concrete specimen. The distributions along other radii lay within the limiting curves shown in these figures (the fringe orders for radii at 45° are given in Appendix Table A.1.6.).

In Figure 3.15 the observed fringe orders have been standardised for direct comparison with the theoretical parabolic distribution. A standardising factor of $\frac{1}{N_s'}$, has been applied, where N_s' is the white light fringe order at the points ($\frac{r}{b}$ = 2.0, θ = 0^o,90^o,180^o,270^o). These points were chosen because of their remote positions relative to the inner and outer surfaces of the annulus. All experimental data is given in Appendix Table A.1.6.

Several features are apparent from these results. First, the fringe orders at the points ($\frac{r}{b}$ = 1.0, θ = 0 and 180^o) were significantly higher than the fringe orders at the corresponding positions in the (θ = 90^o and 270^o) direction. (The long axis of the rectangular specimen was aligned with θ = 0^o). The maximum and minimum values of fringe order at the inner boundary consistently appeared at these four points and the circumferential distribution was thus elliptical rather than circular with respect to the axis of the inclusion, the major and minor axes of the ellipse being aligned with the principal axes of the concrete specimen. As Figure 3.12 shows, the eccentricity of the ellipse increased with time. This feature must be attributed to differential shrinkage (or a "shape effect"), an unavoidable possibility which had been appreciated when the rectangular specimens were first prepared.

Since no transverse or internal shrinkage measurements were made, the shrinkage gradients in this test-piece cannot be described quantitatively but this behaviour would appear to be consistent with the concept of a column in which drying predominantly occurs through the long faces. (The Demec gauge lines on this specimen were originally prepared so that transverse strains could be measured with a 2 in. Demec gauge. These readings were reluctantly abandoned at a very early stage after repeated practical difficulties with the available 2 in. gauge.)

Secondly, fringe orders showed a linear variation with shrinkage (see Figure 3.13) over the range covered by the effective fringe order observations, (275-500 $\mu\varepsilon$). Ignoring unknown shape effects, the elastic analysis also indicates a linear variation between fringe order and shrinkage but the orders

of magnitude are significantly different to the practical results. The observed values were approximately 40 per cent of the elastic values calculated by the method discussed in Section 3.2. The implication of this observation is that the "lag" in the inclusion stresses was produced by a relaxation process which varied linearly with stress. This would be consistent with the occurrence of creep in concrete[57] when the applied stresses are small in comparison with the ultimate strength.

It will be noted that within these comments no mention has been made of the time dependent properties of the epoxy adhesive which presumably play some part in the relaxation process. Results given by Moore[84] show that the adhesive used in these tests can exhibit significant time dependent deformation under the action of sustained compressive stress but the stresses in the adhesive layer and the properties of the epoxy resin need to be investigated in more detail before the importance of this effect can be assessed.

Thirdly, it will also be noted from Figures 3.12 and 3.13 that small negative fringe orders were measured at the edge of the axial hole when the stressmeter was first applied. This indicates the presence of residual tangential tensile stresses produced during manufacture; they decreased rapidly with distance from the hole surface and the zero fringe order condition was achieved within the distance $\frac{r}{b} \rightarrow 2.0$. The residual stresses will be responsible for a decrease in the shrinkage stresses produced at the bore of the stressmeter; the displacements of the highest fringe order points in Figure 3.15 are probably explained by this effect.

The actual shrinkage fringe order produced at the bore was therefore the sum of the residual and observed fringe orders. Hence the maximum shrinkage fringe order produced during the observation period at points ($\frac{r}{b} = 1.0$, $\theta = 0^{\circ}$ and 180°) was:

$$N_{s_{max}} = 0.50 + 2.00 = + 2.50 \text{ fringes}$$

The corresponding stress $\sigma_\theta'_{r=b}$ becomes:

$$\sigma_\theta'_{r=b} = + \frac{N_s \times f_g}{l_g} = + \frac{2.5 \times 1220}{3.0}$$

$$= + 1015 \text{ p.s.i.}$$

Referring this value to equation (3.8) for the corresponding interface stress:

$$p_s = + 490 \text{ p.s.i.}$$

For equilibrium to be maintained, it has been shown that:

$$\text{At } \frac{r}{b} = 5.0, \quad \sigma_r = + p_s, \; \sigma_\theta = - p_s \qquad (3.6)$$

Assuming that the adhesive layer does not significantly modify the boundary stresses, a maximum tangential tensile stress of 490 p.s.i. must therefore exist in the host matrix at the interface. This tensile stress is less than the nominal tensile strength of the material at the same age as indicated by the results of Brazil Tests on specimens from the F1 mix. (Figure 3.16 (data in Table A.1.7) shows that the tensile strength increased during the shrinkage observation period. When the stressmeter was first applied (day thirty two) the observed tensile strength was already in excess of 500 p.s.i.; an increase of approximately 20 per cent occurred during the succeeding seventy days).

It may also be mentioned here that the measured inner diameter (2b) of the stressmeter was 0.015 in. higher than the value of 0.250 in. required by the standard annulus ratio of 5:1. This 6 per cent increase was consistently observed in the 1.25 in. diameter annular stressmeters used throughout the present tests. With the aid of the computer programme referred to in Chapter 4, it has been shown that the change in diameter produces no significant change in the inclusion stress distribution for uniaxial applied load, except in the immediate vicinity of the hole boundary. The

fringe order measurement points for uniaxial and biaxial loadings are sufficiently remote from this boundary for the sensitivity of the device to be unaffected. For convenience a standard value of 2b = 0.250 in. has been used in the derivation of $\frac{r}{b}$ terms quoted in the results of this Chapter.

The fourth conclusion from the shrinkage stress observations refers to the radial distribution of fringe order. It is apparent from Figure 3.15 that the distribution was not truly parabolic as predicted by simple analysis. Difficulties in experimental technique and the residual stress problem prevent any firm conclusions about the distribution in the immediate vicinity of the axial hole but an increasing fringe order gradient expected from the elastic analysis was clearly apparent. Towards the outer boundary low fringe orders, and the consequent difficulty of accurate resolution, were necessarily involved but the observed deviations from the parabolic distribution are significant. This feature shows that the boundary conditions are different from those implicit in the simplified analysis, a point which will be referred to again in Chapter 5.

3.6.4. Experimental Superposition of Shrinkage and Loading Stresses

After a significant shrinkage fringe order change had occurred in the stressmeter, specimen F3-4 was loaded in uniaxial compression in the manner originally intended for the F1 series specimens previously described. In this case it was more convenient to use a universal testing machine rather than the loading rig of Figure 3.7; the test was carried out when the initial shrinkage fringe orders had the magnitude and distribution already given in Figures 3.14 and 3.15.

Fringe orders were measured at the edge of an opaque collar (external radius $\frac{r}{b}$ = 1.40 after Dhir[20]) on the diameter defined by $\theta = 90^{\circ}$-270°. The mean values of the fringe orders at the ends of the collar diameter are shown in Figure 3.17; individual readings are given in Table 3.4. The observed fringe pattern profiles which appeared with increasing load are also

given in Table 3.4, using Dhir's notation. The elastic modulus of the concrete specimen was determined from longitudinal Demec gauge readings (giving $E = 3.4 \times 10^6$ p.s.i.).

In these test conditions both the inclusion and concrete behaved as Hookean materials and the fringe order measurements were therefore expected to be linear with the external applied stress p. This was verified by the experimental points shown in Figure 3.17; the theoretical response predicted by the superposition equations (3.14) (3.25) is also shown in this Figure for comparison.

The following points refer to the arithmetical derivation of the theoretical response. Restating equation (3.25) for convenience:

$$(\sigma_1'-\sigma_2')_T = \left[\{k_1(p+q)-k_2(p-q)\cos 2\theta-k_4(p_s+p_t)\}^2 + k_3^2(p-q)^2\sin^2 2\theta\right]^{\frac{1}{2}} \qquad (3.25)$$

In this case $q = 0$, $\theta = 90^\circ$ and $p_t = 0$ (the constant test temperature was the same as the stressmeter datum temperature; see Figure 3.12). Equation (3.25) can therefore be simplified:

$$(\sigma_1'-\sigma_2')_T = \left[(k_1+k_2)p - k_4 \cdot p_s\right] \qquad (3.25a)$$

Using equations (3.24a), (3.7), (3.8) and the stress optic law:

$$k_4 p_s = (\sigma_r'-\sigma_\theta')_s = -(\sigma_\theta'-\sigma_r')_s$$

$$= -\frac{N_s f_g}{l_g}$$

Thus $$(\sigma_1'-\sigma_2')_T = (k_1 + k_2)p + \frac{N_s \cdot f_g}{l_g}$$

$$N_T = (\sigma_1' - \sigma_2')_T \frac{l_g}{f_g} = (k_1 + k_2)p \cdot \frac{l_g}{f_g} + N_s$$

$$p = \frac{(N_T - N_s)}{l_g (k_1+k_2)} \cdot f_g \qquad (3.26)$$

The term (k_1+k_2) must be determined separately; in this case it can be found conveniently by interpolation of data given by the computer programme of Chapter 4 (see below).

From the computer results:

$$\text{At } \frac{r}{b} = 1.40,\ \theta = 90^{\circ};\ (k_1+k_2) = +1.71$$

Using numerical values for all constant terms, equation (3.25) becomes:

$$p = \frac{(N_T - 1.06) \times 1220}{3.0 \times 1.71}$$

$$p = 238\ N_T - 252 \qquad (3.27)$$

The line given by this equation represents the theoretical response of the stressmeter in specimen F3-4 to a uniaxial compression stress p superposed on the stated initial shrinkage condition.

It can be seen from Figure 3.17 that the theoretical and experimental lines agree to within 7 percent and this is unexpected in view of the wider discrepancies between theory and practice previously observed in the uniaxial tests of Section 3.6.1. (In the earlier tests fringe orders were measured at point $(\frac{r}{b} = 1.60,\ \theta = 45^{\circ})$; the results are discussed in Chapter 5.)

Since fringe orders have been measured on a principal radius of the stressmeter the shrinkage increment N_s and the external load increment N_L are directly additive. The experimental N_T line may therefore be transposed as shown in Figure 3.17; by definition this line passes through the origin. The sensitivity factor expressed by this line (S_n = 222 p.s.i./fringe) is in good agreement with the value deduced from Figure 5.6, which refers to a similar stressmeter and concrete specimen in an independent uniaxial loading test.

The photographs of Figure 3.18 show the observed fringe order profiles (without the opaque collar) at two different increments of uniaxial load

superposed on the initial shrinkage condition. Without knowledge of the shrinkage fringe order distribution, these patterns would clearly be ambiguous with Dhir's illustrations for biaxial stress systems produced by external load without shrinkage (see Figures 2.1-2.5).

3.7. Conclusions

As a result of the preceding discussion the following preliminary conclusions can be made concerning the effect of shrinkage on the response of the annular stressmeter.

First, the significant response predicted by a simple elastic analysis was not observed in specimens from three high strength concrete mixes. Shrinkage changes of up to 450 με over a period of sixty five days produced no measurable response in the inclusion; this implies that any fringe order change produced by shrinkage could not have exceeded 20 per cent of the value expected from the elastic analysis.

However, a prominent response was observed in a double sensitivity stressmeter during shrinkage of 275-500 με in a special mix containing no coarse aggregate. Although differential or secondary shrinkage effects occurred in the concrete specimen it is reasonable to conclude from the observed distribution of fringe orders that the response was largely due to primary shrinkage. The magnitude of the observed response was approximately 40 per cent of the calculated value using a short-term elastic modulus obtained from separate loading tests. In comparison with this result, observations from an identical specimen in another test series gave no indication of a response to shrinkage of approximately 350 με; from these tests alone it is not possible to comment on the significance of the difference in behaviour.

Secondly, the observed shrinkage fringe orders deviate from the theoretical parabolic distribution particularly near the outer boundary of the stressmeter. It is considered that this effect was caused by the boundary conditions provided by the concrete-epoxy adhesive combination, and since the

fringe orders were produced by an integration of principal stress difference through the axial thickness, it would appear that the anomaly was significant along most of the length of the stressmeter. The test conditions do not allow further comment on the boundary conditions or the distribution of individual stress components in the glass.

Thirdly, the expected superposition of inclusion fringe orders produced by shrinkage and short-term external loads has been verified for a point on a principal radius of the stressmeter. This property provides a means of correcting a stressmeter reading for the undesirable shrinkage increments. The effect was demonstrated satisfactorily for a simple uniaxial loading condition, but in general the load fringe order increment will be a function of biaxial stresses and a single observation of fringe order on the minor principal axis of the pattern will be insufficient to determine the individual applied stress components.

The superposition of shrinkage and load increments in the stressmeter clearly produced fringe pattern profiles which were ambiguous with those illustrated by previous authorities for external biaxial stresses applied without shrinkage. The pattern profile method for identifying the applied stressratio alone is therefore unsatisfactory when shrinkage is sufficient to produce a measurable response in the annular stressmeter.

From the laboratory observations it is clear that the shrinkage response in the stressmeter cannot be predicted with accuracy at the present time. However, it seems reasonable to conclude that no measurable response will be produced in either the standard or double sensitivity stressmeters for shrinkage changes less than 250 με. This statement should apply to a wide variety of mixes including high strength concretes but it should be considered with caution until more is known about the relaxation process which clearly occurs around the inclusion during shrinkage especially in concrete at an early age. Attention should be given to the possibility of relaxation varying with environment temperature, particularly in view of the experience with the epoxy adhesive at temperatures above 80°F.

The environment temperature must also be referred to the mismatched thermal properties of the stressmeter and host material. The brief discussion of the fundamental similarity between thermal and concrete shrinkage problems has implied that the conclusions relating to shrinkage stresses will also apply to steady state thermal stresses, making due allowance for the possible state of tension which can be produced in the stressmeter by a rise in temperature. In short-term investigations with restricted creep effects, the elastic thermal analysis should be sufficient, within the limitations of the two-dimensional approach, to calculate the thermal fringe order increment of a stressmeter reading. The method has not been tested experimentally in view of a current independent investigation.

CHAPTER 4

The Stressmeter Subjected to Biaxial Stresses of Opposite Sign

4.1. Introduction

Since rocks and cementitious materials can only tolerate relatively low tensile stresses earlier laboratory work by other investigators concentrated on the calibration of the stressmeter in simple compressive stress conditions. The resulting isochromatic patterns and sensitivity characteristics have already been summarised in Chapter 2.

In practice principal stress combinations of compression and tension frequently exist in rock and concrete; if an annular stressmeter is used in such conditions the resulting distribution of isochromatics will not necessarily be similar to cases which involve two applied principal stresses both of the same sign.

The ability of the device to withstand tensile stresses will also be brought into question since significant tensile stresses can be produced at the bore and relatively small applied stresses in the host material may cause early failure of the measuring element.

At the same time tensile stresses will occur over portions of the interface between the stressmeter and host material and it is a requirement of the conventional theoretical analysis of the inclusion stresses that continuity is maintained at all points on this boundary. The stressmeter adhesive must therefore be able to withstand tensile stresses if the observed photoelastic patterns are to be compared with the existing method of calculating the inclusion stresses.

Given these circumstances it is worthwhile to consider the behaviour of the annular and solid stress meters in more detail. In theory the behaviour of the solid stressmeter should be known from Dhir's calibration data (see Figure 2.6), since the photoelastic response of the solid inclusion

is a direct function of the difference between the applied principal stresses in the host material. It is independent of the ratio between the magnitudes of the applied principal stresses.

For the annular stressmeter the photoelastic response is not independent of the applied stress ratio and the presence of a minor tensile stress in the host material can significantly effect the magnitudes and profiles of the isochromatic fringes.

Oppel[58] has described the effects of compression-tension combinations in the similar problem of the annular photoelastic strain gauge. It can be seen from Figure 4.1, that in annular discs of his geometry isochromatics for stress ratios between 1:-$\frac{2}{3}$ and 1:-1 (i.e. η values of -0.67 and -1.0 respectively) bear little resemblance to the isochromatic patterns given by Dhir for the annular stressmeter, but for conditions where the minor tensile stress is less than one-third of the major compressive stress the pattern bears a distinct resemblance to the profile in Dhir's uniaxial stress condition.

The theoretical isochromatic pattern in an annular stressmeter for any stated compression tension condition can be derived by substitution of appropriate arithmetical values into the Hiramatsu-Barron equation (2.2). This procedure becomes practicable with the aid of a computer although a full study of the various combinations which might occur in practice would clearly require extended computation directly similar to Barron's work (loc.cit.) with a two-dimensional compression stress system.

On the other hand, experimental verification of the general problem could involve several difficulties of technique. For example, the loading system would have to be capable of applying infinitely variable combinations of in-plane compression and tension to a plate of dimensions consistent with the area of influence of the stressmeter. Such a system would clearly require considerable care and effort to develop and might in itself justify a separate programme of work.

As an initial alternative a particular case can be considered by taking advantage of the singular combination of compression and tension which exists at the centre of a diametrically loaded disc. This system has the advantage of minimising the practical problem of load transmission to the test-piece, (the disc is loaded only through two diametrically opposed narrow bands at the rim) whilst the known theoretical symmetric stress distribution allows different measurement techniques to be used in comparison with the stressmeter method. In addition the disc test-piece may be turned in a vertical plane so that the load can be applied across different diameters. This property allows any directional bias to be detected either in the disc material or in the instrumentation system under test. The disc test-piece has therefore been used in the first attempt at a study of the stressmeter in an applied two-dimensional state of compressive and tensile stress.

In the investigation described below, both the annular and solid stressmeters have been used at the centres of large fine aggregate concrete discs loaded across a diameter. Surface displacements at discrete points have also bee measured with electrical resistance strain gauges and a demountable mechanical gauge (the Demec gauge). Where possible experimental measurements have been compared with the appropriate theoretical values.

4.2. Theoretical Stresses in a Loaded Disc

The theoretical stresses in an elastic homogeneous and isotropic disc line loaded across a diameter have been discussed by several authors, notably Timoshenko[54] and Frocht[30]. For discs of concrete and rock where the assumptions of linear elasticity are necessarily imperfect, the problem is continuously discussed within the context of the Brazil Test for the determination of tensile strength. A recent paper by Desayi[59] and its list of references may be quoted as an example.

In the linear elastic case the rectangular stress components at any point are given by:

$$\sigma_x = + \frac{2P'}{\pi l}\left[\frac{(R-y)}{r_1^4}\,x^2 + \frac{(R+y)}{r_2^4}\,x^2 - \frac{1}{d}\right] \tag{4.1}$$

$$\sigma_y = + \frac{2P'}{\pi l}\left[\frac{(R-y)^3}{r_1^4} - \frac{(R+y)^3}{r_2^4} - \frac{1}{d}\right] \tag{4.2}$$

$$\sigma_{xy} = - \frac{2P'}{\pi l}\left[\frac{(R-y)^2}{r_1^4}x - \frac{(R+y)^2}{r_2^4}x\right] \tag{4.3}$$

The notation is apparent from Figure 4.2, compressive stresses being given positive signs as before. Knowing these three stress components, the principal stresses at the point under inspection can be calculated either from the following equation or by the semi-graphical method using the Mohr Circle for stress:

$$p,q = \tfrac{1}{2}(\sigma_x + \sigma_y) \pm \sqrt{(\sigma_x - \sigma_y)^2 + 4\tau_{xy}^2} \tag{4.4}$$

For points along the loading diameter equations (4.1)-(4.3) can be simplified to the forms:

$$\sigma_x = - \frac{2P'}{\pi l d} \tag{4.1a}$$

$$\sigma_y = + \frac{2P'}{\pi l}\left[\frac{2}{(d-2y)} + \frac{2}{(d+2y)} - \frac{1}{d}\right] \tag{4.2a}$$

$$\tau_{xy} = 0 \tag{4.3a}$$

For the perpendicular diameter:

$$\sigma_x = - \frac{2P'}{\pi l d}\left[\frac{d^2 - 4x^2}{d^2 + 4x^2}\right]^2 \tag{4.1b}$$

$$\sigma_y = + \frac{2P'}{\pi l d}\left[\frac{4d^4}{(d^2 + 4x^2)^2}\right]^{-1} \tag{4.2b}$$

$$\tau_{xy} = 0 \tag{4.3b}$$

Equations (4.1)-(4.3) depend on an assumption of line loading which in practice cannot be ideally achieved. It is more realistic to consider the load distributed as a uniform radial stress over a short arc of the circumference. Wright[60] quoted approximate equations for the stresses on the principal diameters of the disc in such a condition; more detailed equations have since been derived by Hondros[61] as follows (with minor changes in notation):

For the loaded diameter OY:

$$\sigma_x = -\frac{2p_r}{\pi}\left[\frac{(1-\frac{r^2}{R^2})\sin 2\psi}{(1-\frac{2r^2}{R^2}\cos 2\psi+\frac{r^4}{R^4})} - \tan^{-1}\frac{(1+\frac{r^2}{R^2})}{(1-\frac{r^2}{R^2})}\tan\psi\right] \quad (4.5)$$

$$\sigma_y = +\frac{2p_r}{\pi}\left[\frac{(1-\frac{r^2}{R^2})\sin 2\psi}{(1-\frac{2r^2}{R^2}\cos 2\psi+\frac{r^4}{R^4})} + \tan^{-1}\frac{(1+\frac{r^2}{R^2})}{(1-\frac{r^2}{R^2})}\tan\psi\right] \quad (4.6)$$

$$\tau_{xy} = 0 \quad (4.7)$$

For the perpendicular diameter OX:

$$\sigma_y = +\frac{2p_r}{\pi}\left[\frac{(1-\frac{r^2}{R^2})\sin 2\psi}{(1+\frac{2r^2}{R^2}\cos 2\psi+\frac{r^4}{R^4})} + \tan^{-1}\frac{(1-\frac{r^2}{R^2})}{(1+\frac{r^2}{R^2})}\tan\psi\right] \quad (4.8)$$

$$\sigma_x = -\frac{2p_r}{\pi}\left[\frac{(1-\frac{r^2}{R^2})\sin 2\psi}{(1+\frac{2r^2}{R^2}\cos 2\psi+\frac{r^4}{R^4})} - \tan^{-1}\frac{(1-\frac{r^2}{R^2})}{(1+\frac{r^2}{R^2})}\tan\psi\right] \quad (4.9)$$

$$\tau_{xy} = 0 \quad (4.10)$$

For a small loading arc, as might be expected from a consideration of St. Venant's Principle, equations (4.5)-(4.10) are in close agreement with the corresponding line loading equations for regions remote from the loading points. At the centre of such a disc the two sets of equations agree exactly.

The simple line loading condition predicts a uniform value of tensile stress (magnitude - $\frac{2P'}{\pi dl}$) all along but perpendicular to the loading diameter OY, even as the infinite stress condition is approached at the loading point. For loading along a finite arc the tensile stress rapidly changes sign and magnitude as the loading arc is approached but an almost uniform tensile stress still exists over much of the OY diameter. A particular condition is shown in Figure 4.3, which also includes the corresponding strain distribution along the principal axes for the plane stress condition.

For both plane stress and plane strain conditions the stresses along and perpendicular to OY and OX axes take principal values since no shear stresses exist along these diametrical planes. At the extremities of the OX diameter all stress components are zero. The principal stresses at the centre of the disc are therefore given by:

$$\sigma_y = p = + \frac{6P'}{\pi dl} \quad , \quad \sigma_x = q = - \frac{2P'}{\pi dl} \tag{4.11}$$

The corresponding principal strains for the plane stress case can be found from the relations:

$$\varepsilon_1 = \frac{1}{E} (p - \mu q) \tag{4.12}$$

$$\varepsilon_2 = \frac{1}{E} (q - \mu p) \tag{4.13}$$

Equations (4.12) and (4.13) can clearly be applied to any point in the disc if the principal stresses are already known as a result of equations (4.1)-(4.3).

For a given applied load the principal stresses and strains vary continuously in magnitude and direction with co-ordinate position in the disc. The maximum variations occur near the loading points where high stresses and strains exist simultaneously with much lower values nearer the centre of the disc.

The disc is not therefore an ideal calibration member for any stress or strain sensor, but conditions may be acceptable for practical purposes if the sensor has a small zone of influence or gauge length in comparison with the gradient of the function to be measured. For instance, careful selection of dimensions will allow the use of a small inclusion stressmeter at the centre if the disc is large enough to give a reasonable approximation to a field of uniform stress over an area which can accommodate the zone of influence of the meter. Resistance strain gauges need not be restricted to the same region since they are readily available with short gauge lengths and they can therefore be applied over a much wider area of the same disc, with the qualification that discrepancies may be expected at points near the loading arcs where the strain gradients are severe. Similarly it is unreasonable to consider the Demec gauge for general strain measurements on the disc although it can be applied satisfactorily in the special case where the two location studs are equi-spaced about an axis of stress symmetry. This feature is referred to below in Section 4.6.4.

4.3. Test-Piece Details

Three test discs of a low modulus fine aggregate concrete were required to provide the optimum conditions for the stressmeter and comparison strain gauges. The mix was therefore prepared to the F specification already described in Chapter 3.

The discs were cast in fully enclosed shutters with the faces vertical; this ensured the same surface finish for the two faces of each disc. Silicone rubber dowels were bolted through the shutter to provide access holes in the

disc for the later installation of photoelastic stressmeters. This method provided minimum restraint to early shrinkage and the dowels were easily removed with the shutter after twenty-four hours.

All specimens were then laboratory stored for seven days with a small quantity of free water inside a sealed polythene wrapping. Subsequently they were matured and tested in a known laboratory environment.

The disc diameter was governed by the available testing machine; the thickness was determined by considering the strength of the disc in relation to the response of the central stressmeter, the aim being to secure a reading range of approximately 0-4 fringes without risking a tensile or buckling failure of the disc. The resulting dimensions were $23\frac{3}{8}$ in. diameter by $3\frac{1}{4}$ in. thickness (see Figure 4.4).

To provide a further calibration base for the measurement techniques two rectangular section slabs were prepared from the same concrete mix. These slabs were identical to those already described in Section 3.6.1., i.e. dimensions 15 in. x 8 in. x $3\frac{1}{4}$ in. Instrumentation details are shown in Figure 4.6 . The slabs were kept in the same environment as the discs throughout and were tested in uniaxial compression immediately before the discs.

4.4. Instrumentation Details

The disc instrumentation layout is shown in Figure 4.4, and appropriate co-ordinates are given in Tables 4.1 and 4.2. Both the annular and solid stressmeters were tested at the centre point of separate discs; resistance strain gauges were mounted at the centre point of the third disc.

As a subsidiary demonstration of the stressmeter response in conditions of non-uniform host stresses extra annular inclusions were used at discrete points in two of the discs. Since the photoelastic inclusion gives an integrated response to the surrounding stresses it will be appreciated that the results from these extra stressmeters cannot be considered for general calibration purposes.

In every case the stressmeter was bonded into a $1\frac{3}{8}$ in. diameter hole with an epoxy adhesive forty-eight hours before test. The adhesive has already been referred to in Chapter 3. The stressmeter dimensions were $1\frac{1}{4}$ in. diameter by 3 in. length.

With the exception of those gauges at the centre point of the third disc, the resistance strain gauges were bonded to the disc surface in 3-gauge 45° rosettes which were matched on each side to reveal bending effects. For convenience the rosettes were placed symmetrically to the subsidiary stressmeters and the bridge circuit was arranged to give individual gauge readings (by the "null-deflection"method).

The gauge length was selected by considering the shortest gauge which could be used without large errors from aggregate effects in the concrete discs. In this case the coarse grit sand used as the aggregate had been purposefully graded below $\frac{3}{16}$ in. (for grading details see Table 3.3), and since the majority fell within smaller size ranges gauges with $\frac{1}{2}$ in. gauge length were chosen. (This gave a disc diameter-gauge length ratio of 47:1 which was considered to be satisfactory for the strain gradients theoretically involved at the instrumented points).

It may be mentioned here that the conclusions of Binns and Mygind[62] and Cooke and Seddon[63] for bonded wire gauges suggest that the $\frac{1}{2}$ in. gauge length could involve serious erros but the overall results of this test series seem to indicate that aggregate effects were not a major source of error.

To minimise the effects of cross sensitivity foil gauges were used; all gauges were taken from one batch (resistance 120 Ω, gauge factor 2.18) and bonded to the specimen with a cold setting epoxy adhesive three days before test.

The demountable strain gauge technique (8 in. Demec gauge) was used primarily to monitor surface shrinkage before and during the test period The gauge lengths were matched on each side and diametrically arranged at

45° around the centre of the disc. Subsequently two perpendicular gauge lengths from this series were made to coincide with the principal diameters by careful orientation of the disc in the loading machine. Extra deformation measurements were thus readily accessible for comparison with the resistance strain gauge data.

The discs were numbered F5-1, F5-2 and F5-3 and the comparison slabs F3-3, F3-4. Centre point annular stressmeters were used in disc F5-1 and slab F3-4; solid stressmeters were used in disc F5-3 and slab F3-3. Active resistance strain gauges were not included in slab F3-3 but this specimen provided the base for the temperature compensating gauges of the other circuits.

4.5. Test Procedure

The slab specimens were first tested to provide the basic uniaxial calibration data for all measurement systems used on the discs. (At this stage it is assumed that the stress-strain relationship for the concrete is the same in compression and tension.) The loadingarrangement for each slab has already been described in Chapter 3 (Figure 3.7). All readings were taken under increasing load on the specimen's fourth load cycle.

Stressmeter fringe orders were obtained from a crossed circular polariscope (independent polariser and analyser) with diffused white light illumination. In the case of the solid stressmeter in slab F3-3 the 0° and 90° isoclinics were easily confirmed in the early stages of loading by converting the circular polariser and analyser to a plane polariscope system. These isoclinics were clearly seen in orientation with the major axes of the slab. (The same effect was subsequently observed in the solid stressmeter of disc F5-3).

In the disc tests the load was applied through a ball seating, flat steel platens and carbon paper strips. (An arc loading width of $\frac{5}{8}$ in. $\pm \frac{1}{16}$ in. was indicated for the eight loading diameters in the test series.) All

loading areas were dressed and cleaned before use. In each case the disc required careful alignment in the testing machine to ensure loading only along the required diameter. Eccentric loading also had to be minimised although as the results subsequently showed, this effect was never entirely eliminated.

Each disc was first loaded in the 1-1 orientation, and as before, readings were taken under increasing load on the fourth cycle. Since no attempt was being made to study the failure characteristics of the discs or stressmeters, the applied load was restricted to a maximum value which covered the normal white light fringe order reading range of the centre point stressmeters (approximately 0-4 fringes). This maximum loading produced relatively small strains in the areas of primary interest; deformation and fringe order measurements showed a linear variation with applied load.

For the subsidiary stressmeters near the loading point in discs F5-1 and F5-2 the polariscope system had to include a colour filter to identify the high fringe orders developed at the 45° reading points (approximately 7 fringes). An Ilford 606 yellow filter was used to produce a close approximation to monochromatic sodium light; this filter was separately calibrated for fringe order measurements using the method described in Section 2.5.1. As expected the filter revealed fringe orders closely similar to those observed in sodium or white light for given conditions of stress and birefringence.

For discs F5-1 and F5-2, the load test in orientation 1-1 was repeated in turn for orientations 2-2 and 4-4. In the case of disc F5-2 the compatibility requirement for the centre point could be checked by comparison of gauge readings in any two of the three disc orientations. This feature is discussed in the results. With disc F5-3 only two orientations were used; in each position the theoretical alignments of the 0° and 90° isoclinics were confirmed.

4.6. Results

Experimental results are presented graphically in Figures 4.8-4.30; test data is tabulated in Appendix 2.

4.6.1. Specimen History

Figure 4.8 shows the observed surface shrinkage of the disc and slab specimens before and during the test period. Daily readings of laboratory temperature and relative humidity were taken with the whirling hygrometer referred to in Section 3.5.1.

Throughout the twenty-three day test period shrinkage continued at a significant rate; all specimens showed a change of approximately 260 microstrains during this time. Since simultaneous temperature changes occurred the shrinkage readings necessarily include thermal strain increments but they are clearly insufficient to affect the form of the general shrinkage curve.

The shrinkage changes did not influence the stressmeter behaviour during the test period; this would be expected from the experience described in Chapter 3. Approximately ten days after application some of the stressmeters showed a small disturbance in their zero fringe orders but this could not be related to any surrounding stress system or observed shrinkage change. In the slab specimens the disturbance did not produce a significant change in stressmeter sensitivity. (Subsequent to the completion of this test series significant fringeorder changes were observed in the stressmeter of slab F3-4 but this has been discussed separately in Sections 3.6.3-3.6.4).

It is of secondary interest to record that large shrinkage strains occurred in all specimens over the period of interest between ages seven and sixty days. A small variation in measured strains occurred between the three discs and values were always lower than the corresponding strains for the slab specimens. There was no difference between the measured strains on both slabs.

4.6.2. Uniaxial Compression Tests

Figure 4.9 shows the solid stressmeter results and the longitudinal deformation measured by the Demec gauge for slab F3-3. (Experimental data is given in Appendix Table A.2.1.) It can be seen that the theoretical solution based on the Muskhelishvili equations[39] for the "welded boundary" condition clearly underestimates the response of the stressmeter to applied stress. In other words the average through-the-thickness principal stress difference created at the centre of the inclusion exceeded the theoretical value, the observed difference being approximately 21 per cent. The fringe order distribution was parabolic across the face of the inclusion the peak value occurring at the centre.. (This feature is discussed in more detail in Chapter 5.) It will also be noted that the measured fringe orders were higher than the values predicted from Dhir's earlier experimental observations (see Figure 2.6).

The Demec gauge readings indicated a linear response between stress and deformation; a small degree of in-plane and out-of-plane bending was apparent. The slope of the stress-deformation line was in satisfactory agreement with the corresponding values from the similar slab F3-4.

Figure 4.10 shows the annular stressmeter response from slab F3-4. (Experimental readings are given in Appendix Table A.2.2.) Again there is a significant difference between the theoretical and experimental sensitivities. In this case the measured fringe orders were 15 per cent in excess of the theoretical values; this result is in good agreement with the similar test-pieces described in Section 3.6.1. The theoretical results have been calculated from the Hiramatsu-Barron equation (2.2).

The resistance strain gauge and Demec gauge readings are shown in Figure 4.11. If allowance is made for the out-of-plane bending effect revealed by both series of measurements the results are consistent with each other and the Demec gauge results from slab F3-3.

Assuming that end effects did not cause significant errors in these test-pieces the results showed a linear compression stress-strain characteristic for this fine aggregate concrete within the range 0-1000 p.s.i. The three values of Young's Modulus deduced from these tests vary between $E = 3.15 \times 10^6$ p.s.i., and $E = 3.35 \times 10^6$ p.s.i. The corresponding Poisson's Ratios are 0.18-0.20.

If the further assumption is made that tension conditions involve the same elastic constants, they can be applied to the measured disc strains for comparison with the calculated stresses, or alternatively the theoretical disc strains can be computed for comparison with observed values. Both methods are included in what follows.

4.6.3. Disc Tests: Resistance Strain Gauge Results

Before considering the strain gauge data reference should be made to the effect of the finite loading strip width on the disc stresses at the points of interest. Table 4.3 compares the principal stresses at the rosette points nearest the loading strip (where the most significant effect would be expected) with the stresses calculated from the line loading condition. There is no significant difference between stresses calculated from the two boundary conditions and the simpler line loading equations have therefore been used throughout the following discussion.

Resistance strain gauge readings are shown graphically in Figures 4.12 and 4.17-4.19; examples of experimental data are given in Appendix Tables A.2.3., A.2.5, A.2.6. The full lines shown in comparison with the experimental values represent the calculated gauge readings for an assumed isotropic disc with the stated elastic constants. It will be observed that the constants obtained from the preceding uniaxial compression tests have been modified before application to disc F5-1; the reason for this is explained below (see page 75).

Before considering the centre point strain gauges and the subsidiary rosettes reference may be made to Table 4.4, which shows the calculated gauge strains for each gauge at maximum test load in the three disc orientations. In some cases the calculated maximum strains barely exceed the lower limit of resolution for the strain gauge circuit employed, i.e. 0-5 microstrains, and many of the test readings from these gauges are likely to be of limited significance. The results showed this effect and, in particular, the A rosette, orientation 2-2, has been excluded from this discussion since all three gauges were subjected to low strains.

4.6.3.(i) Centre Point Strain Gauges Disc F5-2

In disc orientation 1-1 these gauges measured principal strains ε_1 and ε_2; the results are shown in Figure 4.12, in comparison with the calculated theoretical values for an isotropic disc using the elastic constants obtained from the preceding uniaxial compression tests.

On preliminary inspection the measured and calculated strains might appear to be in reasonable agreement but allowing for bending in the usual manner the stresses calculated from the measured strains do not match the theoretical values (see Table 4.5). Specifically, the minor tensile stresses differ by 20 per cent; the major compressive stresses show a smaller difference of 7 per cent. Despite these discrepancies in the individual principal stresses it is interesting to note the coincidental agreement between the measured and calculated principal stress differences $(p - q)$.

As an alternative approach, if it is assumed that the measured strains are produced by the theoretical stresses, the calculated constants become $E = 3.55 \times 10^6$ p.s.i. $\mu = 0.29$. Although not unreasonable these values are somewhat higher than expected.

The actual constants applicable to the discs were therefore checked experimentally by preparing rectangular elements from two discs after completion of the primary tests. The gauges were protected during the dissection operation (carried out with a diamond saw) and the elements were capped before test in the manner already referred to in Chapter 3. One element carried the centre point gauges and smaller elements were prepared for the A,B rosettes (see Figure 4.15).

The centre point strain gauges were thus retested in a condition of uniaxial compression at the centre of a slab element having the same dimensions as F3-3 and F3-4. The results are shown in Figure 4.13 (experimental readings are given in Appendix Table A.2.4.); they give constants $E = 3.27 \times 10^6$ $\mu = 0.22$. These values are in satisfactory agreement with the constants previously obtained from slabs F3-3 and F3-4 ($E = 3.25 \times 10^6$ p.s.i., $\mu = 0.18$) and the discrepancies in the disc centre point strains must therefore remain.

(A further conclusion can be drawn from this rectangular element test. Demec gauge points were specially incorporated to conform with the pattern used on F3-3 and F3-4. As Figure 4.13 shows the measured strains were in good agreement with the resistance strain gauge readings after allowing for bending effects. From this test it is concluded that end effects produced no significant error when using the 8 in. Demec gauge on slab elements of this geometry.)

There is another point of interest in the centre point strain gauge results. By loading the disc along different diameters the two gauges are effectively turned about the centre of the disc and the readings in any two positions should satisfy the fundamental compatibility requirement. Expressed algebraically with the notation of this test series, the condition for compatibility at the disc centre may be written:

$$(\varepsilon_{G_1} + \varepsilon_{G_2})_{1-1} = (\varepsilon_{G_1} + \varepsilon_{G_2})_{2-2} = (\varepsilon_{G_1} + \varepsilon_{G_2})_{4-4} \qquad (4.14)$$

This geometrical relationship must be satisfied on both sides of the disc regardless of any bending or inelastic behaviour. Figure 4.14 shows the measured strains considered in this manner; on both sides of the disc the sum of the readings from any perpendicular point falls within a narrow band of results and this can be considered to satisfy the compatibility condition within the limits of the measuring system. Thus, it may be concluded that the strain gauges functioned satisfactorily at the centre of the disc.

4.6.3.(ii) Rosette Readings

The subsidiary rosette readings, represented by the mean observed strains at the maximum test load, are given in columns 4, 5 and 6 of Table 4.5. These strains have been obtained by plotting the readings from each gauge against disc load; for corresponding gauges from both sides of the disc lines have been drawn through the experimental points and the mean value taken at the maximum test load. These values have been used to calculate the stresses at the rosette points for comparison with stresses derived from the theoretical equations (4.1)-(4.3).

Of the several methods available for calculating the principal strains from the rosette readings, a simple graphical construction due to Murphy[64] has been used. The magnitudes and directions of the principal strains are given from the Mohr Circle produced by this construction; using the constants available from the earlier uniaxial tests the principal stresses are then easily found from the relations:

$$p = \frac{E}{(1 - \mu^2)} (\varepsilon_1 + \mu\varepsilon_2) \qquad (4.15)$$

$$q = \frac{E}{(1 - \mu^2)} (\varepsilon_2 + \mu\varepsilon_1) \qquad (4.16)$$

Table 4.5 shows that the major principal stresses derived in this manner are generally in reasonable agreement with the theoretical values but significant differences again occur in the minor principal stresses. In four cases the orientations of the major principal stresses are also appreciably different.

The subsequent behaviour of two rosette pairs on dissected disc elements confirmed the assumed values of elastic modulus and Poisson's Ratio used in Table 4.5 ($E = 3.25 \times 10^6$ p.s.i. $\mu = 0.18$). Details are given in Figure 4.16. The B rosettes from disc F5-2 gave results ($E = 3.25 \times 10^6$ p.s.i. $\mu = 0.19$) in satisfactory agreement with the similar test on the centre point strain gauges from the same disc ($E = 3.27 \times 10^6$ p.s.i., $\mu = 0.22$). The element with the A rosettes from disc F5-1 gave constants $E = 3.5 \times 10^6$ p.s.i., $\mu = 0.22$. In the rosette calculations of Table 4.5, it has been assumed that the measured elastic constants apply in both compression and tension.

Examples of the rosette strains measured during the loading tests are shown in Figures 4.17-4.19. It can be seen that in general the measured strains varied in a linear manner. (The lines through the experimental points have been used to determine the mean observed strains at maximum test load in Table 4.5 as mentioned above.) The most significant discrepancies in the illustrated comparisons appear in the minor tensile strains at the B position orientation 1-1, i.e. gauges no. 3, Figure 4.18.

In Figure 4.19 the calculated strain lines for the A rosette orientation 4-4 have been corrected for the gauge "position effect". It is already apparent from Figure 4.4 that in each rosette two of the three gauges are offset from the point of interest and some error will therefore be produced when the three gauge readings are used to calculate the stresses at this point. The effect is most noticeable with the A rosette in orientation 4-4; as would be expected, the comparison between measured and calculated strains for gauge no. 2 is improved when allowance is made for the position of the gauge with

respect to the stated co-ordinate position of the rosette. The calculated strains shown in Figure 4.19 do not therefore refer to a single point on the disc surface.

On the other hand Figures 4.17 and 4.18 show strains calculated for the stated co-ordinates of each rosette (see Table 4.1) and no significant improvement is achieved in the comparison with the measured strains by allowing for the offset positions of some of the gauges.

4.6.3. (iii) Elastic Constants in Tension

Because of the repeated discrepancies in the calculated tensile stresses for the discs a uniaxial tension specimen was prepared from disc F5-2 to consider the elastic constants in tension. Axial and transverse straingauges were applied to the shutter faces of the rectangular element as shown in Figure 4.20. Loads were applied by a universal testing machine and the loading rate was matched to the theoretical tension loading rate applicable to the earlier centre point strain gauge measurements on disc F5-2. The results are shown in Figure 4.21 (see Appendix Table A.2.7.).

Despite experimental precautions to maintain true axial loading the longitudinal strains clearly show a significant bending effect and confident conclusions with regard to the effective elastic constants must be reserved. Nevertheless, these results show that the modulus of elasticity intension differs by a small but significant amount from the equivalent value in compression. (The tension value is approximately 12 per cent below the compression value).

The same test also reveals an even larger difference in Poisson's Ratio for stresses of opposite sign. This is significant because the value of Poisson's Ratio is fundamental to the minor principal stresses calculated from the rosette strain measurements.

Assuming that the actual stresses in the disc are given by the theoretical solution, it is worth considering what effect the different elastic constants will have on the measured strains. In particular, consider the centre point strain gauge position of disc F5-2.

The principal stresses are given by equation (4.11), viz:

$$p = + \frac{6P'}{\pi d l}, \qquad q = - \frac{2P'}{\pi d l} \tag{4.11}$$

Suppose that the elastic constants in compression and tension are (E_C, μ_C) (E_T, μ_T) respectively. Applying the principle of superposition, the principal strains now become:

$$\varepsilon_1 = \frac{p}{E_C} - \frac{\mu_T q}{E_T}$$

$$\varepsilon_2 = \frac{q}{E_T} - \frac{\mu_C p}{E_C} \tag{4.17}$$

Substituting with equation (4.11):

$$\varepsilon_1 = \frac{2P'}{\pi d l} \left[\frac{3}{E_C} + \frac{\mu_T}{E_T} \right]$$

$$\varepsilon_2 = - \frac{2P'}{\pi d l} \left[\frac{1}{E_T} + \frac{3\mu_C}{E_C} \right] \tag{4.17a}$$

Suitable numerical values for the elastic constants are given by Figures 4.13, 4.21, viz:

$$E_C = 3.27 \times 10^6 \text{ p.s.i.} \qquad \mu_C = 0.22$$

$$E_T = 2.90 \times 10^6 \text{ p.s.i.} \qquad \mu_T = 0.09$$

Considering the maximum test load, the disc terms become:

$$P' = 21{,}000 \text{ lb}, \quad d = 23.375 \text{ in.}, \quad l = 3.265 \text{ in.}$$

Therefore:

$$\varepsilon_1 = + 166 \ \mu\varepsilon$$

$$\varepsilon_2 = - 96 \ \mu\varepsilon \tag{4.17b}$$

The corresponding strains calculated with the compression test elastic constants applied to both compression and tension are:

$$\varepsilon_1 = + 172 \ \mu\varepsilon$$
$$\varepsilon_2 = - 89 \ \mu\varepsilon \qquad (4.17c)$$

The differences between (4.17b) and (4.17c) are seen to be small ($\Delta\varepsilon_1$ = - 3.7 per cent and $\Delta\varepsilon_2$ = + 7.7 per cent in comparison with (4.17c)) although the change in minor principal strain should be revealed experimentally.

The mean strains observed experimentally (see Figure 4.12) were:

$$\varepsilon_1 = + 162 \ \mu\varepsilon$$
$$\varepsilon_2 = - 92 \ \mu\varepsilon \qquad (4.17d)$$

Considering the inherent experimental errors in these tests the good agreement between (4.17d) and (4.17b) is possibly fortuitous to some degree but the comparison serves to show that different elastic constants in compression and tension could explain some of the apparent discrepancies in the strain gauge results.

In the present circumstances the explanation should be regarded as possible rather than conclusive because of the limited experimental evidence of the elastic constants in tension. Furthermore, the argument does not successfully explain the comparison between the measured and calculated strains in the B rosette orientation 1-1 (Figure 4.18). This can easily be shown by trial calculation.

4.6.4. Disc Tests: Demec Gauge Results

The Demec points previously considered for shrinkage readings were used to measure strains on the principal diameters of the three discs in each loading orientation.

Since for any diameter the disc stresses are symmetrical about the centre, the Demec gauge measured the radial strains at a point on the diameter

covered by the gauge location stud. For the principal diameters (i.e. vertical and horizontal diameters) the measured radial strain will be one of the two principal strains at the point in question. Assuming the disc has uniform elastic properties the theoretical radial strains are easily calculated from equations (4.1), (4.2), (4.12) and (4.13).

The mean readings from both sides for discs F5-1 and F5-2 are shown in Figure 4.22; as an example of the experimental results, the readings from disc F5-1 are summarised in Appendix Table A.2.8. Readings from vertical and horizontal diameters are plotted against disc load in comparison with theoretical values calculated with the elastic constants derived from the uniaxial compression tests described in Section 4.6.3.(ii).

In every case the observed compression strains from the vertical diameter were less than the theoretical values whilst tension strains from the horizontal diameter were greater than expected from theory. The measured strains were essentially the same in three separate disc orientations and this would appear to indicate a satisfactory degree of isotropism in the disc material. In addition the presence of the stressmeters in discs F5-1 and F5-3 did not have a significant effect on the Demec gauge readings and the repeated trend of the results appears to be similar to that shown by the centre point resistance strain gauges in disc F5-2 (see Figure 4.12).

In this instance it is not possible to derive reasonable alternative values of E and μ from the observed strain behaviour. If the calculation is attempted from the basic assumption that the theoretical disc stresses occur at the stud location points, then the resulting modulii take values $E = 4.1\text{-}4.3 \times 10^6$ p.s.i. and Poisson's Ratio varies between 0.42-0.54. No other measurements on this material infer modulus values in this range and more significantly, it is theoretically impossible for Poisson's Ratio to exceed 0.5.

These observations lead to a further consideration of the elastic constants of the disc material in compression and tension. At maximum test load, the calculated stresses for the gauge points are:

Vertical diameter ($x = 0$, $y = \pm 4.0$ in.): $p = + 617$ p.s.i.

$q = - 175$ p.s.i.

Horizontal diameter ($x = \pm 4.0$ in., $y = 0$): $p = + 386$ p.s.i.

$q = - 110$ p.s.i.

Applying equations (4.17) and the previous numerical values to disc F5-2 the corresponding strains are obtained:

$$\varepsilon_{1y} = + 194 \ \mu\varepsilon$$

$$\varepsilon_{2x} = - 64 \ \mu\varepsilon \qquad (4.18)$$

(These principal strains do not apply to the same point; ε_{1y} is the major principal strain at ($x = 0$, $y = \pm 4.0$ in.) and ε_{2x} is the minor principal strain at ($x = \pm 4.0$ in, $y = 0$), i.e. ε_{1y} and ε_{2x} are the strains measured by the Demec gauge in Figure 4.22)

If it is assumed that the elastic constants determined in the compression tests also apply in tension then the calculated strains become:

$$\varepsilon_{1y} = + 201 \ \mu\varepsilon$$

$$\varepsilon_{2x} = - 60 \ \mu\varepsilon \qquad (4.18a)$$

Again the differences between (4.18) and (4.18a) are small ($\Delta\varepsilon_{1y} = - 3.0$ per cent and $\Delta\varepsilon_{2x} = + 6.25$ per cent in comparison with (4.18a)).

The mean experimental strains from disc F5-2 for the maximum test load were:

$$\varepsilon_{1y} = + 167 \ \mu\varepsilon$$

$$\varepsilon_{2x} = - 65 \ \mu\varepsilon \qquad (4.18b)$$

It can be seen that the measured strain on the horizontal disc diameter is consistent with the stated elastic constants applied separately in compression and tension but there is a clear discrepancy between the measured and calculated strains on the vertical diameter. Specifically, the major strain ϵ_{1y} is approximately 16 per cent less than the value calculated with equal elastic constants in compression and tension, and even if Poisson's Ratio is assumed to be zero in tension, the measured strain is still nearly 12 per cent less than the calculated value. It has not been possible to deduce a satisfactory explanation for this relatively large discrepancy from any other experimental evidence obtained in the present series of tests.

4.6.5. Disc Tests: Photoelastic Stressmeter Results

4.6.5.(i) Solid Stressmeter in Disc F5-3

The observed fringe orders at the centre of the solid stressmeter showed a linear variation with load in two disc orientations (see Figure 4.23 and Appendix Table A.2.9.). Applying the sensitivity factor previously obtained from the uniaxial tests on slab F3-3, the principal stress differences at the centre of the disc are found to be within 5 per cent of the values predicted by the theoretical solution for the disc stresses. It will be noted that this result does not necessarily imply that the individual disc stresses at the centre agree with the theoretical values.

The distribution of fringe order in the glass was the same as that previously observed in slab F3-3, i.e. the fringe orders were symmetrically distributed with a peak value at the centre of the observation face. The stress gradients in the central region of the concrete disc therefore appeared to have no significant effect on the average through-the-thickness principal stress differences in the glass.

If it is assumed that the theoretical principal stress difference occurs at the disc centre then another scale of ordinates may be applied as shown to Figure 4.23. With the same assumption, the theoretical response of the

stressmeter can also be included after calculation from the Muskhelishvili equations. A significant difference between experimental and theoretical response is then apparent; the average principal stress difference measured at the centre of the inclusion clearly exceeds the calculated value. This observation agrees with the preceding results from slab F3-3.

4.6.5. (ii) Annular Stressmeter Results

Readings from the annular stressmeter in three disc F5-1 orientations are shown in Figure 4.24 (see also Appendix Table A.2.9.). The pattern clearly showed symmetric fringe order peaks in the region of the 45° points and all readings refer to these positions. For each disc orientation the fringe pattern showed the same linear response to disc load and the isochromatic profiles were observed to be in alignment with the principal diameters of the disc in accordance with the photoelastic properties of the glass inclusion. The epoxy adhesive around the stressmeter appeared to function satisfactorily throughout the test.

The fringe order profile showed some similarity with the uniaxial case and this was confirmed by the pattern computed from the Hiramatsu-Barron equations. Figure 4.25 compares the two systems; the theoretical plots have been obtained with the aid of the Fortran computer programme given in Appendix 3. The assumed elastic constants are stated in Figure 4.25. It will be noted that the observed fringe order profiles in the disc tests show distinct similarity with the plotted values of principal stress difference for the case $\frac{p}{q} = 1: -\frac{1}{3}$ (i.e. $\eta = -\frac{0.33}{0.67}$) (The photograph in Figure 4.26 is subject to the effects of a non-collimated sodium light source plus a significant "space effect" (Frocht[29]) and it is therefore unsuitable for precise comparisons with the theoretical plots of principal stress difference particularly at the inner boundary.)

A comparison of the theoretical plots of principal stress difference shows that several features differ in detail in the two cases (see Table 4.6).

In particular, the stress concentrations at the inner surface of the stressmeter are increased in the compression-tension loading condition. Assuming that the adhesive bond can be maintained around the stressmeter throughout loading, the increase in tensile stress concentration at the points ($\frac{r}{b}$ = 1.0, $\theta = 0^{o}$ and 90^{o}), will be responsible for an earlier failure of the glass annulus. In this instance the working range of the stressmeter (expressed in terms of the applied major principal stress) will be theoretically reduced by a factor of 52 per cent.

Assuming that the observed fringe pattern is caused by the theoretical stresses, the experimental sensitivity of the inclusion can be described in terms of the applied major principal stress. From the slope of the line in Figure 4.24, the sensitivity becomes S_n = 148 p.s.i./fringe which represents a significant increase on the observed uniaxial sensitivity in the slab specimen F3-4 (S_n = 192 p.s.i./fringe). It can also be seen that the stressmeter is again more sensitive to applied stress than the theoretical solution predicts (the theoretical sensitivity factor deduced from the computed principal stress difference pattern is S_n = 173 p.s.i./fringe).

Just as the strain gauge rosettes were subjected to further confirmation tests, the annular stressmeter from disc F5-1 was also retested in uniaxial compression after preparing a rectangular element from the centre of the disc with the same dimensions as slabs F3-3, F3-4. The results of this test are shown in Figure 4.27 (see Appendix Table A.2.10). The sensitivity factor is in very good agreement with the value already observed in slab F3-4. The axial strains measured by the Demec gauge were consistent with the elastic modulus E = 3.5 x 10^{6} p.s.i. previously deduced from the A rosette strain gauges from disc F5-1.

4.6.5. (iii) Subsidiary Stressmeter Results

The subsidiary annular stressmeters at the M2, M3 positions in discs F5-1, F5-2 are shown in Figures 4.28-4.30. In each case the asymmetric fringe orders were observed to be aligned with the calculated principal stress

directions for the disc point corresponding to the centre of the stressmeter. and this feature was consistently repeated for both discs in different loading orientations. It can be seen from Figure 4.5 that the M3 inclusion is positioned in a low stress condition in orientation 2-2 and taking into account the lower limits of fringe pattern resolution, no significant response can be expected in this case.

In the M2 position orientation 1-1 the fringe pattern was symmetrical about the major axis in line with the loaded diameter of the disc but the two pattern quadrants nearest the disc loading point showed higher fringe orders than the other pair. The increase was approximately 10 per cent at the 45° points. This difference is consistent in a general sense with the predicted stress gradients in the disc.

The pattern is shown in Figure 4.26 and measured fringe orders are plotted against disc load in Figure 4.28. A conspicuous feature of these observations was the "fringe loss" on the major axis of the upper quadrants in the pattern. Beyond a meter reading of 6 fringes the first fringe was no longer visible on the major axis and a miscount of the integral fringe order at the 45° point could easily occur. Confusion need not arise if loads are applied incrementally as in this instance but this potential source of error should be considered when high stress levels are to be measured with stressmeters greater than the normal length of 1.5 in.

Similar results were observed with the M3 stressmeter in orientation 4-4. In this case lower fringe orders were produced since the stressmeter was nearer the disc centre and therefore further away from the loading point and its associated higher stresses. Figure 4.29 shows the observed response.

Stressmeter M3 in orientation 1-1 and stressmeter M2 in orientation 4-4 take positions nemote from the principal diameters of the discs. The stresses in this region of the disc vary continuously in direction as well as magnitude; the major principal stresses are also much larger than the minor tensile principal stresses. These conditions were reflected in the observed quadrant

fringe orders for each case. The patterns were aligned with the general directions calculated for the theoretical disc stresses (approximately θ_D = 25°) and the fringe orders were of the expected magnitudes.

The observations from the M2 and M3 stressmeters clearly cannot be considered for calibration purposes. The results merely show typical effects on the annular stressmeter response of surrounding stresses which vary in magnitude and direction. Similar effects would be observed in practical applications with, for example, well defined gradients produced by bending action or stress concentrations. No further comments will be made on the subsidiary stressmeters in this test series.

4.7. Conclusions

The main conclusions from this investigation concern the annular and solid stressmeters and their response to the theoretical biaxial combination of compressive and tensile stresses at the centre of the disc test pieces. In this instance the strain measurements are of secondary importance although it is clear that this aspect of the results can be discussed at some length.

It seems fair to assume that the theoretical principal stresses were produced at the centre of the disc specimens despite the fact that this is not at first confirmed by the corresponding resistance strain gauge readings. In this instance the assumption is supported by three other features of experimental evidence:

(a) the similarity between the observed and calculated fringe pattern profiles in the centre point annular stressmeter.

(b) the consistent results given by the corresponding solid stressmeter.

(c) the satisfactory agreement with theory of the centre point strain gauge readings when the fine aggregate concrete is assumed to have different elastic constants in compression and tension.

This being the case, the annular stressmeter results have demonstrated two major features revealed by the theoretical calculation of fringe order order distribution.

First, the fringe pattern for the stress ratio $\eta = -\frac{0.33}{0.67}$ has some similarity with the uniaxial loading condition and the presence of the minor tensile stress could easily be overlooked with the simple observation technique recommended by previous authorities. This effect would be even more significant within the range of principal stress ratios $\eta = 0$ to $\eta = -\frac{0.33}{0.67}$

Secondly, a well-defined fringe order peak still occurs in the region ($\frac{r}{b} = 1.60$, $\theta = 45^{\circ}$ etc.) and these can be used without difficulty as measurement positions but the **sensitivity** of the device is then different to the uniaxial case. Theoretically, the fringe orders should be increased by approximately 25 per cent for this particular ratio of the applied principal stresses and this has been confirmed by the experimental observations. However, the observed fringe orders in the disc stressmeter were significantly larger than the theoretical values, an observation which is similar to that already mentioned in Chapter 3 for uniaxial loading.

These two features therefore provide an important limitation to the general application of the annular stressmeter and its current method of interpretation. It is clear that a two-fold error could be produced by confusing a compression-tension fringe pattern with a fringe pattern produced by uniaxial loading. Unless further precautions canbe taken to minimise the potential errors in the determination of the applied stresses, the device should be avoided in practical applications which might involve principal stress ratios in the range $\eta = 0$ to $\eta = -\frac{0.33}{0.67}$.

This disadvantage is not shared by the solid stressmeter for the present tests have shown that this device has the same response to both uniaxial compressive stresses and the compression-tension conditions at the centre of the disc test-pieces. In this respect the results are consistent with the theoretical behaviour of the solid stressmeter, but again, the observed

fringe orders at the centre of the glass inclusion were higher than predicted by calculation; they were also higher than the values deduced from earlier published calibration data.

Nevertheless, it is apparent that the solid stressmeter can be used satisfactorily, once the experimental sensitivity factor is known, to determine the difference between the applied principal stresses in mixed biaxial conditions. From this it may be inferred that the device could be used to advantage with an annular stressmeter if principal stress combinations of compression and tension have to be considered in a practical application of the technique.

Considering the resistance strain gauge results from the disc rosettes, several discrepancies are apparent between the measured and calculated elastic strains. The differences are most obvious when the disc stresses are calculated directly from the rosette readings, particularly in the values of the minor principal stresses. As far as the present tests have allowed, this feature has been investigated in some detail, and as a result, two possible reasons for the discrepancies may be put forward.

First, there is evidence to show that the elastic constants of this fine aggregate concrete are different in compression and tension; the difference appears to be particularly significant in the values of Poisson's Ratio. This feature can be used to explain some but not all of the strain gauge readings. Secondly, it is likely that some of the discrepancies are features of experimental technique, namely geometrical imperfections in the disc specimens and the manner in which the diametrical loads were applied. It would be desirable to substantiate these reasons with more experimental evidence but this would require an extended study of the concrete properties and further refinements in test technique.

On the other hand, the existing experimental evidence eliminates several other possible reasons which might be suggested for the discrepancies. For example, the results from the uniaxial compression specimens, the similar tests

on elements dissected from the discs and the compatibility check at the centre of one specimen all infer that the gauges were applied satisfactorily to the test-pieces. The same tests also indicate that the gauge readings were not influenced by aggregate effects from the underlying concrete.

In addition, the elastic constants applied to the rosette readings would also appear to be satisfactory, for the same tests revealed a consistent value of Young's Modulus and only a small variation was observed in Poisson's Ratio. Furthermore, the Demec gauge readings from the loaded discs infer that the deformation characteristics of the concrete are independent of direction in the plane of the discs, i.e. the material can be considered to be isotropic.

The position of the individual gauges has also been considered and it is apparent that, with one exception, no significant improvement can be obtained in the comparison between measured and theoretical strains by allowing for the off-set positions of some of the gauges in individual rosettes.

The possibility of different properties in compression and tension can also be used to explain the Demec gauge readings on the horizontal diameters of the loaded discs, but the readings on the vertical or loaded diameters were consistently smaller than predicted by calculation. Within the limitations of the present investigation it is not possible to give a satisfactory explanation for this aspect of the results.

The preceding remarks refer to the experimental measurements but the conclusions would be incomplete without some reference to the choice of a diametrically loaded disc for a biaxial calibration condition of compression and tension. It was pointed out early in the discussion that the disc is not ideal for calibration purposes but the stress distribution in the central region of a large disc should be suitable for the calibration of a small inclusion stressmeter to a satisfactory degree of accuracy. In this respect the present tests appear to be satisfactory for they have demonstrated two fundamental features of the annular stressmeter response to the theoretical

biaxial stress condition at the centre of the disc. It is considered that alternative experimental methods of achieving the same results would be considerably more complicated.

However, the results from the strain measurements have emphasised the necessity for a comprehensive knowledge of the stress-strain characteristics of the host material if the behaviour of an inclusion stressmeter is to be compared with conventional indirect methods of stress measurement.

CHAPTER 5

Stress Conditions in the Solid and Annular Inclusions

5.1. Introduction

Reference has been made in Chapters 3 and 4 to the discrepancies between simple theory and experiment which have been observed in the response of both forms of stressmeter to uniaxial loading.

Using Dhir's measurement point defined by ($\frac{r}{b}$ = 1.60, θ = 45°) for the annular stressmeter a uniaxial sensitivity factor S_n = 185 p.s.i./fringe ± 3 per cent has been repeatedly observed for a 3 in. length meter in specimens with a Young's Modulus in the range E = 3.0-4.0 x 10^6 p.s.i. (Comparable results have also been obtained by the writer for 1.5 in. length meters in tests not described here. Examples of the present results can be found in Appendix 5, Tables A.5.1, A.5.2., which refer to the F1 series fine aggregate concrete specimens already described in Chapter 3. Similar results are also shown in Figures 4.10, 4.27.)

The fringe order readings given by the annular stressmeter in this study are thus approximately 17 per cent in excess of the theoretical response. An even larger discrepancy of approximately 28 per cent has been observed for solid stressmeter specimens (see Figures 4.9, 4.23). The response in the compression-tension tests of Chapter 4 was also higher than expected.

Throughout the test programme there has only been one specimen which gave results comparable with the theoretical solution; this was the annular stressmeter of specimen F3-4 described in Section 3.6.4. In this case fringe orders were measured at different datum points ($\frac{r}{b}$ = 1.40, θ = 90°, 270°).

It should be mentioned that compared with earlier experimental results given by Dhir (see Figure 2.6), the present annular stressmeter sensitivity factors appear to be satisfactory although a significant difference occurs

in the solid stressmeter results. (It is possible that the second feature could be explained by an error in the material fringe value appropriate to Dhir's solid stressmeter (f_g = 1050 p.s.i./fr./in. compared with fg = 1220 p.s.i./fr./in. of the present tests) but this could only be checked by repeating the earlier calibration tests.)

As far as the present results are concerned the consistent discrepancies between theory and experiment require further investigation and in what follows the theoretical solutions and their underlying assumptions are briefly discussed, with mention of two associated independent studies described in the literature. The discussion of stress distribution, with one exception, will be restricted to values of average, through-the-thickness principal stress difference since this function has been conveniently available from existing test specimens. A possible explanation is suggested for the experimental observations of the present work.

5.2. Theoretical Solutions for Stresses In and Around the Inclusion

The relevant theoretical solutions refer to plane elastic conditions in which the axis of the cylindrical inclusion is perpendicular to the in-plane loading of the host material. The loads are uniformly distributed in a uniaxial or biaxial sense remote from the inclusion. In this instance two particular solutions are appropriate namely those due to Muskhelishvili[39] and Hiramatsu et al[36]. These writers employ different mathematical methods, Muskhelishvili giving results for the solid inclusion only whereas Hiramatsu considers both the solid and annular forms. As mentioned earlier in Chapter 1, the problem has been discussed analytically by several other writers.

For reference at this point the Hiramatsu two-dimensional solutions will be restated. Using the foregoing notation in polar co-ordinates the solution for a solid inclusion in a state of uniaxial stress gives:

Inclusion stresses:

$$\sigma_r' = 2A_o' - 2C_2' \cos 2\theta \tag{5.1}$$

$$\sigma_\theta' = 2A_o' + (12A_2'r^2 + 2C_2') \cos 2\theta \tag{5.2}$$

$$\tau_{r\theta}' = (6A_2'r^2 + 2C_2') \sin 2\theta \tag{5.3}$$

Host material stresses:

$$\sigma_r = 2A_o + \frac{B_o}{r^2} - (\frac{6B_2}{r^4} + 2C_2 + \frac{4D_2}{r^2}) \cos 2\theta \tag{5.4}$$

$$\sigma_\theta = 2A_o - \frac{B_o}{r^2} + (\frac{6B_2}{r^4} + 2C_2) \cos 2\theta \tag{5.5}$$

$$\tau_{r\theta} = -(\frac{6B_2}{r^4} - 2C_2 + \frac{2D_2}{r^2}) \sin 2\theta \tag{5.6}$$

where A_o, B_o, B_2, C_2, D_2, A_o', A_2', C_2' are constants depending upon the elastic properties of the two component system. Definitions are given in reference[36]. (It should be noted that three of these constants are stated incorrectly in the original and subsequent publications[36], [37]. The corrected terms calculated by the present writer are given in Appendix 4, and with these corrections the Hiramatsu solution agrees with Muskhelishvili's independent result). By applying the principle of superposition equations (5.1)-(5.6) can be modified without difficulty to accommodate two-dimensional biaxial loading in the host material.

The similar solution for the annular inclusion gives:

Inclusion stresses:

$$\sigma_r' = 2A_o' + \frac{B_o'}{r^2} - (\frac{6B_2'}{r^4} + 2C_2' + \frac{4D_2'}{r^2}) \cos 2\theta \tag{5.7}$$

$$\sigma_\theta' = 2A_o' - \frac{B_o'}{r^2} + (12A_2'r^2 + \frac{6B_2'}{r^4} + 2C_2') \cos 2\theta \tag{5.8}$$

$$\tau_{r\theta}' = (6A_2'r^2 - \frac{6B_2'}{r^4} + 2C_2' - \frac{2D_2'}{r^2}) \sin 2\theta \qquad (5.9)$$

The host material stresses are again given by equations (5.4)-(5.6) although the constants A_o, B_o, $A_2'...D_2'$ generally take different values.

It will be remembered from earlier remarks that the photoelastic response of a birefringent inclusion at any point in the plane of observation is proportional to $(\sigma_1'-\sigma_2')$ where σ_1', σ_2' are the principal stresses associated with σ_r', σ_θ', $\tau_{r\theta}'$. Hence the Hiramatsu stress solutions enable the response of the photoelastic stressmeter to be calculated for applied uniaxial or biaxial stresses in systems of known elastic properties.

The above solutions assume the inclusion and host material to be in a state of "generalised plane stress" with a joined or "welded" interface between the two materials. The external boundary conditions for the inclusion (see Figure 5.1) implicit in this description are:

$$\sigma_r = \sigma_r'_{(r=a)}, \quad \tau_{r\theta} = \tau_{r\theta}'_{(r=a)}, \quad u_r = u_r'_{(r=a)}, \quad u_\theta = u_\theta'_{(r=a)} \qquad (5.10)$$

An alternative extreme condition which might be considered for the interface can be defined by:

$$\sigma_r = \sigma_r'_{(r=a)}, \quad \tau_{r\theta} = \tau_{r\theta}' = 0_{(r=a)}, \quad u_r = u_r'_{(r=a)} \qquad (5.11)$$

This definition implies that an "unbonded" interface exists which is incapable of transmitting shear and tangential stress components, i.e.the two materials can be displaced tangentially with respect to each other on either side of the boundary. This situation might be approached by an "exact-fit" inclusion in radial contact with the host material but with a lubricated interface to eliminate friction. The exact fit solution to the stressmeter problem is included in the results described below.

For the more generally considered welded boundary condition, the Hiramatsu solution does not take into account:

(a) Inclusion and host stresses in the z direction (parallel to the axis of the cylindrical inclusion) necessarily involved in an imperfect plane stress situation.

(b) The out-of-plane restraint at the boundary which also produces a distribution of σ_z, σ_z' stresses.

(c) The inevitable finite thickness of an interface adhesive with physical properties different to the inclusion and host materials.

5.2.1. The Plane Stress Approximation

With respect to the first point the concept of "generalised plane stress" (first described by Filon[65] and subsequently applied by most other writers in the theory of elasticity) considers the average values of the in-plane stress components in a plane stress problem and assumes that any σ_z, τ_{rz}, $\tau_{\theta z}$ stresses can be neglected. (When considering the stresses around a transverse hole in a thick plane (a situation which has some relevance to the axial hole of the annular stressmeter) this concept produces an acceptable approximation in the calculation of σ_r, σ_θ, $\tau_{\theta r}$ stress components[66],[67],[68] although stresses are produced in the z direction by virtue of the variable transverse contractions in the vicinity of the hole. Two exceptions appropriate to this example (assuming no out-of-plane restraint at the boundary) would occur if the annular stressmeter was subjected to isotropic external expansions or contractions, e.g. primary shrinkage (see equations (3.7), (3.8)), or two-dimensional hydrostatic mechanical loading in the host material. In both cases the term $(\sigma_r' + \sigma_\theta')$ remains constant along the thickness of the annulus and the ideal plane stress condition is achieved. For the solid stressmeter equations (5.1)-(5.3) show that $(\sigma_r' + \sigma_\theta')$ is also constant for simple

uniaxial loading ($A_2' \neq 0$, see Appendix 4) and it can be shown that this is true for general biaxial loading as well as applied isotropic expansion or shrinkage.)

Since the photoelastic observations in the glass inclusion are produced by an integrated response through the thickness a generalised plane stress calculation should therefore give a satisfactory explanation of stressmeter sensitivity as long as the reading points are remote from the boundary. This reservation leads to the second point.

5.2.2. Out-of-Plane Restraints

The out-of-plane restraint at the boundary is much more difficult to assess. The assumption of a welded boundary is inconsistent with the requirement that no boundary restraint is produced in the z direction and localised stresses will be produced in both materials whenever different elastic properties are involved. This is the "pinching effect" described by Durelli[69],[70],[71] although the stressmeter problem for both shrinkage and mechanical loading is considerably more complicated than the simplified examples of pinching discussed in the literature. The problem is partially illustrated by Sampson's experiment[72] and its possible approximate solution as proposed by Rhines[73].

Sampson's model is shown in Figure 5.2; the curing process of an annular epoxy resin disc involved thermal shrinkage which was restrained by a rigid circumferential ring. The disc was allowed to bond with the ring at the outer rim.

Sampson gives results for the σ_r', σ_θ' ($\tau_{r\theta}' = 0$ by symmetry) stress components determined photoelastically from the cured model. For the purpose of this discussion the results have been recombined to show dimensionless isochromatic fringe orders against radial position (see Figure 5.2). In this form the results can be compared with the previously mentioned annular stressmeter shrinkage fringe orders (see Figure 3.15) within the limits of the

fundamental differences which exist between the two models. It will be observed that the epoxy model is bonded to a "rigid" host material without an intermediate adhesive.

In both cases the generalised plane stress solutions predict a parabolic distribution of fringe order. The epoxy model results are in reasonable agreement with this theory over most of the radius but a large discrepancy appears at the outer boundary. In the annular stressmeter a discrepancy also occurs at the outer boundary but it is less pronounced. (Comment has already been made on this distribution in Section 3.6.3.)

The out-of-plane restraint in Sampson's model has subsequently been discussed by Rhines (loc.cit.) who proposes that the restraint produced an average out-of-plane stress σ_z' which decayed exponentially with distance into the epoxy model.

$$\sigma_z' = A e^{\beta(r-a)} \qquad (5.12)$$

where β is an assumed exponential decay factor and A is a constant to be determined from the boundary conditions (it is not to be confused with the same symbol used elsewhere in the present discussion). Equation (5.12) has been evaulated by Rhines to consider two cases in which σ_z' decayed to 1 per cent and 3 per cent of its maximum value at a distance from the outer boundary equal to the disc thickness. Modified in-plane average stresses, σ_r', σ_θ' were then derived for direct comparison with Sampson's results.

Translated into terms of dimensionless principal stress difference $\left(\frac{\sigma_1'-\sigma_2'}{E'\alpha't}\right)$ Rhine's "1 per cent solution" is shown in Figure 5.2. Good agreement is achieved with the experimental data. Rhines therefore concludes that the prominent rise in the fringe order distribution near the outer boundary of the epoxy model can be explained by the out-of-plane restraint at the interface.

Rhines' method clearly cannot be applied directly to the annular stressmeter shrinkage results but it seems reasonable to conclude that the rise in fringe order distribution near the outer boundary shown in Figures 3.14, 3.15,

could be produced by an out-of-plane restraint condition. The stressmeter adhesive presents a complicating factor in this instance.

Of greater significance is the fact that the out-of-plane effects appear to be considerably diminished at the stressmeter reading points remote from the outer boundary. Although the inclusion stress distribution produced by mechanical loading is, in general, different to that in the shrinkage problem, it therefore seems unlikely that the out-of-plane boundary restraints can explain the anomalies in the stressmeter loading tests of this study. This leads to a consideration of the boundary adhesive effects on the inclusion stresses.

5.3. Inclusion Stresses in Practice

The welded boundary condition defined by equation (5.10) is assumed to be achieved when an inclusion gauge has been cast into a wet concrete mix. When this is not possible and the inclusion has to be applied to an existing structure or test-piece a thin layer of adhesive is assumed to provide the same condition.

As the dimensions of the inclusion decrease it becomes more difficult to maintain a "thin" layer of adhesive. With the standard size of photoelastic stressmeter for instance (diameter 1.25 in.) a circumferential thickness of $\frac{1}{16}$ in. ($\frac{a}{10}$) is commonly used, as in this study; this thickness is a reasonable minimum for the current application technique and has so far been accepted as satisfactory in view of Dhir's results[19] with different thicknesses for a variety of epoxy adhesives.

At this point it is worthwhile to consider the inclusion stresses produced in practice during mechanical loading with or without the presence of an adhesive layer. Considering the photoelastic stressmeter cast into a concrete specimen for test without an adhesive, the difficulty of superposed shrinkage stress arises during mechanical loading. From the discussion of Chapter 3 it seems unlikely that the initial inclusion shrinkage stresses

could be simply defined in such a specimen and the test has not therefore been attempted. However, some indication of the inclusion stress distribution might be deduced from a similar test with a copper inclusion described by Stephen and Pirtz[74].

5.3.1. Bonded Inclusion:Stephen and Pirtz

In this test a solid cylindrical copper inclusion was cast into a fine aggregate concrete specimen very similar in mix and dimensions to the F series specimens described in Chapter 3. The problems of superposed shrinkage stresses during uniaxial mechanical loading were eliminated by using a photoelastic coating to measure the distribution of principal stress difference in both materials, the single piece coating being applied to one surface of the two component specimen immediately before test. The authors claim that the coating satisfactorily reproduced the underlying strain conditions in both materials although the results at the inclusion boundary might be questioned in this respect.

The results are reproduced in Figure 5.3 in comparison with the theoretical elastic distributions calculated by the Muskhelishvili solution equivalent to equations (5.1)-(5.6). The principal strain distributions were measured along the axes of symmetry; the strain compnents $\epsilon_r, \epsilon_\theta$ in Figure 5.3 thus represent principal strains but the (r,θ) notation has been preserved for clarity.

In two-dimensional elastic conditions the principal strain difference and principal stress difference are related by:

$$(\epsilon_1 - \epsilon_2) = \tfrac{1}{2}.G.(\sigma_1 - \sigma_2) = (\tfrac{1+\mu}{E})(\sigma_1 - \sigma_2) \qquad (5.13)$$

where G is the shear modulus for the material. As the authors infer, there is some doubt about the validity of equation (5.13) for the measured principal strain differences in the stress concentration zone of the host material near the inclusion.

It can be seen that the stress distribution in the inclusion is approximately uniform over the central area but a sharp rise occurs in the principal strain differences near the boundary. It is not possible to deduce from the results why the general level of principal strain difference is significantly higher than theory predicts or why the experimental readings are incompatible at the centre point of the inclusion. On the $\theta = 90^{\circ}$ axis the sharp transition of principal strain difference at the interface is not revealed by the coating measurements. (It should be noted that in the original paper the calculated maximum shear strains at the point are incorrectly given direct equality. From fundamental considerations, this cannot be the case. The appendix of the paper also wrongly states two of the Muskhelishvili constants (x, x_c) for this problem and gives wrong signs in the equations for the host stresses τ_{θ}, $\tau_{r\theta}$. The theoretical distributions of principal strain difference in Figure 5.3 have been recalculated in the correct manner.)

On the major principal axis ($\theta = 0^{\circ}$) the principal strain differences in the inclusion near the interface are more similar to the predicted values but in the host material the measured values are significantly different to the calculated elastic distribution. On this axis the stress disturbance extends to at least four times the inclusion radius; on the minor axis the disturbance would appear to extend to approximately half this value.

From the point of view of this discussion the Stephen and Pirtz results are not entirely satisfactory, but it would appear that the concentration of principal stress difference in a relatively rigid inclusion bonded to the host material without an adhesive is significantly higher than the calculated two-dimensional elastic value (approximately 40 per cent higher in this instance). As might be expected from previous considerations the maximum divergence between the theoretical and experimental values occurs near the interface; in this case the principal stress difference is higher than the central region of the inclusion.

5.3.2. Adhesive Bonded Inclusion: Solid Photoelastic Stressmeter

The distribution of principal stress difference in a solid inclusion adhesive bonded to the host material can be illustrated by the solid stressmeter from specimen F3-3 already described in Section 4.6.2.

Figure 5.4 shows principal stress differences (direct functions of fringe order) along the principal diameters as measured photoelastically by Tardy compensation in a diffused light crossed circular polariscope; a radially graduated graticule was introduced between the inclusion and analyser to give reference positions and a telemicroscope was incorporated in the analyser.

Three values of applied uniaxial compressive stress within the range 0-900 p.s.i. were considered, the results being given in dimensionless form in Figure 5.4. All experimental data is given in Appendix Table A.5.3. No attempt was made to identify the individual average through-the-thickness stress components σ_r', σ_θ'. As in the Stephen and Pirtz experiment these stress components are principal stresses for the diameters considered.

The stress distribution in the host material around the inclusion was not determined experimentally; it was considered that the theoretical maximum value of maximum shear strain (calculated to be approximately 330 με at the points $\frac{r}{b} = 5.0$, $\theta = 0^\circ, 180^\circ$) was too small for satisfactory resolution by readily available photoelastic coating techniques. No comment can therefore be made about the effects of the interface adhesive on the local stresses in the host material. For reference purposes the stress distribution given by the generalised plane stress solution for the two component system without an adhesive is shown in Figure 5.5.

It can be seen from Figure 5.4 that the distribution of principal stress difference in the inclusion was again not constant along the diameters as the plane stress solution predicts for a welded boundary. Contrary to the Stephen and Pirtz experiment without an interface adhesive, the maximum value

of principal stress difference occurs at the centre point of the inclusion and the function decreases towards the inclusion-adhesive interface. In this instance the minimum values occur at the interface on the major diameter, i.e. parallel to the direction of the applied stress p. Along the minor diameter the curvature of the principal stress difference line is less pronounced. At the centre, the principal stress difference is 28 per cent in excess of the calculated plane stress solution.

For purposes of comparison the "exact fit" solution to this problem has been included in Figure 5.4. This calculation is more readily accomplished by direct substitution in the Muskhelishvili solution[39] rather than by the Hiramatsu method. It is worth noting that if an exact fit situation was feasible in practice for this system, parting would occur during uniaxial loading on the minor diameter at the interface. A valid stress calculation therefore has to include a symmetric radial prestress to maintain continuity at the interface. If the localised radial tractions are just sufficient to maintain continuity the σ_r', σ_θ' stresses take zero values at the points ($\frac{r}{b} = 5.0$, $\theta = 90^\circ$, 270°) and hence, as in this example, the curve of principal stress difference passes through zero at these positions. (The curve also passes through zero for the corresponding points on the major axis but in this case $\sigma_r' = \sigma_\theta' \neq 0$.)

The fringe pattern produced in the inclusion by these conditions would appear as a series of concentric rings decreasing in fringe order away from the centre point, but in reality the provision of appropriate radial interface tractions would present some difficulty.

5.3.3. Adhesive Bonded Inclusion: Annular Photoelastic Stressmeter

The annular stressmeter of specimen F1-3 (see Section 3.6.1.) has been considered in the same manner as the solid inclusion described above. Figure 5.6 shows the standardised experimental distributions of principal stress difference along the principal axes of the inclusion for uniaxial compression

loading in the direction $\theta = 0^{\circ}$. (Experimental readings are given in Appendix 5, Table A.5.4.). The overall fringe pattern produced in this stressmeter is illustrated in Figure 5.7; the general similarity with the theoretical full field isochromatic distribution can be confirmed by comparison with Figure 4.25.

Along the major axis the principal stress difference again decreases towards the glass-adhesive interface; at the boundary the value is approximately one-third of the generalised plane stress solution. Moving in towards the inner free boundary the experimental values differ from the theoretical distribution particularly in the region of $\frac{r}{b} = 1.50$ but it is possible that the discrepancy is exaggerated by the inherent experimental errors of the non-collimated polariscope.

At the inner boundary it is apparent that the tangential stress component is of the same order as that predicted by the welded boundary theory but it should be remembered that localised residual stress and a degree of oversize in the axial hole is involved in this region (see Section 3.6.3.). Allowing for the oversize factor (the residual stress component is independent of applied loads) the theoretical value of $(\frac{\sigma_{\theta}' - \sigma_r'}{p})$ becomes -1.83 compared with the experimental values of -1.25. This difference is increased still further by the realisation that the tangential residual stress at this point has the same sign as the σ_{θ}' stress due to load (compression loading gives tensile values of σ_{θ}' at $\frac{r}{b} = 1.0$, $\theta = 0^{\circ}$, 180°).

On the minor axis the experimental principal stress difference also decreases towards the outer boundary (limiting value approximately 40 per cent of the plane stress solution). At the inner boundary there is a large difference between theory and experiment; allowing for the oversize factor, the theoretical value of $(\frac{\sigma_{\theta}' - \sigma_r'}{p})$ becomes + 4.95 in comparison with the experimental values of approximately + 2.60. In this case the residual stress and loading stress have opposite sense and low values of $(\frac{\sigma_{\theta}' - \sigma_r'}{p})$ will thus be recorded in practice.

It is important to note that away from the inner boundary there is a region where the experimental principal stress difference is similar to the theoretical solution. At the points corresponding to Dhir's "collar edge" (defined by $\frac{r}{b}$ = 1.40, $\theta = 90^{\circ}, 270^{\circ}$) the experimental and theoretical lines agree to within 7 per cent. Comment has already been made about the stressmeter response as measured at this point (see Section 3.6.4.). The effects of residual stress and inner boundary oversize diminish rapidly, before this point is reached.

An "exact fit" solution has also been prepared for this annular stressmeter by appropriate modification of the Hiramatsu equations (5.4)-(5.9). The new definitions of the constants A_c, B_c, ... D_2' in this case are given in Appendix 4, for reference. It may be noted that parting does not occur on the minor axis at the interface with the annular inclusion. This is consistent with a decrease in inclusion rigidity produced by the axial hole, a feature which is also reflected in the theoretical distribution of host material stresses on the principal axes. The stresses in the surrounding material for both the annular and solid inclusions are presented for comparison in Figure 5.8.

If required the full field fringe pattern for the "exact fit" condition could be computed by substituting the constants of Appendix 4, into the programme of Appendix 3. In the absence of out-of-plane restraints, Figure 5.6 shows that the "exact fit" fringe pattern in uniaxial loading would display three isotropic points (defined by $(\sigma_1' - \sigma_2') = 0$) on each semi-major axis and one isotropic point on each semi-minor axis near the outer boundary.

5.4. Interim Conclusions

It has been shown that the generally considered two-dimensional welded boundary condition does not allow a satisfactory calculation of the actual stress distribution in the simple inclusion-host material systems of this study.

For both the solid and annular adhesive bonded inclusions considered, it is clear that the principal stress differences in planes perpendicular to the axis of the inclusion decrease from the centre towards the boundary. In both cases the principal stress difference distribution in the boundary region appears to represent a situation between the idealised welded and exact-fit condition.

In the solid inclusion the maximum value, which is significantly greater than expected, occurs at the centre point. This is contrary to published results for a bonded inclusion without an adhesive although the centre point principal stress difference was then still higher than the calculated value.

On both axes of the annular inclusion the tangential stress concentration at the inner boundary is considerably lower than expected, a feature which will be beneficial to the strength of the device in uniaxial loading.

Along part of the minor axis the experimental distribution of principal stress difference approaches the theoretical solution and it is convenient that the "collar edge" measurement point for biaxial loading is located in this region. For these state test conditions it appears that the "collar edge" could be used satisfactorily for measurements in uniaxial loading if comparisons with systematically calculated sensitivity factors are required. In principle this measurement point should be regarded with caution because of the severe fringe order gradients in this region, but in practice the errors of measurement are unlikely to be comparable with the existing sensitivity discrepancies at the "45° point" which originally prompted this discussion.

The increased values of principal stress difference at the "45° point" in the annular stressmeter reflected in the uniaxial sensitivity data contrast with the measured values at the inner boundary. There need to no inconsistency in the fact that the principal stress difference is increased in one region and decreased in another, and in the present state of understanding it seems reasonable to assume that the adhesive layer influences the point-to-point

stress distribution in the glass annulus. Since a finite thickness of adhesive is inevitable for practical applications of the technique it is suggested that further attention be given to the effect of the adhesive on the inclusion stresses, beginning with the obvious parameters of the layer thickness and physical properties.

Although in practice the inclusion stresses are three-dimensional, a two-dimensional approach may give a satisfactory approximate explanation of the observations, particularly in view of integration effects through the thickness which are inherent in the photoelastic measurements. Experimentally, the inclusion stresses will need to be investigated in detail and there are several improvements consistent with the established photoelastic methods which should be made to the simple observational techniques applied in this instance.

However, before proceding with further experimental tests the present results should be compared with a modified two-dimensional Hiramatsu solution, which includes a stress function for the adhesive layer with an initial assumption of welded boundary conditions in the three component system. If a satisfactory approximation is achieved for the inclusion stresses in the region of the measurement points it will then be possible to derive a general solution to which any given practical application may be referred.

Implicit in this approach will be an assumption of a linear elastic adhesive layer. This assumption is probably not unreasonable in short-term observations with stiff adhesives, for earlier compression tests carried out by the writer indicate that there are several filled epoxy resin formulations which behave in an almost linear elastic manner over a stress range which should be adequate for the maximum adhesive stresses generated in a stressmeter application. (Since these tests have so far been of a preliminary and comparative nature, they will not be discussed in detail here. They have been concerned with uniaxial compression stresses in the range 0-2,000 p.s.i. with loading rates of the order of 100 p.s.i./min. The elastic constants appropriate to these

conditions for a variety of filled resins proposed for use with photoelastic stressmeters occur in the ranges $E = 0.8 - 1.5 \times 10^6$ p.s.i. and $\mu = 0.28 - 0.33$.)

However, it has already been pointed out in Chapter 3 that the epoxy adhesives can show significant inelastic behaviour under sustained compressive stresses and this should be remembered when a theoretical analysis is attempted which includes a finite thickness of adhesive. It should be mentioned here that the desirability of a thin layer of stiff adhesive has been appreciated and applied in nearly all of the laboratory and field investigations so far considered in the development of the photoelastic stressmeter.

CHAPTER 6

A Photoelastic Stressmeter Application in a Buttress Dam

The present account of some of the characteristics of photoelastic stressmeters will be concluded by a description of a practical application in a buttress dam. In this instance the stressmeters formed part of a wider instrumentation programme under the direct control of the consulting engineers who designed the dam. In so far as the exercise allows, the following discussion attempts to assess the performance of the stressmeters and to make recommendations for the benefit of any future applications of a similar nature.

Before discussing the interpretation of the stressmeter results, the circumstances of the problem will be outlined.

6.1. The Dam Buttress

The stressmeters were installed in one buttress of the Clywedog Dam, Mid-Wales, completed in 1967 to impound a river regulating reservoir. The dam is 237 ft. high and at the time of its completion was the tallest dam in the United Kingdom. The completed dam is shown in Figure 6.1.

The structure consists of eleven round head buttresses; in each case the profile is based on a 60° equilateral triangle. The three central buttresses are of equal height and one of these was used for the principal instrumentation investigation. Since the dam is designed to spill over the full length of crest between the buttress sections the downstream spaces between the webs are covered by stepped precast concrete spillway beams. The dam terminates at each flank in a short gravity section.

The downstream face is convex to make the best use of existing geological features; these also provide a foundation which cannot be considered to be either uniform or homogeneous[75].

6.2. Calculated Buttress Stresses

The design of the buttress included a conventional elastic stress analysis in the full dam condition with a linear distribution of normal stresses on horizontal planes. A summary of the principal stress conditions along two particular planes is shown in Figure 6.3.

To confirm the design stresses a finite element analysis was carried out by Professor Zienkiewicz of the University of Wales[76]. This analysis was able to take into account a variety of elastic properties of the buttress and foundation as well as stress conditions which might occur with the presence of pore pressure in the loaded buttress. In certain conditions the analysis predicted tensile stresses in the buttress heel and separate calculations considered the stress distribution which would result from postulated cracks in the heel and foundation. (The possibility of undesirable tensile stresses provided one of the reasons for the later disposition of the internal strain gauges - see below). The results of one calculation with the full water load, pore pressure and gravity stresses, are illustrated in Figure 6.4. The finite element analysis also derived stress components for the empty reservoir condition.

The maximum stresses in the buttress occur in the downstream toe and both methods of calculation predict compressive principal stresses of the order of 450 p.s.i. in this locality. It will be realised that neither method takes into account the incremental construction schedule or the occurrence of thermal and shrinkage stresses during construction. Any knowledge of such stress components will depend entirely on practical observations. In addition, thermal stresses will necessarily exist during the life of the completed buttress and these cannot be calculated without an accurate knowledge of the appropriate thermal parameters. Any redistribution of stress produced by creep also remains unconsidered.

6.3. Instrumentation

Within the instrumentation programme only two techniques are directly concerned with stresses in thebuttress, namely vibrating wire (sonic) strain gauges and the photoelastic stressmeters. The chosen sonic gauge positions are unfortunately not comparable with the stressmeter positions.

6.3.1. The Sonic Strain Gauges

The Dæall sonic gauges are arranged in four-gauge 45° rosettes in the plane of the buttress; only one rosette is situated in the downstream toe, the remainder being positioned at the upstream face so as to include readings of the possible tensile stresses.

To eliminate the deformations caused by non-stress dependent phenomena isolated sonic gauges are embedded in the concrete near each rosette (see Figure 6.2). The isolated sonic gauge readings thus provide bases for the rosette gauges. The creep increments in the resulting measured strains have been systematically allowed for using a modified "rate of creep" method [75],[1] the creep characteristics of the buttress concrete being determined in an independent laboratory investigation[77].

The main features of the stressmeter installation are described below. The instrumentation programme also included measurements of buttress displacements, concrete temperatures, seepage and uplift pressures below the dam.

6.3.2. The Photoelastic Stressmeters

The stressmeter positions are indicated in Figure 6.5. They were installed in two stages at each position, the first during construction, the second immediately before impounding. The optic axes of the stressmeters are perpendicular to the buttress plane except at positions 204, 212. To allow clear access the the stressmeters at position 204 are installed with

their optic axes at 60° to the buttress plane. The stressmeters at position 212 have their axes perpendicular to the western face of the buttress head.

The first stage instruments, which included nine annular and two solid stressmeters, were bonded with a thin layer of epoxy adhesive into graded 8 in. cubes, (maximum aggregate sixe $\frac{3}{4}$ in.) which were subsequently included in the appropriate buttress lift. The temporary supports shown in Figure 6.6 were removed before the mix solidified, leaving the thin walled steel tubes to provide visual access from catwalks on the western face of the buttress. The principal details of the concrete used around the stressmeters are given in Table 6.1.

At any one time, the readings of the first stage stressmeters clearly represent a resultant condition from several different sources of stress. The second stage instruments were therefore used as an attempt to simplify the interpretation of the observed stress changes during the important period of impounding. These nine stressmeters were applied to empty cubes purposefully included in the buttress construction alongside the preceding first stage stressmeters. The procedure involved a modified version of the simple setting tool previously described elsewhere[17].

The specification given in Figure 6.9 applies to the annular stressmeters of both stages. The diameter was chosen for clear visibility of the photo-elastic pattern, the length being consistentwith a required optical response of approximately 0-4 fringes over the estimated stress range of 0-900 p.s.i. (The maximum calculated stresses were arbitrarily multiplied by a factor of two to allow for the unknown stress conditions produced during construction.)

The circular polarising filter for each annular stressmeter was incorporated with the glass element, illumination being provided by a probe light source inserted by the observer for each reading. The white light fringe orders were measured by Tardy compensation from a hand-held analyser at points defined by ($\frac{r}{b}$ = 1.40, θ = 90°, 270°) on the stressmeter pattern.

The principal stress ratios were estimated by the pattern profile technique previously described. The major stress directions were also visually estimated with reference to the upward vertical, the clockwise direction in the western elevation being given a positive sign.

The probe light source could not be used with the two solid stressmeters and in each case additional access was provided from the eastern side of the buttress for a lantern containing the circular polariser. Schematic details for both forms of stressmeter are given in Figure 6.7.

6.4. Stressmeter Interpretation

Before discussing the stressmeter readings it is worthwile to consider the various causes of stressmeter response within the buttress and this consideration must necessarily include the possibility of spurious readings associated with mismatched shrinkage and thermal characteristics. The spurious effects will be considered first.

6.4.1. Shrinkage Effects

The response of the annular stressmeter toprimary shrinkage has already been included in Section 3.5, but it will be apparent from that discussion that the observed behaviour is not yet fully understood and for the time being, each practical application must be considered with reference to its own particular circumstances.

In this instance the shrinkage behaviour of the buttress concrete is indicated by the isolated sonic gauges. Figure 6.16 shows the results from four such gauges over a three year period. From this data it is concluded that, after the first few weeks of installation, a small degree of swelling occurred in the buttress consistent with a large mass of concrete in which little or no drying takes place. This feature is deduced from the small upward trend of the gauge readings, the cyclic behaviour being a function of the mismatched thermal properties of the gauges and surrounding concrete

(see below). The small magnitudes and the signs of the observed strain changes will be noted from Figure 6.16.

None of the isolated gauges installed at nine separate locations, reveal any significant shrinkage effects and it is therefore further concluded that the stressmeter readings do not contain any increments caused by primary shrinkage. It is not known if the readings involve secondary (differential) shrinkage increments but it seems likely that these would be small because the outer faces of the buttress have generally been exposed to a high ambient humidity both during and after construction. (Humidity measurements in the spaces between completed buttresses have indicated relative humidities in excess of 90 per cent.)

6.4.2. Thermal Effects

The mismatched thermal properties of the stressmeter and concrete were considered by reference to the simple analysis described in Section 3.3. In the completed buttress it was considered that temperature changes would follow a gradual seasonal variation of the order of $\pm$ 9°F ($\pm$ 5°C). Also assumed were an effective modulus of $E = 3 \times 10^6$ p.s.i., Poisson's Ratio μ=0.20, and a coefficient of linear expansion $\alpha = 6 \times 10^{-6}$/°F ($10.8 \times 10^{-6}$/°C).

Applying these values to the calculation of Section 3.3 gives a possible spurious thermal fringe order $\Delta N_t = \pm$ 0.05 fr. occurring during an annual cycle. This increment is of the same order of magnitude as the smallest fringe order change which can be confidently measured by the normal technique and a systematic investigation of the thermal mismatch problem was not therefore included in the buttress instrumentation.

Subsequently, the independent laboratory investigation of the buttress concrete revealed arithmetical terms $E = 5.0 \times 10^6$ p.s.i. (see below), μ = 0.18 and $\alpha = 6.4 \times 10^{-6}$/°F ($11.5 \times 10^{-6}$/°C). The original estimates of seasonal temperature variation were verified by measurements in the dam

(see Figures 6.16, 6.17). A new calculation now shows a maximum possible spurious fringe order increment of $\Delta N_t = \pm 0.10$ fr. Although the effect has thus become more significant it will be appreciated that the calculation depends on an elastic analysis and it is not known if this approach adequately explains the practical situation.

There is not sufficient evidence from the remainder of the instrumentation programme to justify more detailed comment and in this instance the problem must remain open to question. Nevertheless, it seems reasonable to conclude that the problem will not be sufficient to significantly effect the present discussion of stressmeter readings. Preliminary experimental results[51] appear to show that the elastic method of calculation over-emphasises the effects of mismatched thermal properties.

(In the preceding comments on shrinkage effects reference was made to the cyclic behaviour of the isolated sonic gauge results. In this instance the behaviour illustrated a degree of "over-compensation" in the sonic gauges, i.e. the effective coefficient of expansion of each gauge is greater than the concrete value and when the environment temperature rises a state of compression is induced in the gauge. The effect is reversible. From the independent laboratory concrete data and the comments of Section 3.3, it is apparent that the photoelastic stressmeter should be very slightly "under-compensated" in this application.)

6.4.3. Buttress Stresses

The preceding comments refer to increments of the stressmeter readings which might be wrongly translated in terms of buttress stresses. It is now necessary to consider the real stresses in the buttress; their principal causes have already been briefly referred to in Section 6.2.

To assess the stressmeter performance it is clearly necessary to identify those components of the readings which are associated with the calculated conditions and when gravity stresses are involved there exists a fundamental difficulty.

Immediately before impounding the first stage stressmeter readings include gravity effects but at that time the response has already been complicated by additional stresses occurring during construction which cannot be allowed for by calculation. These additional stresses are produced for instance by complex thermal and shrinkage effects as new lifts of concrete are added to the partially completed buttress, and together with the gravity stresses, they eventually form a system of residual stresses in the final structure. (The significant stressmeter readings observed before the beginning of impounding will be seen later in Figure 6.9-6.15). Experimentally, it is not possible to isolate the gravity stresses from this residual stress condition before impounding and consequently the gravity stresses cannot be included in the later comparison between stressmeter readings and calculated stresses in the full dam condition.

It might also be argued that similar complications are produced by thermal stresses and creep during the impounding period, but by making two additional assumptions, it is possible to derive increments from the stressmeter readings which can be attributed solely to the total water load. The calculation of corresponding buttress stresses presents no fundamental difficulty. The two assumptions are:

(a) Creep and stress redistribution do not significantly effect the buttress stresses during the impounding period.

(b) Thermal stresses in the completed buttress are repeated in a regular annual cycle.

Although there is very little evidence to support it, other than the relatively small stress levels predicted by design, the first assumption is probably not unreasonable. (It will also be implicit in any comparison which involves the original design or finite element calculations.) The second assumption is justified by practical observation (see Figure 6.17 and reference (75)) and it implies that differences between annual stressmeter readings are independent of thermal stress conditions.

In this instance it is convenient that impounding took place in just less than thirteen months. The total water load increments at a given position can therefore be obtained by subtracting the readings taken immediately before impounding from the first reading in the full dam condition. The resulting values for all stressmeters along one horizontal plane in the buttress are then to be compared with a calculated full dam stress distribution from which the gravity stress components have been removed.

To minimise the arithmetical computation involved with the relatively complicated geometry of the buttress, the linear analysis has not proceeded beyond the vertical normal stress components along the lower instrument level (745'O.D.). This form of presentation also has the advantage of not requiring further independent assumptions for the distribution of shear stress along thebuttress cross-section which would be necessary before a system of principal stresses could be derived.

The distribution predicted by the finite element calculation has been found by subtracting the vertical stresses due to gravity only from the vertical stresses due to gravity and total water load. Linear interpolation has been necessary to derive stresses applicable to the cross-section of interest. For the sake of brevity, arithmetical working has not been included in this account; appropriate values can be found in the independent report[76].

The corresponding vertical stress components in the stressmeter readings have been obtained by applying the Mohr Stress Circle construction to the readings relative to a datum at the beginning of impounding.

The comparison of water load stresses outlined above represents the nearest approach which can be made to a fundamental assessment of stressmeter performance. The comparison must therefore be considered as the primary feature of the results and although some other aspects of the stressmeter

readings are included in what follows, these must remain secondary to the discussion of water load stresses.

6.4.4. Stressmeter Sensitivity

A note of explanation should be given for the sensitivity factor necessary to convert the stressmeter readings into buttress stresses. The factor has been derived from Dhir's[23] earlier experimental data, taking into account the material fringe value for the Clywedog stressmeter glass (see Figure 2.9), and the instantaneous elastic modulii observed in the independent laboratory tests on the buttress concrete (see Figure 6.18).

It will be seen from the results that the stressmeter patterns indicated biaxial stress conditions throughout the measurement period. The appropriate sensitivity factors for various compressive principal stress combinations have already been summarised in Figure 2.7, but in the present circumstances it seems reasonable to apply a mean value for the variable biaxial conditions of the buttress. The arithmetical terms required for the sensitivity factors of Figure 2.7 are f_g = 1220 p.s.i./fr./in. and l_g = 3.0 in. The mean sensitivity factor then becomes S_n = 213 p.s.i./fr., values for all principal stress ratios lying with ± 5 per cent of this figure.

The limited data of Figure 6.18 shows that the instantaneous elastic modulus of the concrete increased with time to a value of E = 5.0 x 10^6 p.s.i. thus exceeding the original estimate made before the buttress was constructed, and also the low modulus conditions implied in Figure 2.7. The mean sensitivity factor should therefore be modified to account for the increase in concrete modulus.

With existing information the correction can only be deduced by assuming proportionality between the biaxial and uniaxial response of the stressmeter for a given modulus condition. The variation of uniaxial response with host modulus is indicated in Figure 2.6; the difference in sensitivity between conditions E = 3.0 x 10^6 p.s.i. and E = 5.0 x 10^6 p.s.i.

is seen to be small and after correction for the higher modulus the mean sensitivity factor becomes S_n = 230 p.s.i./fr. Although it has not been possible to verify this figure in the buttress results, it has been applied to all annular stressmeter readings in the following discussion.

After the comments of Section 5.3.3. concerning the fringe order distribution around the point ($\frac{r}{b}$ = 1.40, θ = 90°, 270°) it might be argued that in this instance the stressmeter sensitivity factor could be calculated from the Hiramatsu generalised plane stress solution. Such a calculation indicates a higher mean sensitivity figure, but at the present time its validity would depend on one laboratory test and it is more reasonable to rely on the value which has been derived from a wider experimental background. Nevertheless, the possibility should be acknowledged that the sensitivity of the buttress stressmeters could be exaggerated by the independently deduced sensitivity factor and this point would clearly merit further attention in future investigations.

6.5. Stressmeter Results

Stressmeter readings until Spring, 1969, are shown in Figures 6.9-6.15. All readings are tabulated in Appendix Tables A.6.1.-A.6.9. For each station the observed fringe order, indicated major stress direction and indicated principal stress ratio are plotted against time. The development of buttress construction and water levels are shown in each Figure for purposes of comparison. The principal stressmeter constants are given in Figure 6.9.

It should be noted that since November, 1967, station 213 has been inaccessible on all but one occasion. Meters 210/21, 212/21, and 214/22 have ceased to operate after a period of satisfactory use because of failure of the polarising filters. Meters 302/22 and 204/22 were damaged during the second stage installation procedure.

6.5.1. Readings during Construction

In general the first stage instruments gave readings approximately two months after installation and from the beginning, biaxial stress conditions were indicated by the clearly defined symmetrical fringe patterns. In all cases both principal stresses were compressive and the magnitude of the minor principal stress was approximately three-quarters of the major principal stress. There was some fluctuation of indicated principal stress directions; these subsequently diminished once the buttress was subjected to a stable external loading condition.

The highest stresses appeared in the buttress web at position 208 and 214. When impounding began the indicated major stress level at position 214 was approximately 650 p.s.i. in a nearly vertical direction, but elsewhere stresses did not exceed 450 p.s.i. and were frequently much lower, e.g. in the buttress head (position 204), the buttress toe (position 213) and the upper level positions 302, 304. In this respect the distribution of stress magnitudes through the buttress does not appear to be unreasonable but the absence of comparative measurements prevents a critical assessment of the stressmeter readings during the complex stress conditions of the construction period.

6.5.2. Readings during Impounding

In general the net changes in the stressmeter readings during this period were less significant than the changes produced in the preceding period of construction.

It has not been possible to trace the development of water load stress increments in the stressmeter readings taken throughout impounding because of simultaneous thermal stress changes but the assumption discussed in Section 6.4.3. enables the thermal stresses to be eliminated on the occasion of the first full dam condition. Using this assumption, the

vertical normal stress increments implicit in the stressmeter readings produced solely by the total water load are summarised in Table 6.2. With the exception of the two stressmeters at the higher instrument level (795'O.D.) the vertical stress increments in the last column of Table 6.2. are included in Figure 6.19.

Using conventional elementary beam theory, the linear variation of vertical stress along the buttress section is given by:

$$\sigma_V = \frac{V_w}{A_n} \pm \frac{V_w . e_n . x_s}{A_n} \qquad (6.1.)$$

The appropriate definitions and arithmetical terms are summarised in Figures 6.20, 6.21, and the result is included (line AB) in Figure 6.19. The maximum and minimum values of σ_V occur at the downstream and upstream faces respectively.

The foregoing solution assumes an impervious dam foundation; when the buttress is subjected to uplift forces the corresponding stresses are derived in a similar manner. For the purposes of this comparison, it has been assumed that uplift pressure varies linearly from the full hydrostatic head to zero over the buttress head (see Figure 6.22). This would appear to be the worst case and in reality the measured pressures on site have revealed a smaller effect. Appropriate terms are indicated in Figure 6.22; the resulting vertical stress distribution is shown by line CD in Figure 6.19.

Also included in Figure 6.19 are the corresponding results from the finite element calculation; two cases are considered, the first for an impervious dam and foundation , the second for a given condition of buttress pore pressure (which includes an implicit definition of uplift). The main reason for the difference between these results and the linear theory is that the finite element method takes into account the stress distribution in the foundation (excluding in-situ residual stresses).

Before commenting on the comparisons revealed by Figure 6.19, a further point should be raised. It is assumed in the calculated stress distributions that the water load is applied to a completed buttress but in reality this was not the case. At the beginning of impounding the highest buttress level was 860'O.D., nearly 70 ft. below full height and construction of the buttress cap was eventually completed approximately seven months afterwards. The cap represents a significant proportion of the total buttress weight and consequently it provides a significant increment of vertical stress at the lower 745'O.D. level of interest. This increment is necessarily included in the stressmeter results.

In practice the additional stress distribution caused by the cap is unknown nor can a possible solution be deduced from existing finite element data. Alternatively, a likely order of magnitude can be deduced from the preceding method of linear analysis. To reduce the arithmetical computation the buttress cap has been simplified to a combination of prismatical forms. This simplification is purposefully exaggerated; appropriate terms are summarised in Figure 6.23. Evaluating another equation of the form (6.1) gives a maximum downstream vertical stress increment of 50 p.s.i. with a minimum upstream value of 24 p.s.i. Superposing the line defined by these two values onto the preceding distributions, the lines EF, GH are obtained in Figure 6.19.

It can be seen that the distribution is still significantly different from the stressmeter result and although improvements might be made to the preceding representation of the buttress cap, further inspection shows that it is not possible to derive a linear distribution of vertical stress which gives stress components similar to the stressmeter results.

It is possible that the comparison could be improved by a separate finite element calculation which purposefully considers the construction of the cap during the impounding period. Until such a calculation is made, the

divergence between stressmeter results and the calculated stress distribution must remain, and in the circumstances of this exercise it is not possible to say whether this is due to some feature of stressmeter technique or the the unrealistic nature of some of the assumptions which are implicit in the theoretical calculations.

The preceding remarks refer to the stress components produced solely by the total water load. In absolute terms at the end of impounding, the comparisons between stressmeter readings and calculated conditions are illustrated by Table 6.4 and Figure 6.24. It can be seen that the indicated stress magnitudes are substantially higher than calculation predicts, although thereis an encouraging agreement in stress directions. The indicated minor compressive principal stresses are still conspicuous.

6.5.3. Readings after Completion of Impounding

Since the completion of impounding the buttress has been subjected to an approximately constant water load. There are not yet sufficient stressmeter readings available to comment on the significance of the changes which have occurred during the full dam condition (see Figures 6.9-6.15).

6.5.4. Stressmeter 213/21

The annular stressmeter 213/21 is situated in the vicinity of the highest buttress stresses produced by water and gravity loading. It is also the nearest stressmeter to a sonic strain gauge rosette (no. 102). The results from this stressmeter during the impounding period are therefore of some interest.

The readings are shown on Figure 6.13 but for purposes of comparison with calculated stresses, it is necessary to consider the readings with reference to a datum level at the beginning of impounding. The stress condition on 22nd December, 1966, has therefore been subtracted from the subsequent readings to give the relative principal stresses and directions shown in Figure 6.25 (Also see Appendix Table A.6.10). As before, this excludes the

gravity stresses, but the relative principal stresses will include the effects of thermal stresses and the buttress capping operation. As a result, the stresses given by the stressmeter readings do not necessarily increase in phase with the changes in water level.

Also included in Figure 6.25 are the corresponding results given by the 102 rosette strain gauges (see Appendix Table A.6.11). (The results have been obtained from the data shown in Figure 6.17 in which the sonic gauge stresses have already been corrected for creep but not geometric compatibility. In common with the method used in the independent assessment of the strain gauges, the error in compatibility, $(\sigma_{G_1}+\sigma_{G_2}) - (\sigma_{G_3}+\sigma_{G_4})$ has been distributed equally between the four stresses before deriving the principal stresses of Figure 6.25.) An alternative method of comparison is shown in Figure 6.26. In this case the principal stress conditions of Figure 6.25 have been resolved into normal and shear stress components in vertical and horizontal planes (using the notation $\Delta\sigma_v$, $\Delta\sigma_h$, $\Delta\tau_{vh}$).

When observing the differences between the stressmeter and strain gauge results, allowance should be made for the dissimilar instrument positions in the buttress. The geometry of the cross-section is different in the two cases and in the independent instrumentation report it has also been concluded that the 102 rosette readings have been influenced by the different thermal properties of the concrete and foundation. (The stressmeter is installed in the downstream pilaster (width 12 ft.) of the buttress, whereas the sonic gauge rosette is situated in the lower stressed region of the buttress footing. The maximum width of the footing, which is intended to reduce the stresses in the foundation below the buttress, is 30 ft.)

The significance of the low reading shown by the stressmeter in November, 1967, is not known and its occurrence emphasises the importance of frequent instrument readings in the final stages of impounding. A reduction in compressive stress could be predicted during winter months by considering the restraint provided by the main body of the buttress to cooling of the

exposed downstream face. The existence of a temperature gradient in this region is confirmed by the isolated sonic gauges 209/11, 211/11 (see Figure 6.26) but approximate calculations show that it is an unlikely explanation for the stress decrease indicated in Figures 6.25, 6.26. This deduction is supported by the reading in March, 1968, for the same reasoning would also predict a stress value significantly lower than that actually observed.

Since the 213/21 stressmeter was inaccessible on the occasion of the first full dam (January, 1968) the March, 1968 reading is the only one available for comparison with the total water load condition. From the measured concrete temperatures it is reasonable to translate the March reading in terms of the first full dam condition although, as before, this approach assumes that creep produces a negligible redistribution of stress during the two month interval.

Considered in this manner, the relative major principal stress from the stressmeter result is at least 30 per cent higher than predicted by calculation., a feature which is already apparent from Section 6.5.2. In (p, q, θ_B) notation, the stressmeter result is (+370 p.s.i., +39 p.s.i., +150°). (It is interesting to note that, making due allowance for buttress geometry, the relative major principal stress indicated by the sonic gauge rosette is also higher than expected by roughly the same amount.)

The angle of the relative major stress is clearly satisfactory, and although equilibrium dictates a zero value of the minor principal stress at the downstream face, it should be noted that the instrument is situated approximately ·2 ft. from the free surface and a small minor principal stress might therefore be expected. The significance of the results from this stressmeter could be improved by regaining access for further observations in the full dam condition.

6.5.5. Stressmeters 208/21 and 214/21

The response of stressmeters 208/21 and 214/21 to the total water load has already been included in Section 6.5.2. but their results throughout the impounding period are of some interest because of the assumed plane stress loading condition in the buttress web. Meter 208/21 is situated on the buttress centre line and although 214/21 is close to one of the free faces both instruments would be expected to show similar behaviour in the assumed absence of stress variations through the thickness of the web. (Although the two positions differ by approximately 20 ft. along the buttress section the finite element calculations predict only very small differences between the stress conditions at each point.) It should also be mentioned that the independent report[75] concludes that no significant stress differentials occur through the thickness of the completed web as a result of thermal or shrinkage effects, although the measurements for this deduction were not made in the vicinity of the two stressmeters.

It is apparent from Figure 6.27 that in practice no consistent similarity exists between the response of the two stressmeters. (Data is given in Appendix Tables A.6.12, A.6.13) In this presentation the instrument readings have been referred to a datum level at the beginning of impounding and the observed principal stress conditions have been resolved into normal and shear stress components in vertical and horizontal planes. As before, it is not possible to say whether the differences are due to some feature of the stressmeter technique or the actual stress conditions in the web.

Two additional points might be raised here. First, stressmeter 214/21 is situated very close to a "flat jack" pressure transmitter and it is not known how this affects the instrument readings. (The flat jack consists of a thin flexible steel envelope which is only rarely pressurised for demonstration purposes.) Secondly, the lower access gallery through the buttress web passes between the two instrument positions and it might be postulated that

this aperture could be responsible for a dissimilar redistribution of stress in the vicinity of each stressmeter.

On further inspection, this explanation would appear to be unlikely; the finite element calculation purposefully considered the elastic stress concentrations around the gallery and the results predicted negligible effects at the stressmeter positions. In addition, there is evidence in the literature to question the occurrence of elastic stress concentrations around apertures in concrete[78],[79] and it is possible that even the finite element calculation does not realistically represent the effect of the gallery.

6.5.6. The Second Stage Stressmeters

The results from the second stage stressmeters (shown by the code numbers 204/22, 206/22, etc.) are included in Figures 6.9-6.15.

During impounding and the early part of the full dam condition the indicated changes of major principal stress, principal stress ratio and stress direction generally differed from the corresponding changes in the first stage instrument readings. A proper comparison is therefore difficult to visualise from the presentation of Figures 6.9-6.15, and the indicated principal stress conditions are best resolved into components in vertical and horizontal directions.

An example is given in Figure 6.28 which shows normal and shear stress components in the plane of the buttress as implied by the two annular stressmeters at position 206. (see Appendix Tables A.6.14, A.6.15). The stress components have been obtained directly from the indicated principal stress conditions of Figure 6.10. Similar comparisons have been made at positions 206 and 304; the results show similar features to position 206.

From the first stage instrument (206/21) it can be seen that the significant changes in the vertical normal stress component occurred before impounding and the subsequent fluctuations were relatively small in magnitude. The horizontal normal stress and shear stress components appear

in a similar manner although the later fluctuations are more significant in relation to the initial values when impounding began.

From the second stage instrument readings the vertical normal stress component increased throughout impounding and at the full dam condition this stress component had achieved a value corresponding to that indicated by the first stage stressmeter. Subsequently, both stressmeters indicated similar values of vertical normal stress. The horizontal normal stress components followed a similar pattern, although towards the end of impounding, and also in April, 1969, the second stage stressmeter indicated a higher value than the first stage instrument. The significance of this feature, and the associated differences in shear stress components, is not understood but it seems likely that most of the differences could be explained by experimental errors in the stressmeter readings, particularly in the estimation of the principal stress ratio n.

On this evidence the behaviour of the second stage stressmeters is inconsistent with the concept of an elastic inclusion applied to an isotropic elastic host material. This observation is not entirely unexpected since the buttress concrete cannot be described in purely elastic terms over long periods of time, the time dependent deformation characteristics being more relevant to linear viscoelastic behaviour.

The problem of a rigid inclusion in these circumstances has so far received little attention. Hult[80] has briefly discussed one aspect of the problem which involves the state of stress in a rigid inclusion gauge applied to a linear viscoelastic material already subjected to a constant external load. Berry and Fairhurst[81] described the principles of the same problem with particular reference to a solid cylindrical inclusion. Both contributions show, in specified conditions, that the stress in the inclusion increases until it reaches a level required by elastic equilibrium. In other words, the gauge reading will increase continuously until

it "catches up" with the reading from a similar device which has experienced the full loading history of the viscoelastic material. Thereafter, the inclusion stress level stays constant as long as the host material stresses remain unchanged. A limited experimental verification of the phenomena has recently been described by Hawkes[52] with particular reference to the photoelastic stressmeter applied to frozen sand.

The period of time required for the "catch-up" process will depend upon the creep parameters of the system and in the present state of understanding it is not possible to predict the times which might be required at the various stressmeter positions in the buttress. From the evidence of Figure 6.28 the process appears to have occurred within twelve months at position 206. This relatively short period of time clearly prevents interpretation of the second stage stressmeter readings, as was originally hoped, solely in terms of the buttress stress changes during impounding.

Subsequently, the readings should be reliable as duplicates of the first stage stressmeter results although it would be desirable to improve the comparison by continuing observations at frequent intervals in the full dam condition.

Similar comments apply to the results at the other positions where both stressmeters are still operative, e.g. 208, 304. It is also interesting to note that the failure of stressmeters 210/21, 212/21 may now be less significant for stability apparently exists in the corresponding second stage instrument readings (Figure 6.12). From the above discussion it may be possible to justify interpretation of these second stage readings after impounding in terms of buttress stresses. The major principal stresses and the stress directions derived by this approach appear to be in reasonable agreement with the results from the other stressmeters in the buttress.

6.5.7. The Solid Stressmeters

The limited readings available from the two solid stressmeters at positions 206/23 and 208/23 are given in Table A.6.5, Appendix 6.

Throughout the programme these instruments could not be used satisfactorily. Illumination difficulties occurred in both cases and at position 208/23 it was not possible to rectify an early fault in the light unit. When readings were available, the observed fringe orders were erratically distributed in the glass inclusion and Tardy compensation could not be applied with confidence.

This behaviour was inconsistent with earlier laboratory tests and in a strict sense it is not possible to make a comparison with the corresponding principal stress differences deduced from the neighbouring annular stressmeter. If such a comparison is attempted, as in Appendix Table A.6.5., the general lack of agreement is immediately apparent.

6.6. Conclusions

The following conclusions may be drawn within the limitations of the results so far available:

(1) The isolated sonic strain gauge results show that shrinkage can make no significant contribution to the stressmeter response in this application. From the observed concrete temperatures it would also appear to be unlikely that mismatched thermal characteristics have any significant effect. Although the thermal characteristics of the stressmeter require further investigation , it must be concluded that, as far as present information allows, the clearly defined symmetrical fringe patterns can only be interpreted according to the procedure described by previous investigators.

(2) The stressmeter readings during the construction period therefore indicate the presence of significant biaxial compressive principal

stresses in the plane of the buttress, and in some cases, their magnitudes exceed the subsequent calculated stresses in the loaded structure. In the absence of comparative measurements, the true significance of these stressmeter readings cannot be assessed and the results must await comparison with similar applications in the future.

(3) The significance of the construction stresses was reflected in the stressmeter readings at the end of impounding when the indicated absolute principal stresses clearly exceeded the calculated values. The two stressmeters near the centre of the web at the lower instrument level indicated the highest stresses, the maximum value being approximately twice the highest stress level in the buttress predicted by calculations which ignore the stress history during the construction period. At the same time the indicated minor compressive principal stresses were higher than expected by calculation but despite these differences in stress magnitude, the indicated stress directions after impounding were similar to the calculated conditions.

(4) The increments of the stressmeter readings at the lower instrument level produced solely by the total water load imply a distribution of stress which does not agree with calculated distributions. Although the comparison has been hindered by the final stages of buttress construction, no satisfactory explanation can yet be given for this fundamental aspect of the stressmeter results.

(5) It is not possible to trace the development of water load stresses within the series of stressmeter readings obtained during impounding since there is insufficient data to allow separation of the varying thermal and water load stress increments. Similarly more instrument readings are required before detailed comments

can be made about stressmeter behaviour during the approximately constant water load condition which has existed in the buttress subsequent to impounding.

(6) The two stressmeters near the centre of the web at the lower level do not demonstrate the plane stress loading conditions during the impounding period which are assumed in the calculations. There is no independent experimental evidence of the plane stress assumption and it is therefore difficult to make further comments about the significance of these two stressmeter results in this respect.

(7) The behaviour of the two solid stressmeters was unsatisfactory throughout the programme; the reading difficulties experienced in this first field application appear to be features of practical technique and further development of the device is clearly necessary.

(8) The second stage annular stressmeter readings during impounding do not agree either with the earlier stressmeters or the expected buttress behaviour. In all cases the response appears to be consistent with that of an inclusion applied to a linear visco-elastic material which is already subjected to long-term loading. The problem requires fundamental investigation; in this instance, clarification would be improved by further readings. There is sufficient evidence to show that the second stage instruments have been unsuccessful in uniquely identifying the stress changes which occurred during the impounding period, but it is expected that the subsequent readings will be available for comparison with the first stage stressmeters.

(9) Continued observations in the buttress would be justified. A particular objective should be to obtain a closely spaced series of

readings in all the operative stressmeters throughout at least once complete annual cycle in the full dam condition. It will then be possible to attempt a separation of the thermal and water load stress increments.

(10) The details of practical technique employed in this exercise appear to have been generally satisfactory and those failures which have occurred in the annular stressmeters are understood and could be prevented in future work. The probe light source provided a simple and reliable means of illuminating the annular stressmeters although its assembly and dismantling accounted for a significant proportion of the total site observation time. In this respect the light source employed with the solid meters is more convenient, although it requires additional access to the other side of the buttress. The method of casting in empty cubes, or briquettes, during construction also presents an economical and simple means of access for later stressmeters and the method could be used to advantage in tests requiring the investigation of stress increments produced by short-term loading.

(11) The results of the programme are such that it is not possible to comment on the practical techniques used in measuring fringe orders, principal stress ratios and stress directions. However, it is clear that in field applications of this nature an assessment of stressmeter performance will depend on observed changes in the stressmeter fringe pattern rather than the absolute condition at any given time. It therefore seems reasonable to conclude that the value of the annular stressmeter could be improved by further developments in the observational techniques which are currently employed with the device.

6.7. Recommendations

Several recommendations can be made for obtaining the additonal data necessary for a substantial assessment of stressmeter performance in future investigations of this nature:

(1) There is an immediate need for direct comparisons between stressmeter results and a conventional in-situ strain or stress measuring technique to confirm the nature of the biaxial stress conditions indicated by the stressmeters in this application. The obvious recommendation would be to install at least one stressmeter in the immediate neighbourhood of a strain gauge rosette (which should also include transverse gauges to allow evaluation of the full three-dimensional state of strain). If the comparison position was situated near the downstream face of a buttress there would also be easy visual access for a second stressmeter installed perpendicular to the first, thus supplying further comparison data.

(2) More quantitative evidence is clearly desirable for the response of the meter in concrete subjected to long-term stresses. In some respects stressmeter interpretation is more complicated than conventional strain or stress sensing methods in so far as the stressmeter is a biaxial rather that a uniaxial device. Attention should be paid to its response in both uniaxial and biaxial applied stress conditions.

(3) An in-situ calibration facility could be used to distinct advantage. This would provide realistic experimental evidence of the stressmeter sensitivity factor which, as in this instance, might otherwise have to be deduced from earlier independent laboratory calibration data. In principle a uniaxial test facility could be provided by a simple modification of the isolated strain gauge installations employed in the Clywedog buttress, the stress source being a "flat jack" pressure transmitter mounted between the top of the concrete column and the roof of the chamber.

By including an annular stressmeter, together with axial and transverse sonic strain gauges in the concrete column, the advantages would be:

(a) Regular stressmeter calibration tests could be carried out throughout the life of the buttress in realistic conditions of temperature and moisture content. The uniaxial sensitivity factors so indicated would also enable the biaxial sensitivity factors to be determined with considerable confidence. .

(b) The same tests would indicate the variation of instantaneous elastic modulus and Poisson's Ratio with time. This sonic gauge data would also provide independent comparative evidence for the supporting laboratory creep tests, etc., required by the strain gauge rosettes in the dam.

(c) In the periods between calibration tests the stressmeter could be observed in the free standing column to provide for the possibility of spurious fringe orders caused by shrinkage, swelling or mismatched thermal properties.

CHAPTER 7

Conclusions

The individual conclusions from the investigations described in this account have already been given at the end of each chapter, but it now becomes necessary to review their implications to the photoelastic stressmeter technique as a practical method of measuring stresses in concrete. Although several fundamental features have been beyond the scope of the present investigation, the overall conclusions are perhaps best referred to the appropriate requirements of an ideal stress gauge which were stated at the beginning.

The first requirement concerned the ability of the device to respond to stress changes in the host material without confusing effects from what have been called extraneous deformations. In this respect the only new evidence from the present discussion concerns some of the effects of shrinkage on the stressmeter readings, although one aspect of the creep problem has also been revealed by the buttress dam measurements. In addition some other features of the stresses in the inclusion have been shown by the laboratory work with shrinkage and stresses from external loads.

As far as shrinkage is concerned, it is clear that the stressmeter can be influenced to a significant degree, although the effects appear to be much smaller than predicted by conventional elastic calculation. From the experimental observations with a specimen subjected to shrinkage and uniaxial compression, it must be concluded that considerable errors of interpretation will be possible if the existing methods of taking readings are relied upon to identify the two principal stresses in the plane of the stressmeter when large shrinkage strains occur around the device. Specifically, the superposed effects of shrinkage and stresses from external loads can produce stressmeter patterns which are ambiguous with other patterns produced by external biaxial stresses alone.

To remove this ambiguity improvements should be made to the interpretation technique so that the shrinkage increment of the stressmeter fringe pattern can be isolated and thus allow measurements on the fringe pattern which can be interpreted solely in terms of the two applied principal stresses. Due allowance must be made in this procedure for the differences revealed earlier which can occur between the calculated and actual fringe order distribution in the inclusion.

However, it must be admitted that the above remarks are based on only one experimental test-piece; other results from the shrinkage tests were inconsistent with this example in that most of the specimens showed no significant response in similar circumstances (these "no response" specimens were prepared from concrete mixes both with and without coarse aggregate). The reason for the inconsistency remains to be proved but it is possible that the adhesive layer behaved inconsistently throughout the series of test specimens. At the same time, creep and relaxation presumably occurred in the concrete around the inclusion, but the relative significance of the adhesive and concrete properties on the stressmeter response cannot be determined from the existing results alone. This feature could be clarified in future work by carrying out comparable tests without a boundary adhesive.

The importance of the adhesive layer on the stressmeter response to shrinkage can also be deduced from the comparison between the observed and calculated distribution of fringe orders in the one specimen which showed the significant shrinkage response. It is recommended therefore, that the properties and effects of the adhesive layer should be considered in any future study of the stressmeter's response to shrinkage. Such a study should also include the possible effects on the photoelastic pattern of shrinkage which occurs in an axial direction around the inclusion. In the meantime applications of the annular stressmeter which are likely to involve a significant degree of shrinkage should be considered with caution or be supported by purposeful tests to allow for the possible extraneous response of the inclusion.

As far as the effects of mismatched thermal properties and creep are concerned, these have not been investigated here and the only extra evidence from the present work concerns the stressmeter response when the device is applied to a concrete structure already under load. The buttress dam measurements have shown that readings taken over a long period of time cannot be simply interpreted in terms of concrete stress changes which occur subsequent to the application of the stressmeter. Since this could be a relatively common situation in structural applications of the technique this aspect of the creep problem clearly requires further consideration.

On the other hand, it seems reasonable to infer that the device could be used in a structure already under load if the stress changes to be measured are of short duration only. In addition it might also be suggested that an inclusion type stress gauge could be used to determine the absolute state of stress in concrete already under load, assuming that sufficient time would be available for the gauge readings to reach equilibrium. However, this second interesting possibility has yet to be demonstrated conclusively by the experimental readings in the dam.

Reference must also be made to the inclusion stress conditions observed in the laboratory loading tests. In both the shrinkage and disc loading tests it has been shown that the generalised plane stress solutions for the inclusion stresses did not fully agree with the experimental observations, and of three features discussed to explain these effects, the one which appears to be most likely concerns the presence of the adhesive layer at the outer boundary of the stressmeter. It is considered that this aspect of the results could be clarified for both the solid and annular stressmeters by extending the existing theoretical solutions to include the presence of a finite thickness of adhesive. Since in this instance the measured fringe orders were significantly different from the

calculated values at the centre of the solid stressmeter and at the 45° points of the annular stressmeter, this feature should be considered in further detail.

In the same context the present results appear to be in reasonable agreement with earlier results given by Dhir as far as the annular stressmeter in uniaxial loading is concerned, but a significant difference occurs in the solid stressmeter observations. It has also been pointed out that Dhir's results for the biaxial sensitivity of the annular stressmeter do not agree with the theoretical values and anomalies also occur in his figures for uniaxial sensitivity in high modulus materials. Although the last point is not important for rigid inclusion conditions, the anomalies require explanation. It would be desirable to repeat Dhir's experimental work and extend the range of tests particularly in the cases of the annular stressmeter biaxial sensitivity factors and the solid stressmeter data. However, these features of the stressmeter do not of themselves prevent the application of the device provided that the appropriate calibration factors can be determined experimentally for a given situation.

The second fundamental requirement of an ideal stress gauge concerned a well-defined directional response and in this context the annular stressmeter appears to have a distinct advantage over other devices. As far as the present results are concerned the self-orientating property of the device and the immediate visual indication of the applied stress directions have been clearly demonstrated in both series of laboratory tests; the stressmeter readings in the buttress dam also appear to be satisfactory in this respect. No other contemporary instruments for internal stress determinations in concrete possess a similar characteristic.

The third requirement referred to the desirable response to small tensile stresses. This aspect of the photoelastic stressmeter has been discussed in the account of the loaded disc investigation where the tension was

produced as a minor principal stress in combination with a major principal compressive stress.

The results have shown that the current method of taking stressmeter readings is not entirely suitable for use in these circumstances because a double error is possible in the stress determination. First, the stressmeter fringe pattern is similar to the uniaxial case and the presence of the tensile stress could be overlooked. Secondly, the stressmeter sensitivity, as determined at the 45° points of the pattern, can be significantly different to the uniaxial value and thus the major principal stresses deduced from the fringe order measurements would then also be in error.

This conclusion applies to conditions in which the magnitudes of the tensile stresses are less than one-third of the associated compressive stresses. Conditions outside this range have not been considered but other evidence in the literature suggests that the appearance of the stressmeter fringe pattern then changes appreciably. If necessary, the appropriate theoretical fringe order profile can be calculated from the Hiramatsu-Barron solution for the inclusion stresses, but in practice the stressmeter response will depend on the tensile strengths of the glass and the circumferential bond.

On the other hand, the laboratory results show that the existing method of taking readings is satisfactory for the solid stressmeter in compression-tension conditions. This conclusion is consistent with existing knowledge of the solid stressmeter's response to biaxial compressive stresses although as mentioned previously, the sensitivity factor needs to be clarified in rigid inclusion conditions. It is unfortunate that the first field application of the solid stressmeter in the buttress dam did not vindicate the potential advantages of this device.

The dam application has also revealed several desirable features of practical convenience possessed by the photoelastic stressmeter. For instance, no difficulty was experienced in applying the stressmeters to the

buttress both during and after concreting and readings have been taken with a minimum of ancillary equipment over a relatively long period of time. The simple construction of the device and its accessories is an advantage from the point of view of cost and also for long-term applications, although in this instance several instruments were lost after the polarising filters were destroyed by moisture. A recent design modification will eliminate this problem in the future.

However, there is one feature of practical technique which may be a disadvantage in some circumstances. In the present state of development the stressmeter has to be visible to the observer and in this sense the technique only provides semi-remote observations. (The possibility of remote observations from photoelastic transducers is considered in a current project[47].)

As far as the fundamental features of the buttress measurements are concerned, there are several inconclusive features in the results which make it difficult to assess the accuracy of the stress conditions indicated by the photoelastic stressmeters. In this instance it has not been sufficient to compare the stressmeter results with theoretically calculated conditions and it seems reasonable to conclude that in applications of this nature a satisfactory assessment of stressmeter performance will only be achieved by comparing the results with stresses determined by other independent experimental techniques. Nevertheless, the experience derived from the buttress dam application is sufficient to justify further similar investigations and several recommendations have already been made which should allow a clearer demonstration of the photoelastic stressmeter's characteristics in a future application.

In summing up this discussion it may be said that the present work has demonstrated several features of the photoelastic stressmeter which have not been considered by previous investigators. Some of these features have

endorsed the potential advantages of the technique whilst others must be added to the existing problems requiring further study which were referred to in the summary of earlier work.

Of the outstanding problems, the stress distribution in the inclusion and its probable dependence upon the boundary adhesive is considered to be particularly significant since this clearly affects the sensitivity of the device as a stress transducer. At the same time, more quantitative information is necessary for the response of the stressmeter in concrete subjected to creep in both uniaxial and biaxial stress conditions.

These two problems are considered to be the most important of those mentioned in the discussion. All together, the several outstanding problems provide considerable scope for further study if a comprehensive assessment is to be made of the photoelastic stressmeter as a practical device for in-situ stress determinations in concrete.

REFERENCES

(1) ENGLAND, G.L., and ILSTON, J.M. "Methods of Computing Stress in Concrete from a History of Measured Strain." Civ. Eng. & Pub. Wks. Rev., April, May, June, 1965.

(2) HULT, J., KVAPIL, R., and SUNDKVIST, H. "Function and Scope of Stressmeters in Rock Mechanics." Int. Jour. Rock Mech. Min. Sci., Vol. 3, No. 1, p.1-10, 1966.

(3) HAST, N. "Measuring Stresses and Deformations in Solid Materials." Ingeniors Vetenskaps Akademien Handlingar, No. 178, 1945, Stockholm.

(4) CARLSON, R.W., and PIRTZ, D. "Development of a Device for the Direct Measurement of Compressive Stress." Proc.A.C.I., Vol. 49, p.201-216,1953.

(5) McCOY, E.E. "Investigation of the Improved Carlson Stressmeter." U.S.Army Engineers Waterways Exp.Stn., Tech.Rept. 6-454-1957, Vicksburg, Mississippi

(6) LOH, Y.C. "Internal Stress Gauges for Cementitious Materials." Proc.S.E.S.A., Vol. XI, No. 2, p.13-28, 1954.

(7) ROCHA, M. "In-situ Stress and Strain Measurements" "Stress Analysis" edited by O.C. Zienkiewicz and G.S. Holister, John Wiley and Sons, 1965, Chap.17, p.425-461.

(8) RAPHAEL, J.M. and CARLSON, R.W. "Measurement of Structural Action in Dams." Printed by James J. Gillick & Co., Berkeley, Calif., U.S.A.

(9) CARLSON, R.W. "Manual for the Use of Stressmeters, Strain Meters and Joint Meters in Mass Concrete." Printed by James J. Gillick & Co., Berkeley, Calif., U.S.A., 1954.

(10) COUTINHO, A., "Détermination des Contraintes dans le Béton par la Méthode du Tensomètre Photoélastique." Ann. de l'Inst. Tech. du Bat. et des Trav. Pubs., New Ser. No.20, Mai, 1948, Essais et Mesures No. 4.

(11) COUTINHO, A. "Theory of an Experimental Method for Determining Stresses not Requiring an Accurate Knowledge of the Elastic Modulus." Int. Assoc. Bridge & Struc. Engs. Congress, Vol. 9, p.83-103, 1949. (English Translation: N.C.B. Translation Section A.632/A.B.)

(12) SEZAWA, K., and MIYAZAKI, B. "Spherical Problems of Elasticity Solved in Polar Co-ordinates with Applications." Jour.Soc.Mech.Eng., Tokyo, Vol. 31, p.625, 1928.

(13) SEZAWA, K., and NISHIMURA, G. "Stresses under Tension in a Plate with a Heterogeneous Insertion." Rep. Aero. Res. Inst., Tokyo Imp.Univ., Vol. 6, No.68, p.25-43,April, 1931.

(14) GOODIER, J. "Concentration of Stress around Spherical and Cylindrical Inclusions and Flaws." Jour.App.Mechs(Trans., A.S.M.E.), Vol.55, p.39, 1933.

(15) ROBERTS, A., et al "A Laboratory Study of the Photoelastic Stressmeter." Int.Jour.Rock Mechs. Min.Sci., Vol. 1, p.441-457, May, 1964.

(16) WILLIAMS, F.T. "The Measurement of Stresses and Strains in Concrete Structures and in Strata around Underground Excavations." Ph.D. Thesis, University of Sheffield, 1964.

(17) DHIR, R.K. "A Study of Photoelastic Stressmeters." Ph.D. Thesis, University of Sheffield, 1966.

(18) DHIR, R.K. "A Study of Photoelastic Stressmeters." Ph.D. Thesis, University of Sheffield, Chapter 3, p.46-50, 1966.

(19) DHIR, R.K. "A Study of Photoelastic Stressmeters." Ph.D. Thesis, University of Sheffield, Chap.5, p.64.

(20) DHIR, R.K. "A Study of Photoelastic Stressmeters." Ph.D. Thesis, University of Sheffield, Chap.5, p.69, 1966.

(21) DHIR, R.K. "A Study of Photoelastic Stressmeters." Ph.D. Thesis, University of Sheffield, Chap.5, p.74, 1966.

(22) DHIR, R.K. "A Study of Photoelastic Stressmeters." Ph.D. Thesis, University of Sheffield, Chap.5, p.75, 1966.

(23) DHIR, R.K. "A Study of Photoelastic Stressmeters." Ph.D. Thesis,University of Sheffield, Chap.5, p.84, 1966.

(24) DHIR, R.K. "A Study of Photoelastic Stressmeters." Ph.D. Thesis, University of Sheffield, Chap.7, p.95, 1966.

(25) DHIR, R.K. "A Study of Photoelastic Stressmeters." Ph.D. Thesis,University of Sheffield, Chap.7, p.97-99.

(26) FROCHT, M.M. "Photoelasticity" Vol.I, 1941, Vol.II, 1948, John Wiley & Sons, Inc.

(27) FROCHT, M.M. "Photoelasticity." Vol.I, Chap.5, p.156, John Wiley & Sons, Inc.1941

(28) FROCHT, M.M. "Photoelasticity." Vol.I, Chap.10, p.361, John Wiley & Sons, Inc., 1941.

(29) FROCHT, M.M. "Photoelasticity." Vol.I, Chap.11, p.371. John Wiley & Sons, Inc., 1941.

(30) FROCHT, M.M. "Photoelasticity." Vol.II, Chap.4, p.125, John Wiley & Sons,Inc., 1948.

(31) FROCHT, M.M. "Photoelasticity." Vol.II, Chap.10, p.333, John Wiley & Sons,Inc., 1948.

(32) FROCHT, M.M. "Photoelasticity." Vol.II, Chap.10, p.336, John Wiley & Sons, Inc., 1948.

(33) COKER, E.G., and FILON, L.N.G. "A Treatise on Photoelasticity." Revised by H.T. Jessop, Cambridge University Press, 1957.

(34) MINDLIN, R.D. "A Review of the Photoelastic Method of Stress Analysis." Jour.App.Phys., Vol.10, p.222-247, 273-294, 1939.

(35) POST, D. "Photoelasticity." Jour.S.E.S.A., Vol.6, Aug., 1966, p.19A.

(36) HIRAMATSU, Y., NIWA, Y., and OKA, Y. "Measurement of Stress in Field by Application of Photoelasticity." Tech.Reps.Eng.Res.Inst. Kyoto University, Rept. No.37, March, 1957.

(37) HIRAMATSU, Y., NIWA, Y., and OKA, Y. "Measurement of Variation in Stress by a Photoelastic Stressmeter." Mem.Fac.Engng., Kyoto University, Vol.XXIX, Pt.I., Jan, 1967.

(38) BARRON, K. "Glass Insert Stressmeters." Canadian Dept. Min.Tech.Sur., Mines Branch, Div.Rept. FMP64/123-MRL, Oct., 1964.

(39) MUSKHELISHVILI, N.I. "Some Basic Problems of the Mathematical Theory of Elasticity." English Trans. by J.R.M. Radok, P. Noordhoff Ltd., Groningen, Holland, 1953, p.210-217.

(40) PANT, B. "A Method for Determining Integral Fringe Orders in Photoelastic Analysis." Jour.S.E.S.A., Vol.3, July, 1963, p.173.

(41) BREWSTER, D. "On the Communication of the Structure of Doubly Refracting Crystals to Glass, Muriate of Soda, Fluor Spar and Other Substances by Mechanical Compression and Dilatation." Phil.Trans.Royal Soc., p.156-178,1816.

(42) MESNAGER, M. "Determination Complète sur un Modele réduit des Tensions qui se produirant dans un Ouvrage." Ann.Pont.Chauss., Vol.16, No. 4, p.133-186, 1913.

(43) ROBERTS, A., and HAWKES, I. "Optical Load Measurement Techniques on Mine Support Systems." Colliery Guardian, Aug.20, 1965.

(44) HOOPER, J.A. "The Theory and Development of Load Cells Incorporating Photoelastic Glass Disc Transducers." Ph.D. Thesis, Univ. of Sheffield, 1968.

(45) HARRIS, F.C. "The Photoelastic Constants of Glass as Affected by High Temperature and Lapse of Time." Proc.Roy.Soc.(London), A106, p.718-723, 1924.

(46) VAN ZEE, A.F. and NORITAKE, H.M. "Measurement of Stress Optical Coefficient and Rate of Stress Release in Commercial Soda Lime Glasses." Jour.Amer.Ceramic Soc., Vol.41, No.5, p.164-175, 1956.

(47) ATKINSON, M.S. "Load Monitoring Systems incorporating Photoelastic Transducers." Ph.D. Thesis, University of Sheffield, 1969.

(48) WAXLER, R.M. "The Stress Optical Coefficient of Plate Glass." Glass Industry, Vol.34, p.258-259,1953.

(49) ROSE, H. "The Measurement of In-Situ Stress, Strain and Load by Optical Techniques." Postgrad. Sch. Min., Final Tech. Rept. U.S. Army European Res. Office, Dec. 1966, Contract No. 91-591-EUC, R & D 1214. (University of Sheffield)

(50) HOOPER, J.A. "The Measurement of Stress in Concrete using Optical Transducers." M.Eng. Thesis, University of Sheffield, 1966.

(51) RABBETS, J.W. "The Behaviour of Glass Photoelastic Stressmeters under Temperature Changes in Reinforced Concrete." M.Eng. Thesis, University of Sheffield, 1969.

(52) HAWKES, I. "The Evaluation of Stress in Low Modulus and Viscoelastic Materials using Photoelastic Inclusions." S.E.S.A. Spring Meeting, Albany, New York, May, 1968.

(53) TIMOSHENKO, S., and GOODIER, J.N. "Theory of Elasticity." McGraw Hill Book Co., 2nd Ed., 1951, Eng.Soc. Monographs, Int. Student Edition, p.58.

(54) TIMOSHENKO, S., and GOODIER, J.N. "Theory of Elasticity." McGraw Hill Book Co., 2nd Ed., 1951, Eng.Soc. Monographs, Int. Student Edition, p.107-108.

(55) NEVILLE, A.M. "Properties of Concrete." Sir Isaac Pitman & Sons, 1968, Paperback Edition, p.373.

(56) NEVILLE, A.M. "Properties of Concrete." Sir Isaac Pitman & Sons, 1968, Paperback Edition, Chap.8, p.400.

(57) NEVILLE, A.M. "Properties of Concrete." Sir Isaac Pitman & Sons, 1968, Paperback Edition, Chap.6, p.299.

(58) OPPEL, G. "Photoelastic Strain Gauges." Proc. S.E.S.A., Vol.18, p.65,1961.

(59) DESAYI, P. "Strength of Concrete under Combined Compression and Tension - Determination of Interaction Curve at Failure from Split Cylinder Test." RILEM Bull., Mats. & Struc., Vol.2, No. 9, p.175-185, May-June,1969.

(60) WRIGHT, P.J. "Comments on Indirect Tensile Test for Concrete Cylinders." Mag.Conc.Res., Vol.7, No.20, p.87-96, July, 1955.

(61) HONDROS, G. "The Evaluation of Poisson's Ratio and Modulus of Materials of Low Tensile Resistance by the Brazilian (Indirect Tensile) Test with Particular Reference to Concrete." Aust. Jour. of App.Sci., Vol.10, No.3, 1959.

(62) BINNS, R.D. and MYGIND, H.S. "The Use of Electrical Resistance Strain Gauges and the Effect of Aggregate Size on Gauge Length in Connection with the Testing of Concrete." Mag. Conc. Res., Vol.1, No.1, p.35-39, Jan.1949, and Vol.1, No. 2, p.107-8, June, 1949.

(63) COOKE, R.W. and SEDDON, A.E. "The Laboratory Use of Bonded Wire Electrical Resistance Strain Gauges on Concrete at the Building Research Station." Mag. Conc.Res., Vol.8, p.31-37, March, 1956.

(64) MURPHY, G. "A Graphical Method for the Evaluation of Principal Strains from Normal Strains." Jour.App.Mechs. (Trans. A.S.M.E), Vol.12, p.A-209, 1945.

(65) FILON, L.N.G. "On an Approximate Solution for the Bending of a Beam of Rectangular Cross-Section with Special Reference to Points of Concentrated or Discontinuous Loading." Trans.Roy.Soc.(London), Series A, Vol.201,p.67, 1903.

(66) STERNBERG, E. and SADOWSKY, M.A. "Three-Dimensional Solution for the Stress Concentration around a Circular Hole in a Plate of Arbitrary Thickness." Jour.App.Mechs.(Trans. A.S.M.E.), Vol.16, p.27, 1949.

(67) GREEN, A.E. "Three-Dimensional Stress Systems in Isotropic Plates." Phil.Trans.Roy.Soc.(London), Series A, Vol.240, p.561, 1948.

(68) FROCHT, M.M. and LEVEN, M.M. "On the State of Stress in Thick Bars." Jour.App.Phys., Vol.13, p.308-313, 1942.

(69) PARKS, V.J. and DURELLI, A.J.
"Photoelastic Analyses of Plates Subjected to Restrained Shrinkage."
Jour.App.Mechs. (Trans.A.S.M.E.), Vol.87, p.504-510, Sept., 1965.

(70) DURELLI, A.J. et al
"Stresses and Strains in Matrices with Inserts."
Stress Analysis Lab., Catholic Univ. of America, Washington D.C., May,1967, U.S. Dept. Commerce, Clearing House No. AD 653 721.

(71) DURELLI, A.J. and PARKS, V.J.
"Experimental Stress Analysis of Loaded Boundaries in Two-Dimensional Second Boundary Value Problems."
Jour.S.E.S.A., Vol.7, p.381-385,1967.

(72) SAMPSON, R.C.
"Three-Dimensional Photoelastic Method for Analysis of Differential Contraction Stresses."
Jour. S.E.S.A., Vol.3, No.10, p.225-237, Oct.,1963.

(73) RHINES, W.J.
"An Extension of Generalised Plane Stress for Problems with Out-of-Plane Restraint."
Jour.S.E.S.A., Vol.8, p.481-487, Nov., 1968.

(74) STEPHEN, R.M. and PIRTZ, D.
"Application of Birefringent Coating to the Study of Strains around Circular Inclusions in Mortar Prisms."
Jour.S.E.S.A.,Vol.3, p.91-97, April, 1963.

(75) SIR WILLIAM HALCROW AND PARTNERS
"Instrumentation Investigations at Clywedog Dam."
(Private Report to C.I.R.I.A., June, 1969.)

(76) ZIENKIEWICZ, O.C. and CHEUNG, Y.K.
"Consulting Report, Clywedog Dam Stress Analysis."
University of Wales, Civ.Eng.Dept. Report to Sir William Halcrow and Partners, London, April, 1964.

(77) DAVIES, J.D.
"Report on Laboratory Creep Tests of Concrete Specimens, Clywedog Project."
University of Wales, Civ.Eng.Dept., Report to Sir William Halcrow and Partners, London, May, 1968.

(78) WRIGHT, W., and BYRNE, J.G.
"Stress Concentration in Concrete." Nature, Vol.203, No.4952, p.1374, Sept.26th,1964.

(79) EVANS, R.H. and MARATHE, M.S.
"Stress Distribution around Holes in Concrete." RILEM Bulletin, Mats. & Struc., Vol.1, No. 1, p.57, Jan-Feb., 1968.

(80) HULT, J.
"On the Measurement of Stresses in Solids." Trans. Chalmers Univ. of Technology, Gothenberg, Sweden, Nr. 280, 1963.

(81) BERRY, D.S. and FAIRHURST, C.
"Influence of Rock Anisotropy and Time Dependent Deformation on the Stress Relief and High Modulus Inclusion Techniques of In-Situ Stress Determination." A.S.T.M., Special Pub., Testing Techniques for Rock Mechanics, STP402, p.190-206, 1966.

(82) McINTOSH, J.D. and ERNTROY, H.C.
"The Workability of Concrete Mixes with $\frac{3}{8}$ in. Aggregates." Cement & Conc. Ass.Res.Rept., No.2, London, June, 1955.

(83) BARENBURG, A.W.T.
"Psychrometry and Psychrometric Charts." 2nd Edition, Transvaal and O.F.S. Chamber of Mines, Johannesburg, 1965.

(84) MOORE, D.R.
"The Measurement of Ground Movements in Bord and Pillar Workings." M.Eng. Thesis, University of Sheffield, 1967.

TABLES

TABLE 3.1

Details of Concrete Mixes used in Shrinkage Tests

(For Grading Details, see Table 3.2)

Mix	Maximum Aggregate Size in.	Design Strength (28 day x 6 in.cube) p.s.i.	Aggregate/ Cement Ratio	Water/ Cement Ratio	Observed Strength (Average of 3x6 in. cubes) p.s.i.	
					7 Days	28 Days
A	$\frac{3}{8}$	7500	2.6	0.36	8600	9800
B	$\frac{3}{8}$	6500	2.7	0.40	6730	8200
C	$\frac{3}{8}$	5500	3.4	0.45	5760	7200
F	$\frac{3}{16}$	-	1.4	0.44	7500	8800

TABLE 3.2.

Aggregate Gradings used in Concrete Mixes A, B, C.

Sieve Number	Percentage Passing				
	Coarse Aggregate	Fine Aggregate	Combined Aggregate	Grading Line 1 (Ref.82)	Grading Line 1 (Ref.82)
$\frac{1}{2}$ in.	100				
$\frac{3}{8}$ in.	85	100	89	100	100
$\frac{3}{16}$ in.	0.5	97	25	30	45
7		90	23	20	33
14		83	21	17	26
25		68	17	13	18
52		24	7	5	8
100		2	1	0	3

Grading tests carried out in accordance with B.S.812; 1967: "Methods for Sampling and Testing of Mineral Aggregates, Sands and Fillers".

TABLE 3.3.

Aggregate Gradings used in Concrete Mix F

Sieve Number	Percentage Passing					
	F1 Specimens			F3, F5 Specimens		
$\frac{3}{16}$ in.	98	100	100	100	100	100
7	92	92	91	86	92	91
14	86	85	83	73	84	82
25	73	73	70	57	72	67
52	26	29	34	19	36	32
100	3	9	7	3	8	7
200	0.5	1.5	1	0.5	1	1

Test procedure is referred to in

Table 3.2

TABEE 3.4.

Superposition of Shrinkage and Uniaxial Compression Stress

Fringe Orders - Annular Stressmeter, Specimen F3-4, Day 106

Specimen details: See Tables 3.1, 3.3, and Figure 3.7

Stressmeter Dimensions: 1.250 in. diameter x 0.265 in. diameter x 2.992 in.

f_g = 1220 p.s.i./fr./in.

Initial Shrinkage Fringe Order at ($\frac{r}{b}$ = 1.40) = + 1.06

Specimen Load lbs.	Applied Stress p.s.i.	Long-Strain μΣ (Average of 6 Demec Readings)	White Light Fringe Order at ($\frac{r}{b}$ = 1.40, θ=90°-270°)				Observed Pattern Profile (Dhir[21])
			θ=90°	θ=270°	Mean Value N_T	Corrected Value (N_T-N_S)	
0	0	0	1.10	1.04	1.06	0	1:1
3000	115	33	1.55	1.45	1.50	0.44	1:1
6000	231	65	2.15	2.18	2.16	1.10	1:¾
9000	346	97	2.66	2.60	2.63	1.57	1:¾
12000	462	133	3.24	3.18	3.21	2.15	1:½
15000	577	170	3.67	3.87	3.77	2.71	1:½
18000	693	200	4.12	4.05	4.08	3.02	1:¼
21000	808	235	4.97	4.83	4.90	3.84	1:¼

All fringe orders have positive signs - associated with ($\sigma_\theta' - \sigma_r'$) stress differences.

TABLE 4.1

Instrument Centre Points - Disc Rectangular Co-ordinates

1-1 Orientation

Point	Disc No. - Dimensions in Inches											
	F5-1				F5-2				F5-3			
	Diameter: 23.437				23.375				23.437			
	Thickness: 3.265				3.265				3.265			
	x	y	r_1	r_2	x	y	r_1	r_2	x	y	r_1	r_2
A	+5.625	-5.625	18.312	8.250	+5.312	-5.312	17.875	8.250	-	-	-	-
B	0	-8.406	20.125	3.312	0	-8.375	20.068	3.312	-	-	-	-
C	-	-	-	-	0	0	11.687	11.687	-	-	-	-
Meter 1	0	0	11.719	11.719	-	-	-	-	0	0	11.719	11.719
Meter 2	0	+8.468	3.250	20.187	0	+8.562	3.125	20.250	-	-	-	-
Meter 3	-5.625	+5.625	8.125	18.250	-5.550	+5.550	8.270	18.101	-	-	-	-

TABLE 4.2

Instrument Centre Points - Disc Rectangular Co-ordinates

Orientations 2-2, 4-4

Point	Disc F5-1 - Dimensions in Inches							
	Orientation 2-2				Orientation 4-4			
	x	y	r_1	r_2	x	y	r_1	r_2
A	+7.954	0	14.163	14.163	0	-7.954	19.672	3.765
B	+5.945	-5.945	18.637	8.287	-5.945	-5.945	18.637	8.287
Meter 2	-5.990	+5.990	8.280	18.701	+5.990	+5.990	8.280	18.701
Meter 3	-7.938	0	14.181	14.181	0	+7.938	3.781	19.656

Point	Disc F5-2 - Dimensions in Inches							
	Orientation 2-2				Orientation 4-4			
	x	y	r_1	r_2	x	y	r_1	r_2
A	+7.511	0	13.893	13.893	0	-7.511	19.198	4.176
B	+5.923	-5.923	18.579	8.265	-5.923	-5.923	18.579	8.265
Meter 2	-6.050	+6.050	8.270	18.781	+6.050	+6.050	8.270	18.781
Meter 3	-7.843	0	14.081	14.081	0	+7.843	3.844	19.531

TABLE 4.3

Comparison of Calculated Stresses near Disc Loading Point

Disc diameters: F5-1 - 23.375 in., F5-2 - 23.437 in.
Thickness: 3.265 in.
Width of Strip Loading: 0.625 in.
Load: 21,000 lb.

Point	Disc	Orientation	Calculated Principal Stresses - p.s.i.				% Difference $\frac{(a-b)}{a} \times 100\%$	
			(a) Strip Loading (Hondros Equations)		(b) Line Loading Conditions			
			p	q	p	q	p	q
A	F5-1	4-4	+1115	-171	+1123	-175	-0.7	-2.3
B	F5-1	1-1	+1256	-170	+1266	-175	-0.8	-2.9
A	F5-2	4-4	+1013	-172	+1020	-175	-0.7	-1.8
B	F5-2	1-1	+1252	-168	+1266	-175	-1.1	-4.2

TABLE 4.4

Disc Strain Gauge Rosettes

Calculated Strains for Disc Load of 21,000 lbs

Rosette	Disc Orientation (Vertical Diameter)	Calculated Strains - με					
		Disc F5-1 with $E = 3.5 \times 10^6$ p.s.i. $\mu = 0.22$			Disc F5-2 with $E = 3.25 \times 10^6$ p.s.i. $\mu = 0.20$		
		Gauge 1	Gauge 2	Gauge 3	Gauge 1	Gauge 2	Gauge 3
A	1-1	+60.5	-17.0	-8.5	+74.0	-13.0	-7.0
B	1-1	+373	+121	-130	+400	+134	-132
C	1-1	-	-	-	+171	-85.0	-
A	2-2	+14.3	-16.5	+14.3	+18.2	-19.5	+18.2
B	2-2	-15.0	-5.0	+61.0	-15.0	-3.0	+66.0
C	2-2	-	-	-	+43.0	+43.0	-
A	4-4	+105	+283	+122	+103	+277	+120
B	4-4	-15.0	+50.5	+61.5	-15.0	+53.5	+66.0
C	4-4	-	-	-	+43.0	+43.0	-

TABLE 4.5

Comparison of Rosette Point Stresses at Maximum Test Load

($E = 3.25 \times 10^6$ p.s.i., $\mu = 0.18$, $P = 21{,}000$ lb., $d = 23.375$ in., $l = 3.265$ in.)

Rosette Point	Disc Number	Orientation	Mean Observed Strains με			Calculated Stresses - p.s.i.						% Differences $\frac{(b-a)}{b} \times 100\%$	
						(a) From Observed Strains			(b) From Disc Theory				
			G_1	G_2	G_3	p	q	θ_D	p	q	θ_D	p	q
C	F5-2	1-1	+162	-92	——	+489	-211	-	+525	-175	0°	+6.9	-20.5
A	F5-1	1-1	+61	-20	-9	+221	-55	+18.5°	+273	-43	+25.5°	+19.0	-28.0
A	F5-2	1-1	+76	-19	-7	+277	-49	+18.5°	+310	-31	+25°	+10.6	-58.0
B	F5-1	1-1	+390	+122	-110	+1245	-133	+2°	+1266	-175	0°	+1.7	+29.7
B	F5-2	1-1	+360	+140	-98	+1150	-111	-1°	+1266	-175	0°	+9.2	+36.6
B	F5-1	2-2	-16	-6	+67	+244	-42	+18.5°	+236	-32	+27°	-3.4	-31.3
B	F5-2	2-2	-14	0	+72	+256	-27	+17°	+237	-34	+27°	-8.0	+7.6
A	F5-1	4-4	+117	+274	+118	+972	-104	0°	+1123	-175	0°	+13.4	+40.6
A	F5-2	4-4	+93	+263	+115	+905	-77	-3.5°	+1020	-175	0°	+11.3	+56.0
B	F5-1	4-4	-20	+50	+66	+228	-50	-29°	+236	-32	-27°	+3.4	-56.3
B	F5-2	4-4	-14	+58	+72	+256	-29	-28°	+237	-34	-27°	-8.0	+14.7
1	2	3	4	5	6	7	8	9	10	11	12	13	14

TABLE 4.6

Summary of Significant Features from Computed Principal Stress Difference Patterns in the Annular Stressmeter

($\frac{a}{b}$ = 5, E = 3.5 x 10^6 p.s.i., E' = 10 x 10^6 p.s.i.
$\mu = \mu' = 0.20$)

Feature	Applied Stress Ratio η	
	0	-0.33
Tangential stresses at inner boundary:		
(a) Maximum tensile stress ($\theta = 0$)	1.26p	2.61p
(b) Maximum compressive stress ($\theta = 90^\circ$)	4.03p	4.45p
Minimum principal stress difference on major axis ($\theta = 0$):		
(a) Magnitude	0.30p	0.83p
(b) Position, $\frac{r}{b}$	1.40	1.60
Minimum principal stress difference on minor axis ($\theta = 90^\circ$):		
(a) Magnitude	1.17p	1.42p
(b) Position, $\frac{r}{b}$	5.00	2.05
Co-ordinates of optimum reading point: $\frac{r}{b}$	1.60	1.60
θ	45°	50°
Principal stress difference at optimum reading point	1.83p	2.36p

TABLE 6.1.

Details of Concrete used around Stressmeters

Class of Concrete and Mix Design Number	Maximum Size of Aggregate	W/C Ratio	A/C Ratio	Cement lbs/cu.yd.	8 in. Cube Strength		Average Density lbs/cu.yd.
					7 Day Strength p.s.i.	28 Day Strength p.s.i.	
C - 29	3"	0.66	9.5	372	2700 (Av. of 15)	4000 (Av. of 15)	153.5
C - 31	¾"	0.63	8.5	514	2950 (Av. of 2)	4500 (Av. of 3)	152.5
A - 53	1½"	0.60	7.14	480	2850 (Av. of 28)	4330 (Av. of 26)	152.0
A - 57	¾"	0.58	6.02	540	2700 (Av. of 3)	3200 (Av. of 3)	151.5
C - 44 ½% Plastiment	3"	0.61	9.55	375	2950 (Av. of 3)	4450 (Av. of 3)	153.5
C - 38	¾"	0.63	6.3	514	4050 (Av. of 2)	5950 (Av. of 2)	152.0
C - 55	3"	0.66	9.45	375	2550 (Av. of 30)	3850 (Av. of 27)	155.0
C - 58	¾"	0.66	6.6	499	2550 (Av. of 6)	3925 (Av. of 6)	150.0

TABLE 6.1(a)

Mixes used around Stressmeters

Mix Design Number	C 55 - 3" C 31 - ¾"	C 44 - 3" C 38 - ¾"	C 55 - 3" C 58 - ¾"
Stressmeter	214	210 213	208 206 204 212

TABLE 6.2

Vertical Stress Increments from Stressmeter Readings Due to Total Water Load

Position	Indicated Principal Stress Condition Stress Units - p.s.i.						Vertical Normal Stress - σ_y p.s.i.		$\Delta\sigma_y$ p.s.i.
	Empty Dam			Full Dam					
	p	q	θ_B^o	p	q	θ_B^o	Empty Dam	Full Dam	
204/21	295	221	55	313	235	100	246	237	-9
206/21	403	302	165	487	244	160	395	458	65
208/21	391	195	170	690	172	160	398	633	235
213/21	235	176	60	548	274	150	191	479	288
214/21	611	458	15	860	430	155	603	786	183
302/21	92	69	10	288	144	145	92	240	148
304/21	115	58	50	202	151	145	83	186	103

All terms take positive signs unless otherwise stated.

TABLE 6.3

Calculated Vertical Stresses at Upstream and Downstream Faces for Total Water Load

Buttress Level 745' O.D.

Assumed Conditions (Lines AB-GH shown in Figure 6.19)	Vertical Stress p.s.i.	
	Upstream Face	Downstream Face
1. Linear analysis, impervious dam and foundation (line AB)	+ 6	+139
2. Condition (1) including buttress cap (line EF)	+30	+189
3. Linear analysis with uplift (line CD)	-56	+169
4. Condition (3) including buttress cap (line GH)	-32	+219
5. Finite element analysis, impervious dam and foundation	-74	+129
6. Finite element analysis with pore pressures and uplift	-86	+154

TABLE 6.4

Comparison between Observed and Calculated
Stress Conditions at 745' O.D. after Impounding

Position	Finite Element Analysis, $\frac{Ef}{E} = \frac{1}{4}$						Absolute Stressmeter Reading		
	Impervious Dam			With Pore Pressure					
	p	q	$\theta_B{}^\circ$	p	q	$\theta_B{}^\circ$	p	q	$\theta_B{}^\circ$
204/21	160	0	150	160	-18	150	313*	235*	100*
206/21	350	8	150	350	-20	146	487	243	160
208/21	315	7	150	320	6	150	690	172	160
210/21	290	25	150	310	20	150	-	-	-
213/21	345	5	150	380	15	150	547	273	150
214/21	336	6	150	330	4	148	860	430	155

*Out-of-plane values - see pages 109-110

All terms take positive signs unless otherwise stated.

ILLUSTRATIONS

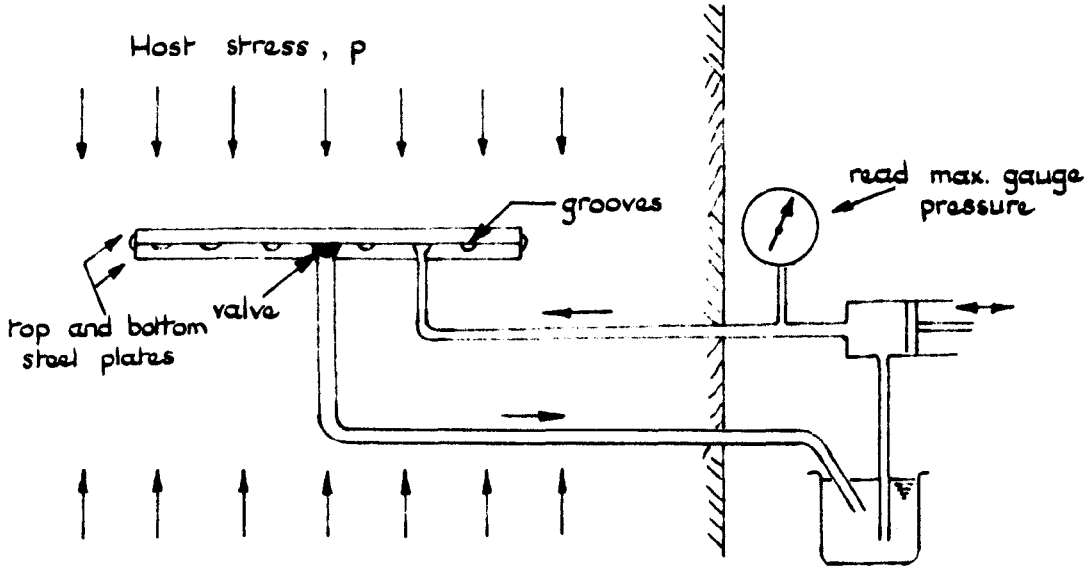

FIG. 1.1. Glotzl Stressmeter

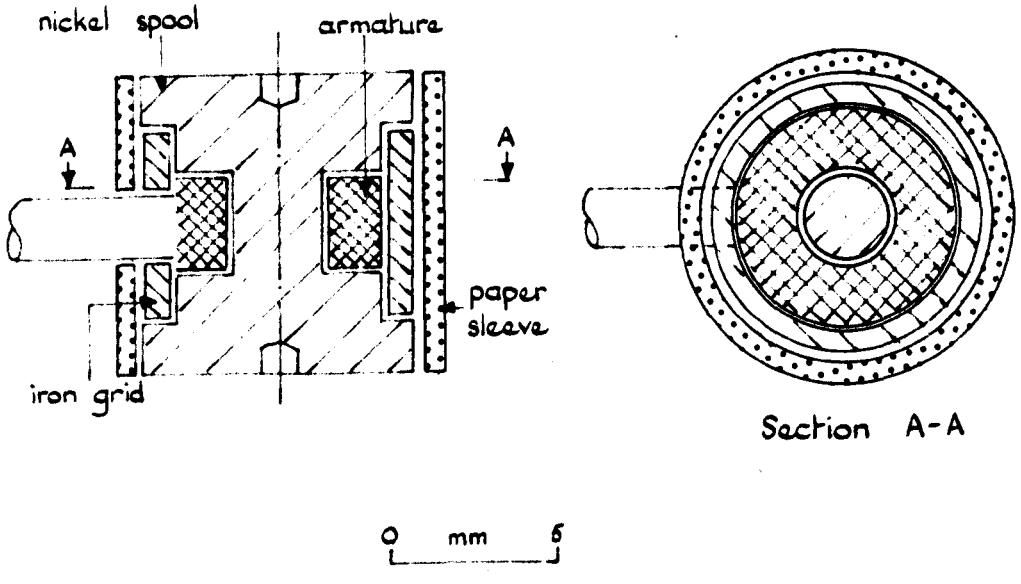

FIG. 1.2 Hast's Stressmeter

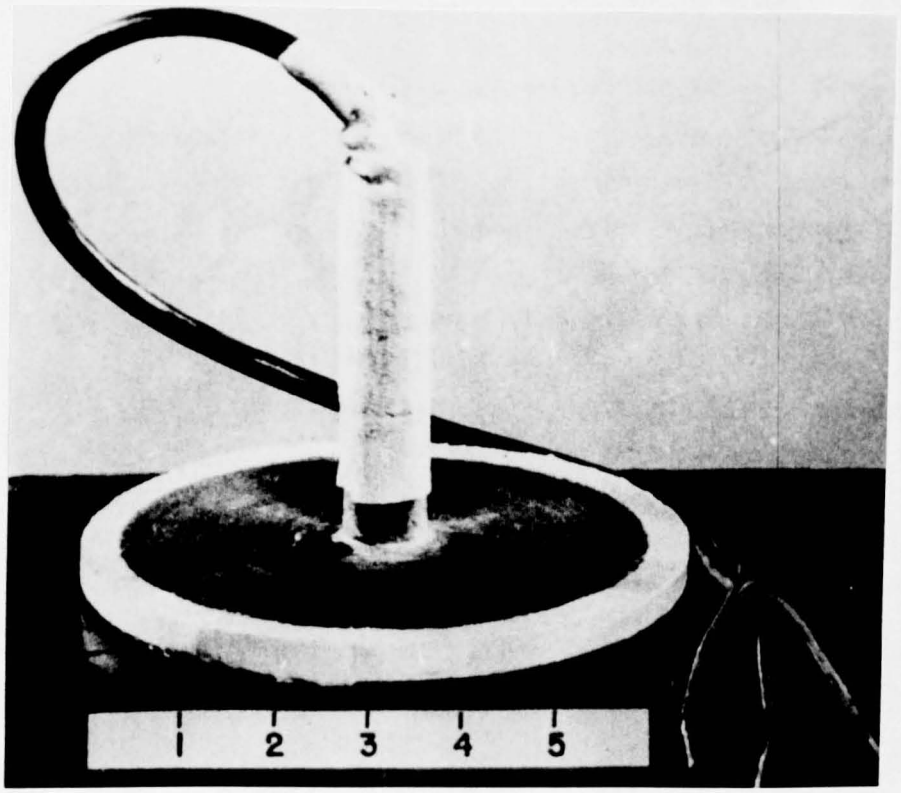

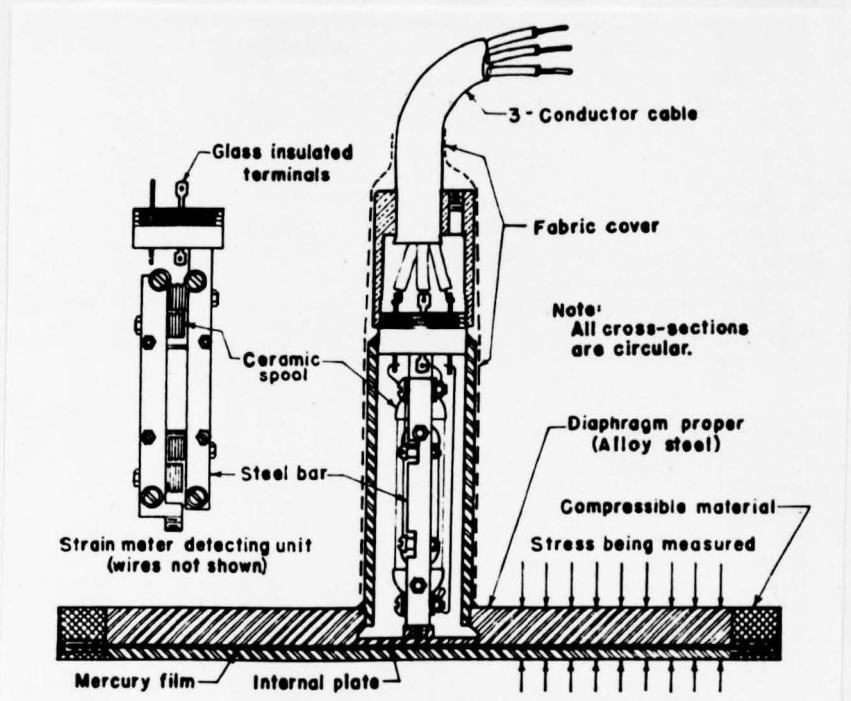

FIG. 1.3. The Carlson Stressmeter

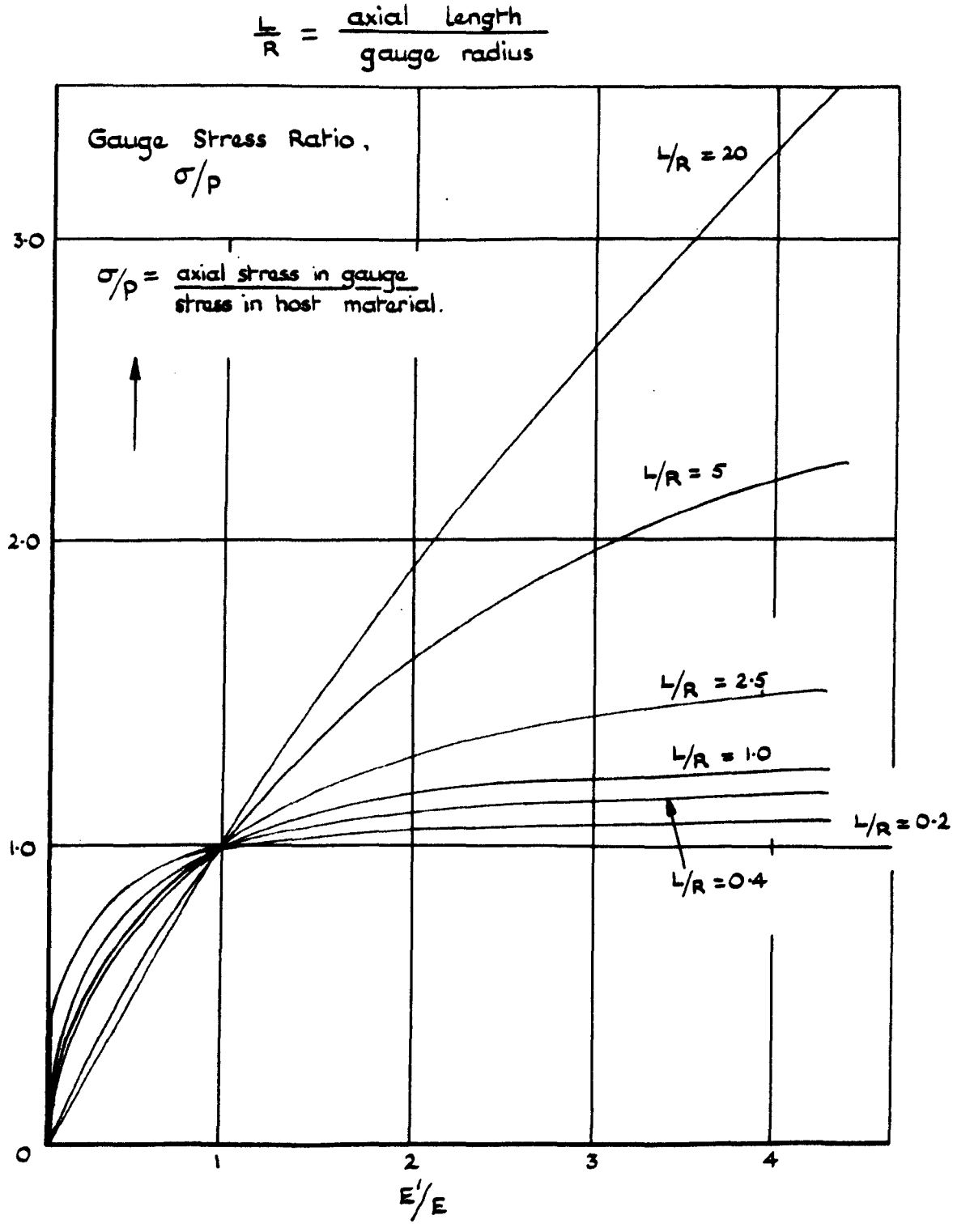

FIG. 1.4. The effect of gauge geometry on induced stress in a stress gauge. [after ref. (6)]

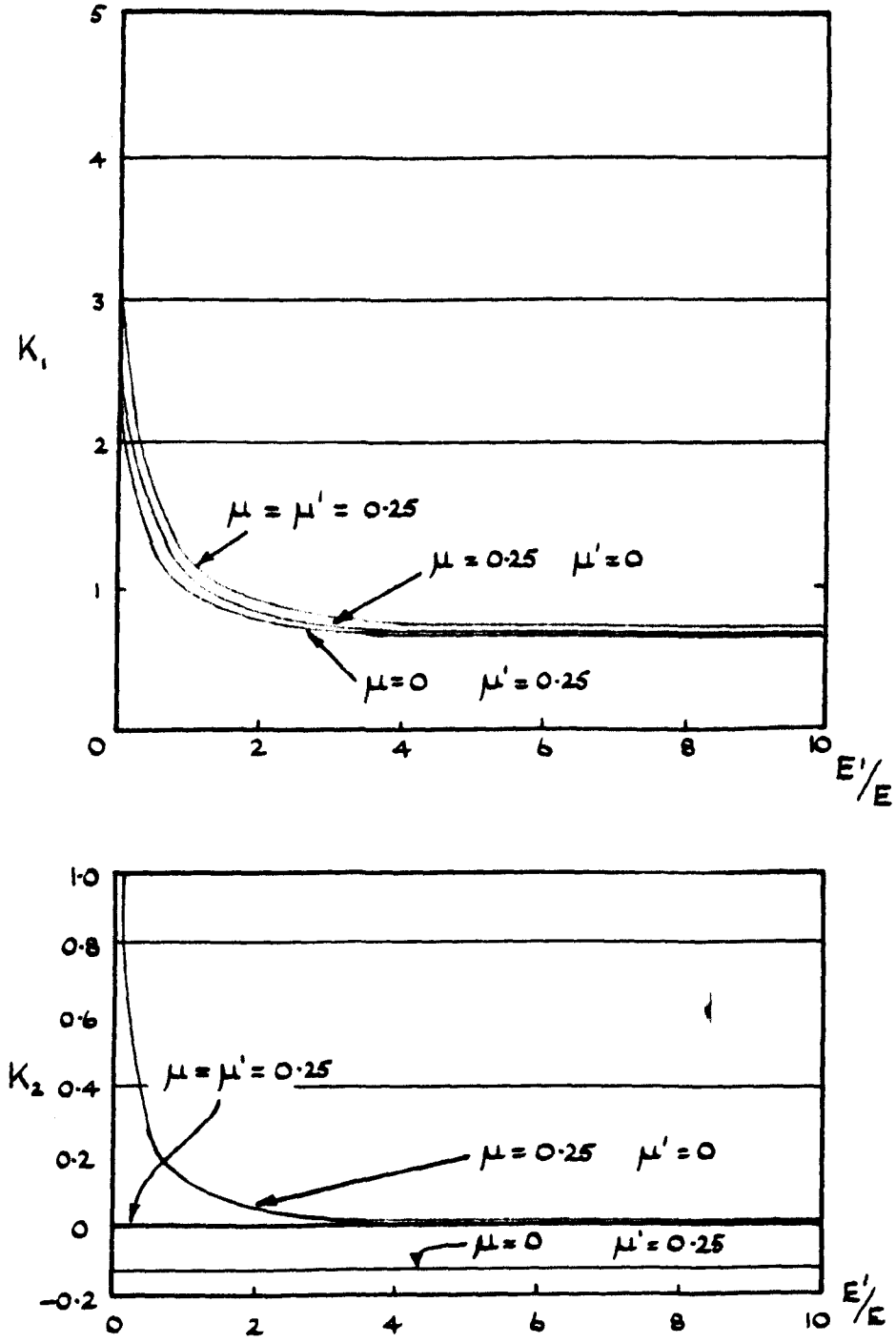

FIG. 1.5. Variation of K_1 & K_2 with modular ratio [after ref (11)]

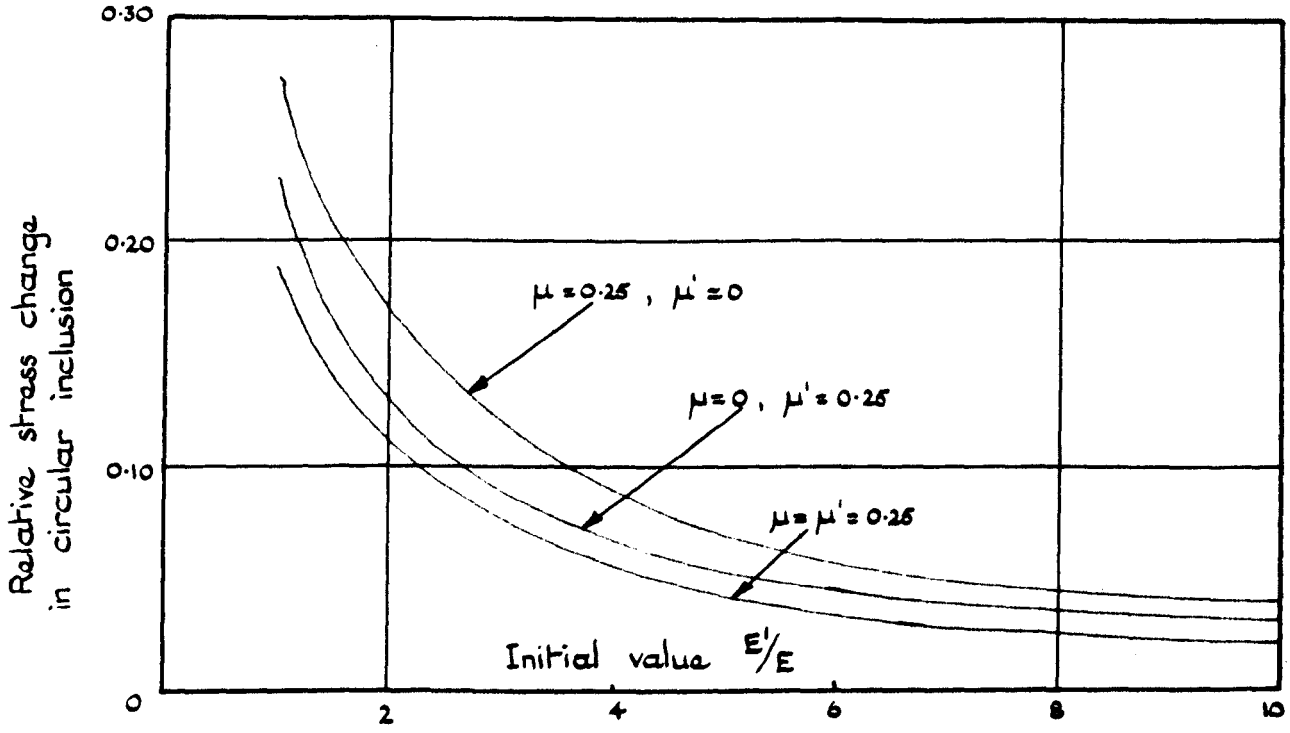

FIG. 1.6 Relative stress change in a circular glass inclusion when modulus of host material changes by 50%. [after ref. (11)]

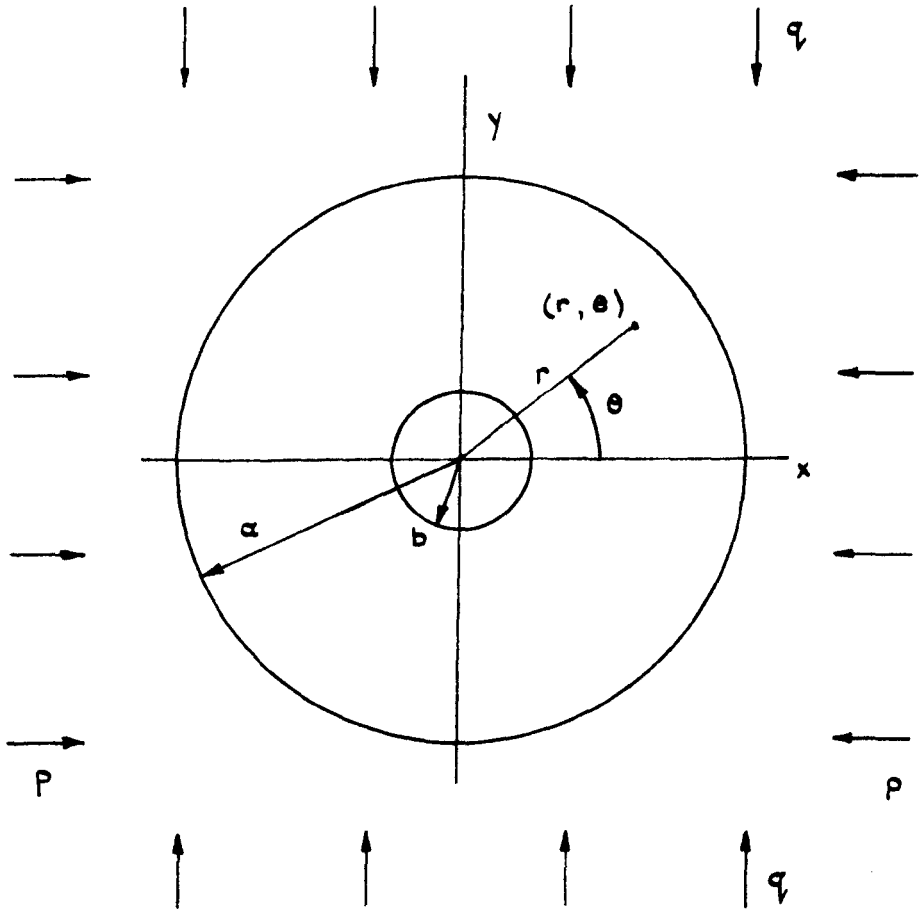

FIG. 1.7 Coordinate system used in Barron's analysis [after ref. (38)]

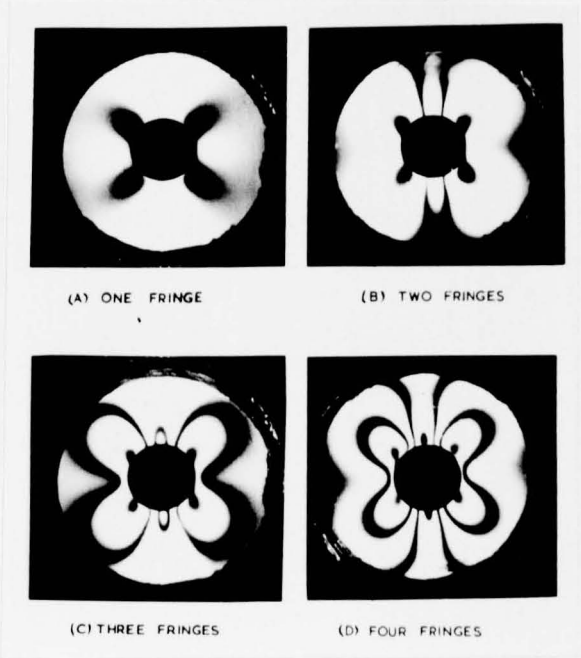

FIG. 2.1. Annular Stressmeter Patterns:
Applied Principal Stress Ratio $\eta = 0$.

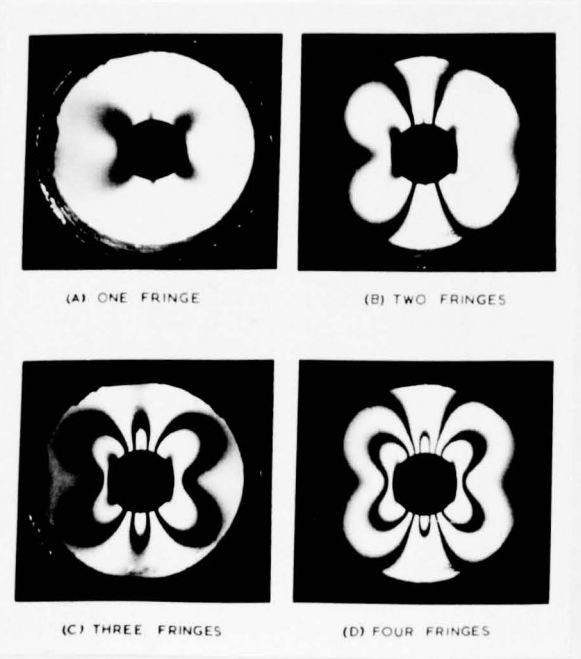

FIG. 2.2. Applied Principal Stress Ratio $\eta = 0.25$

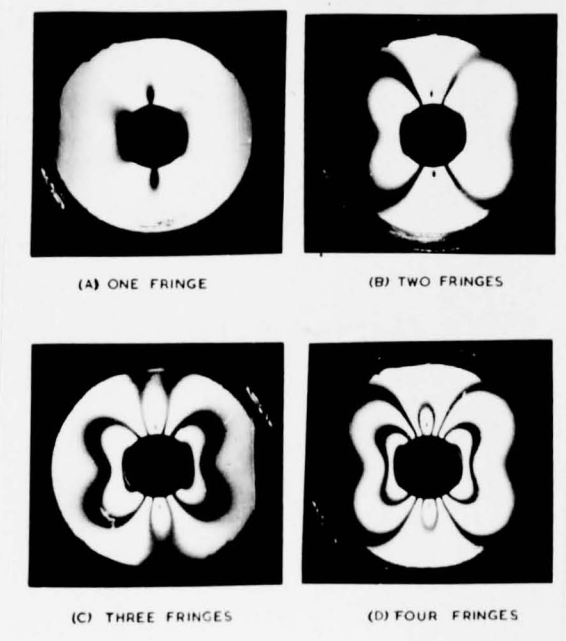

FIG. 2.3. Annular Stressmeter Patterns:
Applied Principal Stress Ratio $\eta = 0.50$

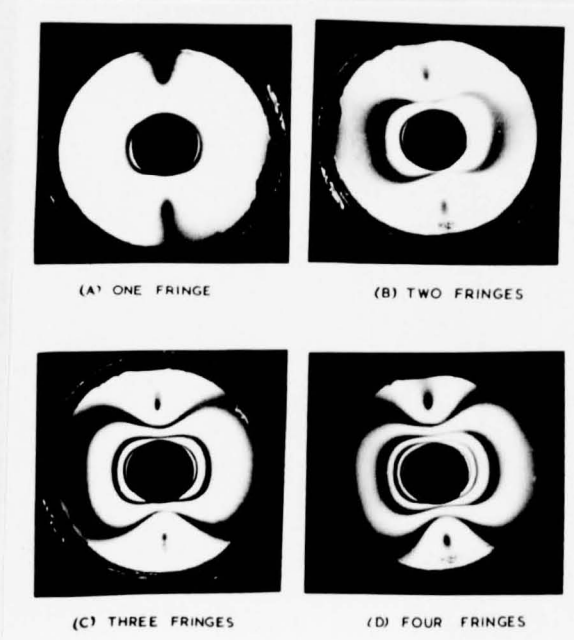

FIG. 2.4. Applied Principal Stress Ratio $\eta = 0.75$

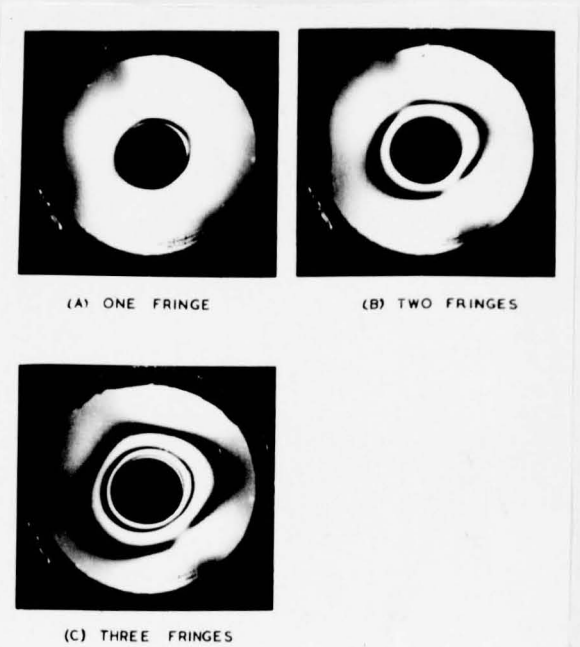

FIG. 2.5. Annular Stressmeter Patterns:
Applied Principal Stress Ratio $\eta = 1.0$.

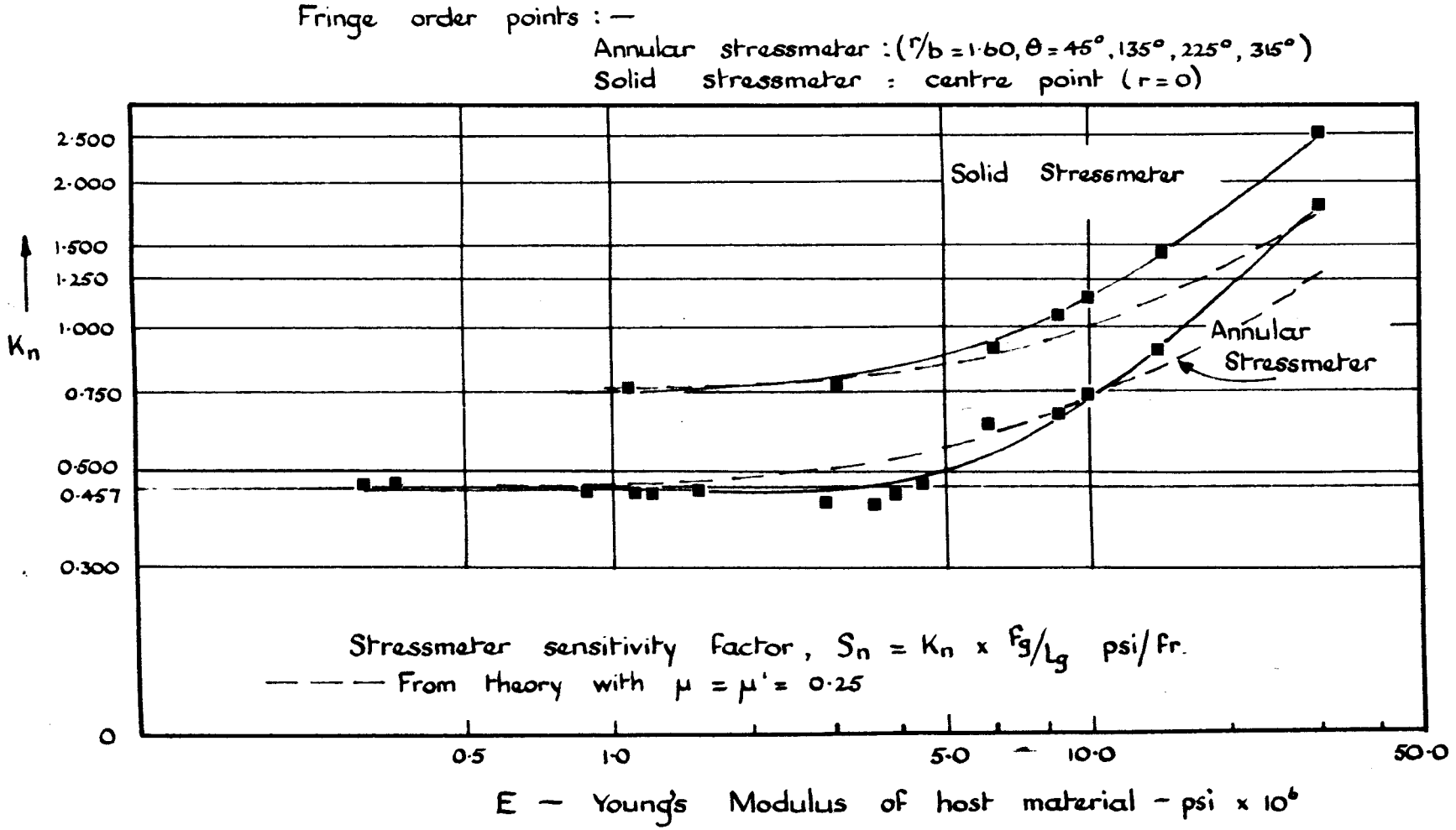

FIG. 2.6 Photoelastic stressmeter : variation of sensitivity factor in uniaxial stress conditions [after ref (23)]

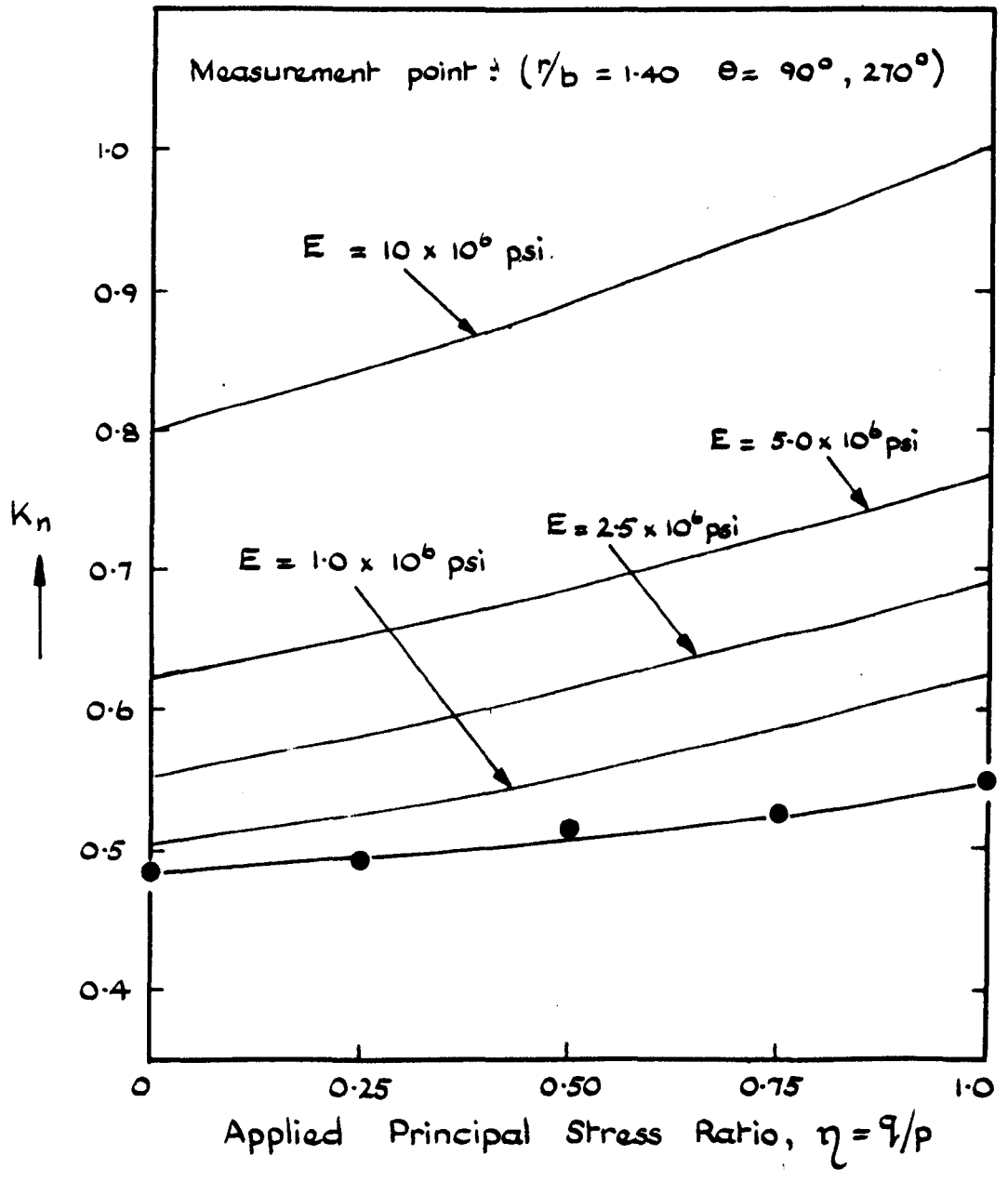

Stressmeter sensitivity : $S_n = \frac{K_n \times f_g}{L_g}$ psi/fr.

● Experimental results from ref. (23) for host materials E = 1·0 — 3·0 x 10^6 psi.

FIG. 2.7. Annular stressmeter sensitivity in biaxial loading.

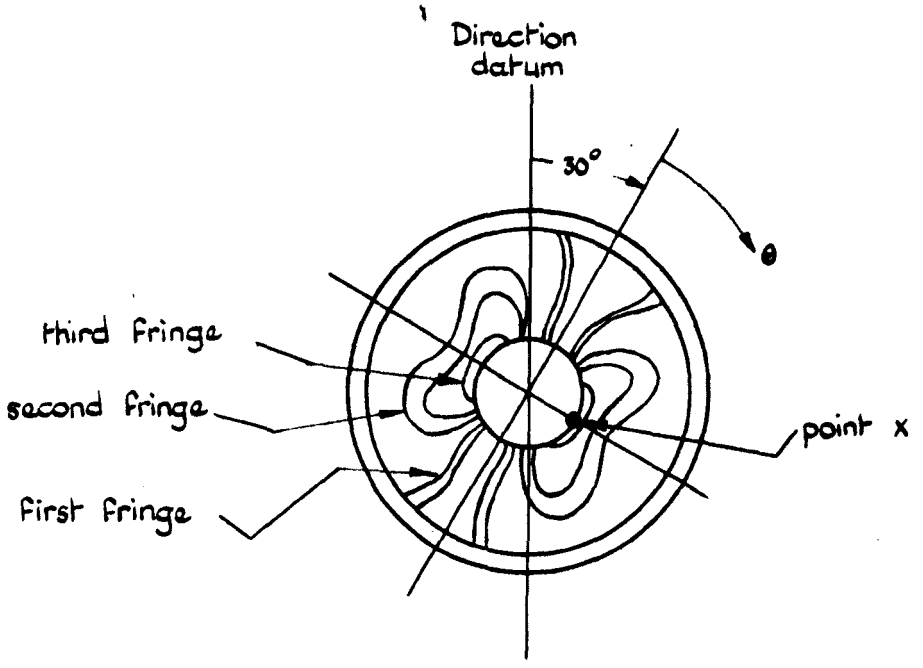

Observation:

Measured fringe order at x ($r/b = 1.40$ $\theta = 90°, 270°$) = + 3.05

Orientation of major principal stress = + 30°

Applied stress ratio, η = 0.50

Stressmeter Parameters:

Length, Lg = 3.0 ins.

Material fringe value, Fg = 1220 psi/fr/in.

Sensitivity parameter, K_n (from Fig. 2.7.) = 0.510

Interpretation:

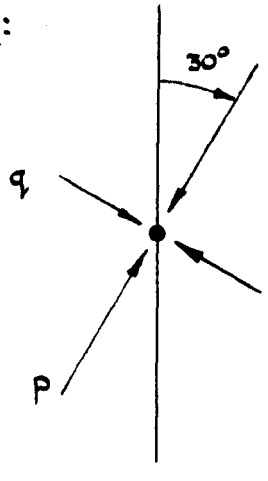

$$p = \frac{+0.510 \times 1220 \times 3.05}{3.0}$$

$$= + 632 \text{ p.s.i.}$$

$$q = +0.50 \times p = +316 \text{ psi.}$$

FIG. 2.8. Annular stressmeter pattern and its interpretation in a low modulus material.

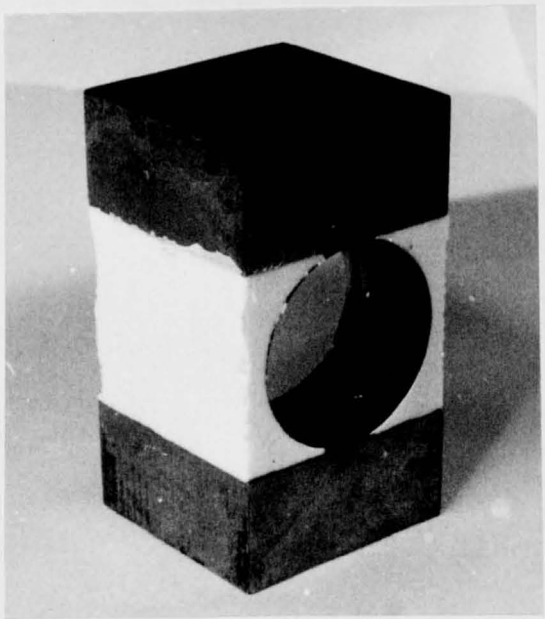

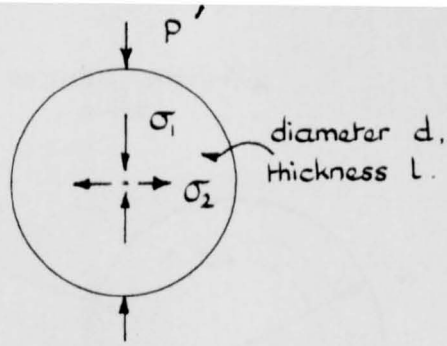

$$(\sigma_1 - \sigma_2) = \frac{8P'}{\pi d l}$$

$$N = \frac{(\sigma_1 - \sigma_2)\, l}{f_g}$$

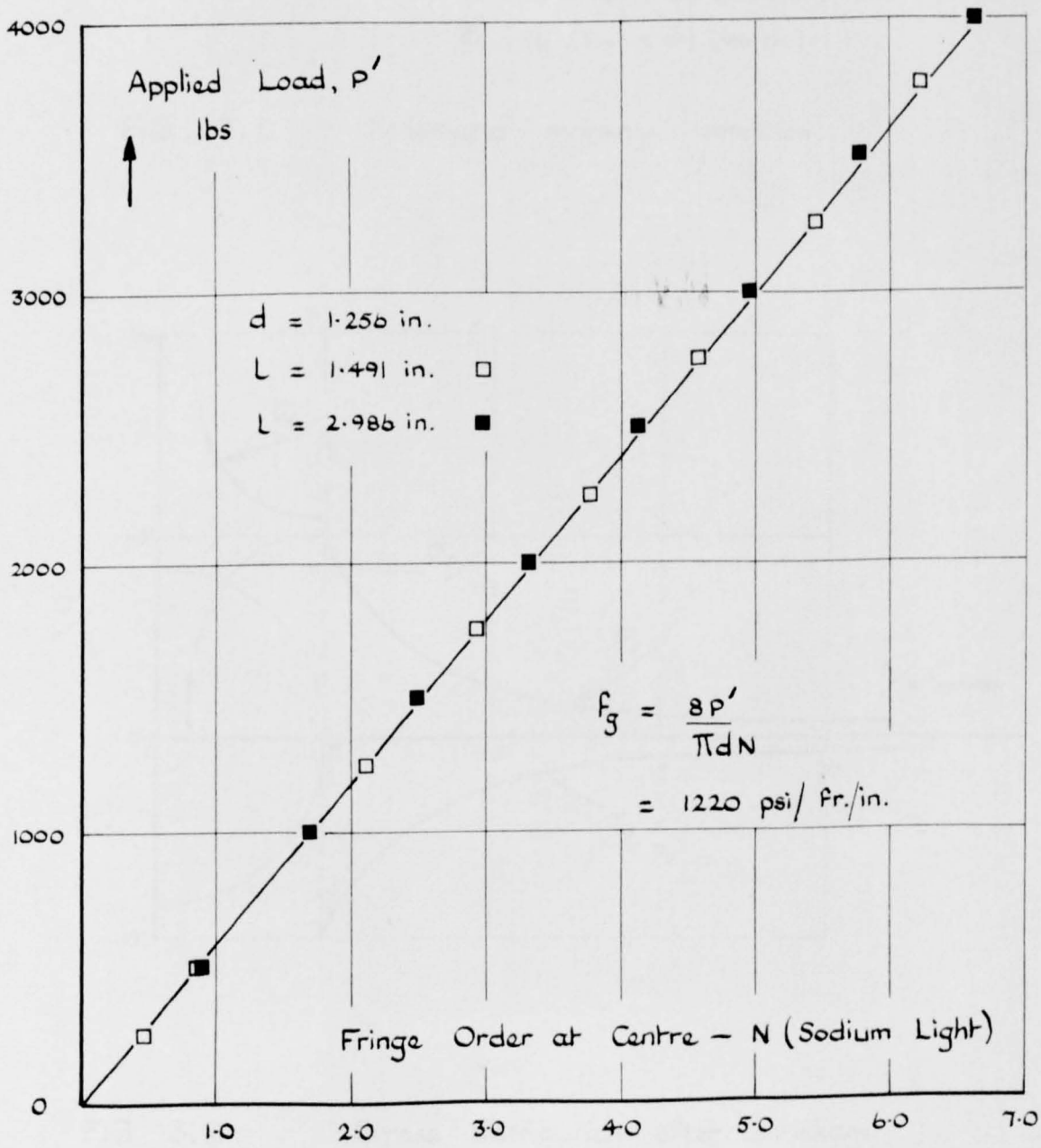

FIG. 2.9. Material fringe value for stressmeter glass.

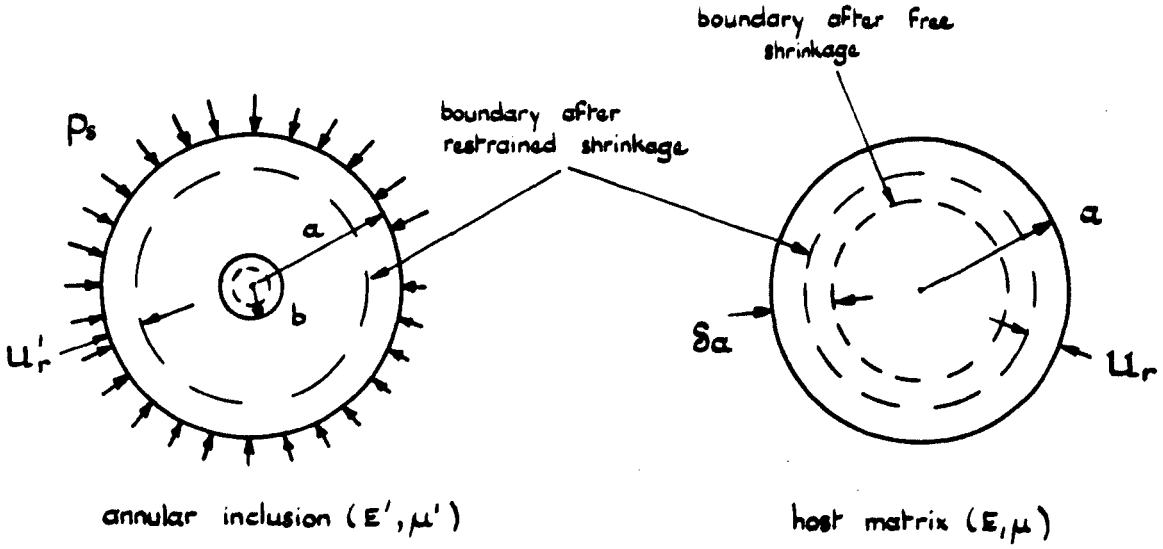

Stresses after shrinkage : σ_r' , σ_θ' ,($\tau_{r\theta}' = 0$) (inclusion)

σ_r , σ_θ ,($\tau_{r\theta} = 0$) (matrix)

FIG. 3.1. Schematic shrinkage condition

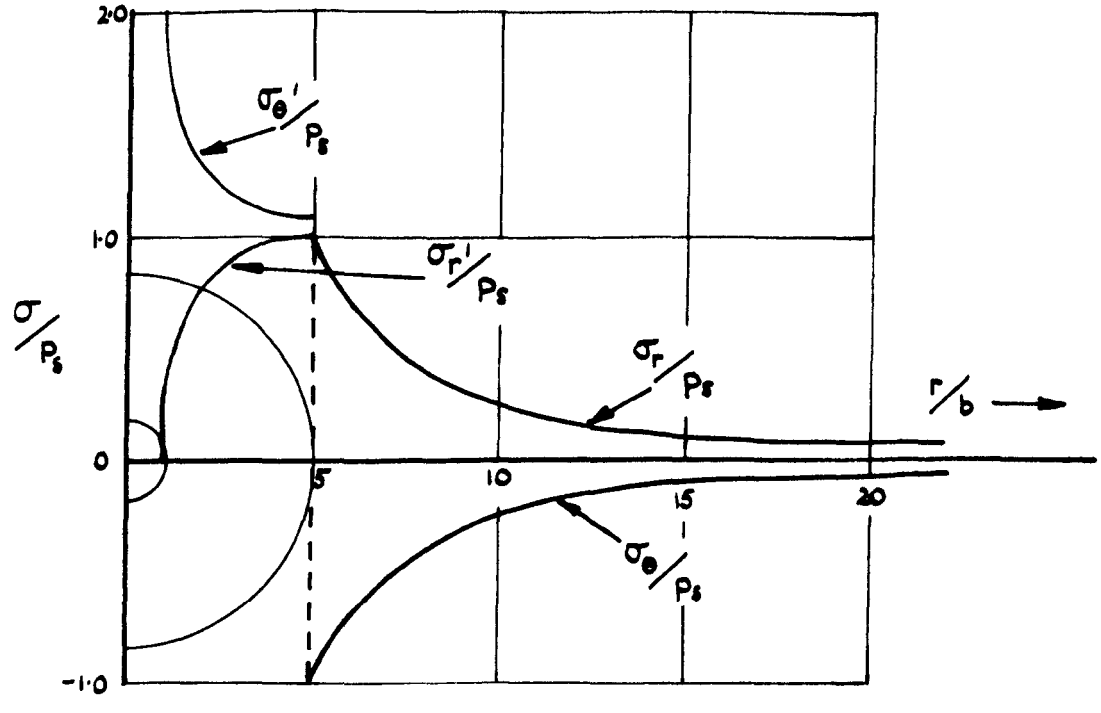

FIG. 3.2. Stress distribution after shrinkage (elastic analysis)

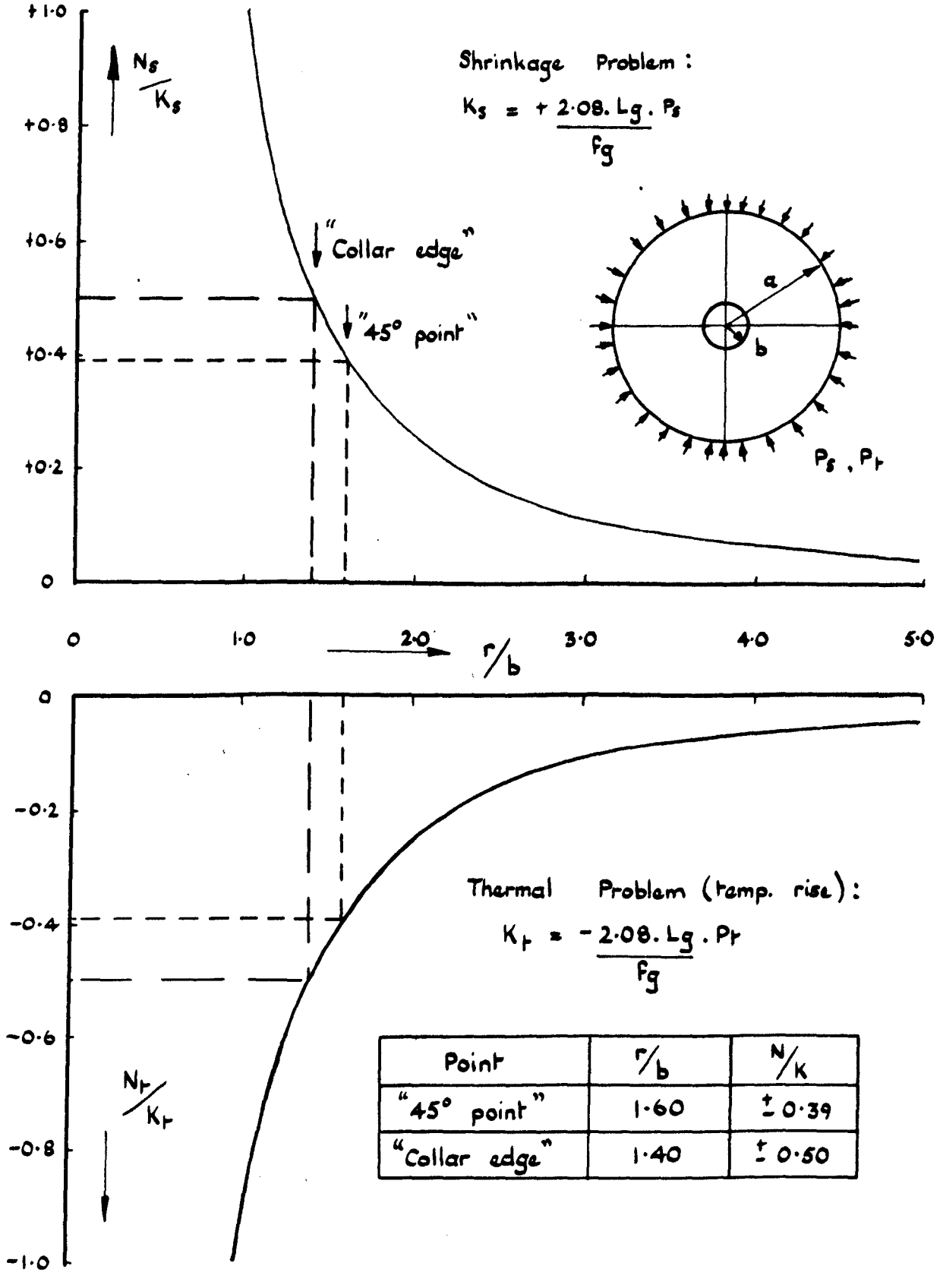

Point	r/b	N/K
"45° point"	1·60	± 0·39
"Collar edge"	1·40	± 0·50

FIG. 3.3. Annular stressmeter fringe order distributions for shrinkage and thermal problems.

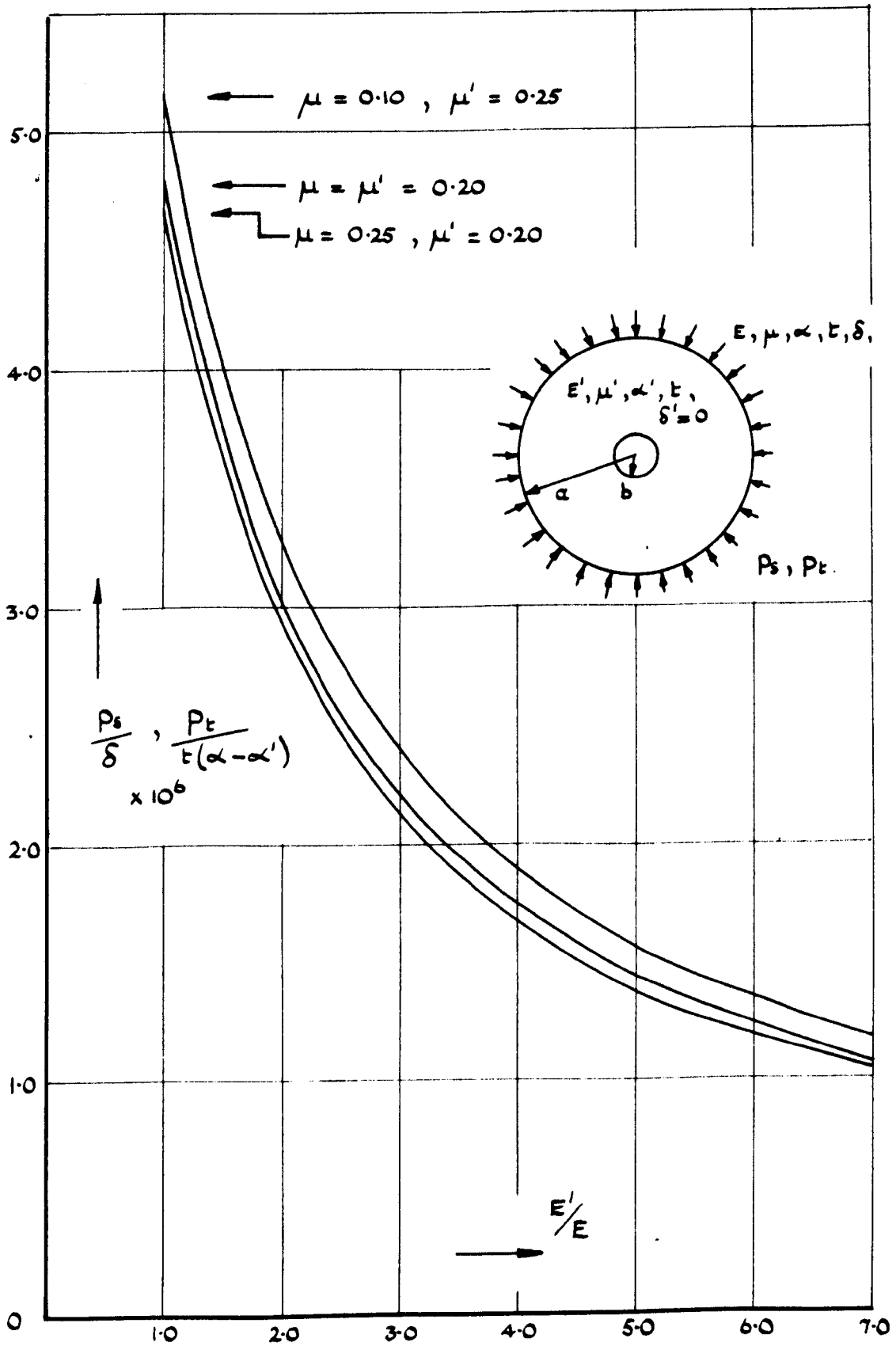

FIG. 3.4. Annular stressmeter boundary stress for shrinkage and thermal problems.

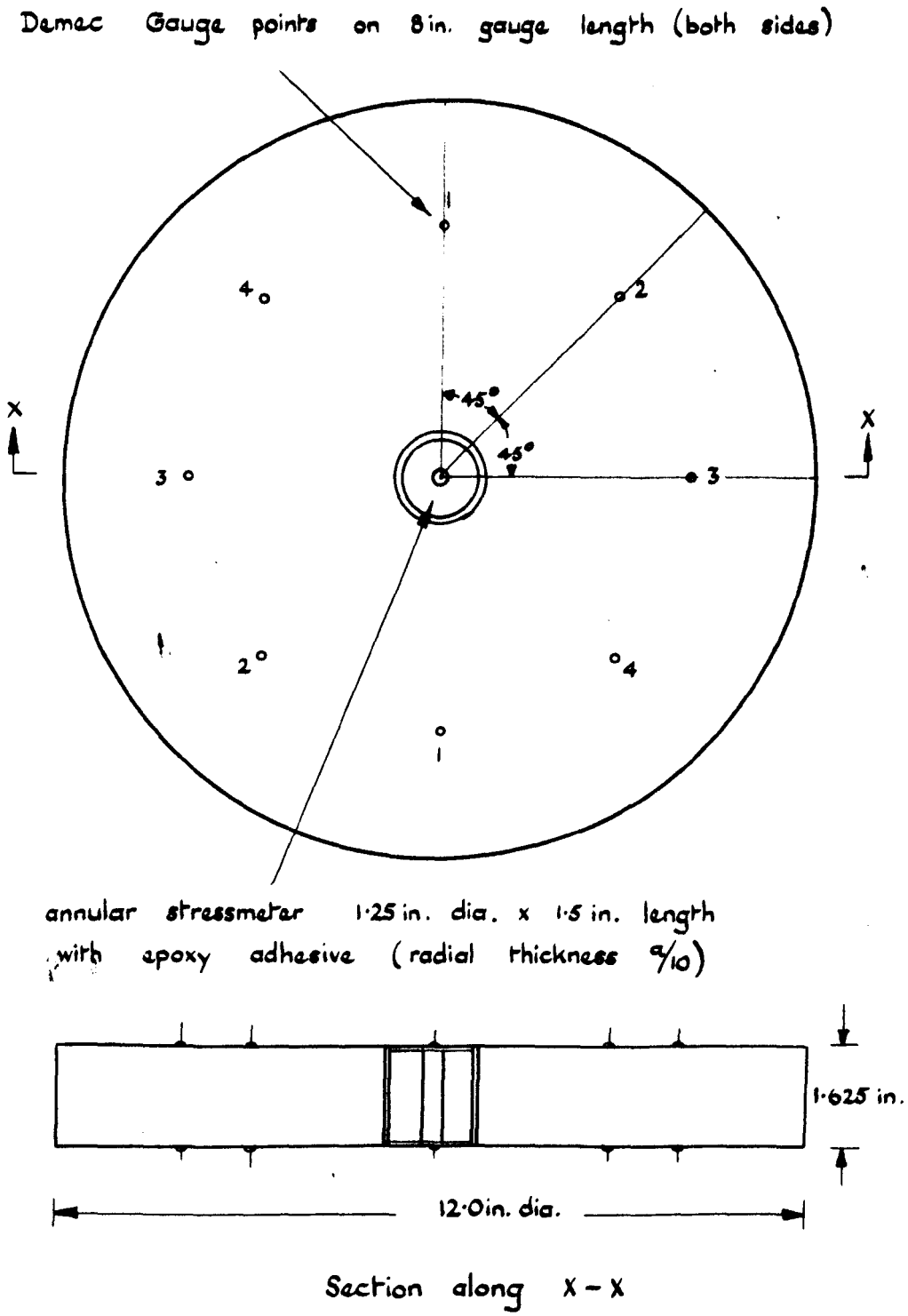

FIG. 3.5. Disc shrinkage specimen, mixes A, B and C.

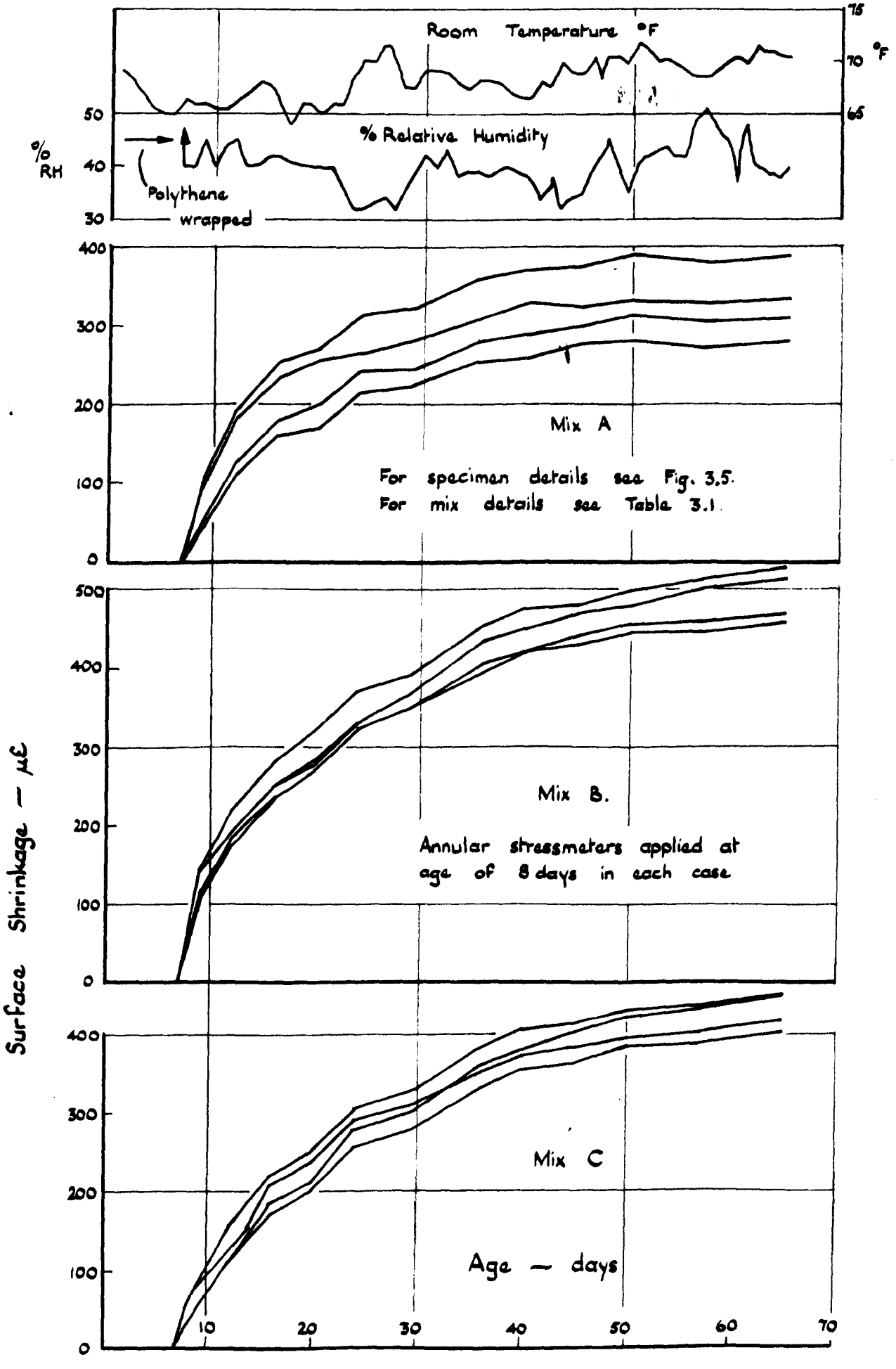

FIG. 3.6. Shrinkage of test mixes A, B & C.

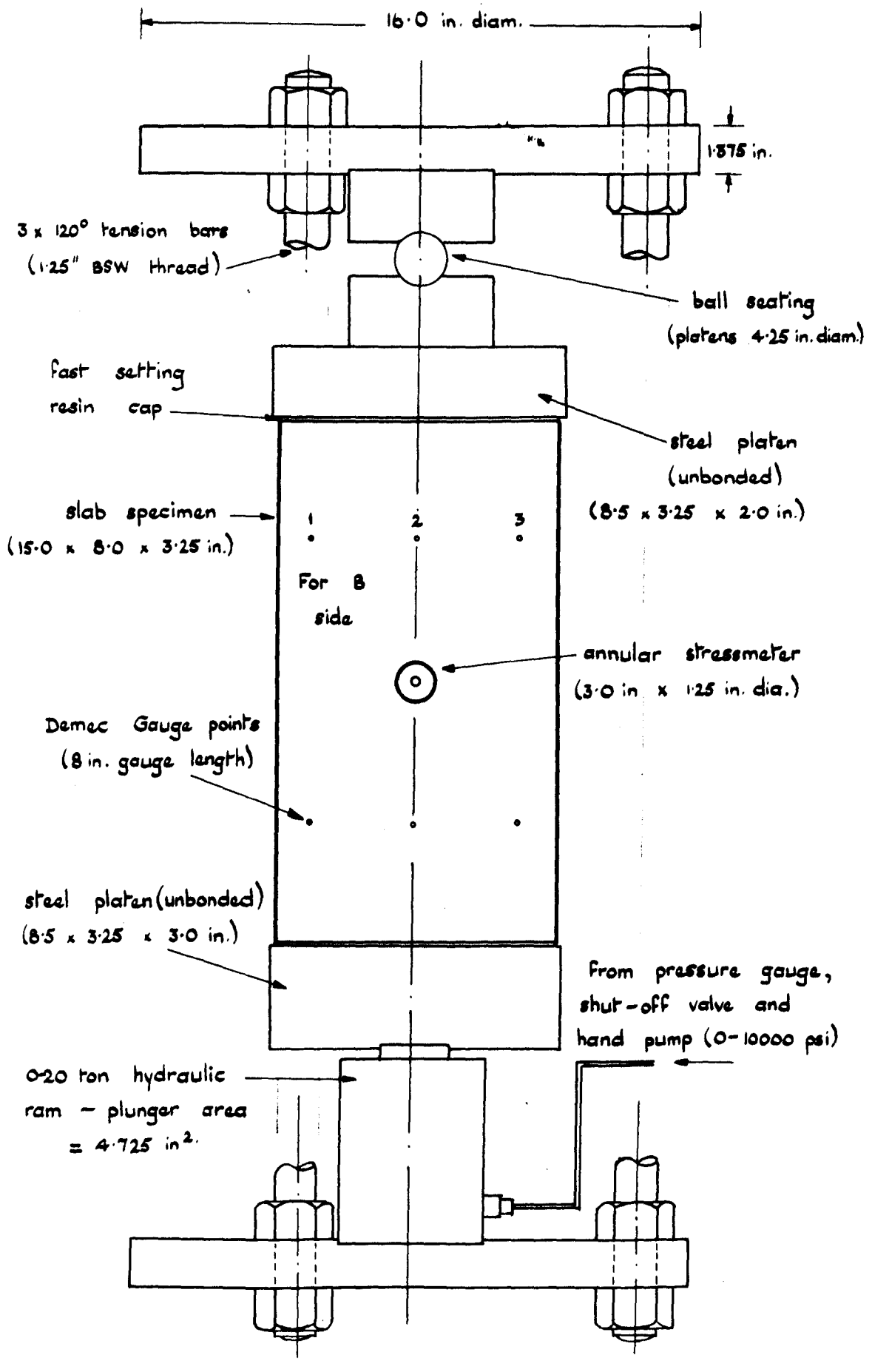

FIG. 3.7. Test rig details : slab specimens
F1 series

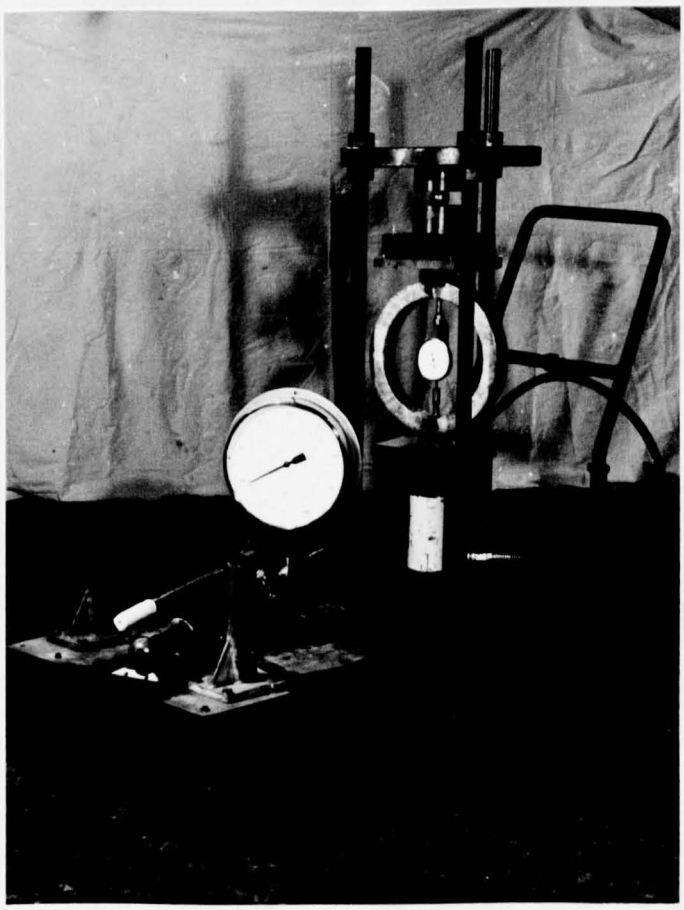

FIG. 3.8. Test Rig Calibration with 0-20 Ton Proving Ring.

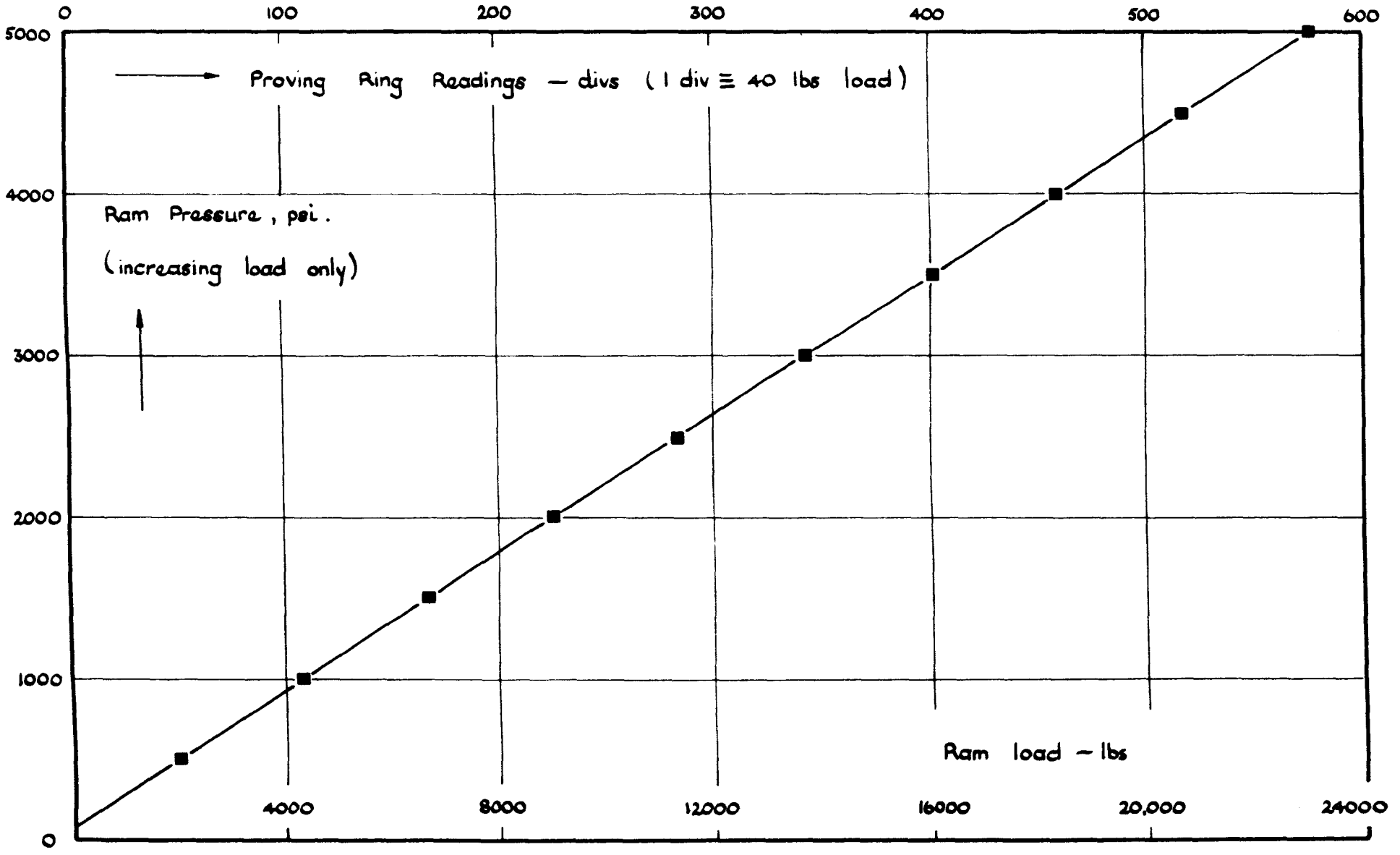

FIG. 3.9. Test rig calibration against 0-20 ton proving ring

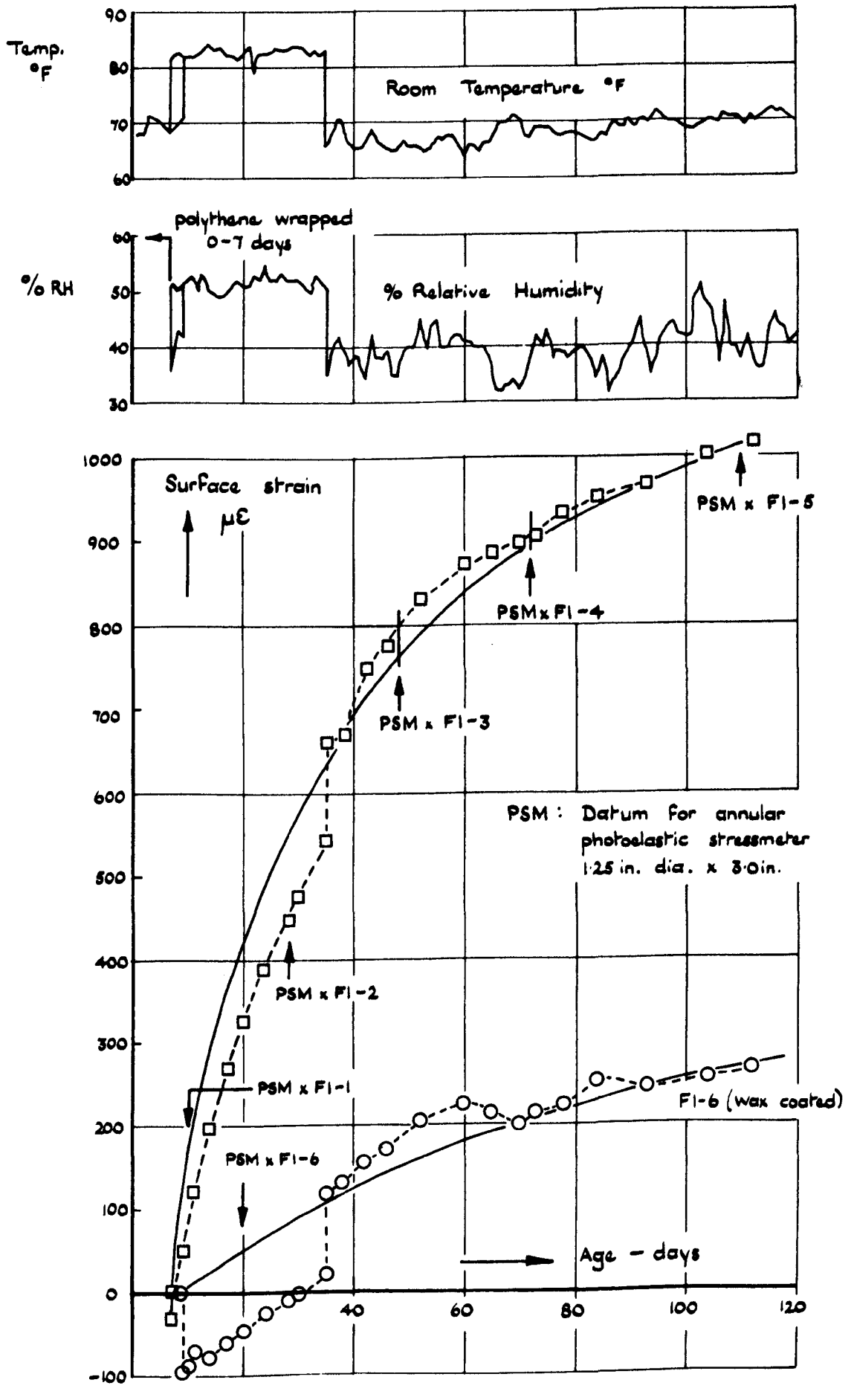

FIG. 3.10. Surface strain history F1 slab specimens

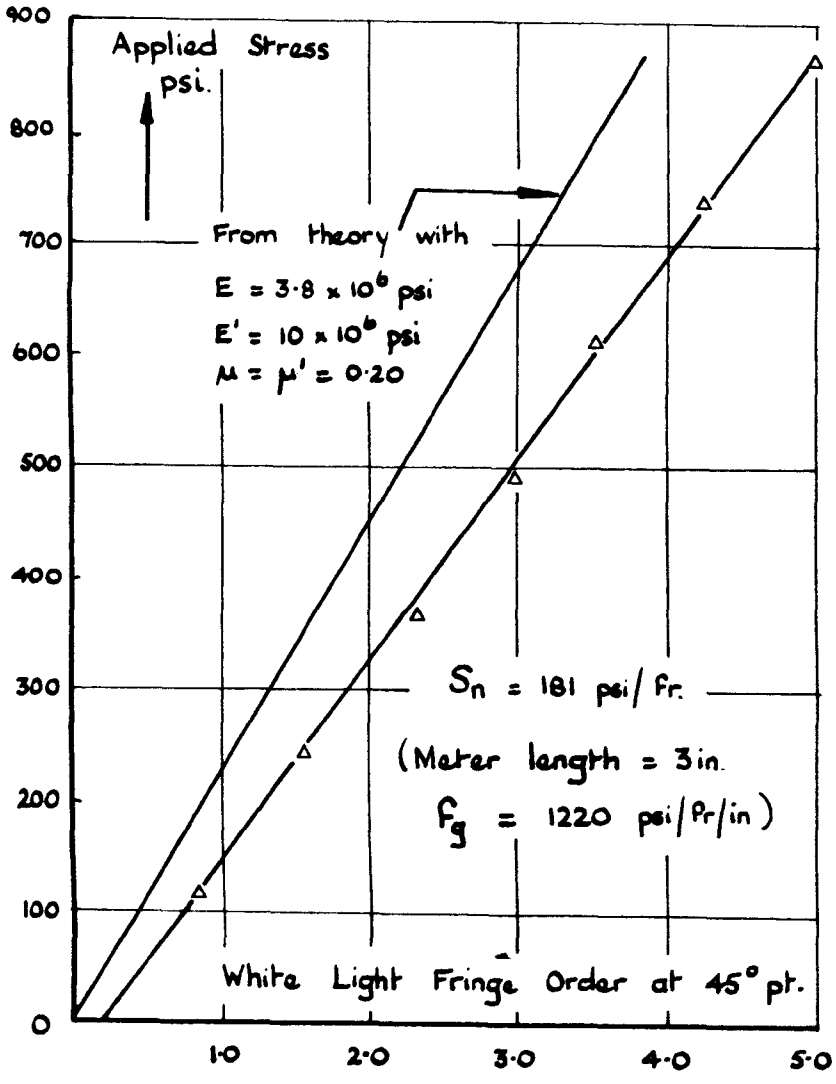

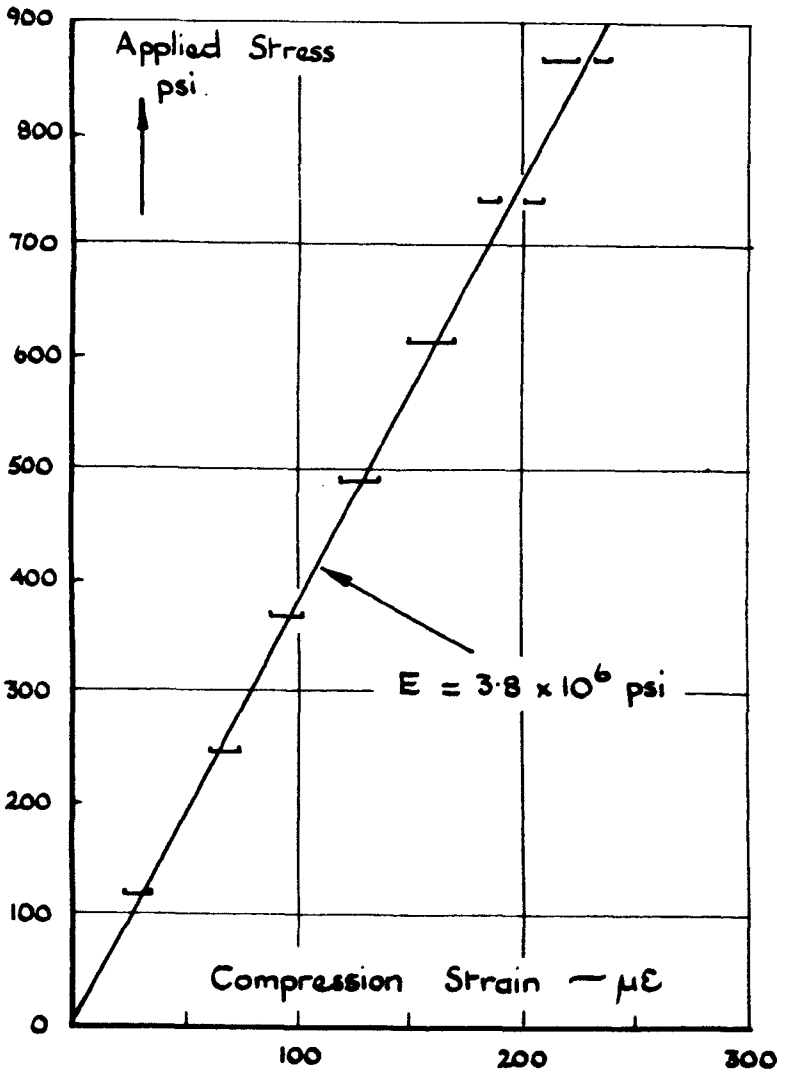

FIG. 3.11. Annular stressmeter and Demec Gauge data — slab F1-6 at 74 days

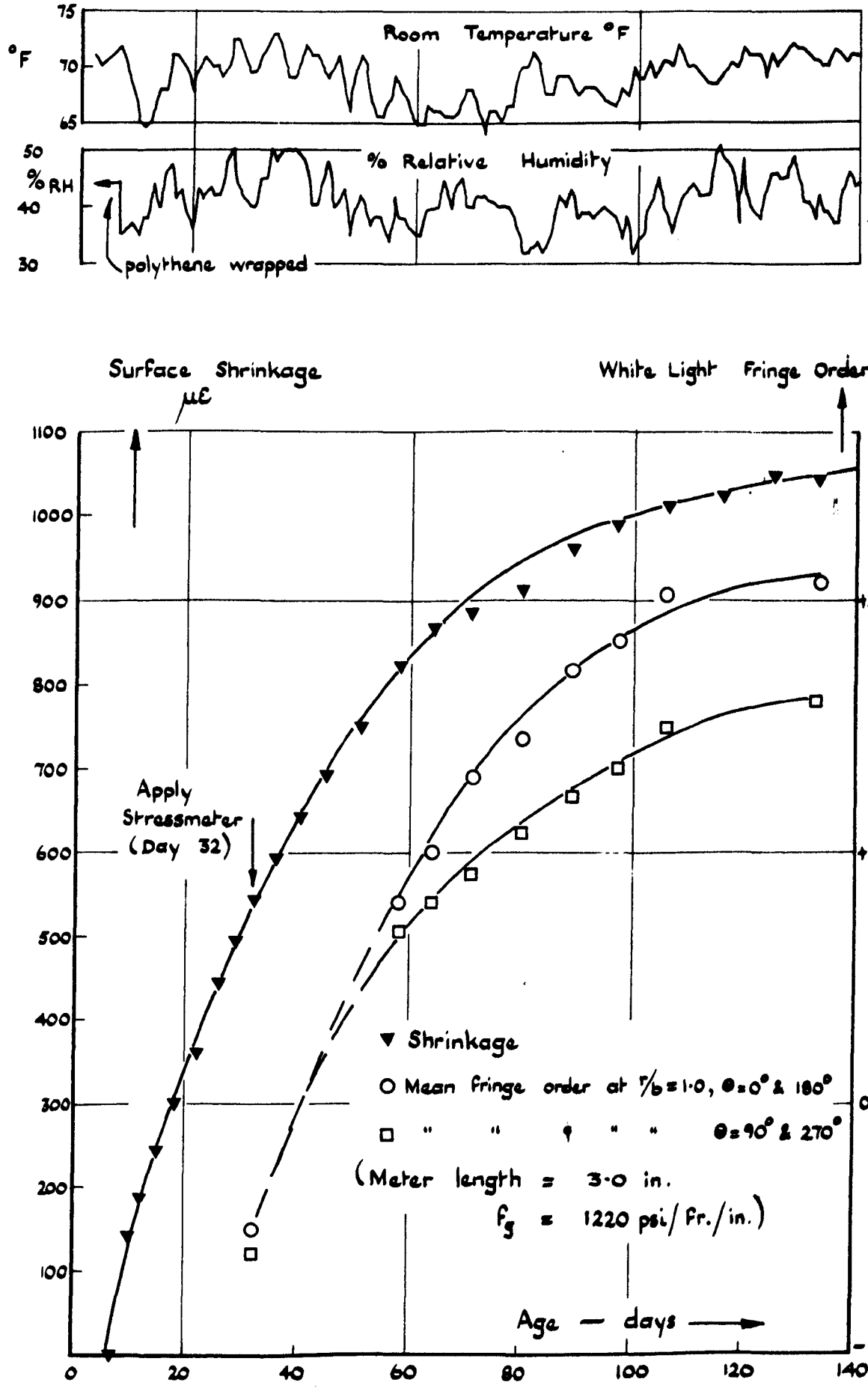

FIG. 3.12. Development of shrinkage fringe orders in specimen F3-4

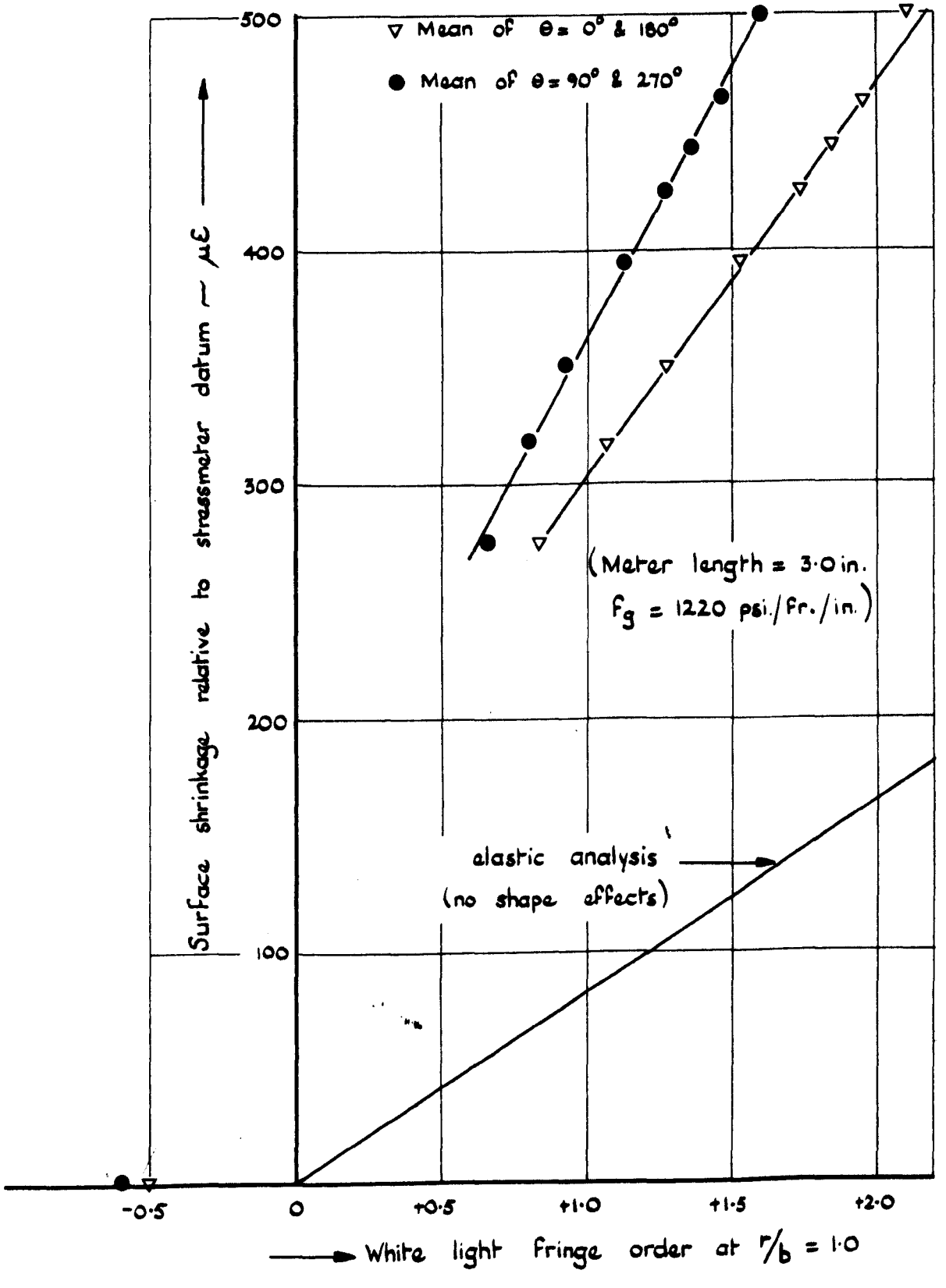

FIG. 3.13. Annular stressmeter fringe orders compared with shrinkage of specimen F3-4.

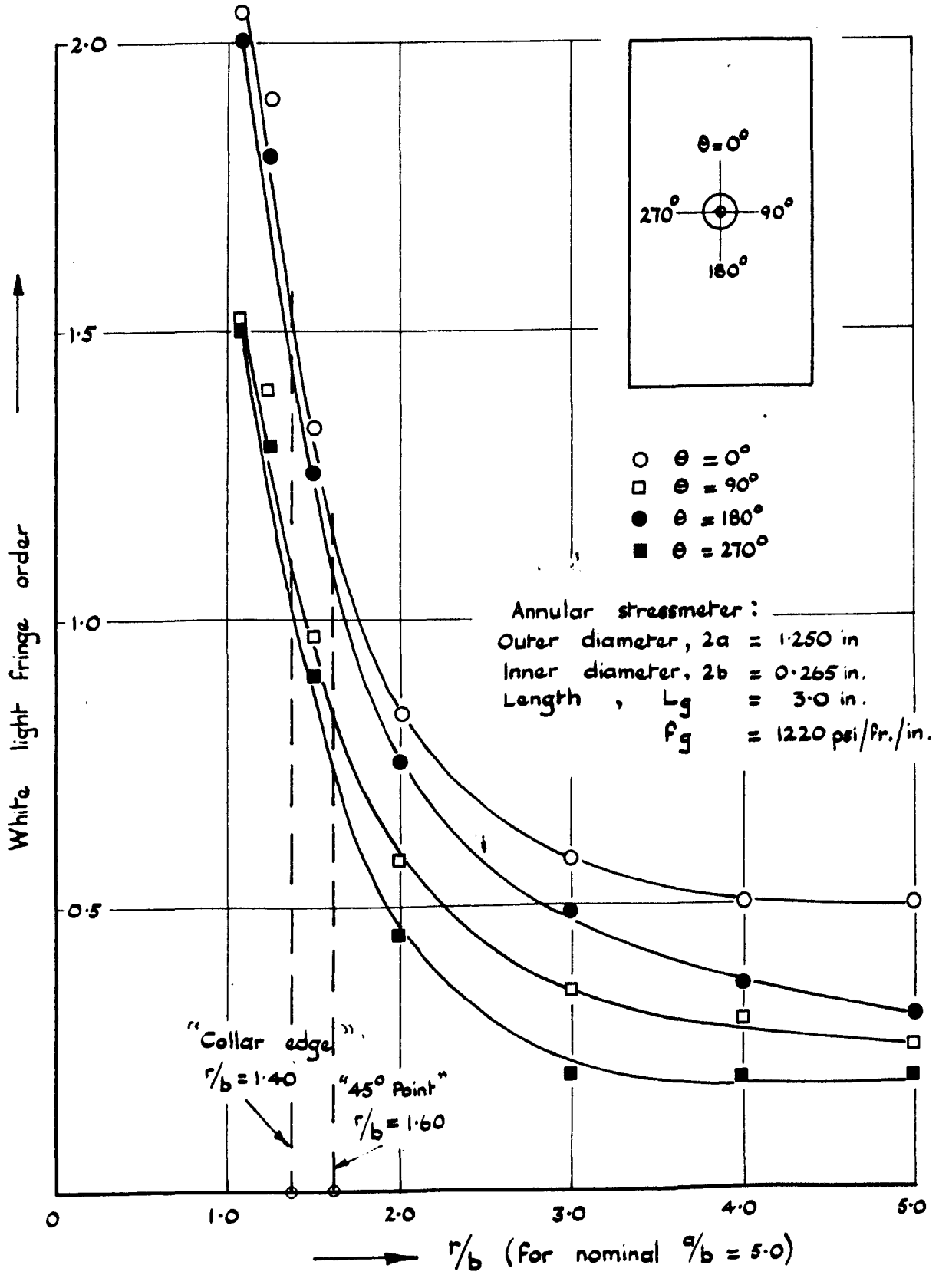

FIG. 3.14. Fringe order distribution in annular stressmeter specimen F3-4 — day 106

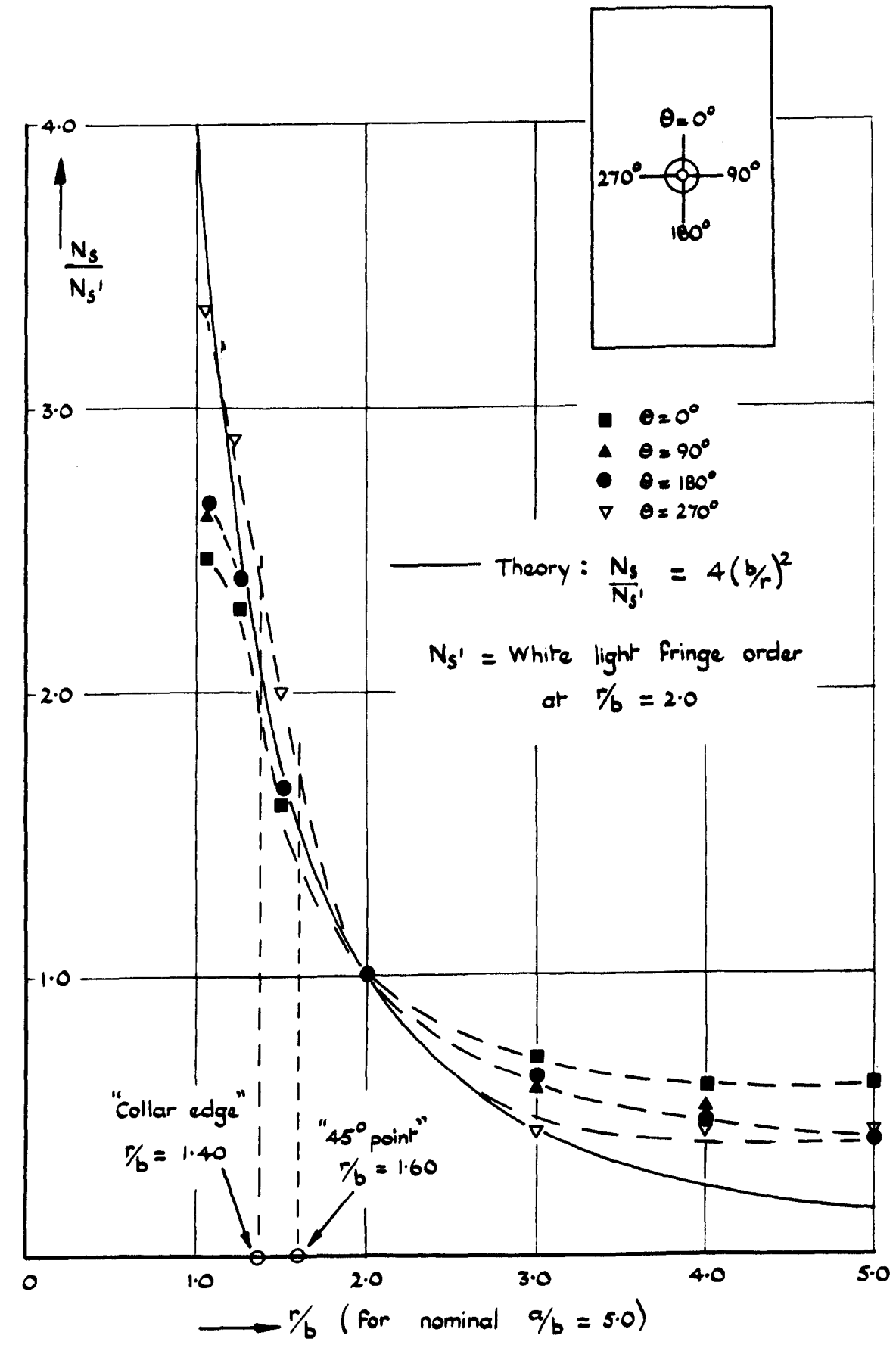

FIG. 3.15. Dimensionless fringe order distribution
(Annular stressmeter, specimen F3-4, day 106)

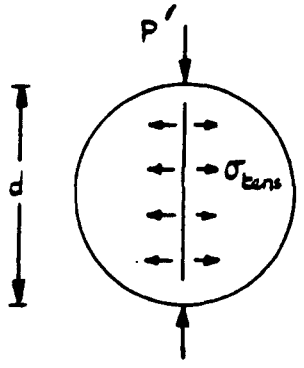

$$\sigma_{tens} = \frac{-2P'}{\pi d l}$$

$d = 4{\cdot}0$ in.

$l = 4{\cdot}0$ in. (nominal)

Load applied via flat steel platens and paper layer

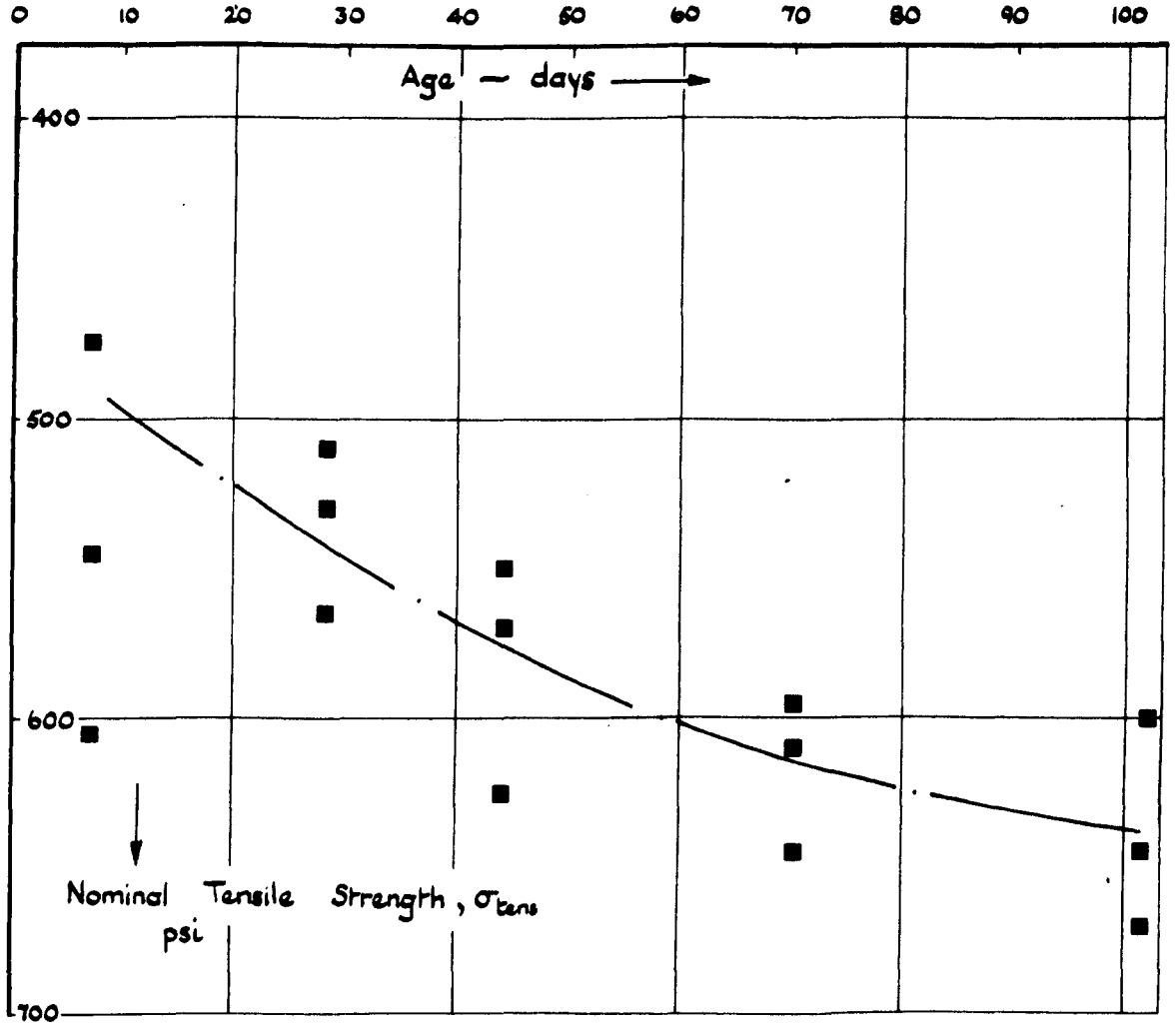

FIG. 3.16. Mix F1 — Brazil Test data

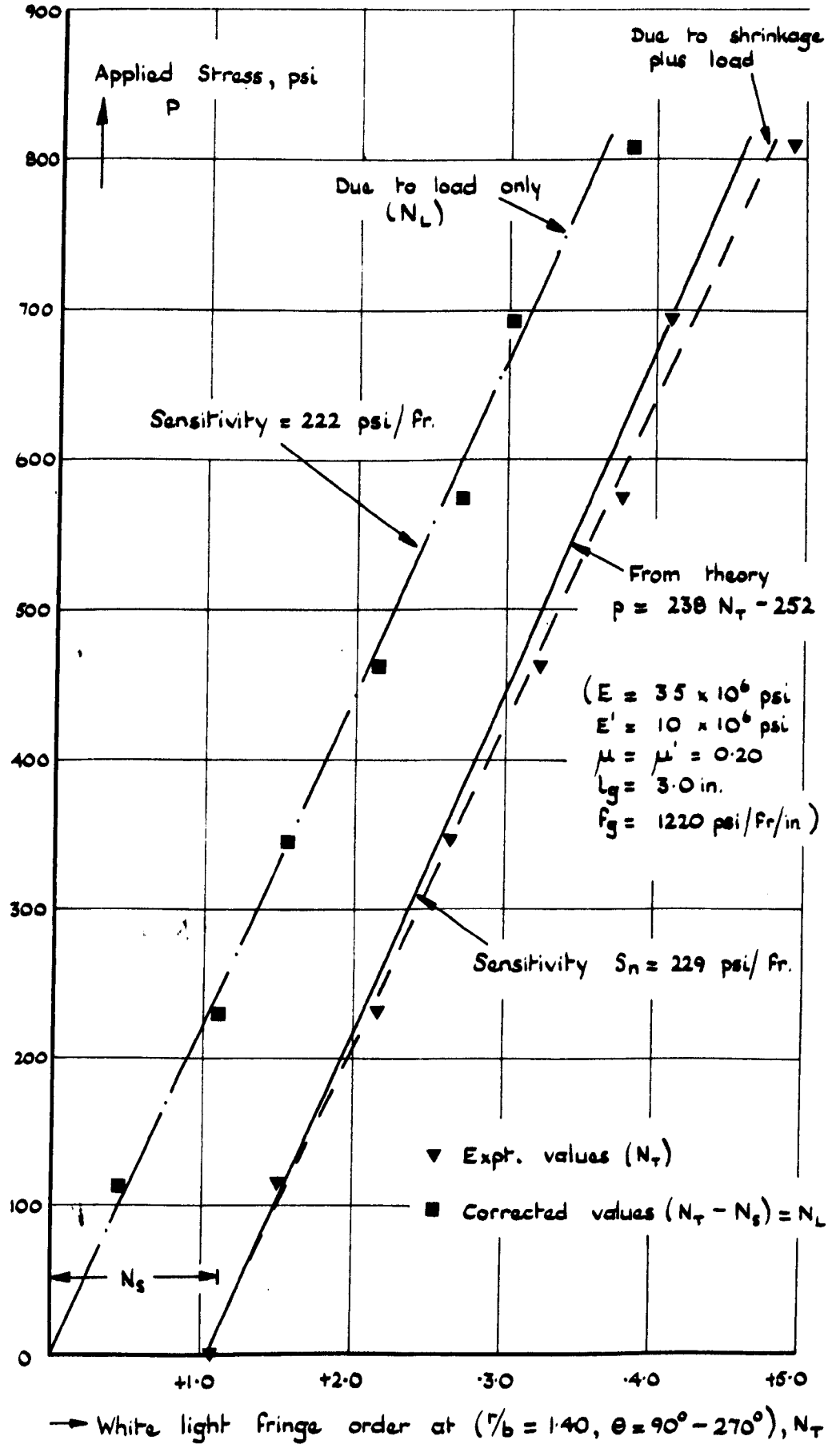

FIG. 3.17. Superposition of shrinkage and uniaxial compression fringe orders — annular stressmeter F3-4, day 106.

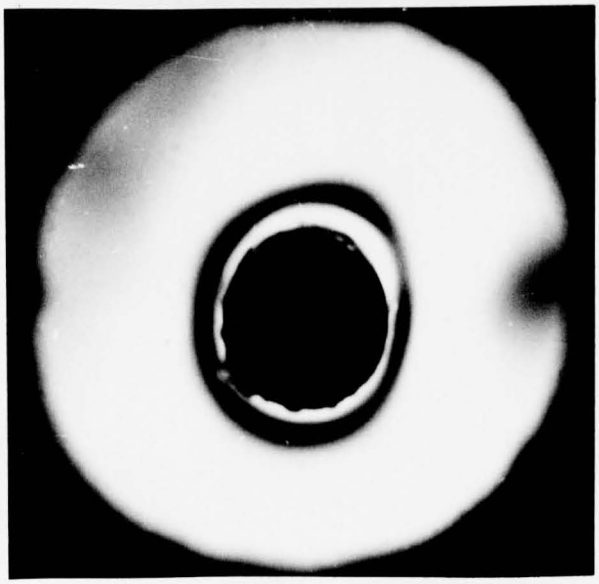

Shrinkage Fringe Order Only

Meter Length = 3.0 in.

f_g = 1230 p.s.i./fr./in.

$\Delta\delta$ = 460με

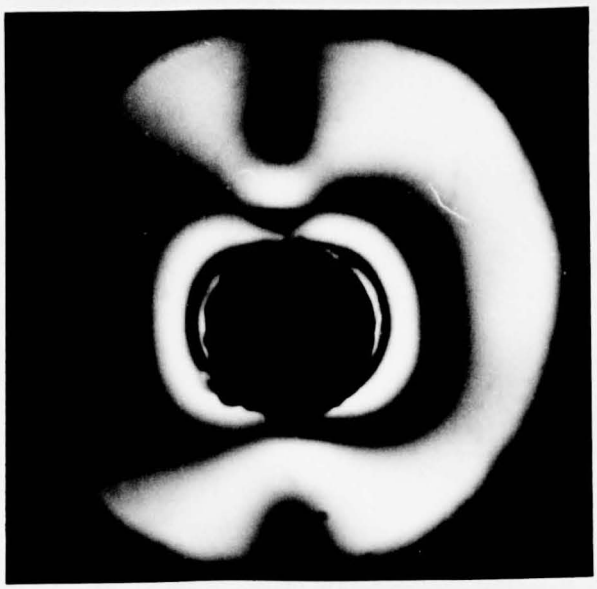

Shrinkage Plus

p = 200 p.s.i.

(p applied vertically)

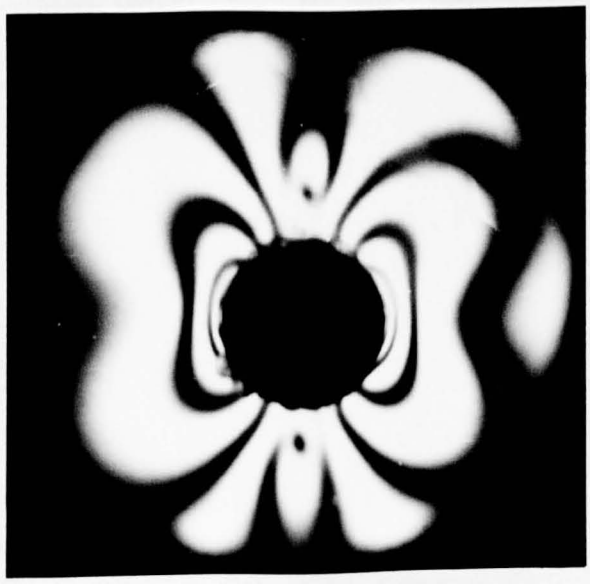

Shrinkage Plus

p = 600 p.s.i.

FIG. 3.18 Superposition of Shrinkage and Uniaxial Compression Stress Fringe Orders - Annular Stressmeter, Specimen F3-4.

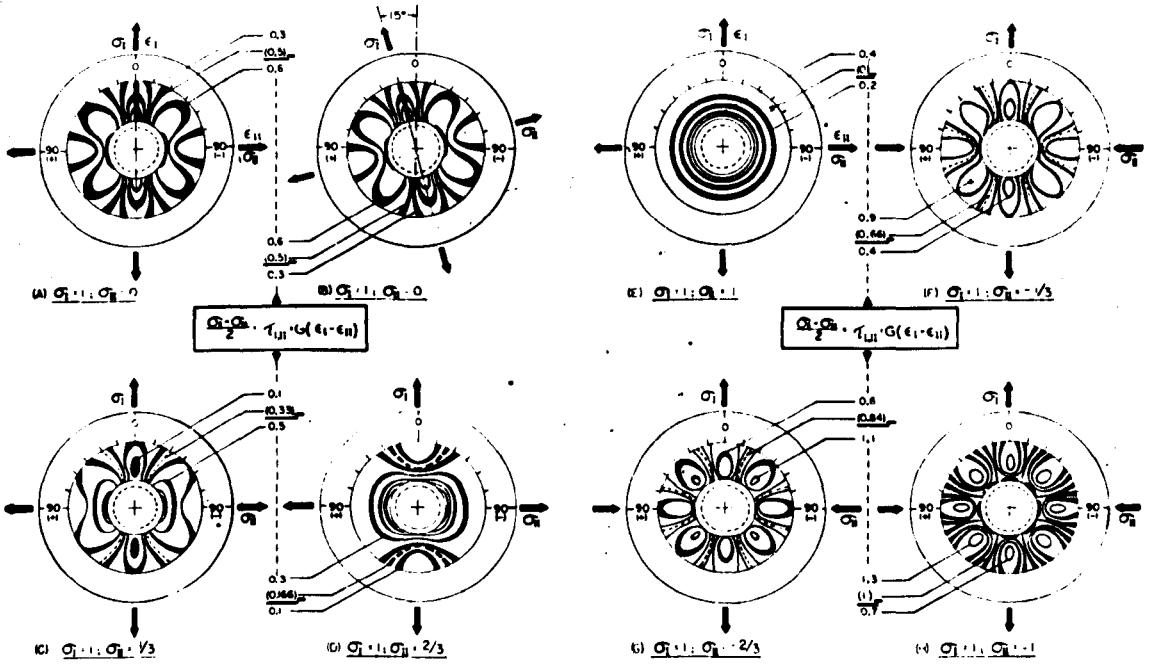

FIG. 4.1. Theoretical Isochromatics in an Annular Disc. (After Oppel[58])

Rectangular coordinates

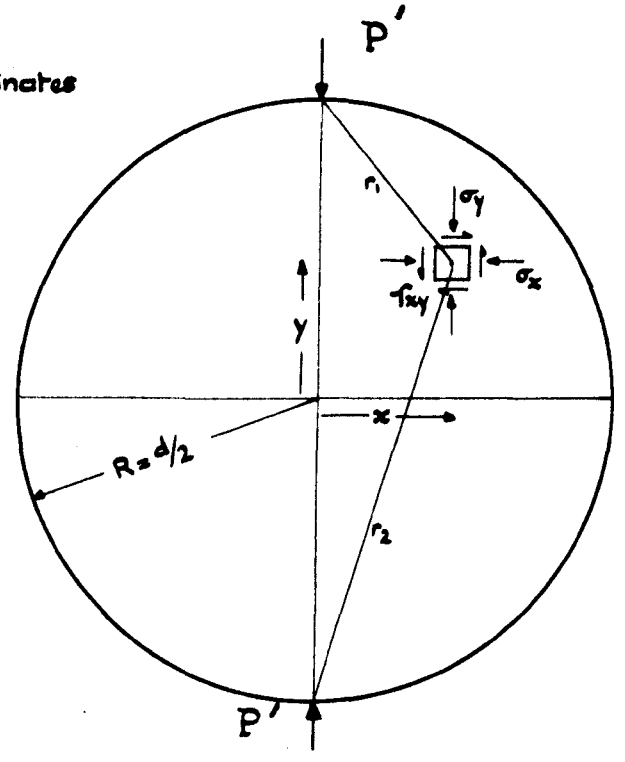

Polar coordinates including strip loading notation

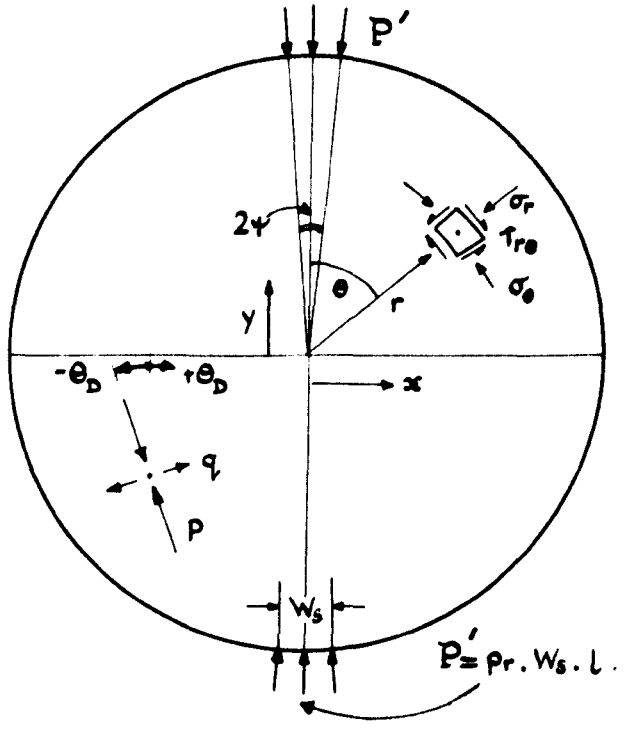

FIG. 4.2. Stress notation for discs (thickness $l = d/7$)

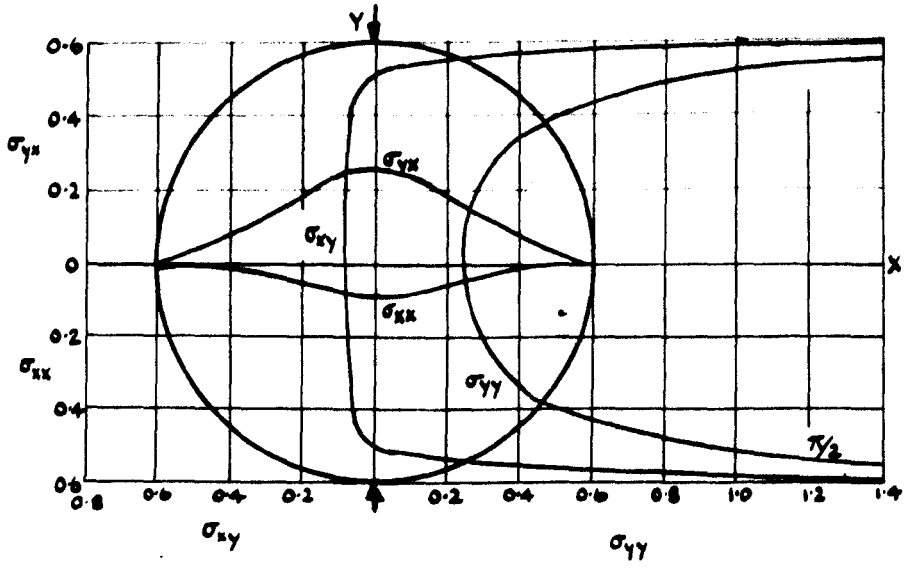

Stresses $2p_r/\pi = 1$

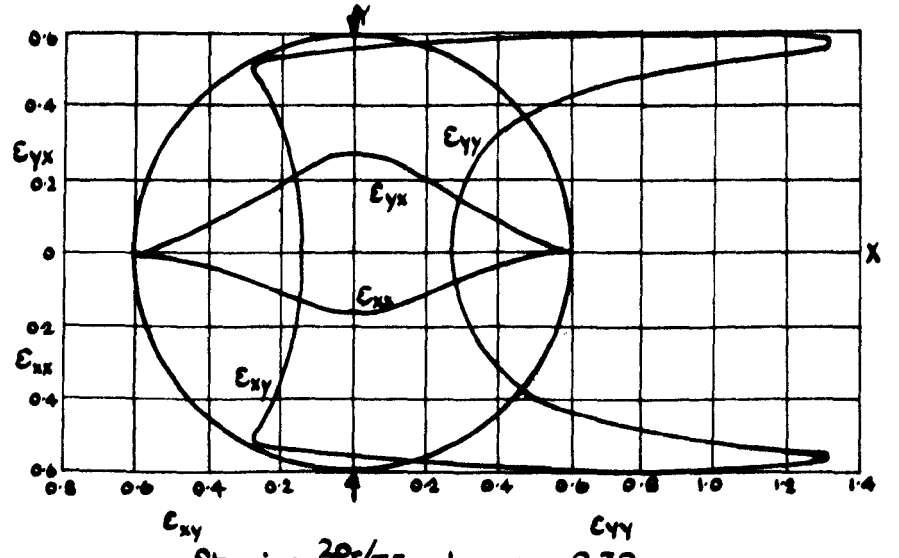

Strains $2p_r/\pi E = 1$, $\mu = 0.30$

FIG. 4.3. Stress and strain distribution along disc axes. (Plane stress - after Hondros).

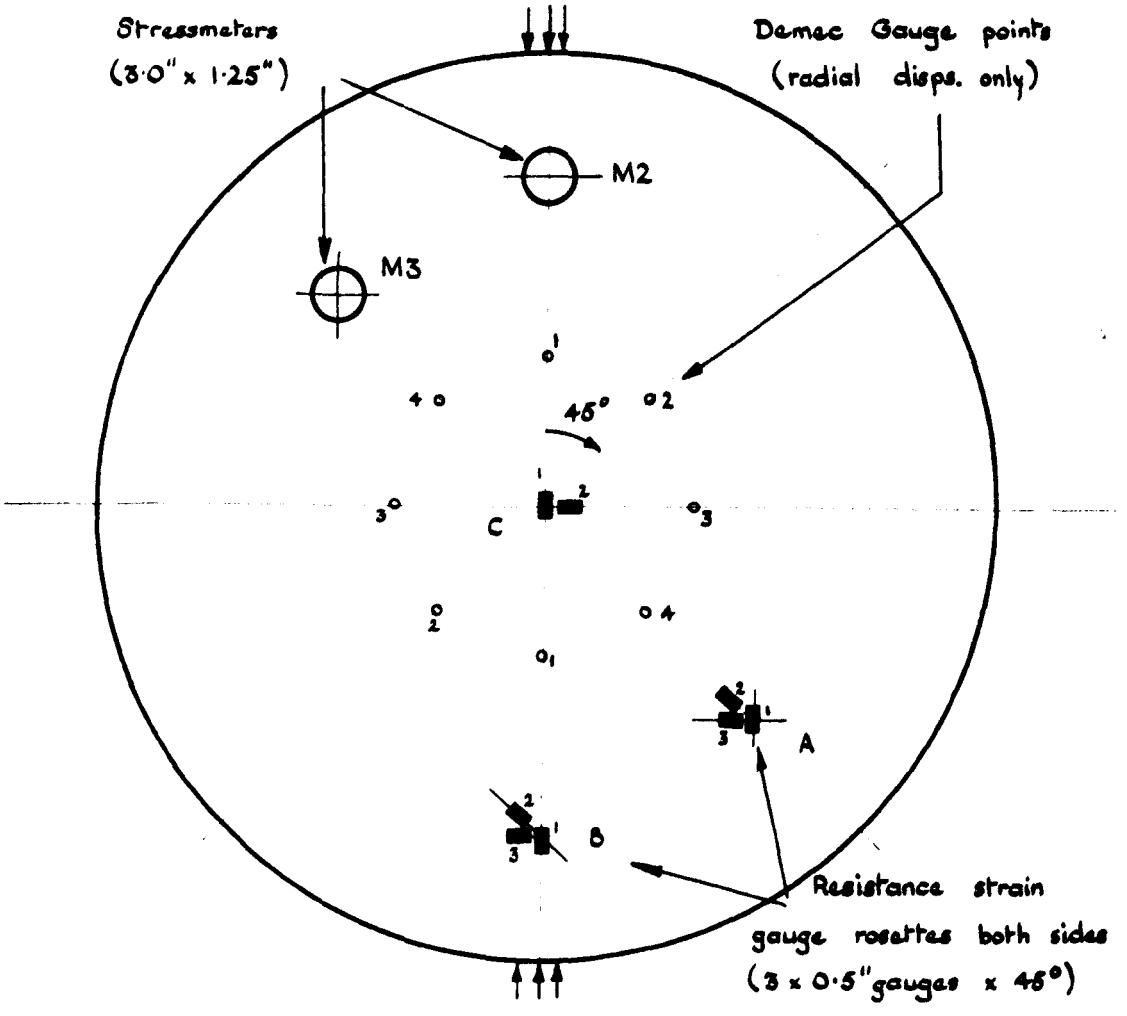

Disc diameter : 23·375 in.
Thickness : 3·265 in.
Loading width : 0·625 in.

Disc F5-1 : Annular stressmeter replaces C rosette.
Disc F5-3 : Demec points and solid stressmeter at centre only.

FIG. 4.4. Instrument layout disc F5-2

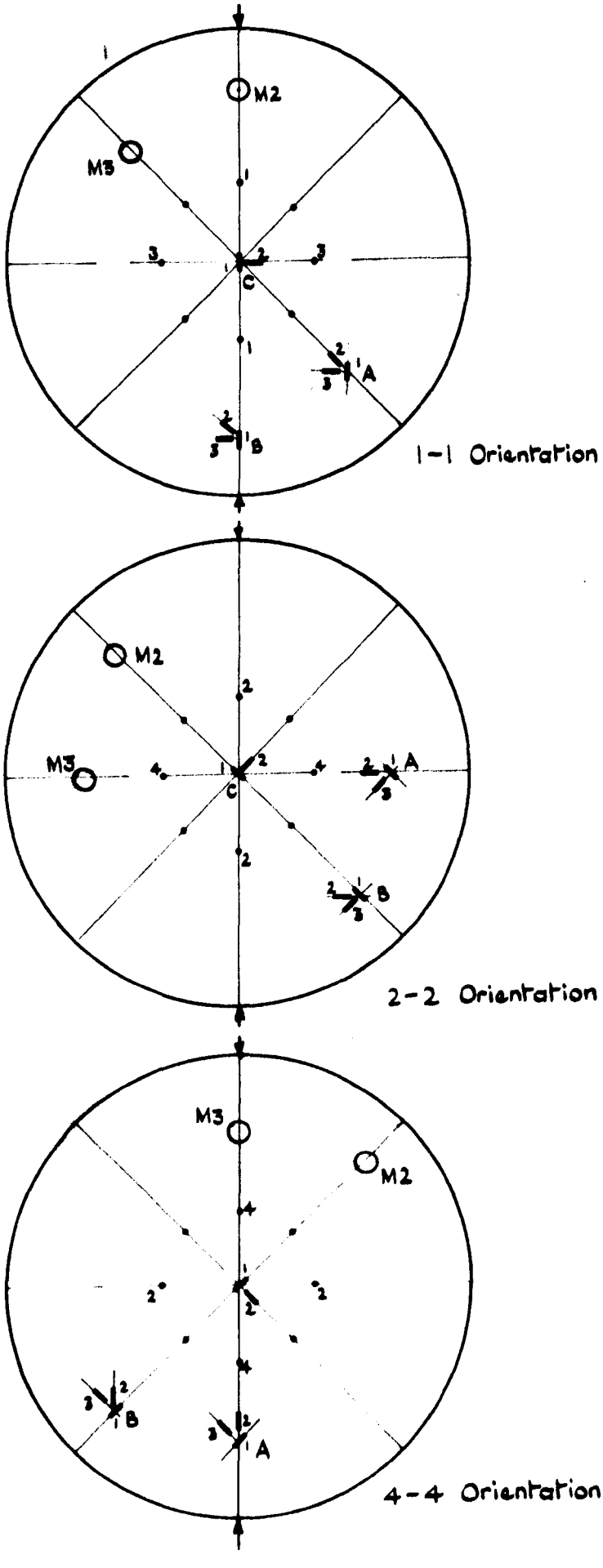

FIG. 4.5 Test orientations for discs F5-1 & F5-2

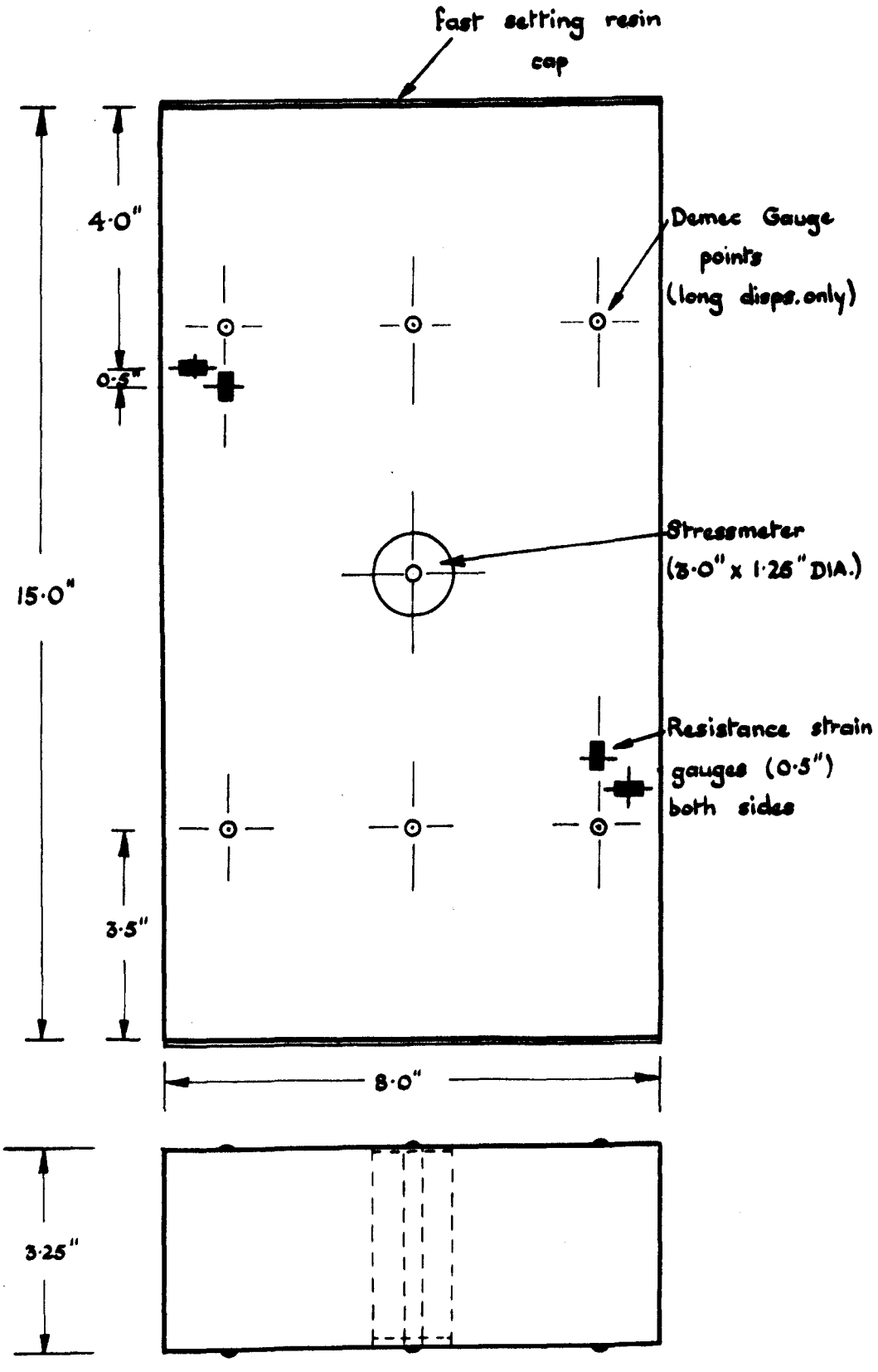

FIG. 4.6. Details for slab F3-4

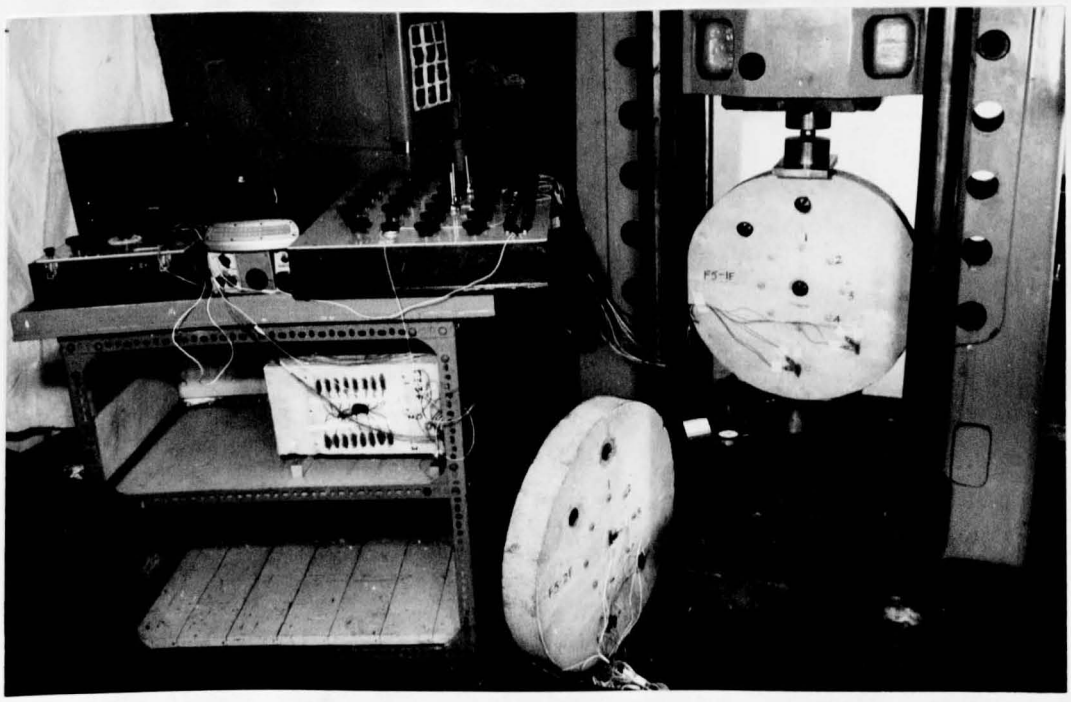

FIG. 4.7. Instrumented Concrete Discs

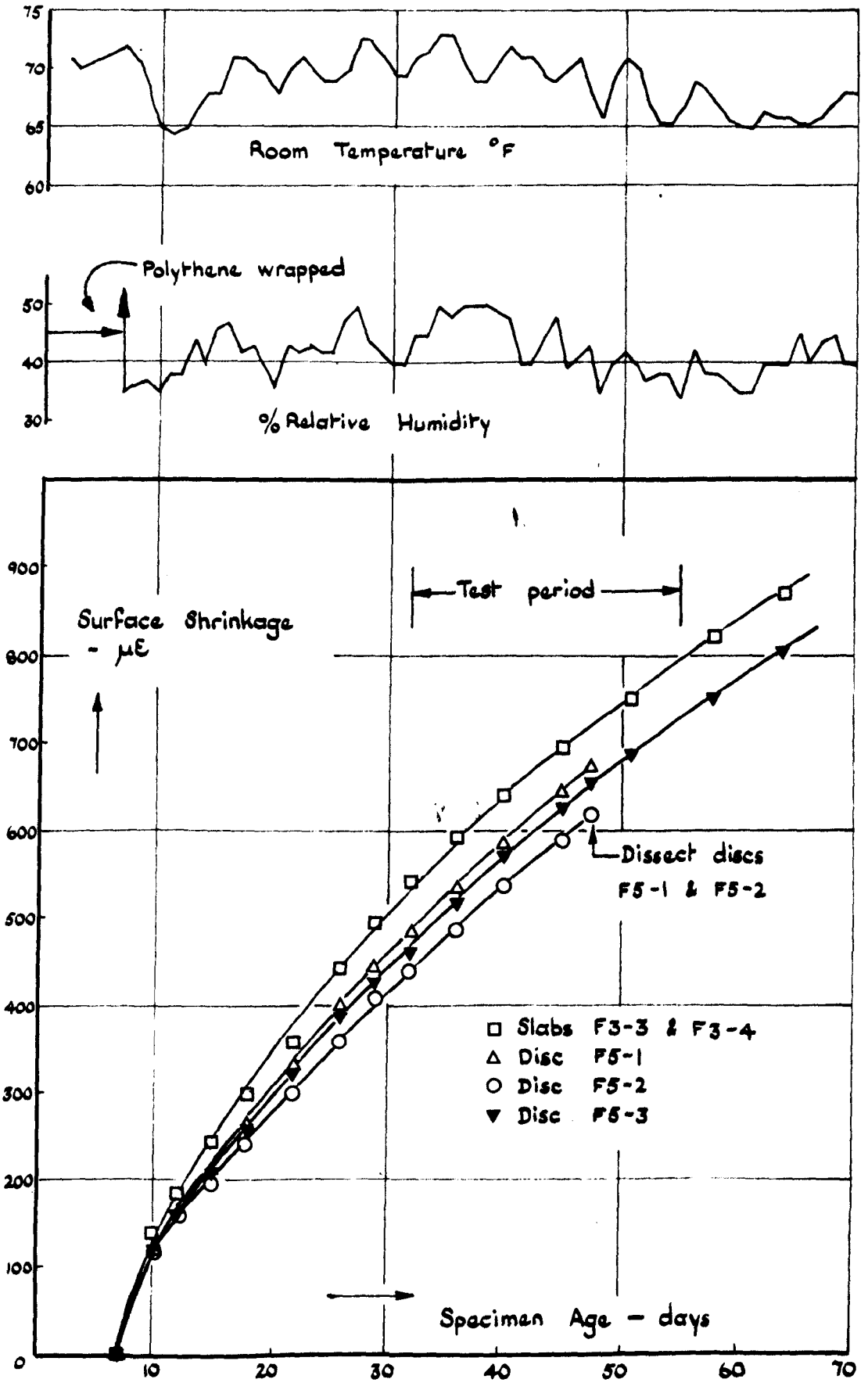

FIG. 4.8. Surface shrinkage of specimens used in disc tests.

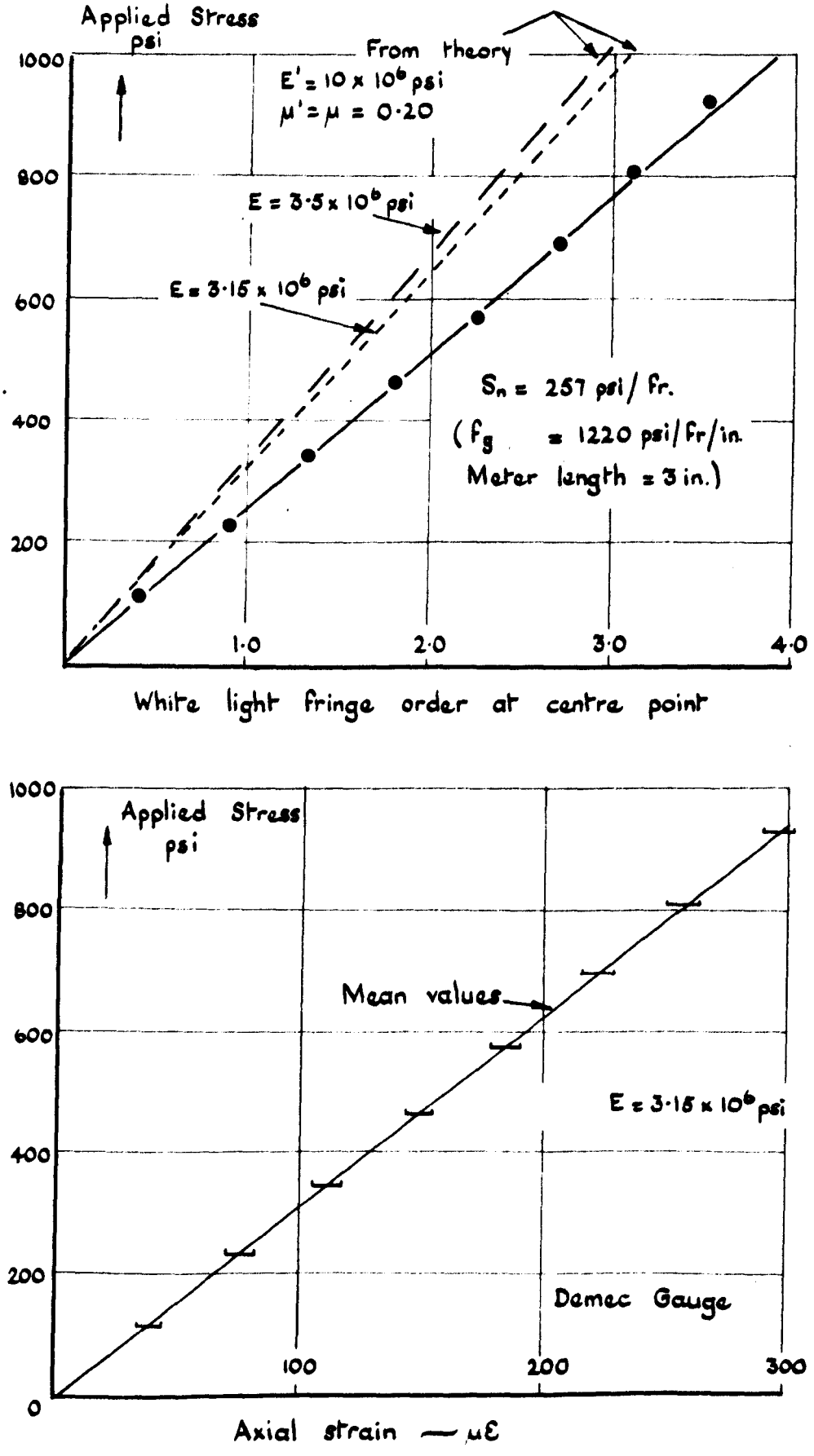

FIG. 4.9 Solid stressmeter and Demec Gauge data

Slab F3-3

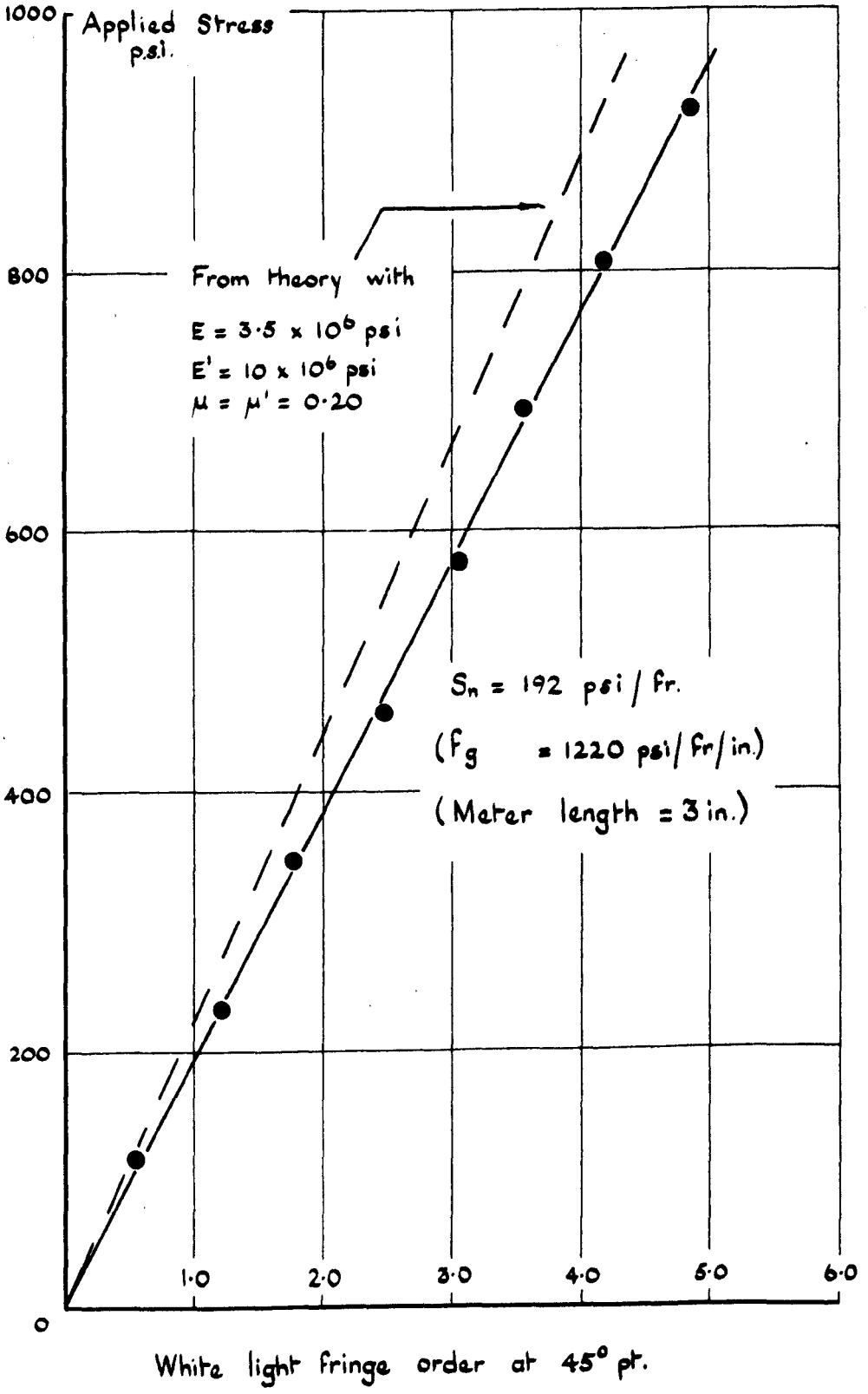

FIG. 4.10. Slab F3-4 Annular stressmeter response

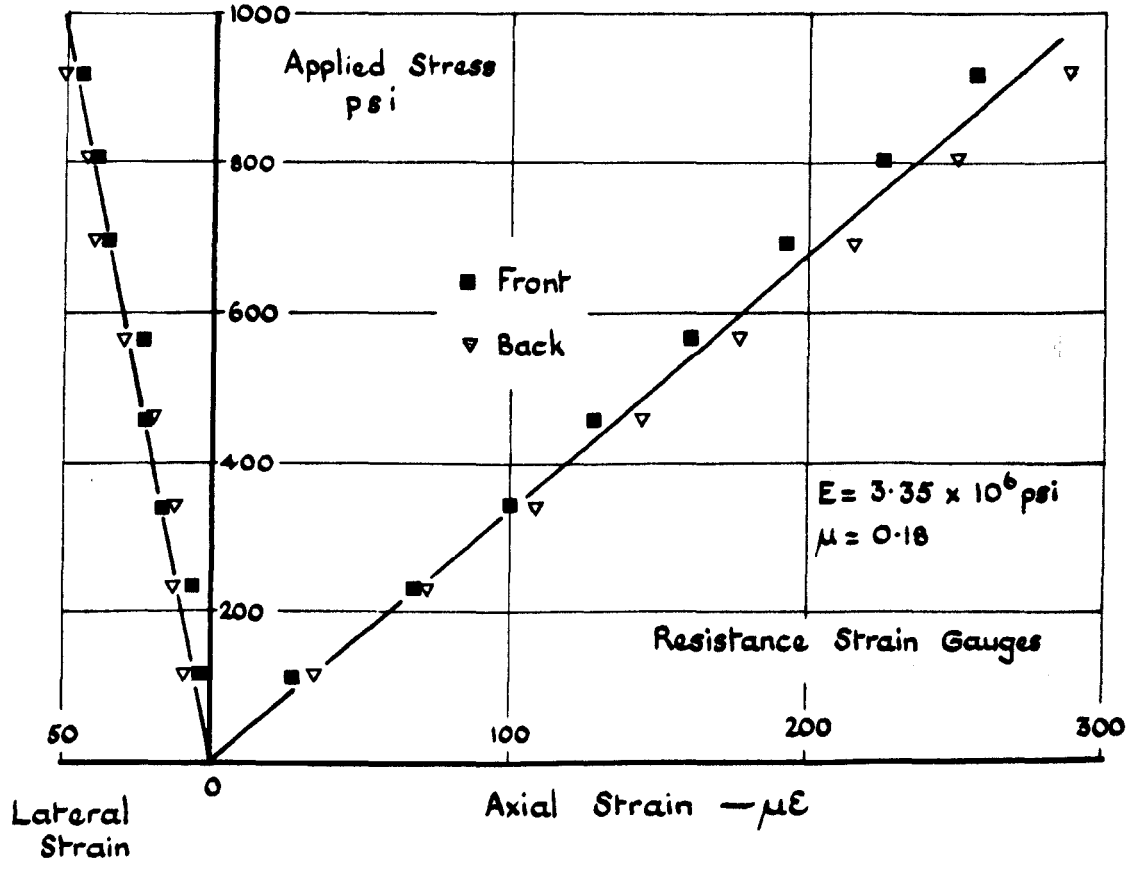

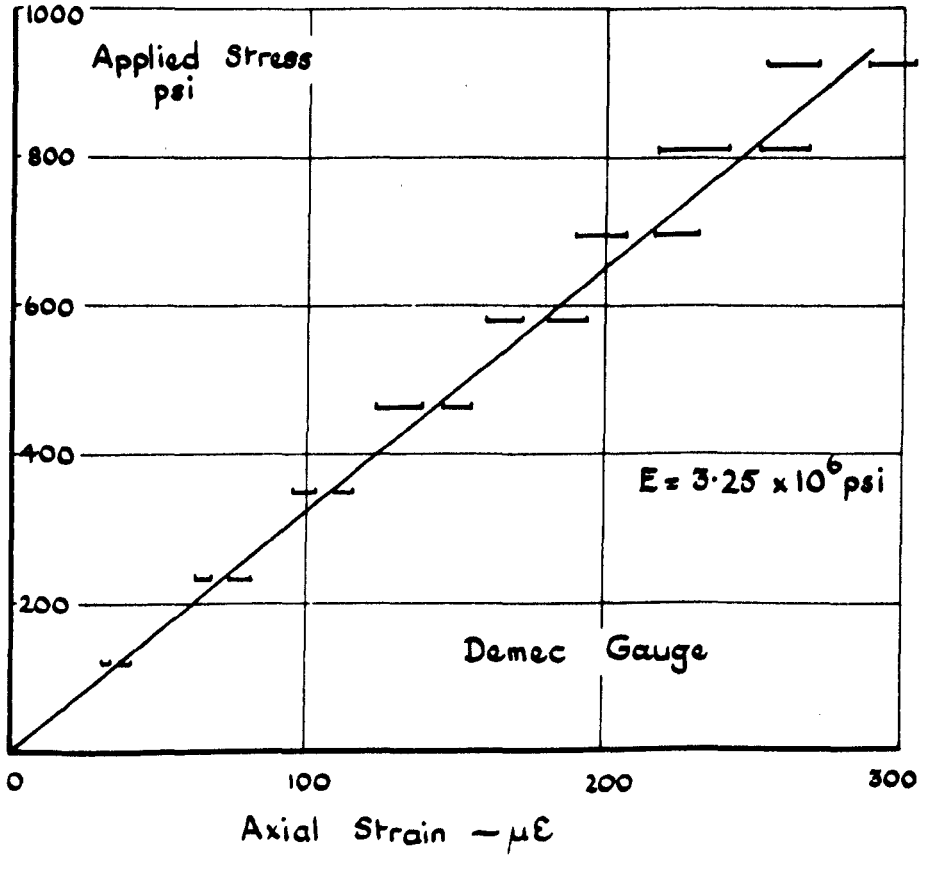

FIG. 4.11. Slab F3-4 — Deformation characteristics uniaxial compression

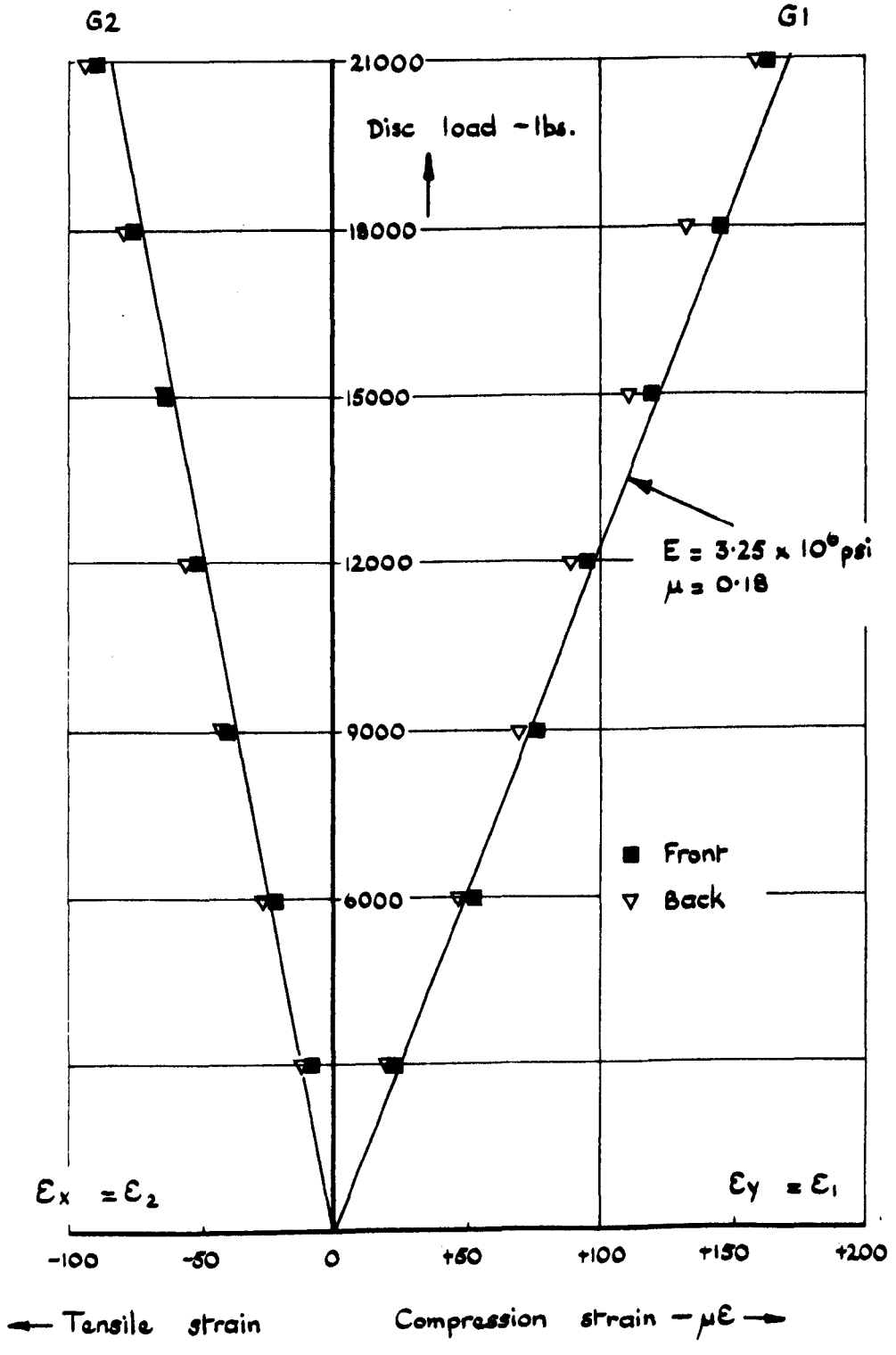

FIG. 4.12. Disc F5-2 centre point strain gauges, orientation 1-1.

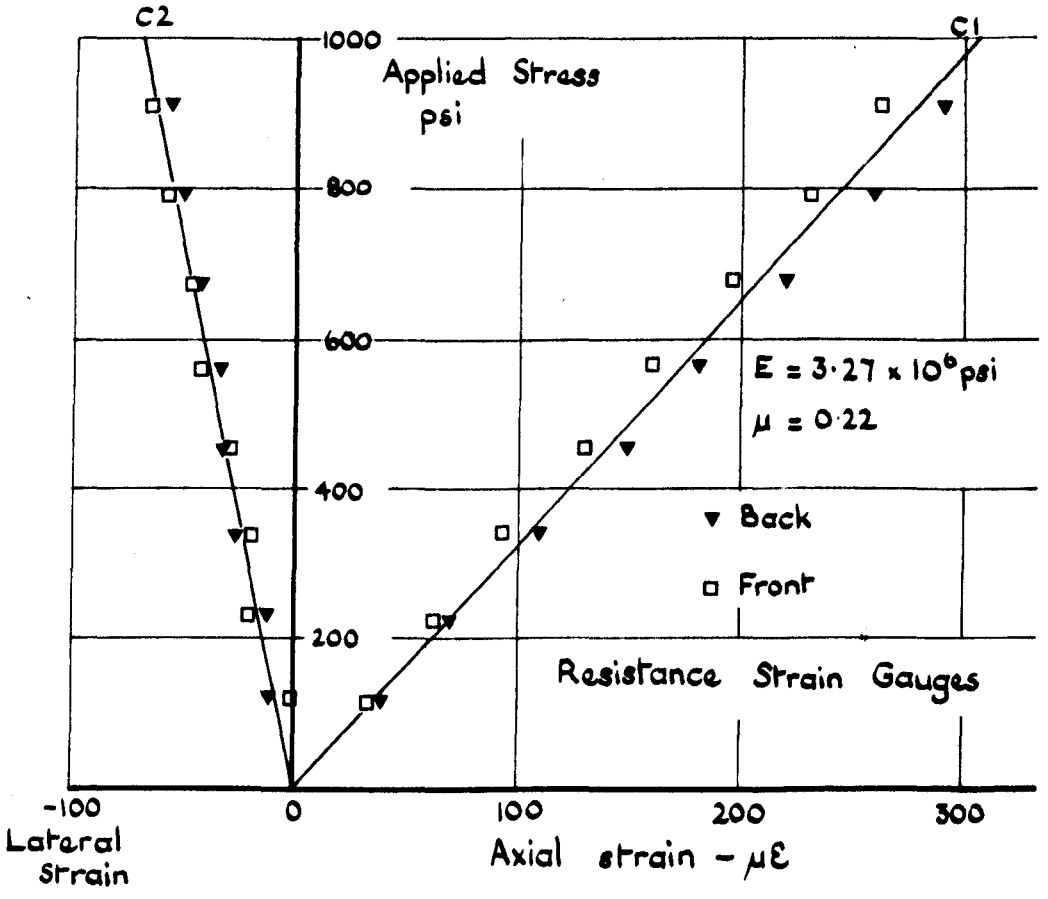

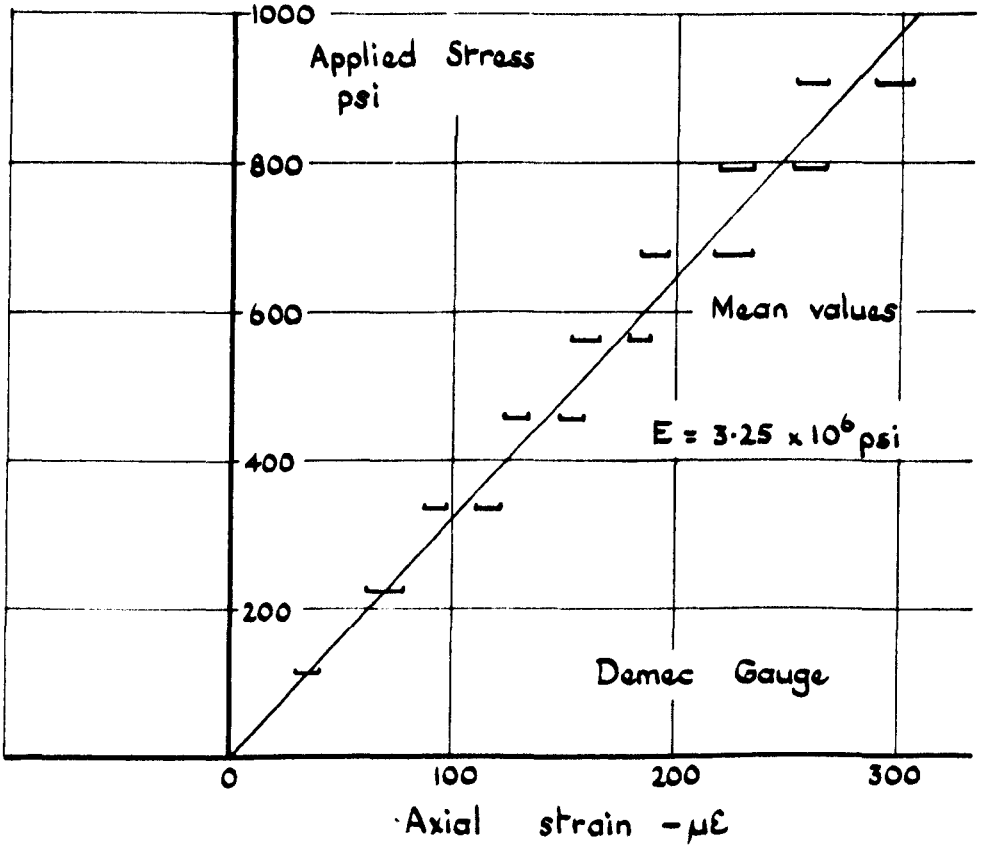

FIG. 4.13. Centre element from disc F5-2 -uniaxial compression

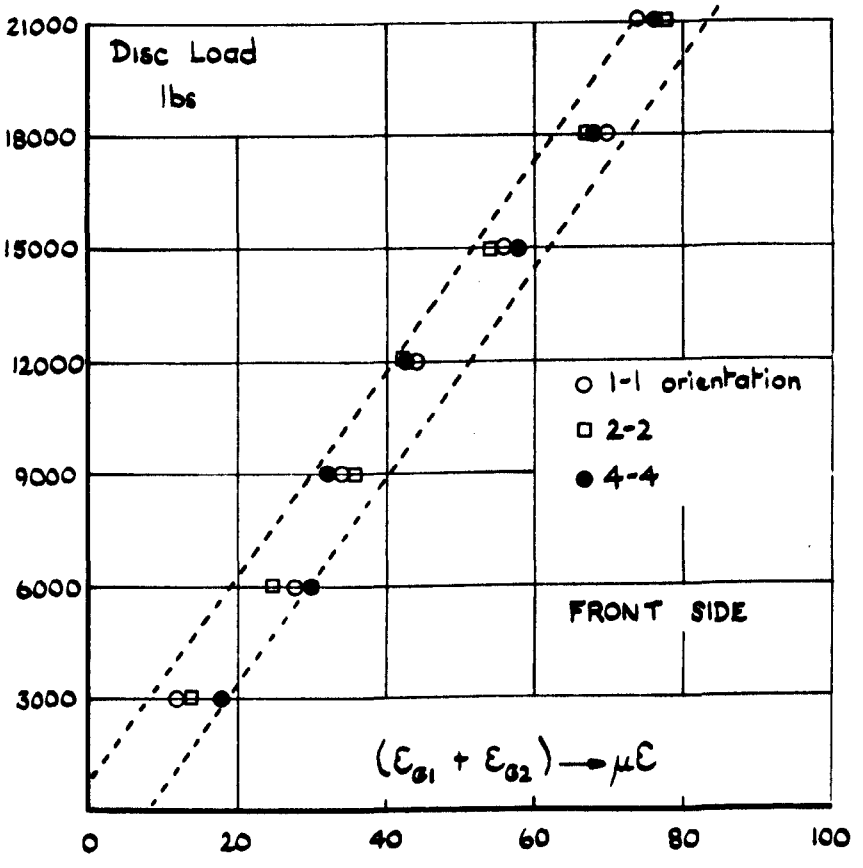

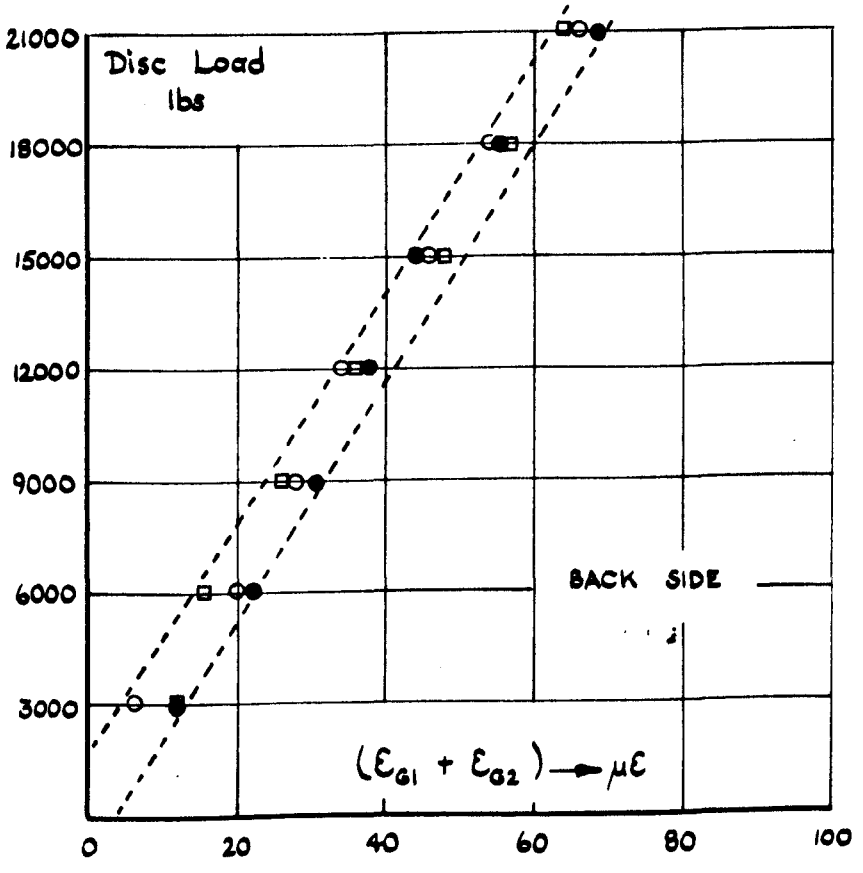

FIG. 4.14. Disc F5-2 centre rosette compatibility check

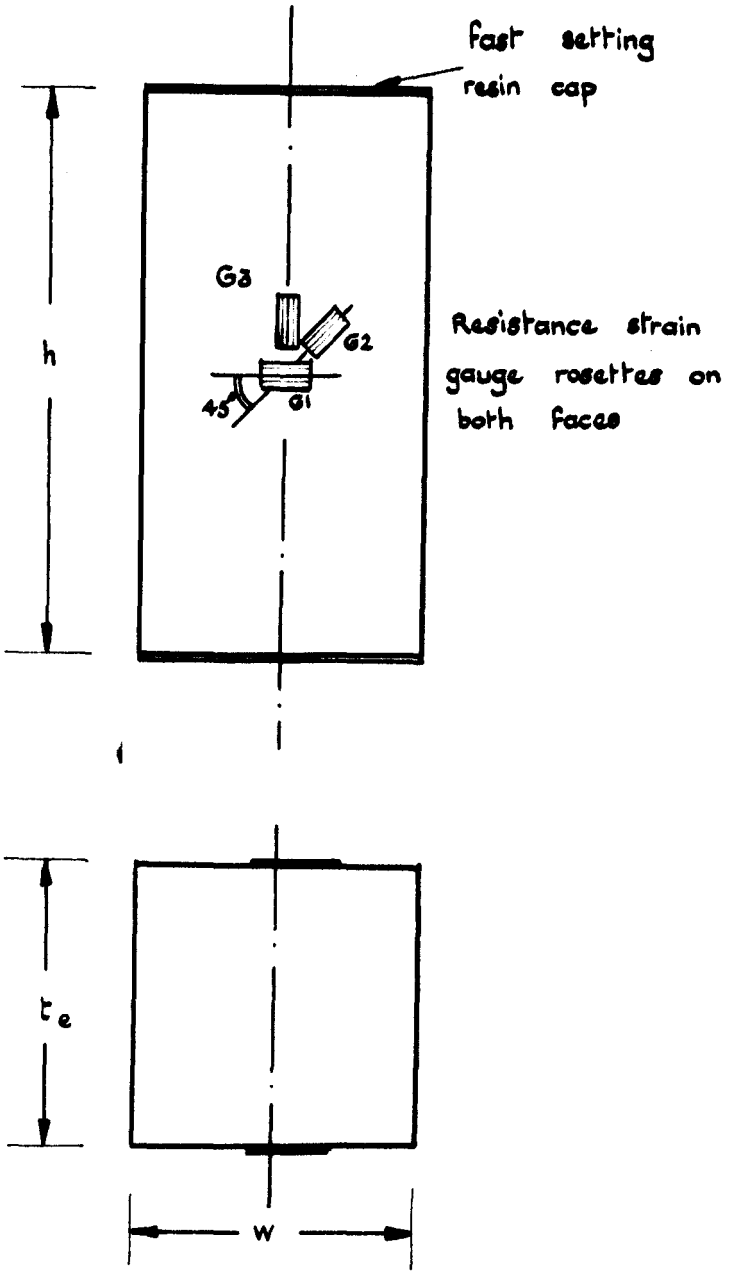

Element	h in.	w in.	t_e in.	Cross Section Area - sq in.
A x F5-1	6·0	3·13	3·265	10·20
B x F5-2	6·0	3·28	3·265	10·70

FIG. 4.15. Dissected disc element used to check A and B rosettes in uniaxial compression.

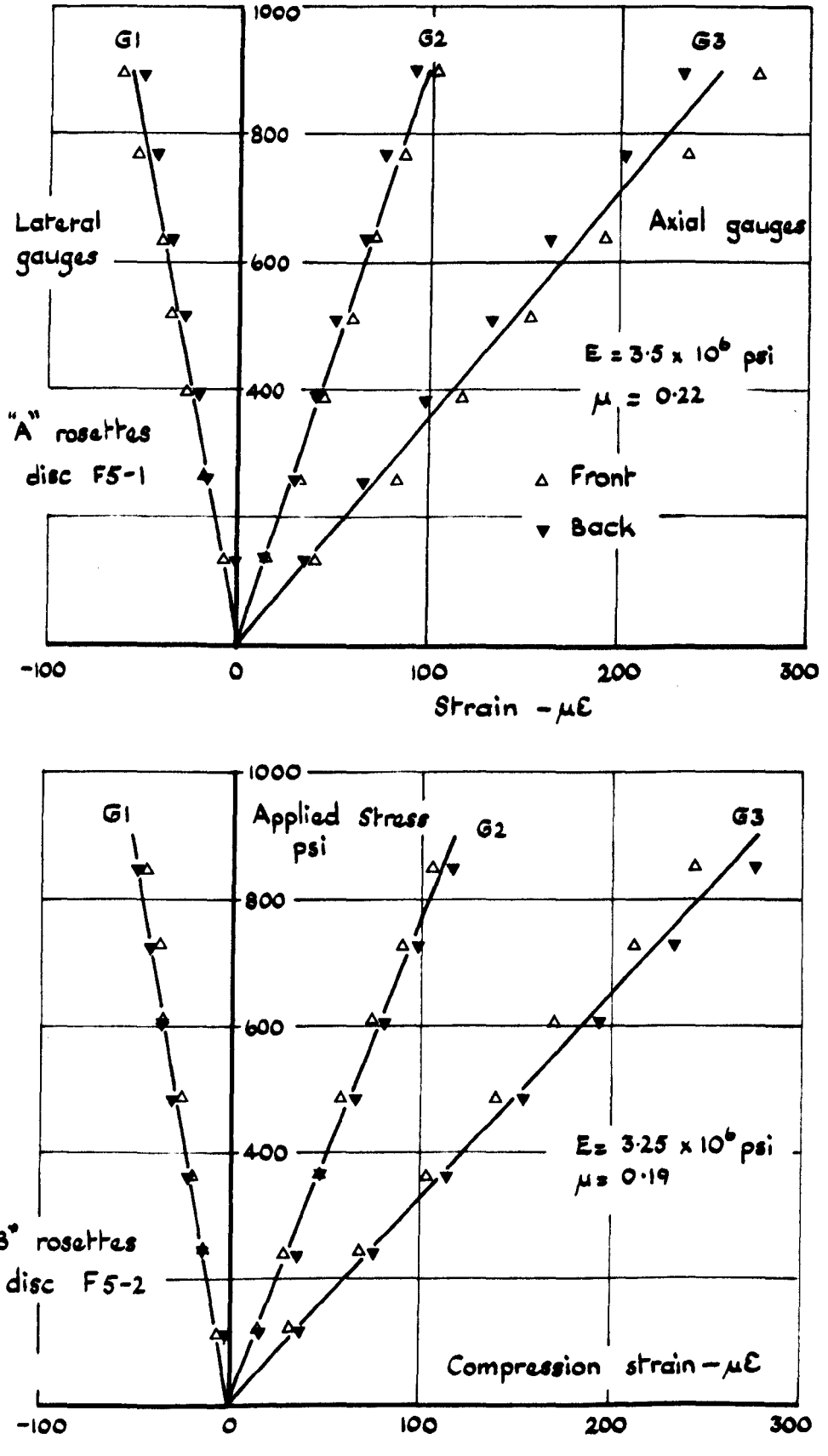

FIG. 4.16. Elements with rosettes from F5-1 & F5-2 -uniaxial compression

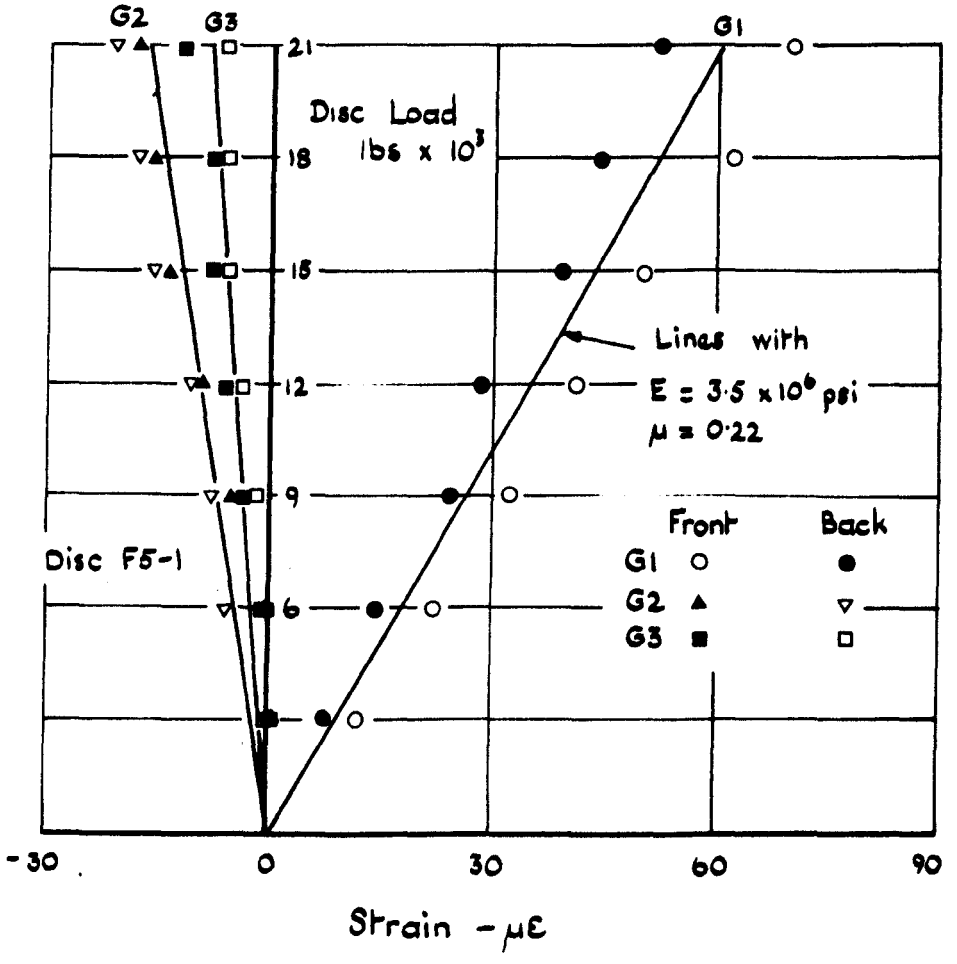

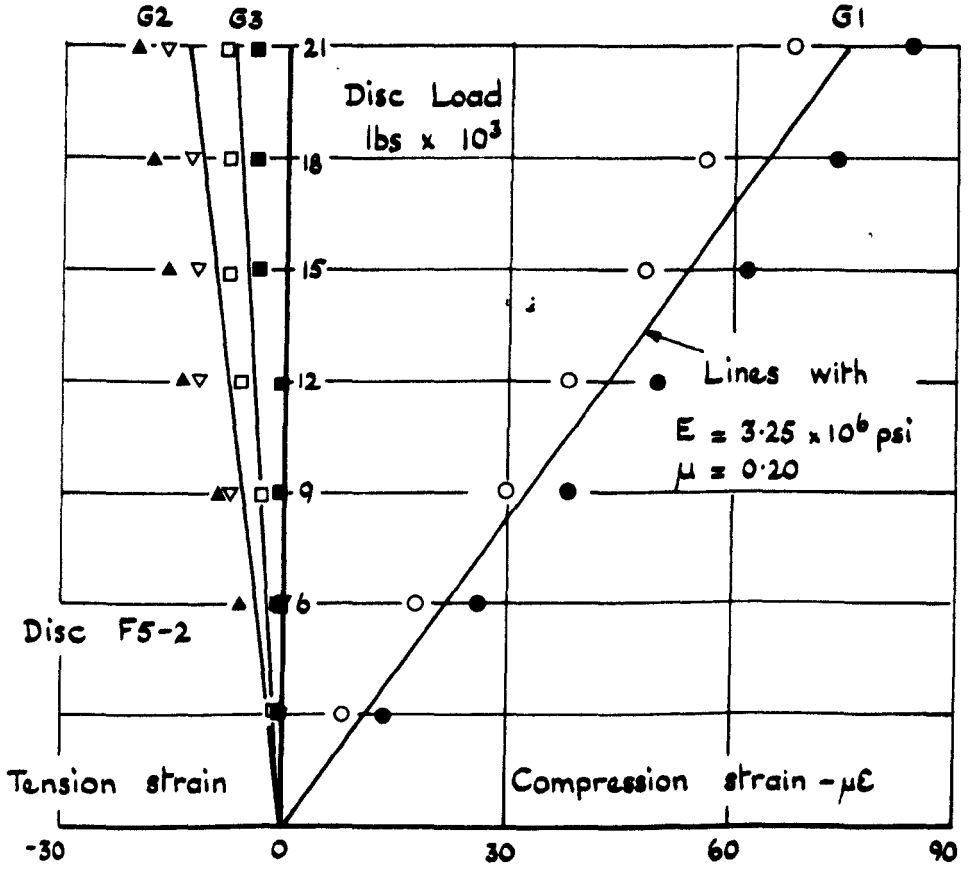

FIG. 4.17. "A" rosette - disc orientation 1-1

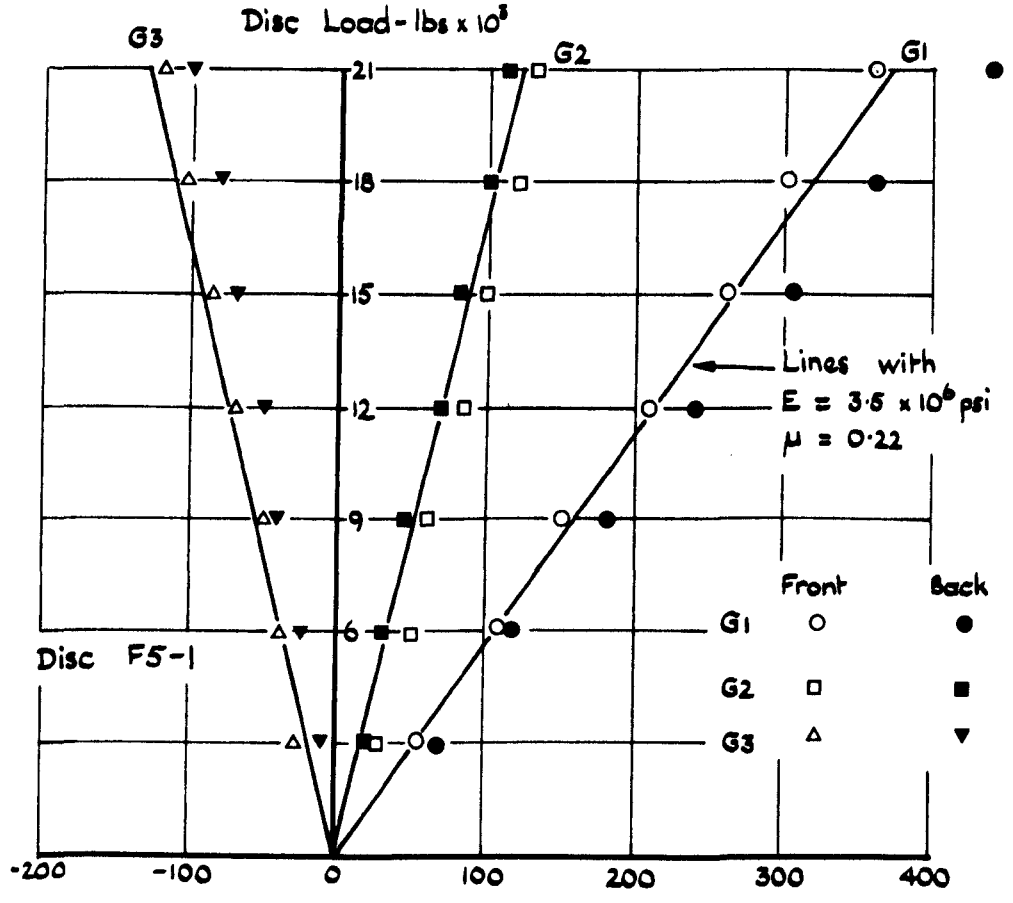

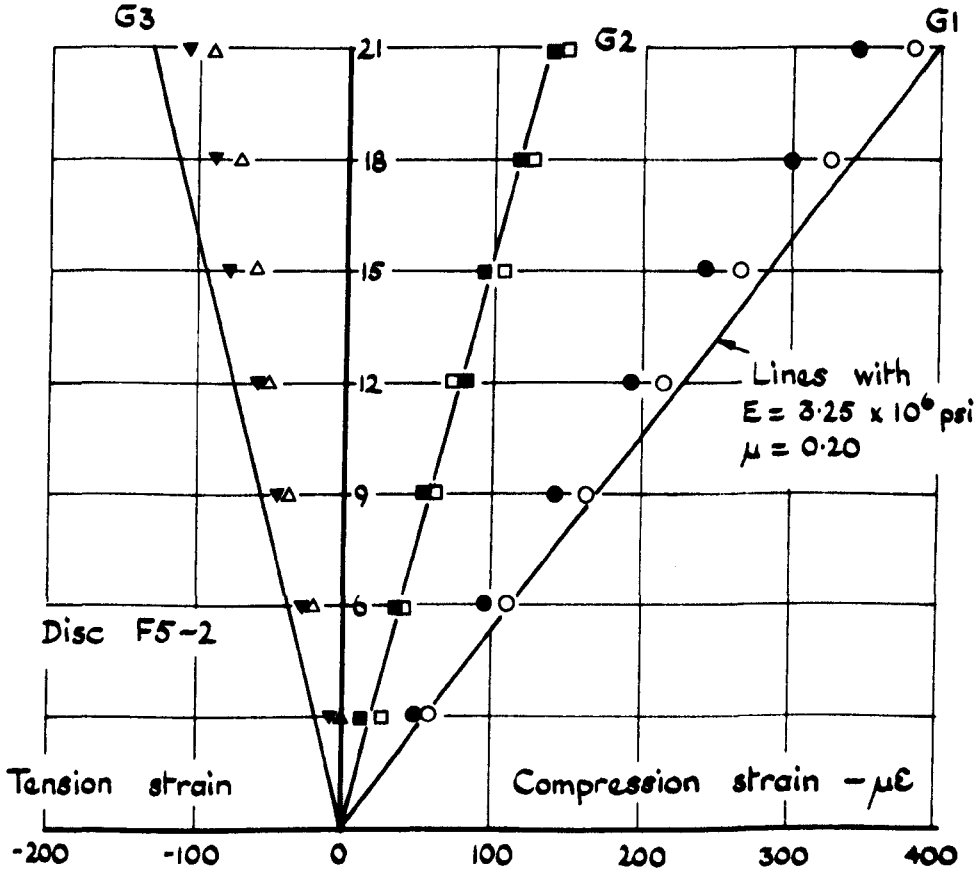

FIG. 4.18. "B" rosette – disc orientation 1-1.

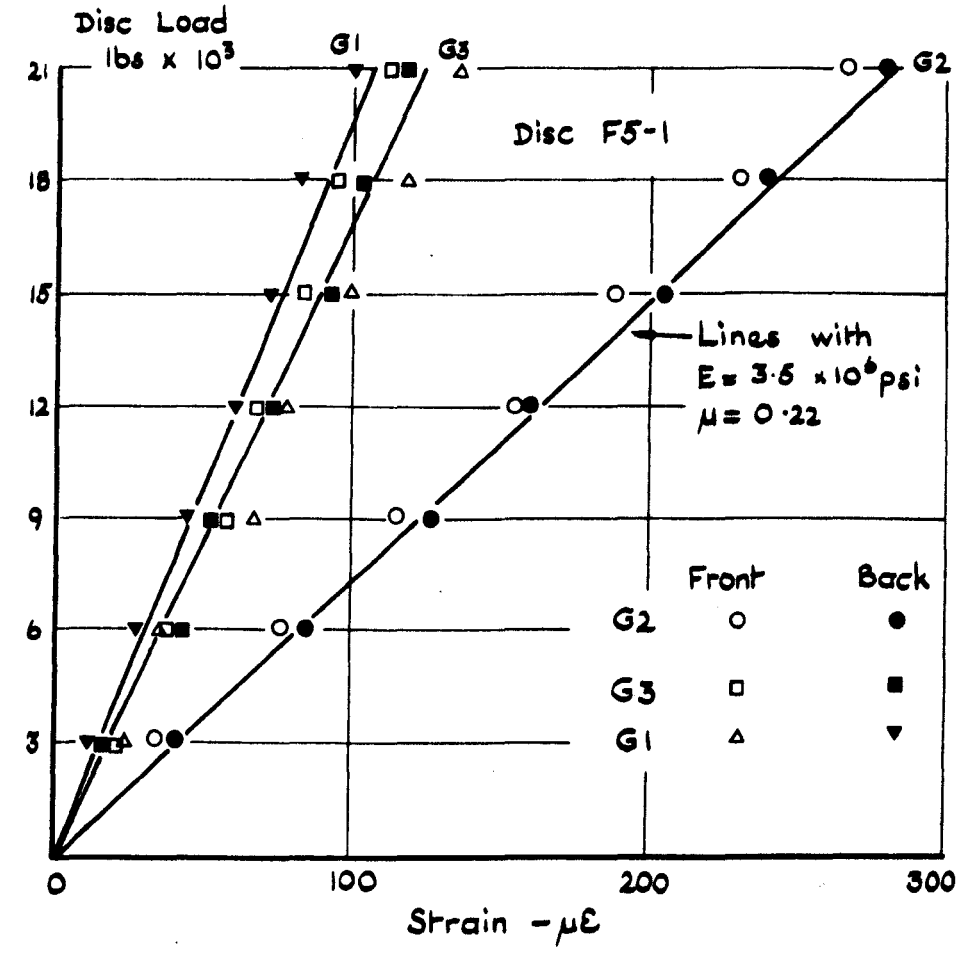

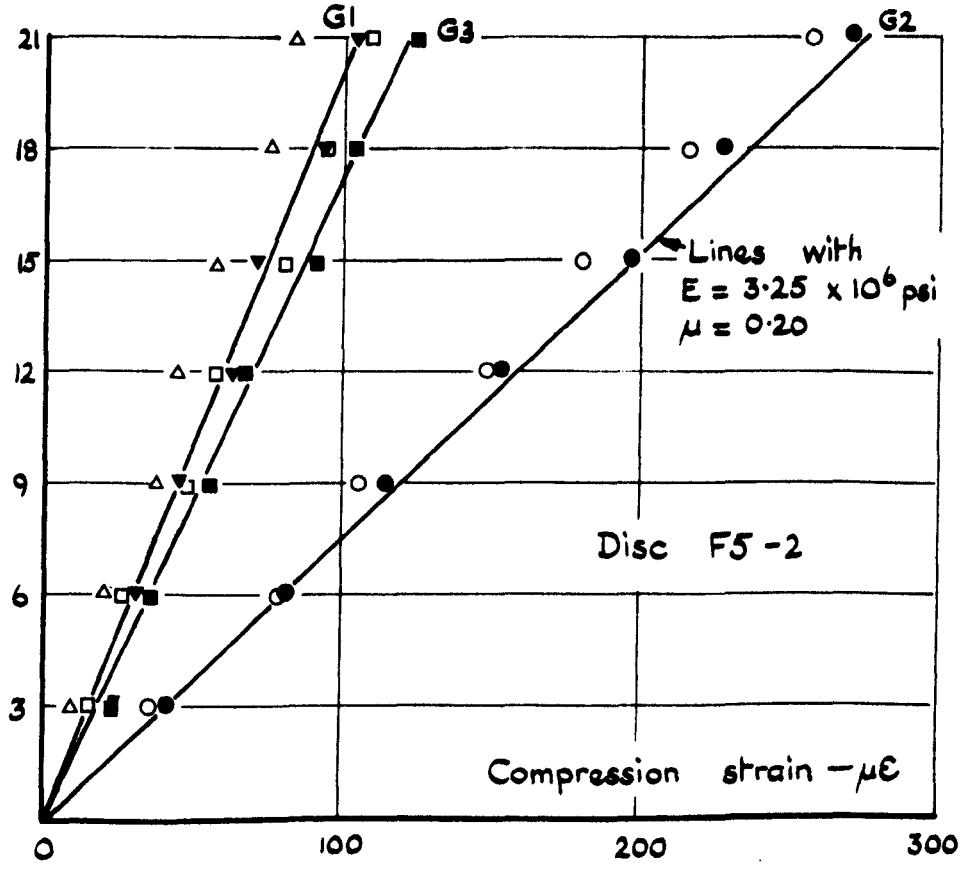

FIG. 4.19. "A" rosette – disc orientation 4-4

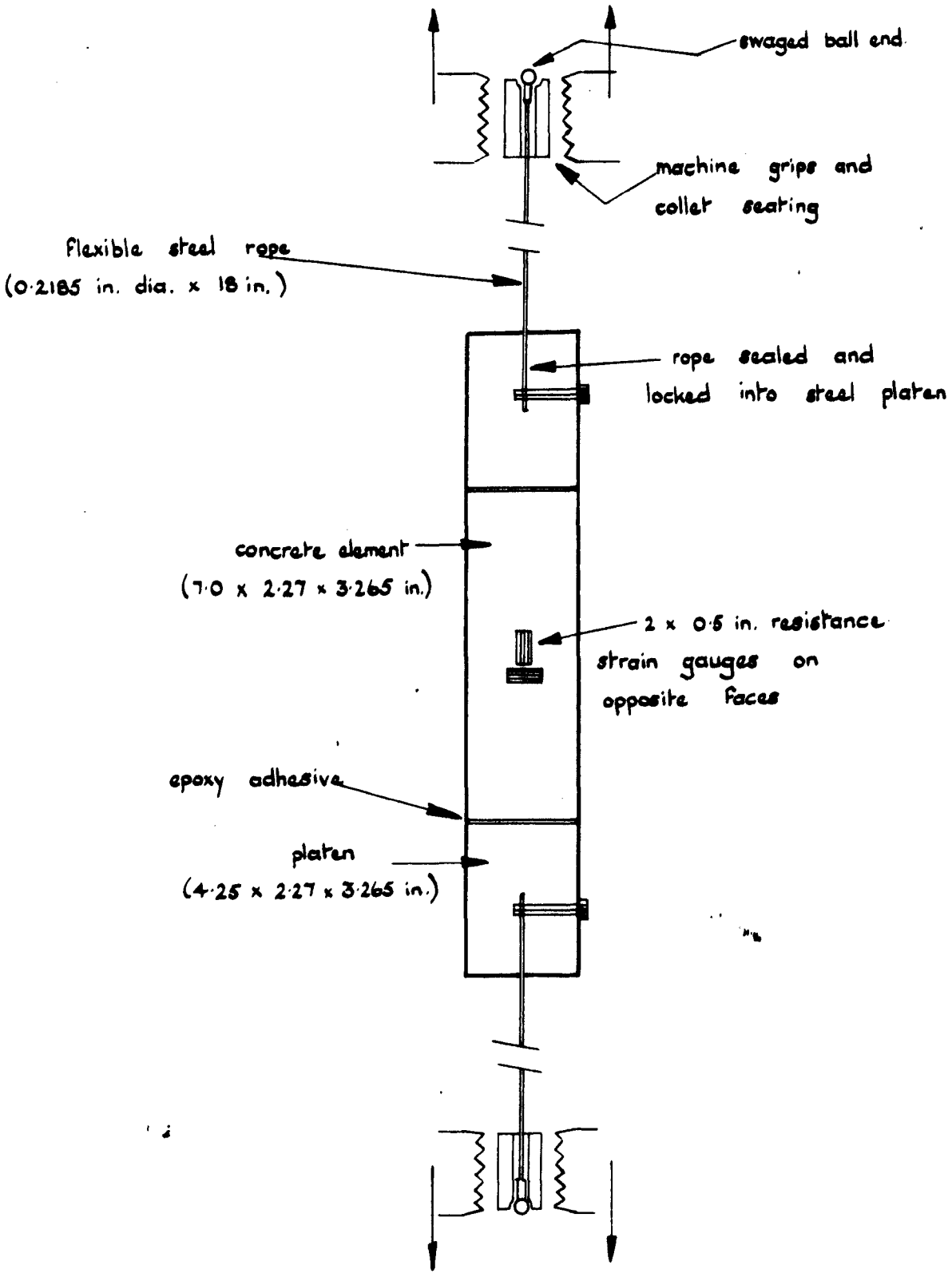

FIG. 4.20. Uniaxial tension test specimen

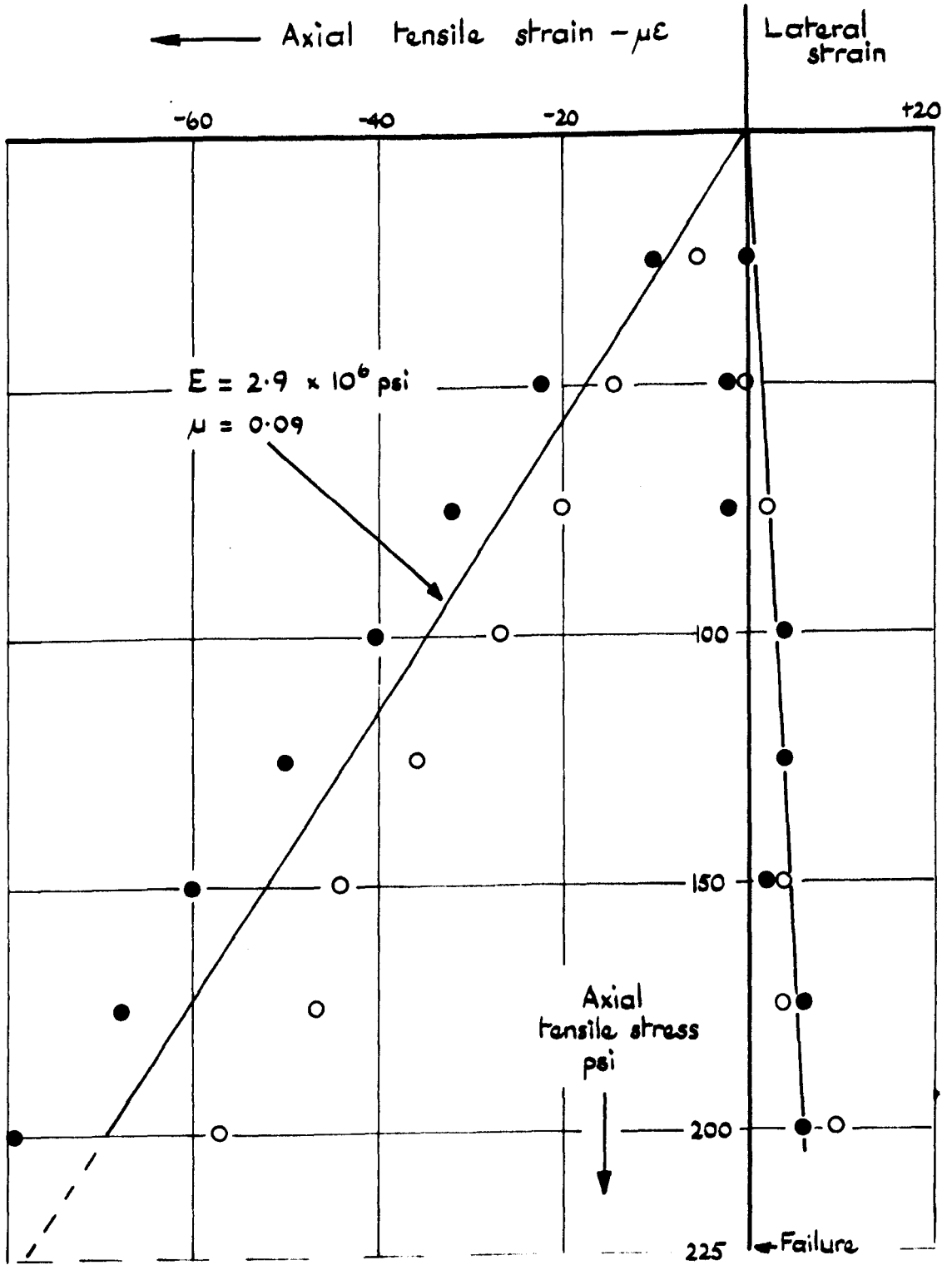

FIG. 4.21. Element from disc F5-2 -uniaxial tension

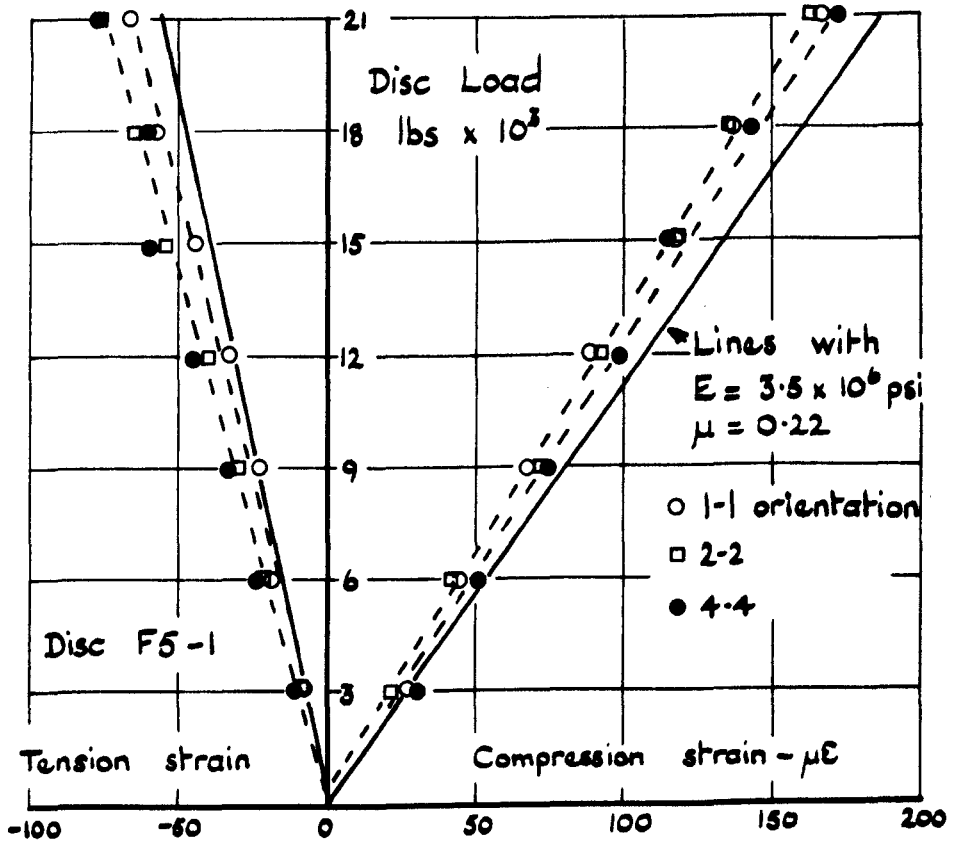

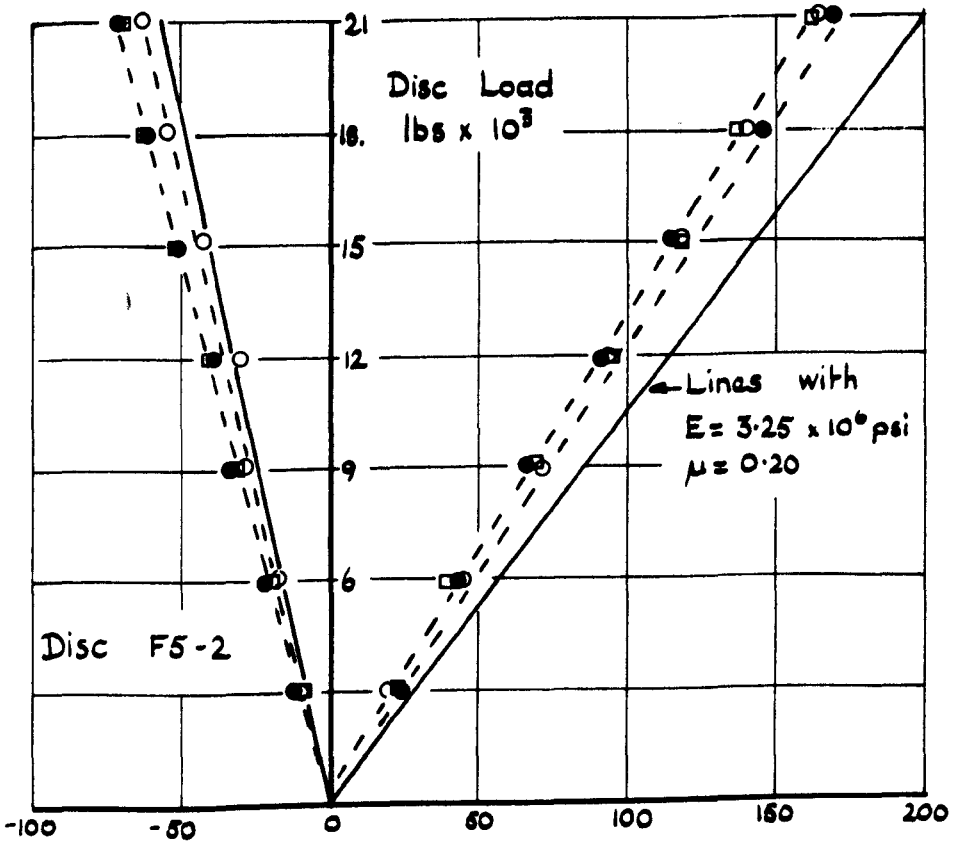

FIG. 4.22 Strains on principal diameters of discs (Demec Gauge).

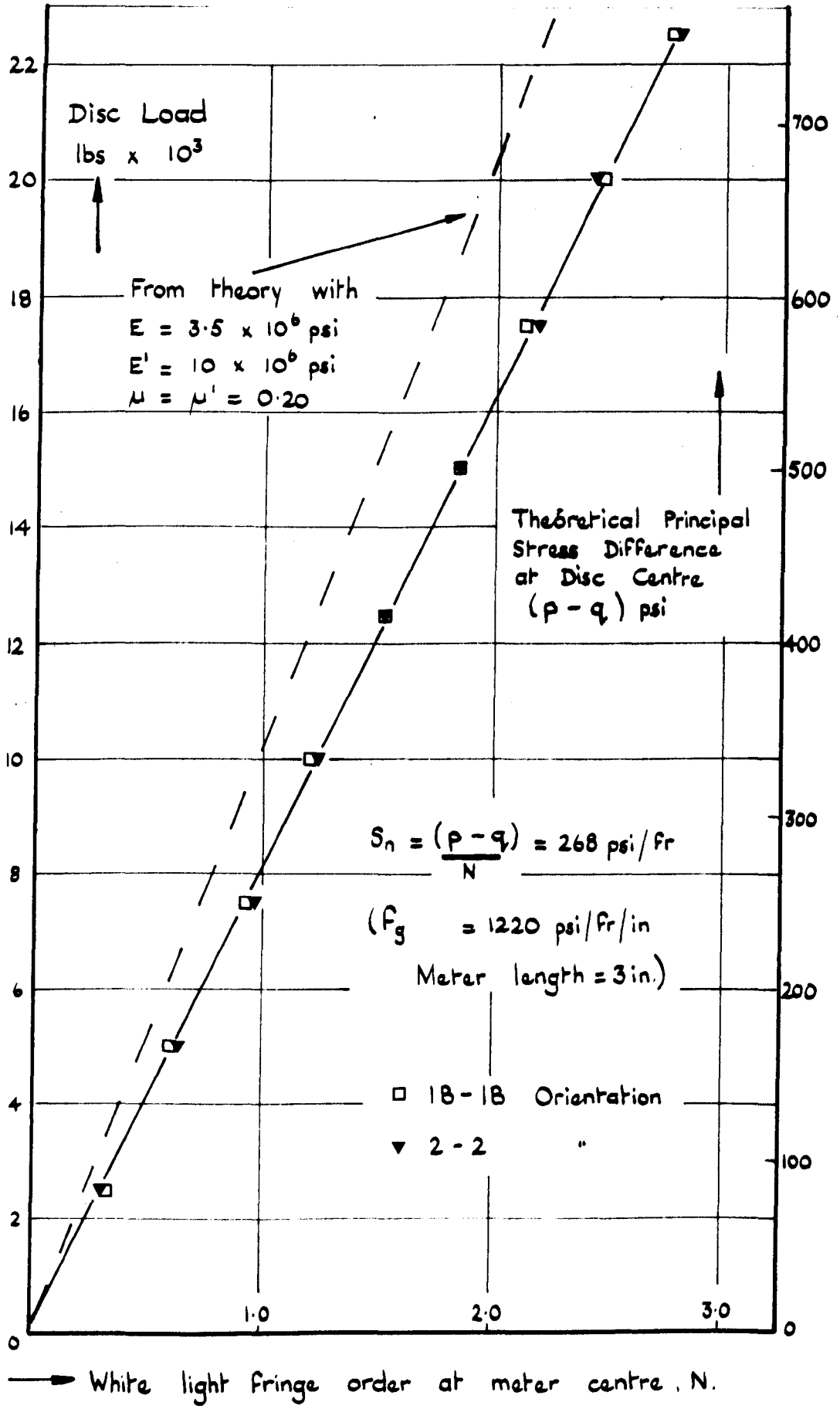

FIG. 4.23 Centre point solid stressmeter, 2 orientations of disc F5-3.

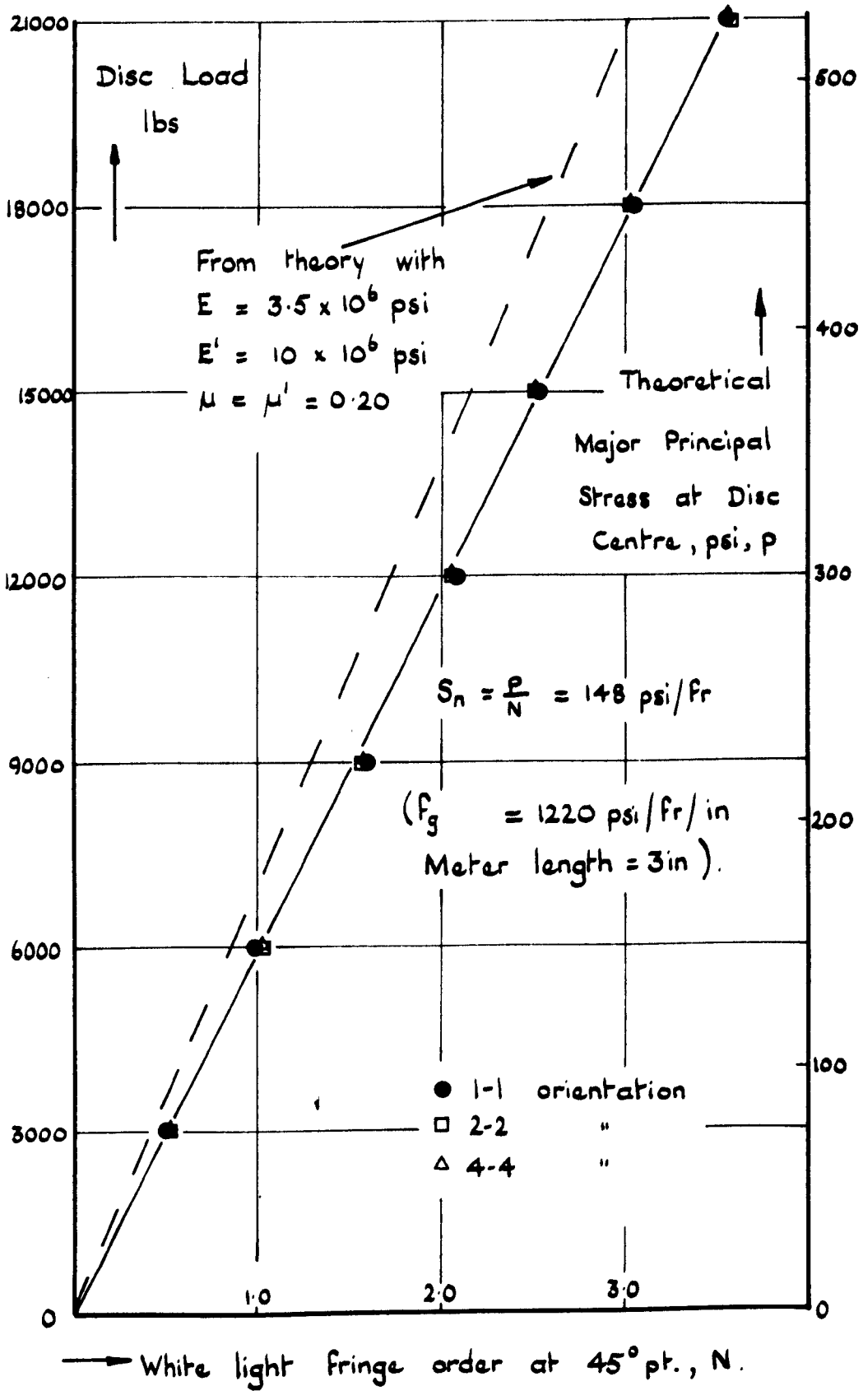

FIG. 4.24. Centre point annular stressmeter - 3 orientations of disc F5-1.

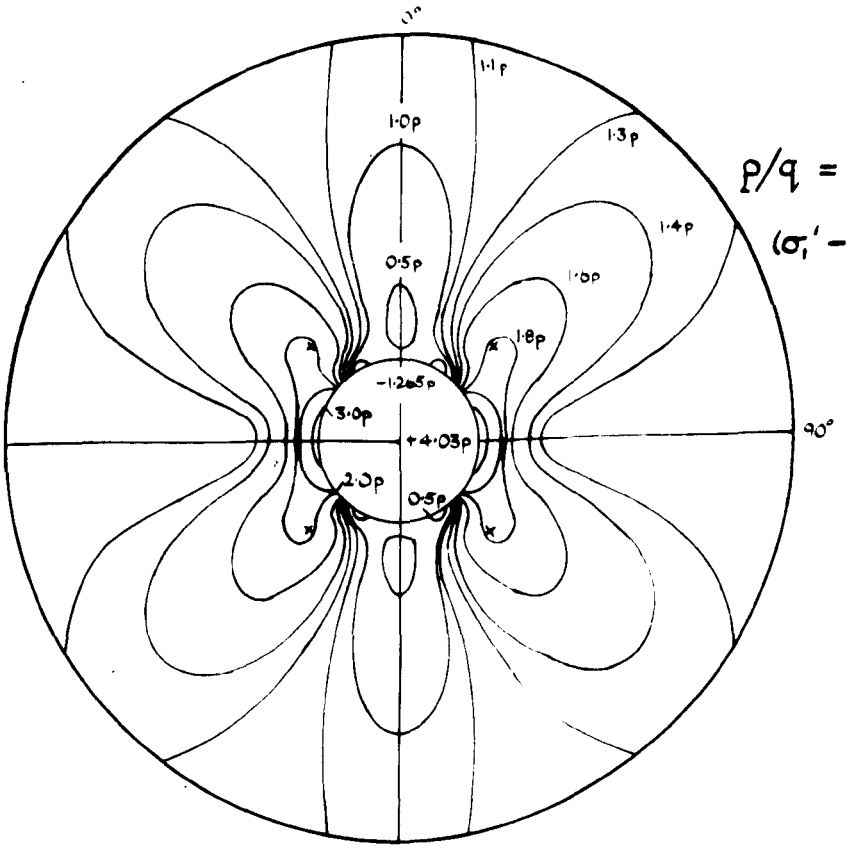

p/q = 1:0

$(\sigma_1' - \sigma_2')_x = 1{\cdot}83p$

$E = 3{\cdot}5 \times 10^6$ psi

$E' = 10 \times 10^6$ psi

$\mu = \mu' = 0{\cdot}20$

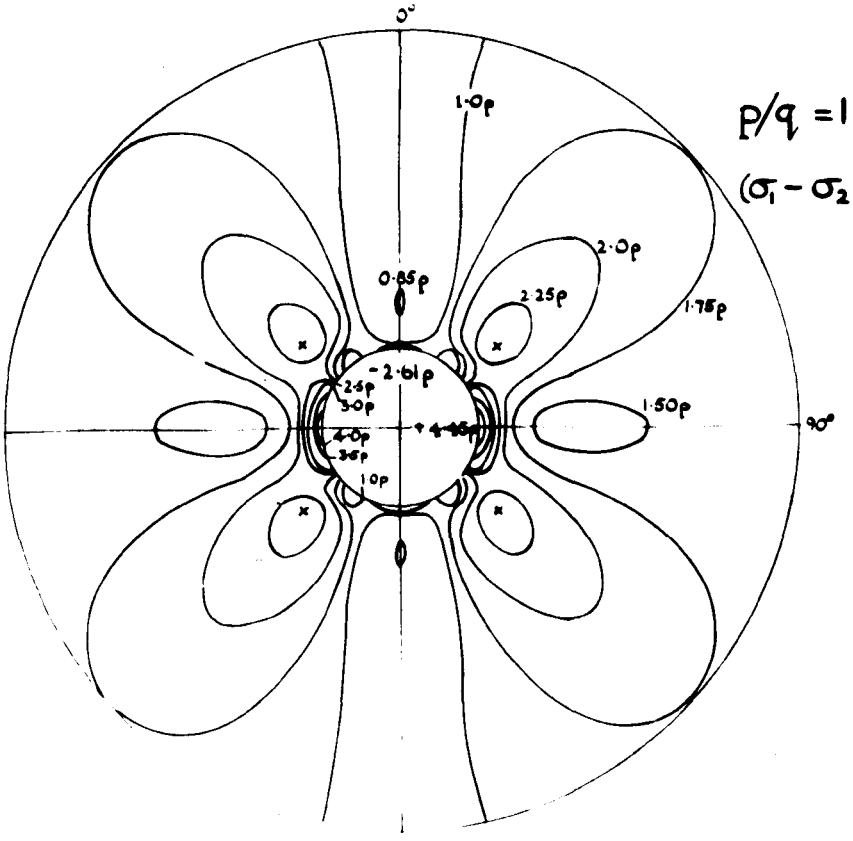

p/q = 1:−⅓

$(\sigma_1 - \sigma_2)_x = 2{\cdot}36p$

Fig. 4·25 Computed isochromatic patterns for annular stressmeter

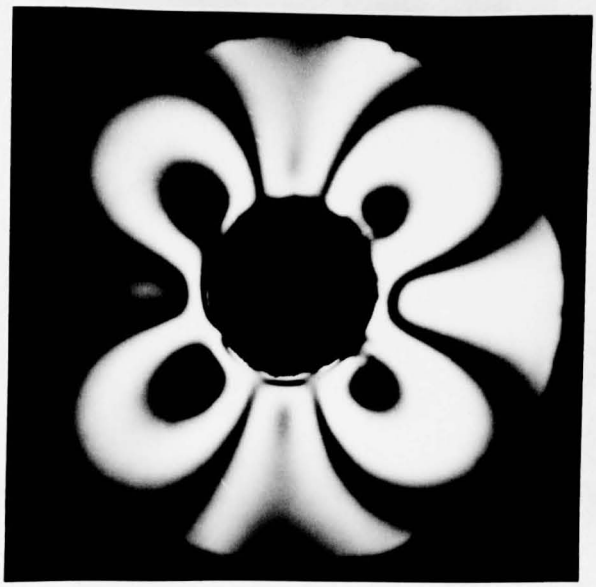

Centre Point Stressmeter

Disc Load = 21,000 lbs.

Calculated Disc Stresses:

p = +525 p.s.i.
q = -175 p.s.i.

Mean Fringe Order at "45° Points" =+3.55

Glass Fringe Value f_g = 1230 p.s.i./fr./in.

Glass Length l_g = 3.0 in.

Nom. Radius Ratio $\frac{a}{b}$ = 5.0

Adhesive Thicksess $\frac{a}{10}$

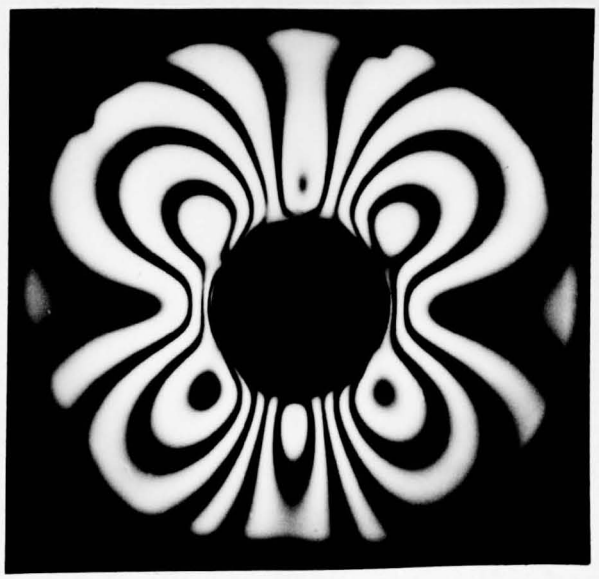

Stressmeter Near Loading Arc (M2)

Disc Load = 18,000 lbs.

Calculated Disc Stresses:

p = + 1170 p.s.i.
q = - 175 p.s.i.

Mean Fringe Orders:

Upper "45° Points" = +6.62
Lower "45° Points" = +6.10

FIG. 4.26 Observed Annular Stressmeter Fringe Patterns, Disc F5-1, Orientation 1-1.

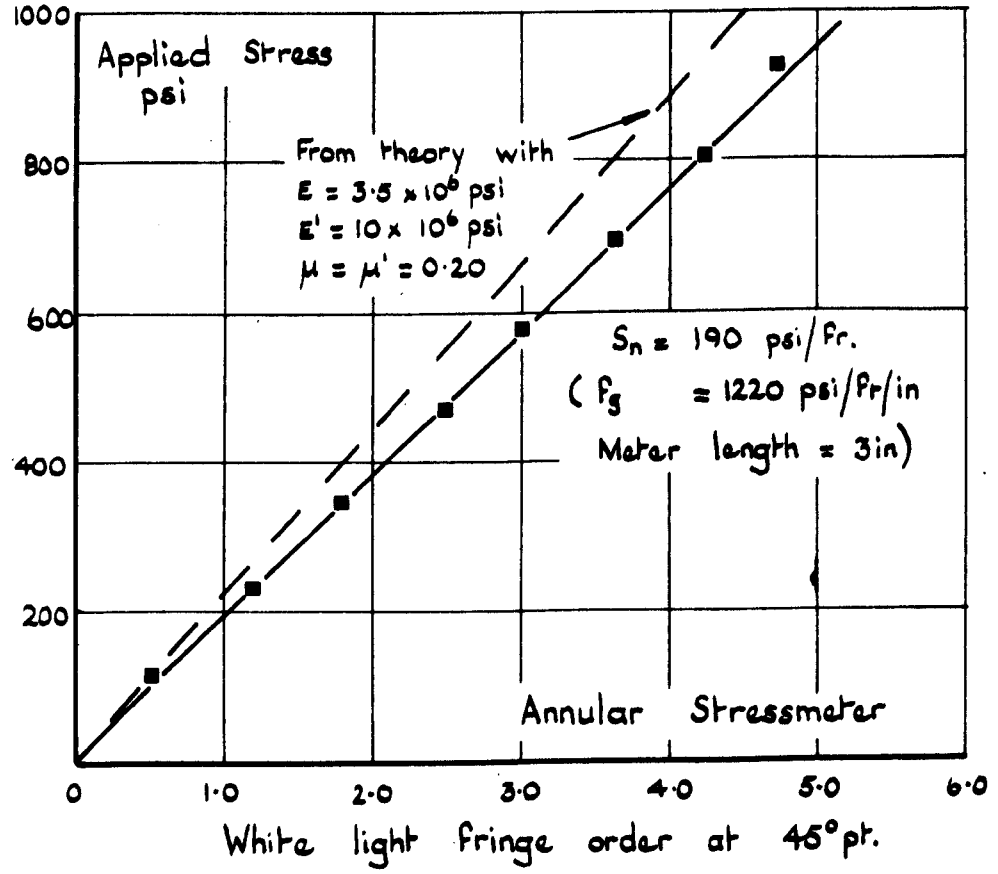

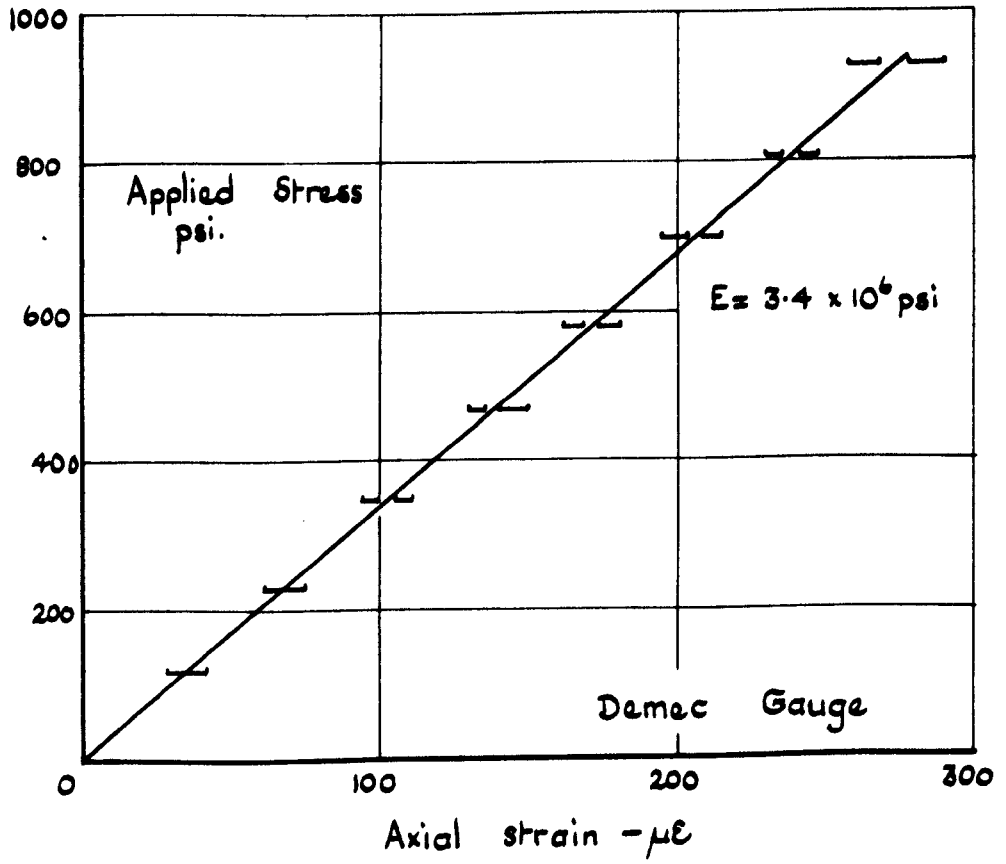

FIG. 4.27. Centre element from disc F5-1 -uniaxial compression

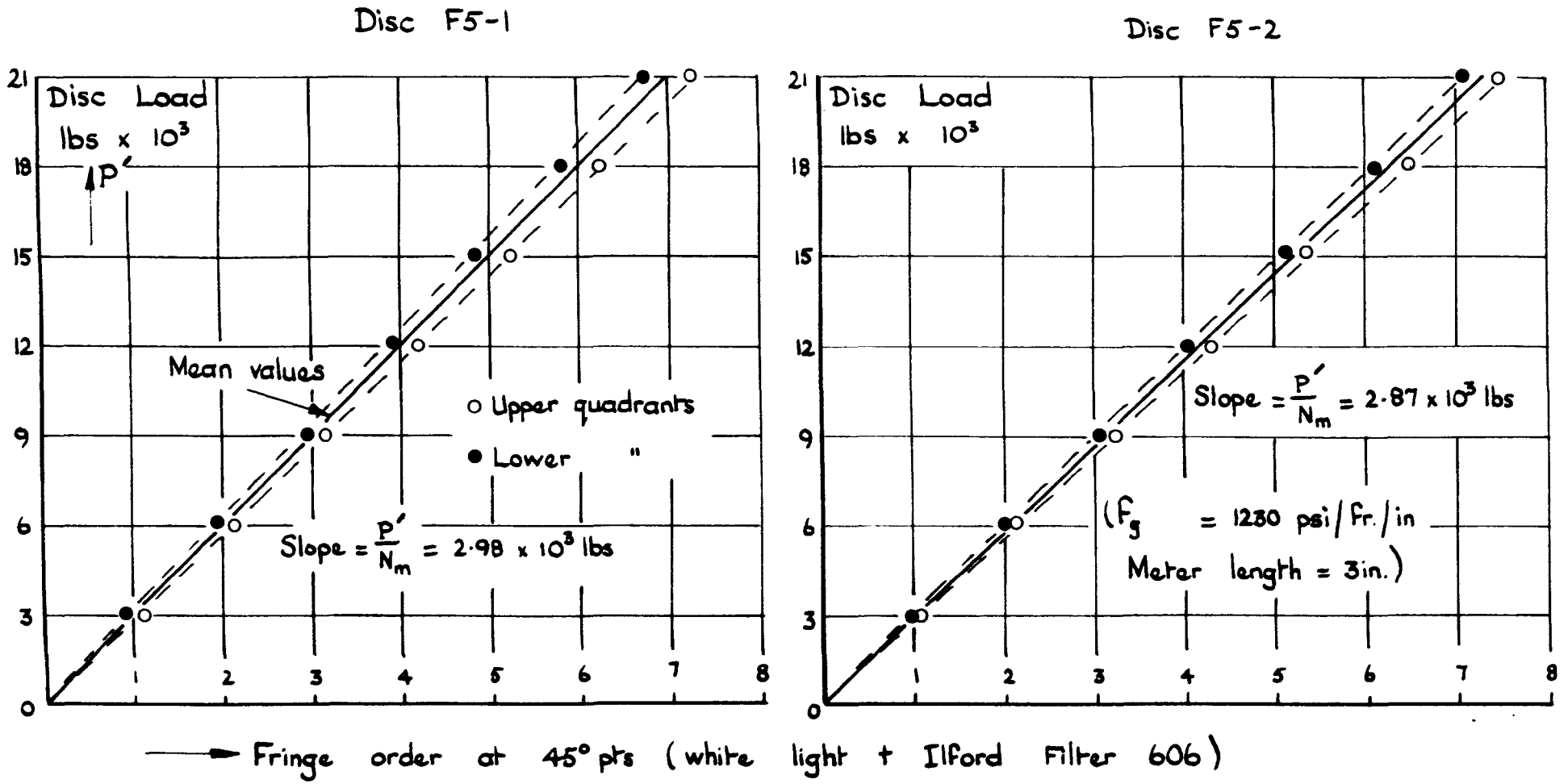

FIG. 4.28. Annular stressmeters – M2 position, 1-1 orientation discs F5-1 and F5-2

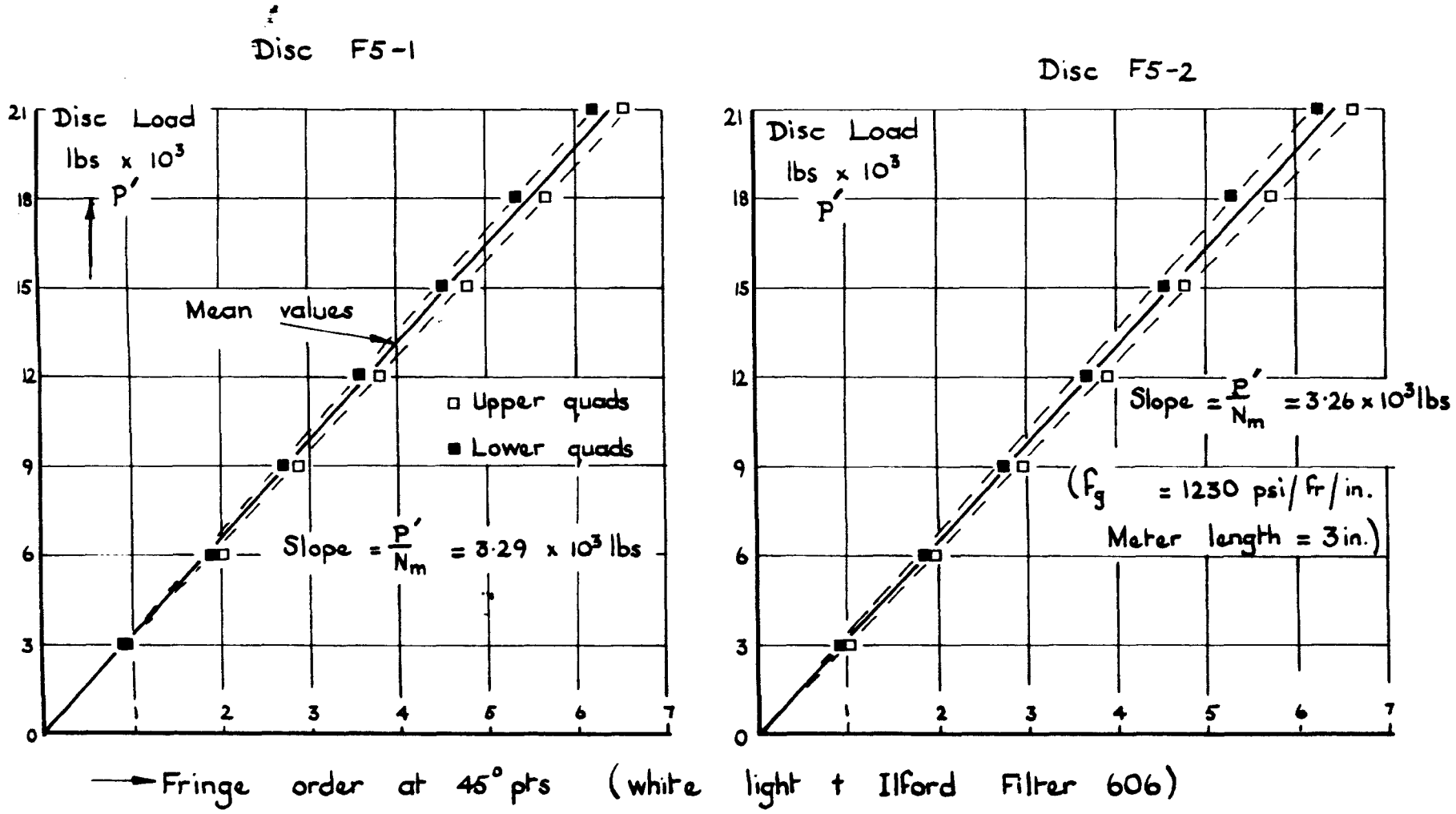

FIG. 4.29. Annular stressmeters – M3 position, 4-4 orientation discs F5-1 and F5-2.

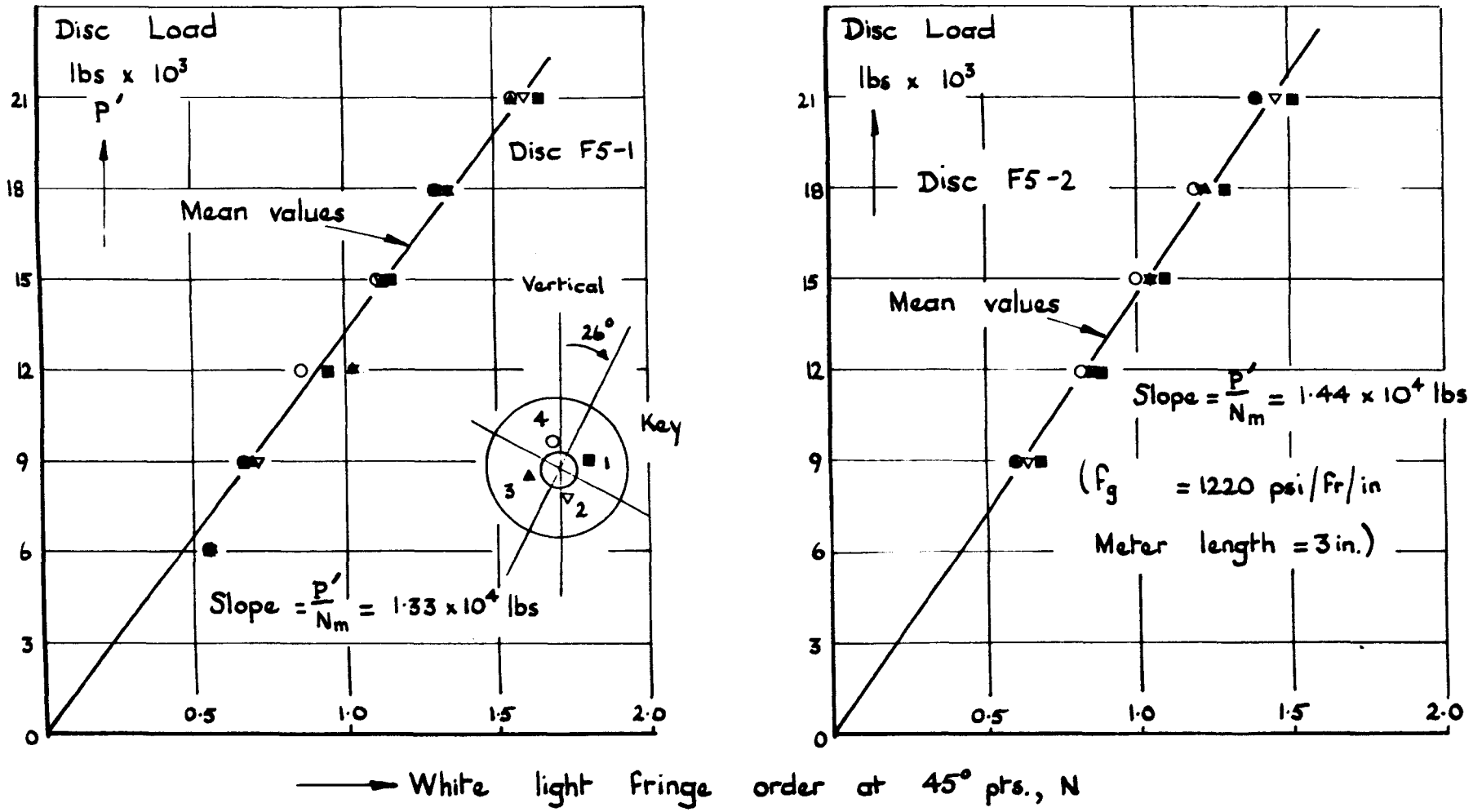

FIG. 4.30 Annular stressmeters – M3 position, 1-1 orientation, discs F5-1 and F5-2

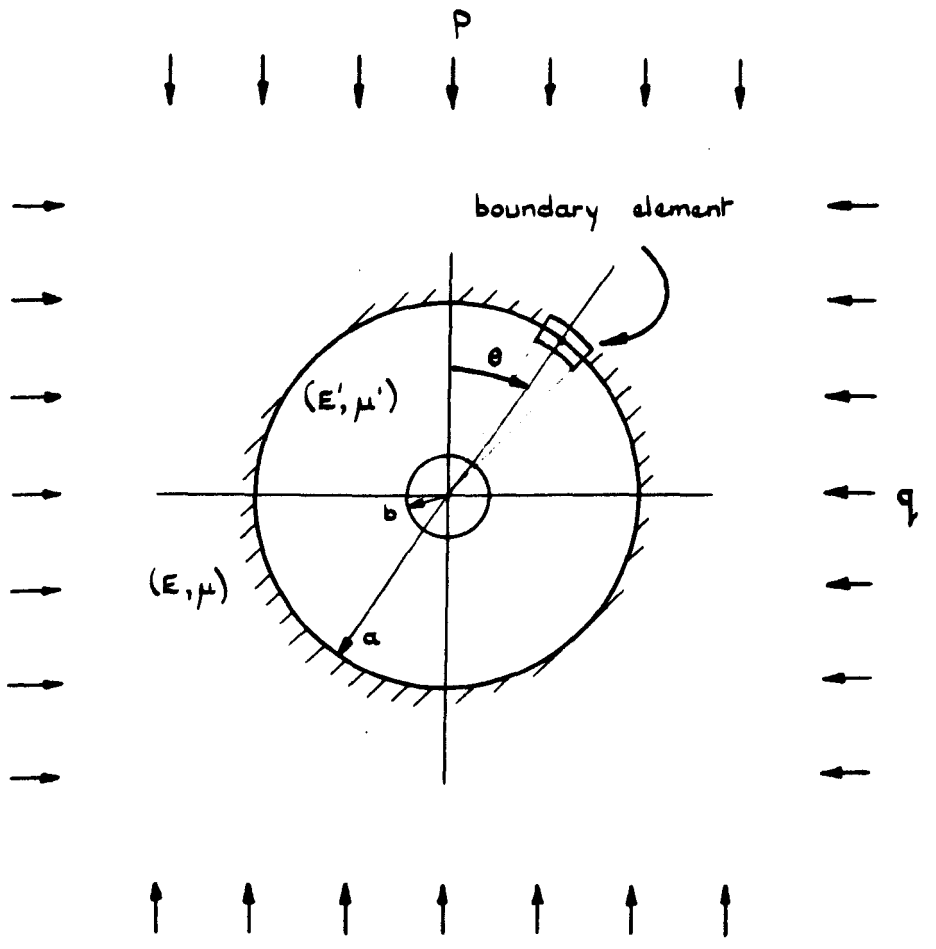

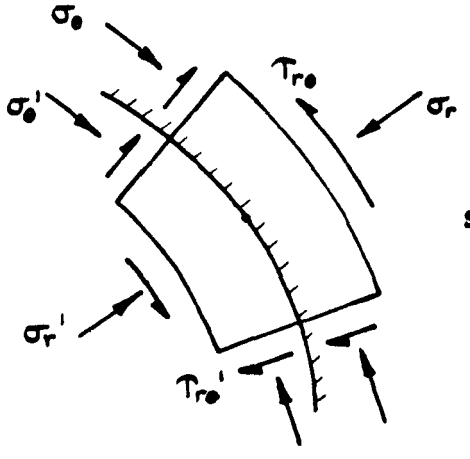

boundary element stress components

Condition	Equalities at (r = a) (Ignoring out-of-plane restraints)
"Welded" boundary	$\sigma_r = \sigma_r'$, $\tau_{r\theta} = \tau_{r\theta}'$, $\varepsilon_\theta = \varepsilon_\theta'$, $\mu_r = \mu_r'$, $\mu_\theta = \mu_\theta'$ $\sigma_z = \sigma_z' = 0$, $\tau_{rz} = \tau_{rz}' = 0$, $\tau_{\theta z} = \tau_{\theta z}' = 0$
"Exact fit" boundary	$\sigma_r = \sigma_r'$ $\tau_{r\theta} = \tau_{r\theta}' = 0$ $u_r = u_r'$ $\sigma_z = \sigma_z' = 0$ $\tau_{rz} = \tau_{rz}' = 0$ $\tau_{\theta z} = \tau_{\theta z}' = 0$

FIG. 5.1. Generalised plane stress boundary conditions

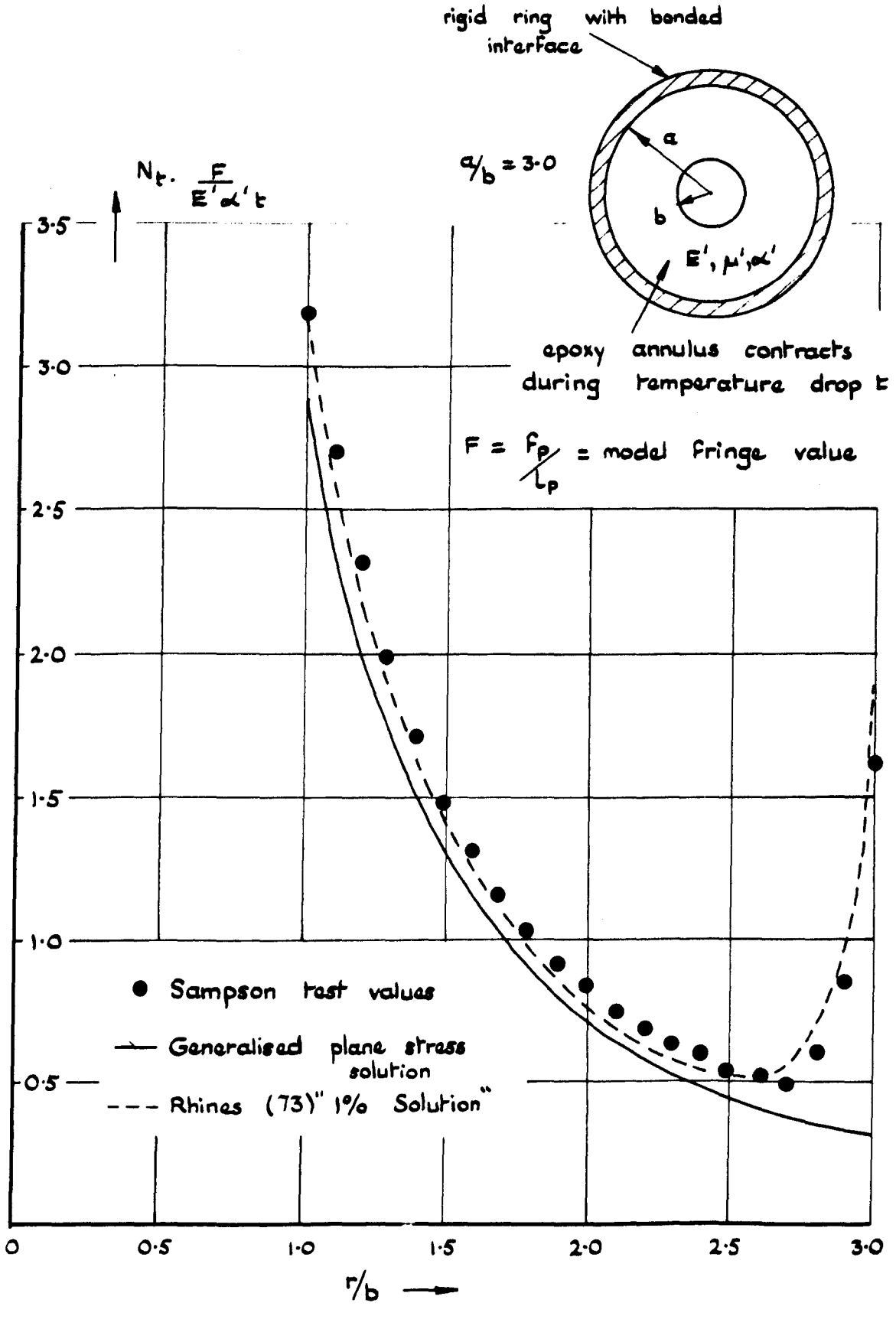

FIG. 5.2. Dimensionless fringe order distribution in epoxy annulus during restrained thermal shrinkage [after Sampson (72)]

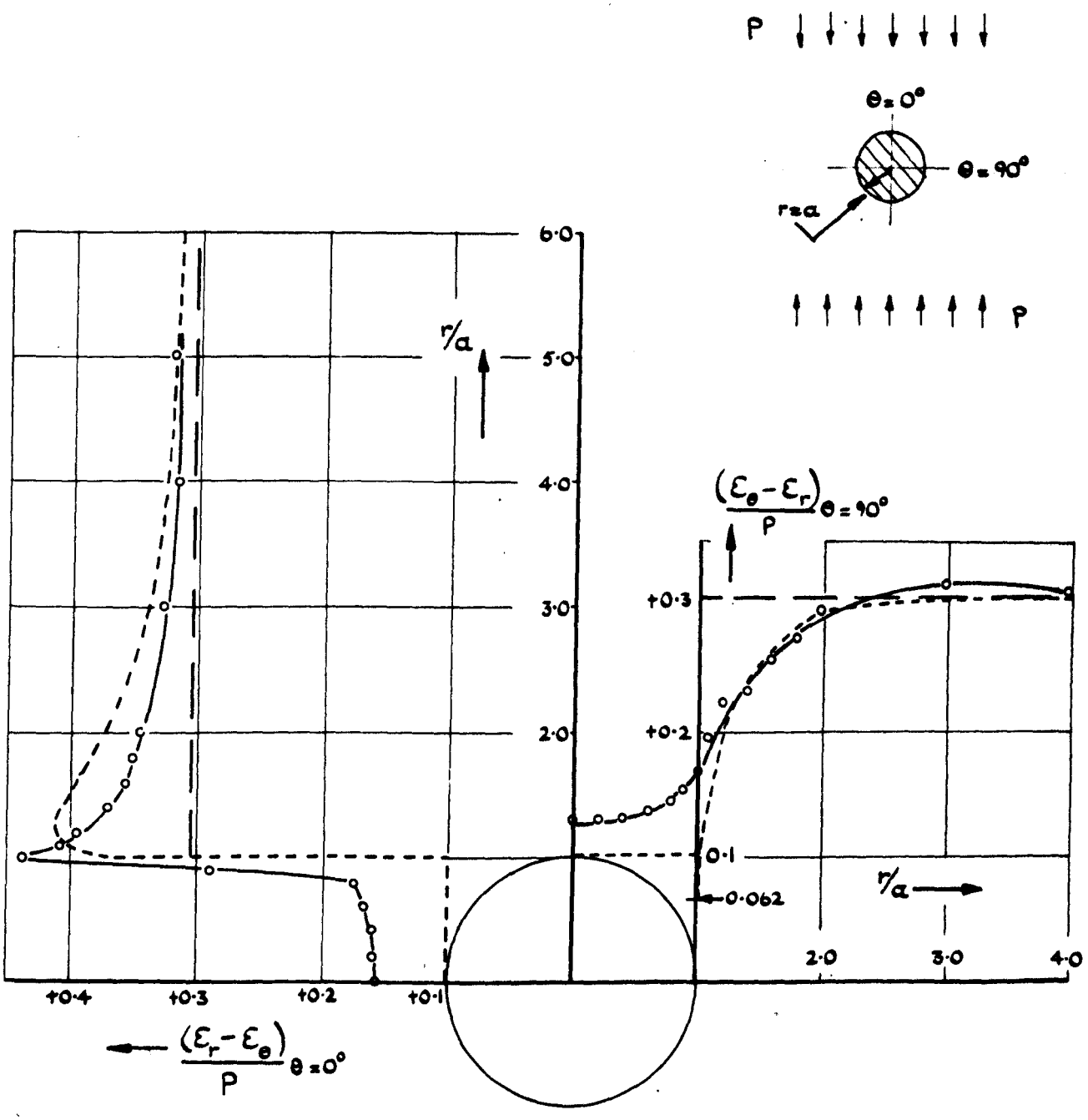

——o—— Results from photoelastic coating (p = 1000 psi)

- - - - - Calculated distribution

—— —— Applied principal strain difference

Host material : $E = 3{\cdot}8 \times 10^6$ psi , $\mu = 0{\cdot}16$

Copper inclusion : $E' = 16{\cdot}7 \times 10^6$ psi , $\mu' = 0{\cdot}33$

FIG. 5.3. Principal strain differences along principal axes on and around solid copper inclusion.

[after Stephen and Pirtz (74)]

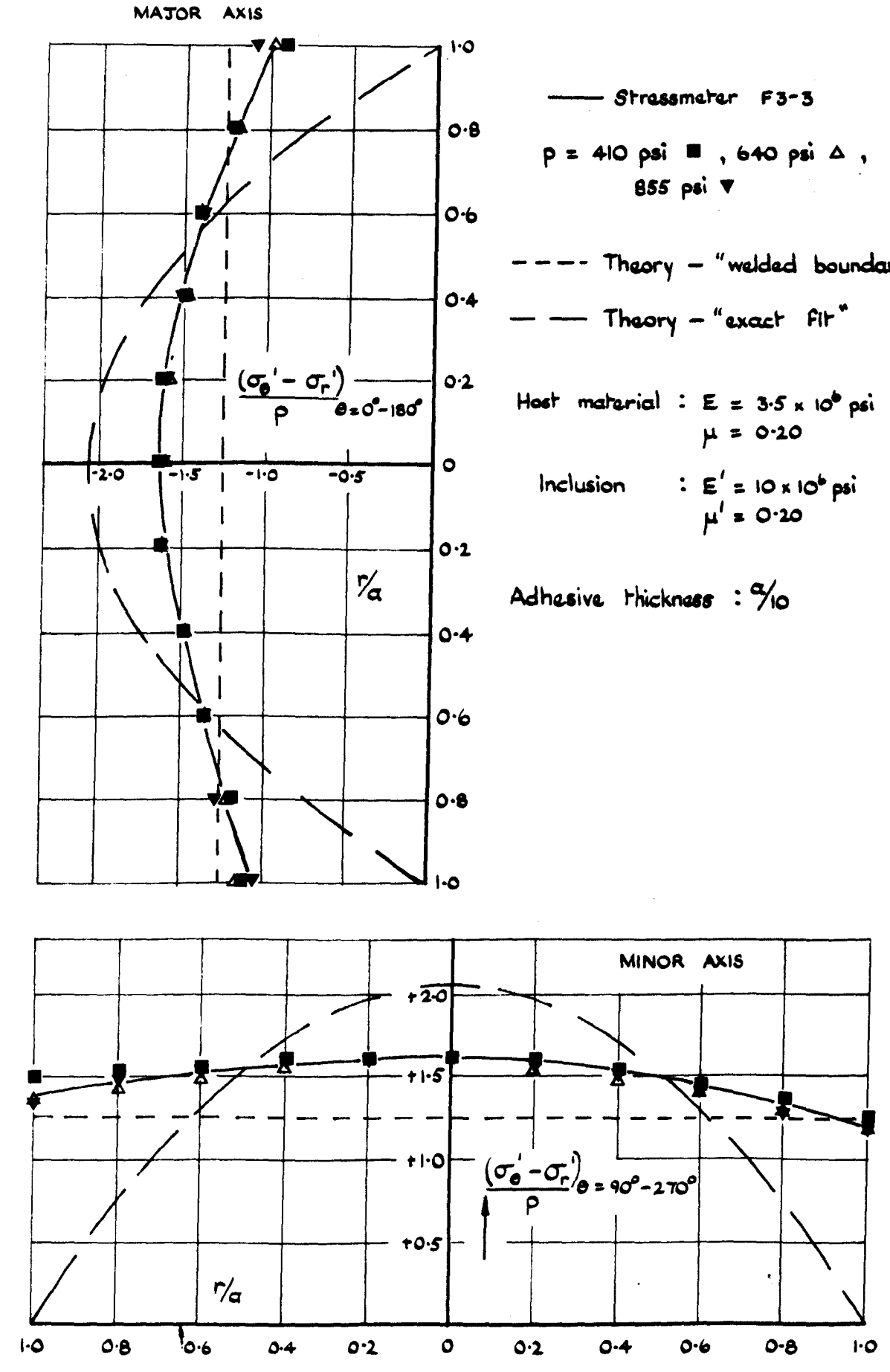

FIG. 5.4. Principal stress differences along principal axes solid stressmeter, uniaxial compression

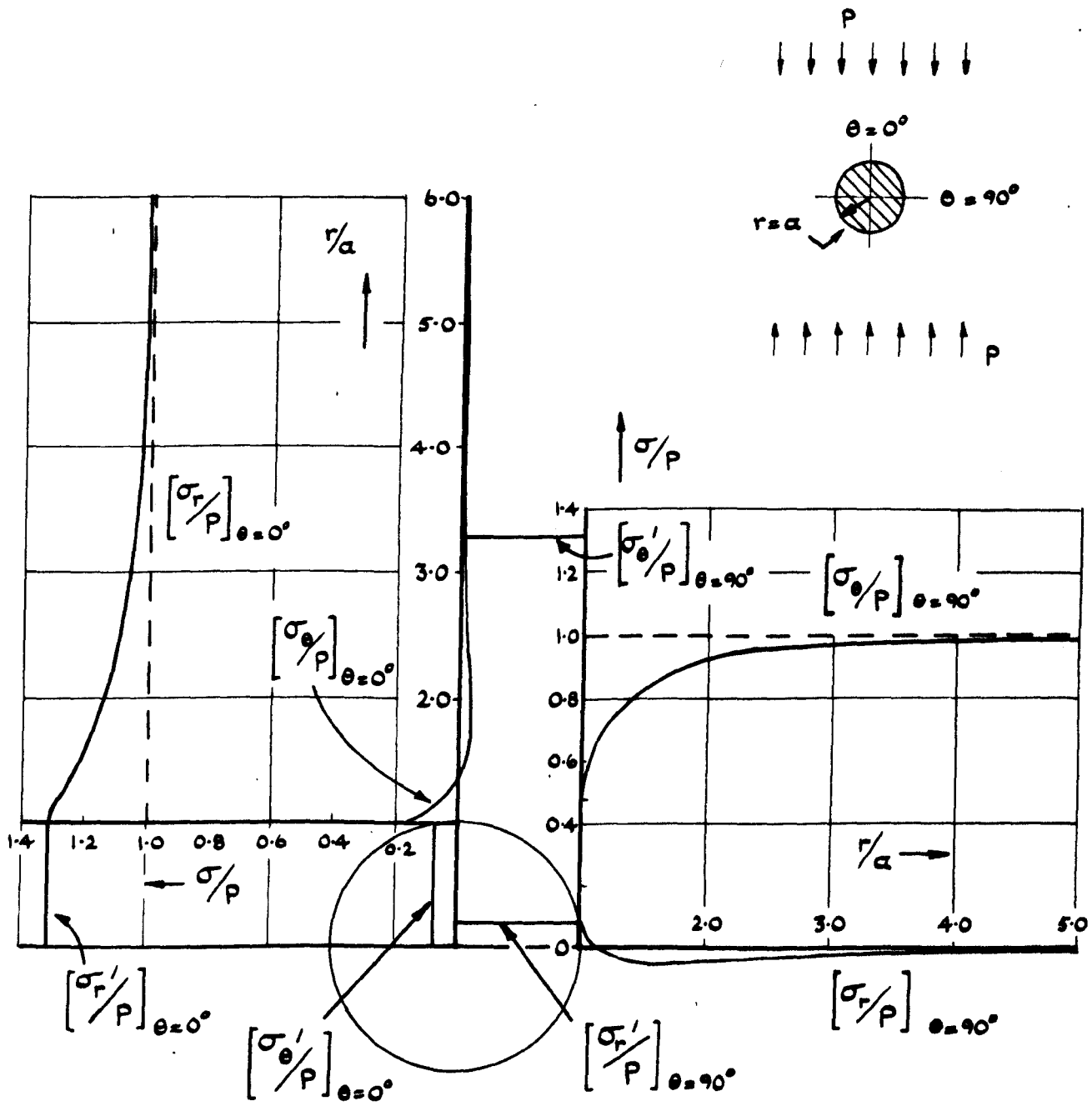

Host material : $E = 3.5 \times 10^6$ psi , $\mu = 0.18$

Glass inclusion : $E' = 10 \times 10^6$ psi , $\mu' = 0.24$

FIG. 5.5. Solid inclusion and host stresses along principal axes — uniaxial compression. (welded boundary, generalised plane stress)

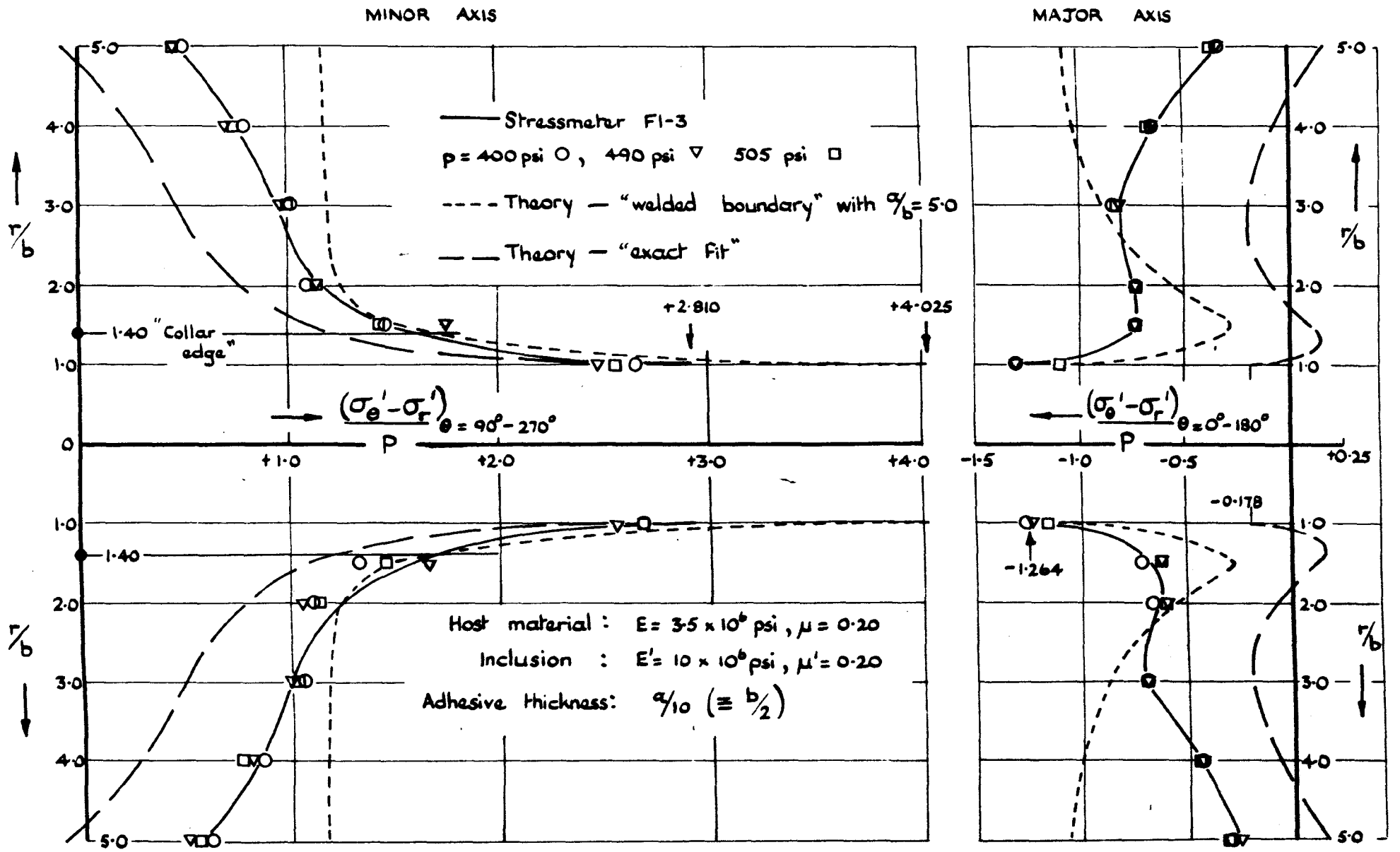

FIG. 5.6 Principal stress differences along principal axes — annular stressmeter, uniaxial compression.

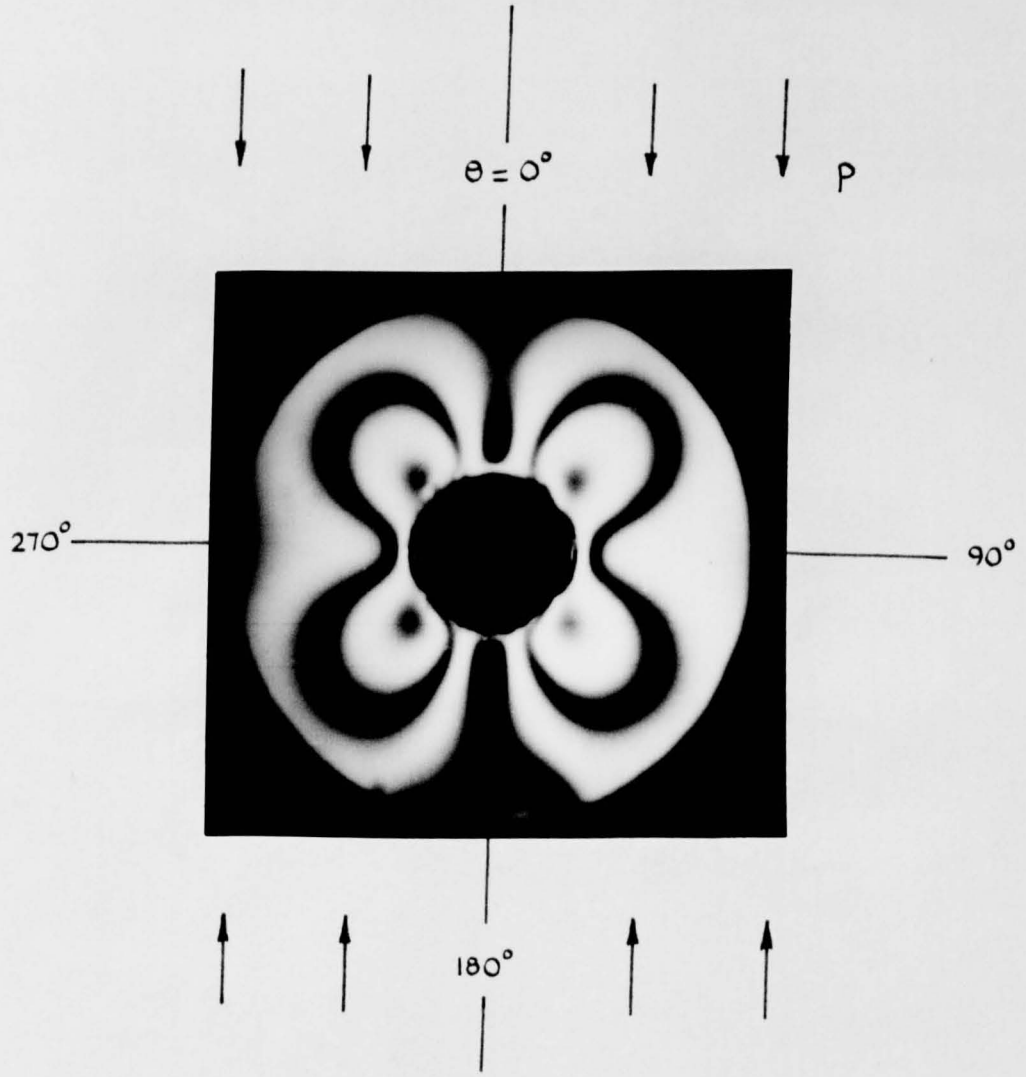

P = + 570 psi

$N_{(45° pt)}$ = + 3·07

f_g = 1220 psi / fr / in

Annulus length, t_g = 3·0 in

Outer diameter, $2a$ = 1·25 in

Adhesive radial thickness = 0·1 a

FIG. 5.7. Annular stressmeter uniaxial fringe pattern specimen F1-3

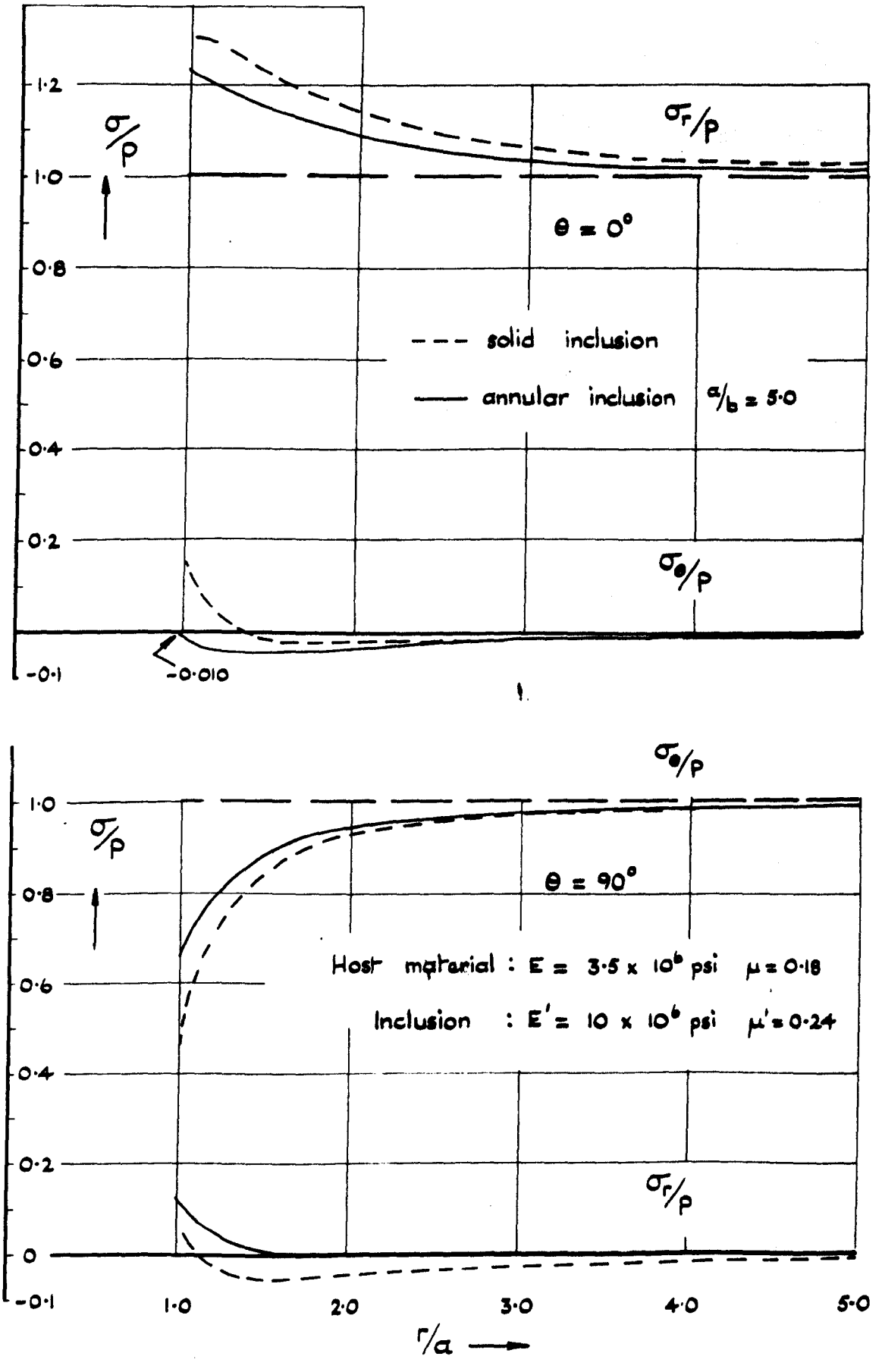

FIG. 5.8. Host stresses along principal axes for solid and annular inclusions — uniaxial compression

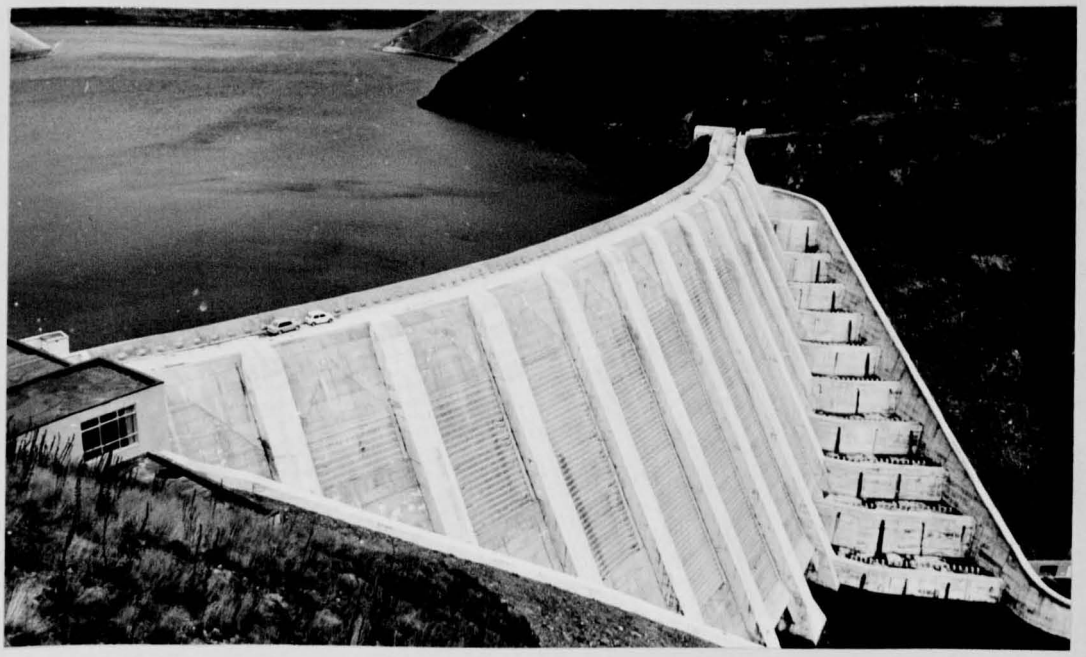

FIG. 6.1 Clywedog Dam

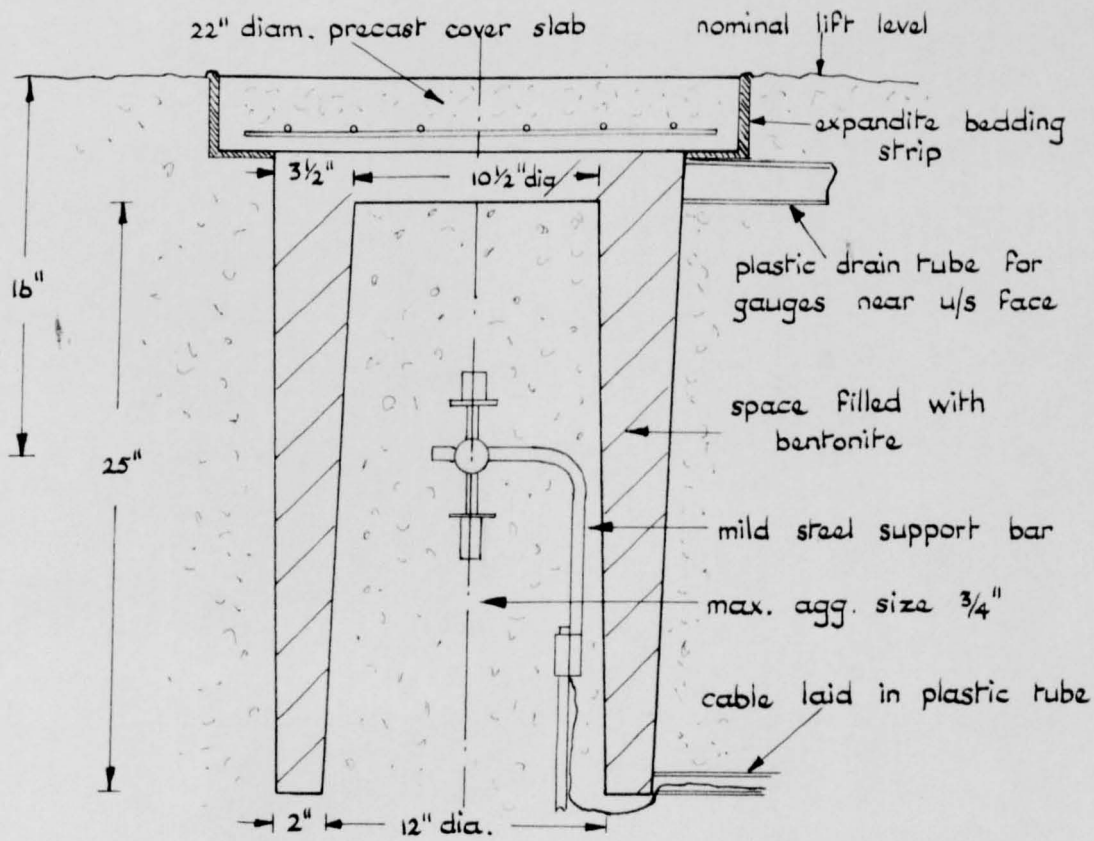

FIG. 6.2 Isolated sonic strain gauge

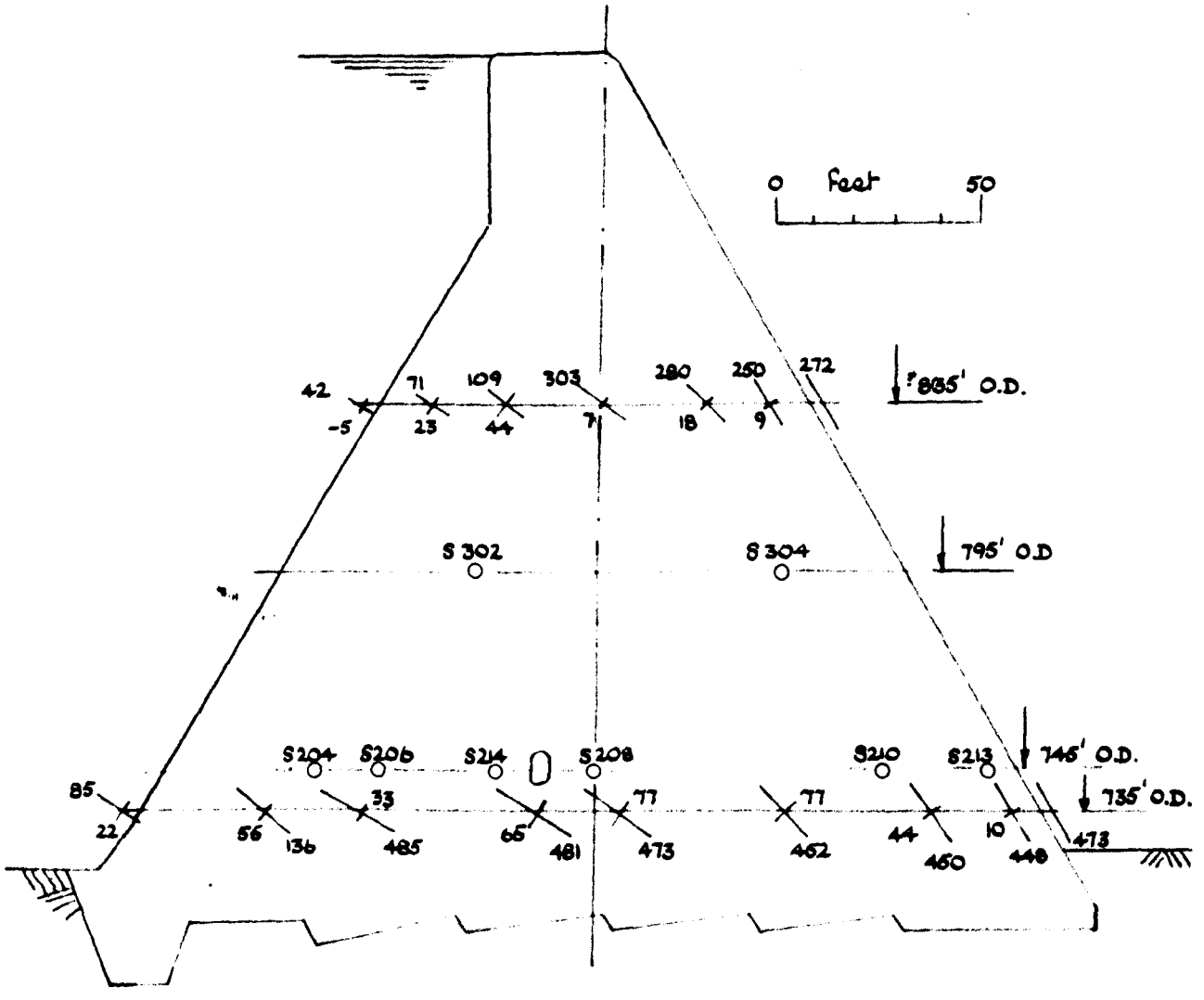

Stress units — p.s.i.

Condition : Flooding reservoir, Full uplift pressure

FIG. 6.3. Principal stresses at two levels from design calculation.

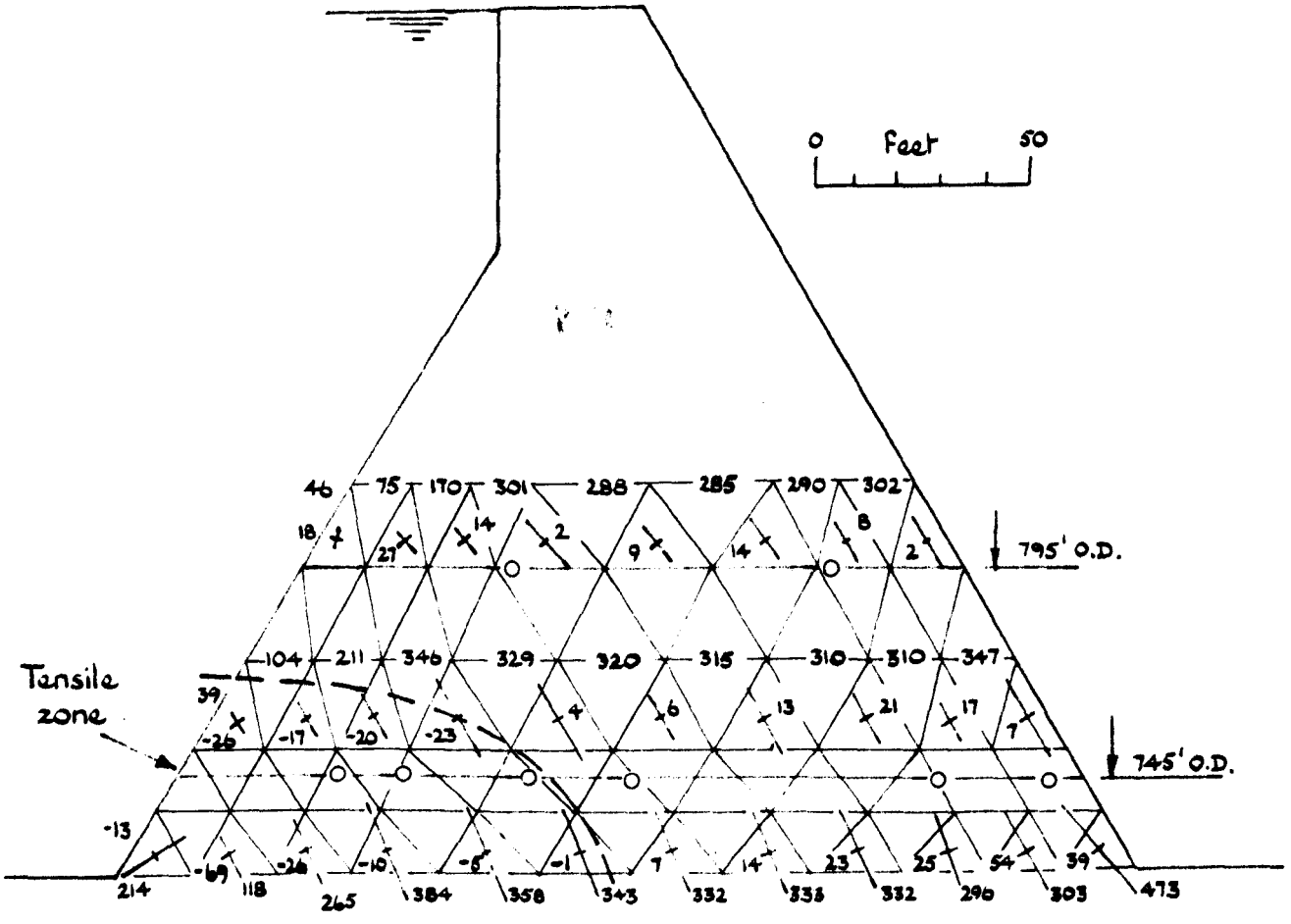

o Photoelastic stressmeter positions.

Tensile stresses shown by negative signs.

Upper buttress elements and foundation elements omitted for clarity.

Stress units – psi.

Condition : Flooding reservoir, pore pressure and gravity loadings, $E_f/E = 1/4$

FIG. 6.4. Principal stresses from finite element calculation. [after ref. (76)]

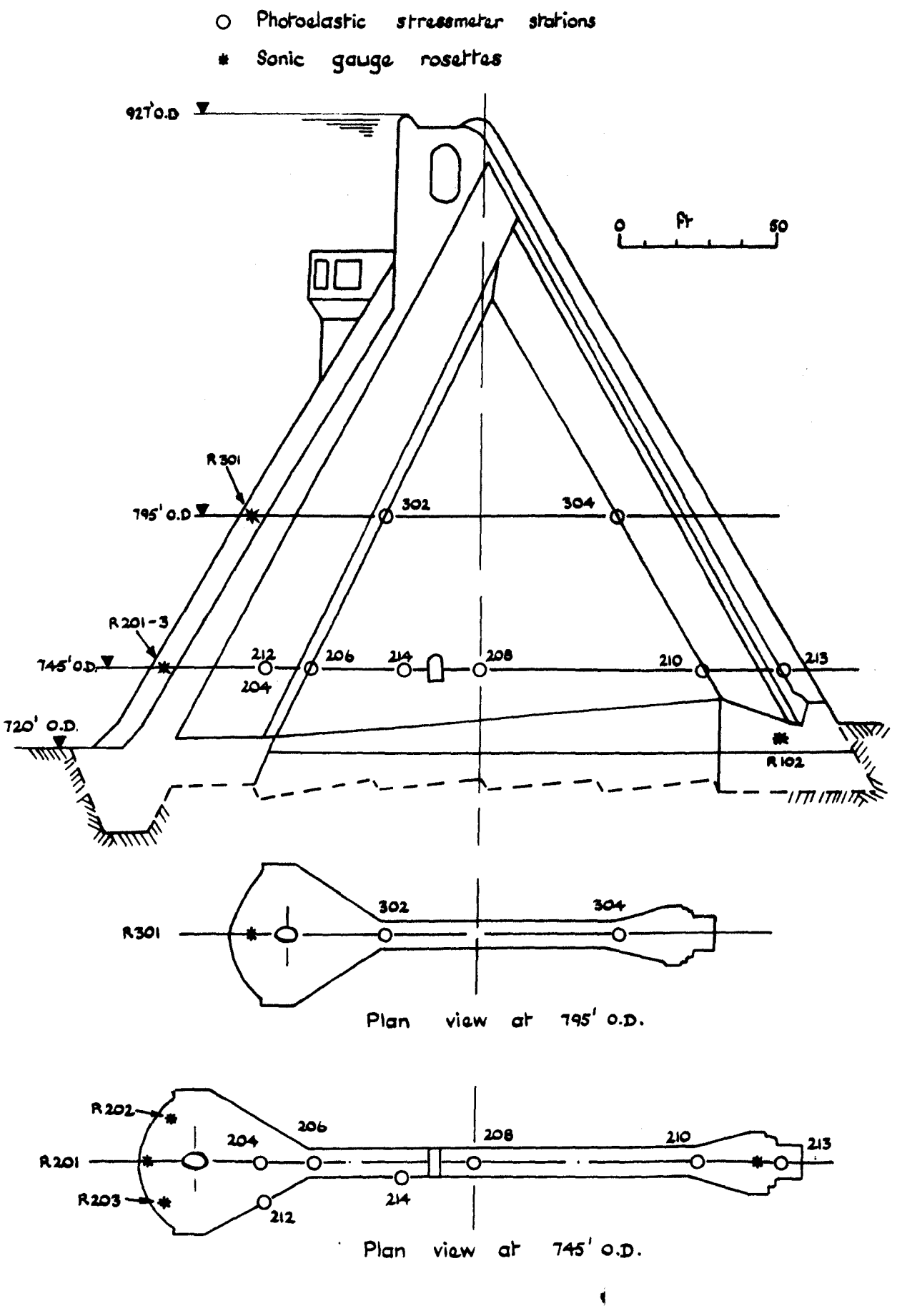

FIG. 6.5. Stressmeter and strain gauge positions west elevation

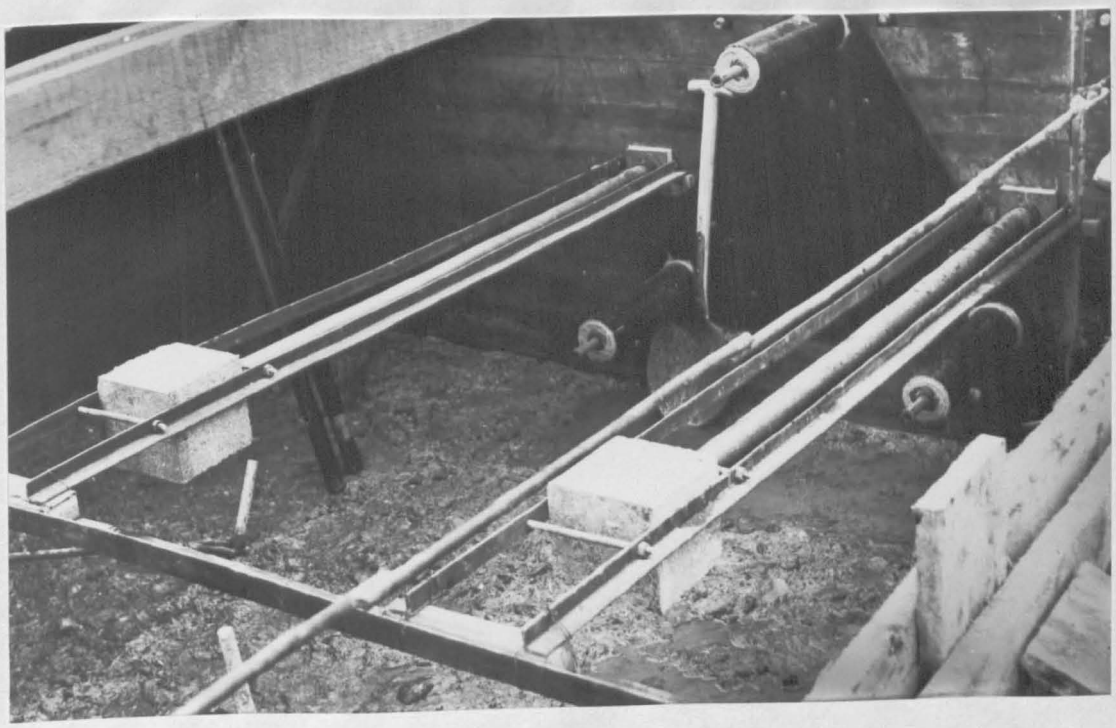

FIG. 6.6. Installation of Stressmeter Cubes

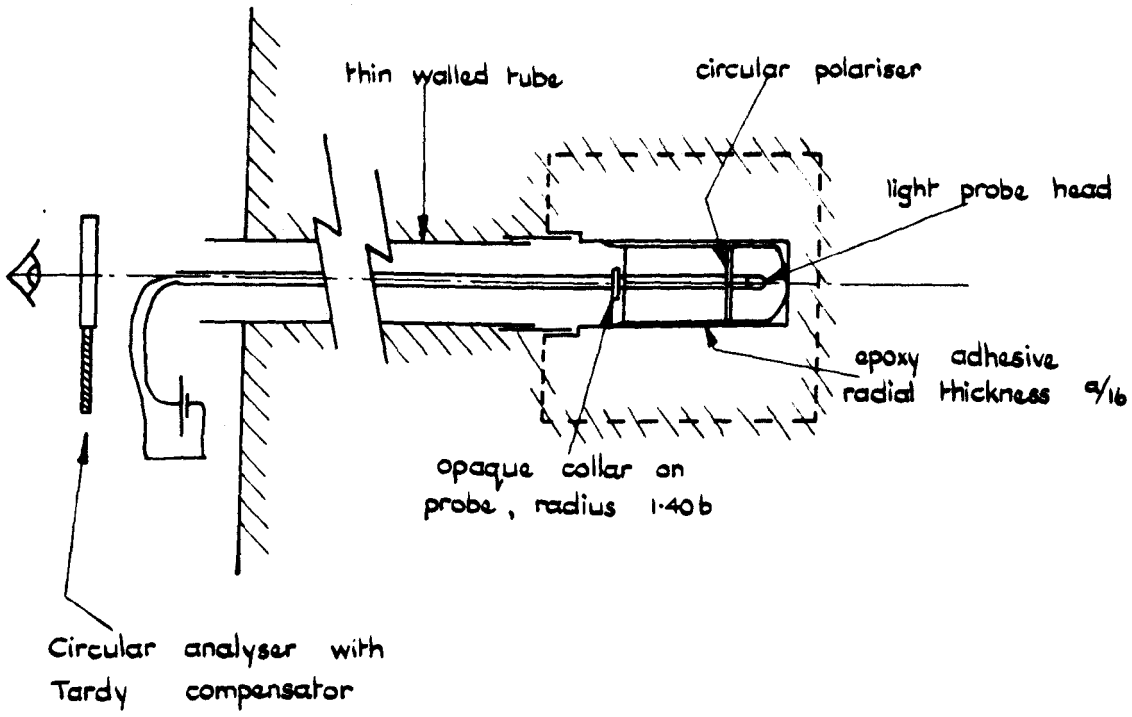

Annular Photoelastic Stressmeter

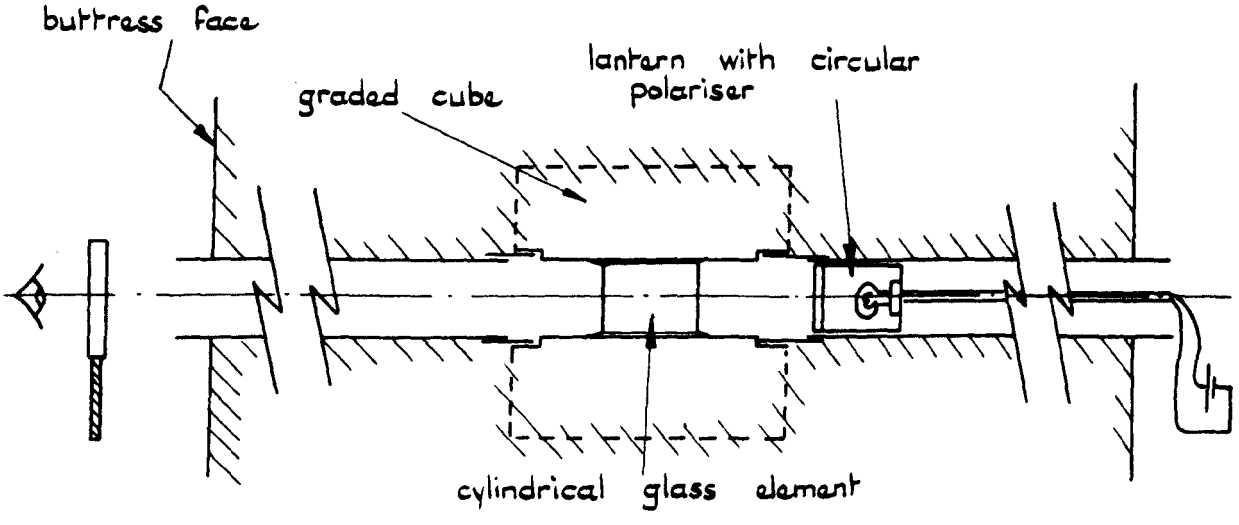

Solid Photoelastic Stressmeter

FIG. 6.7. Schematic details of stressmeter installation.

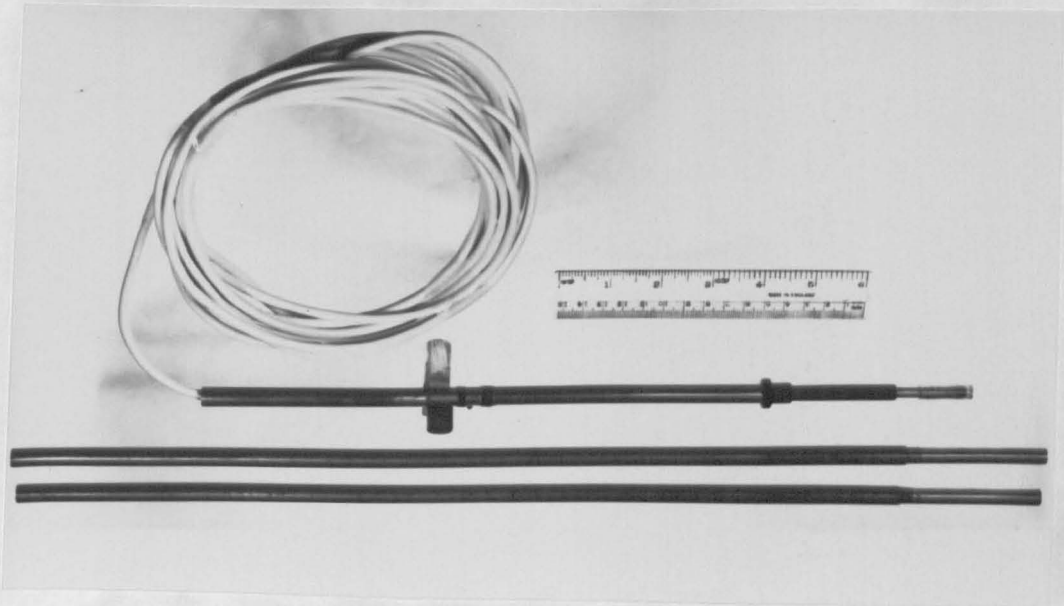

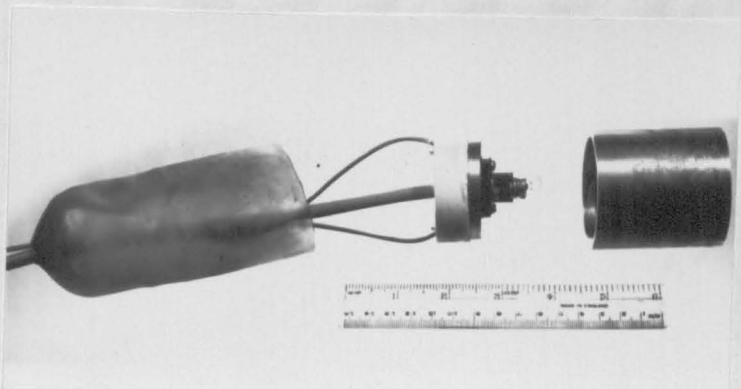

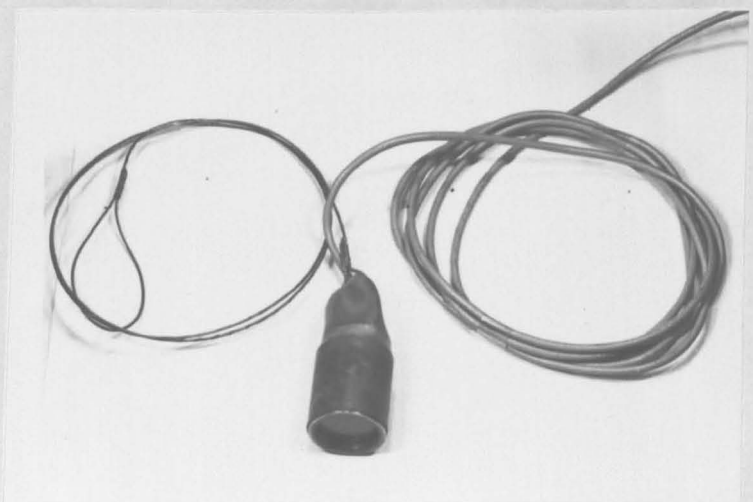

FIG. 6.8. Illumination Units for Annular and Solid Stressmeters.

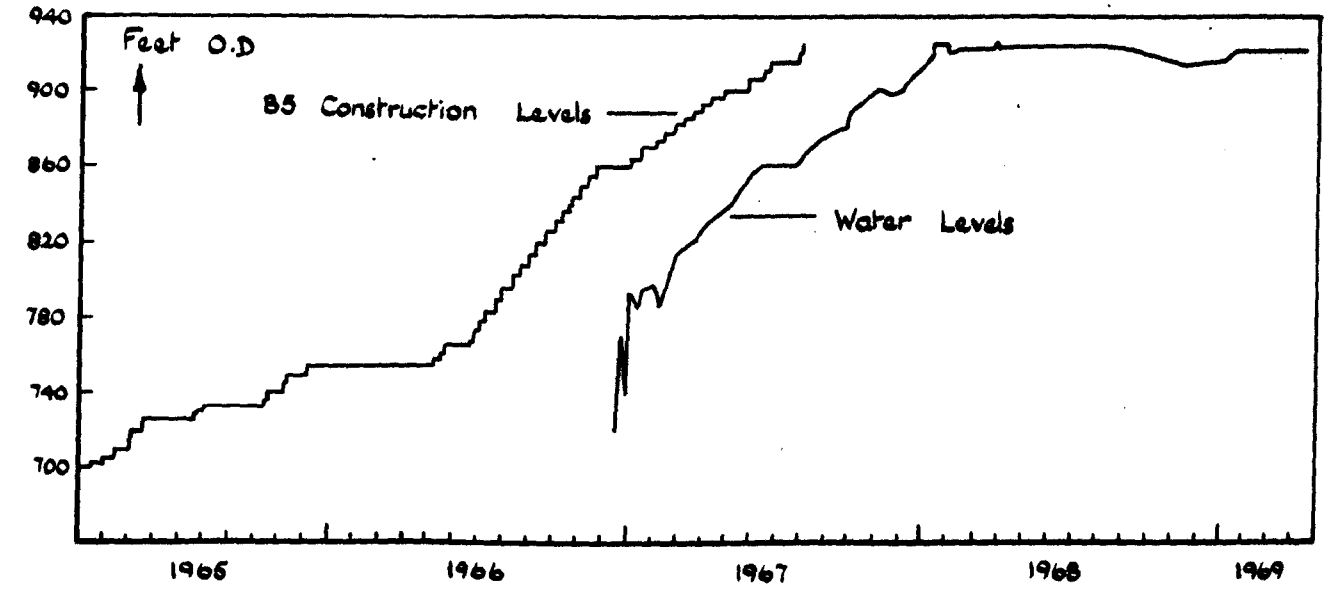

Stressmeter Constants

Length : 3·0 in. Outer Dia : 2·0 in. (a/b = 5·0)

f_g = 1220 psi/fr/in. Adhesive thickness : $a/16$

Measurement Points : r/b = 1·40 , θ = 90° & 270°

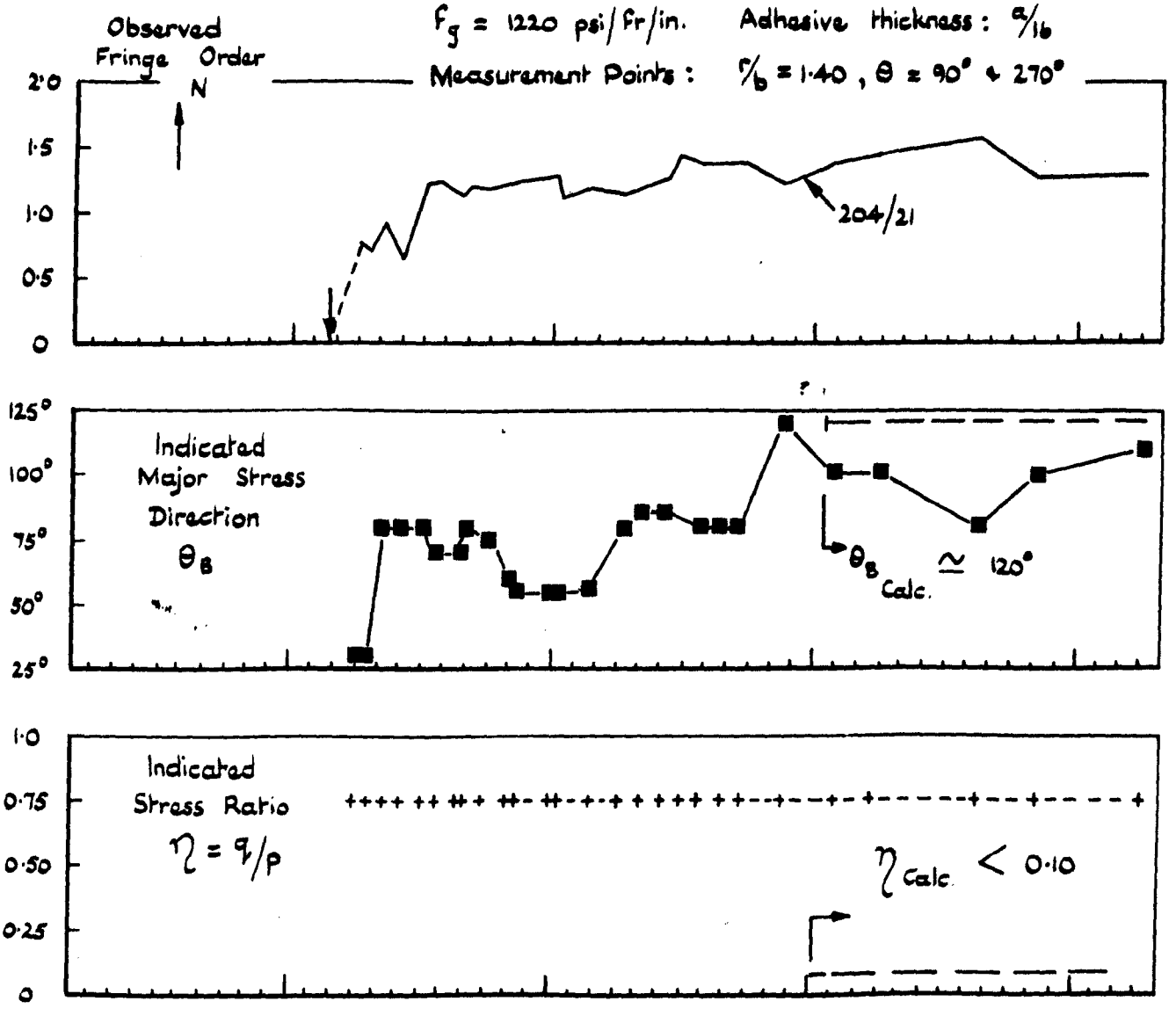

FIG. 6.9. Annular stressmeter readings , station 204.

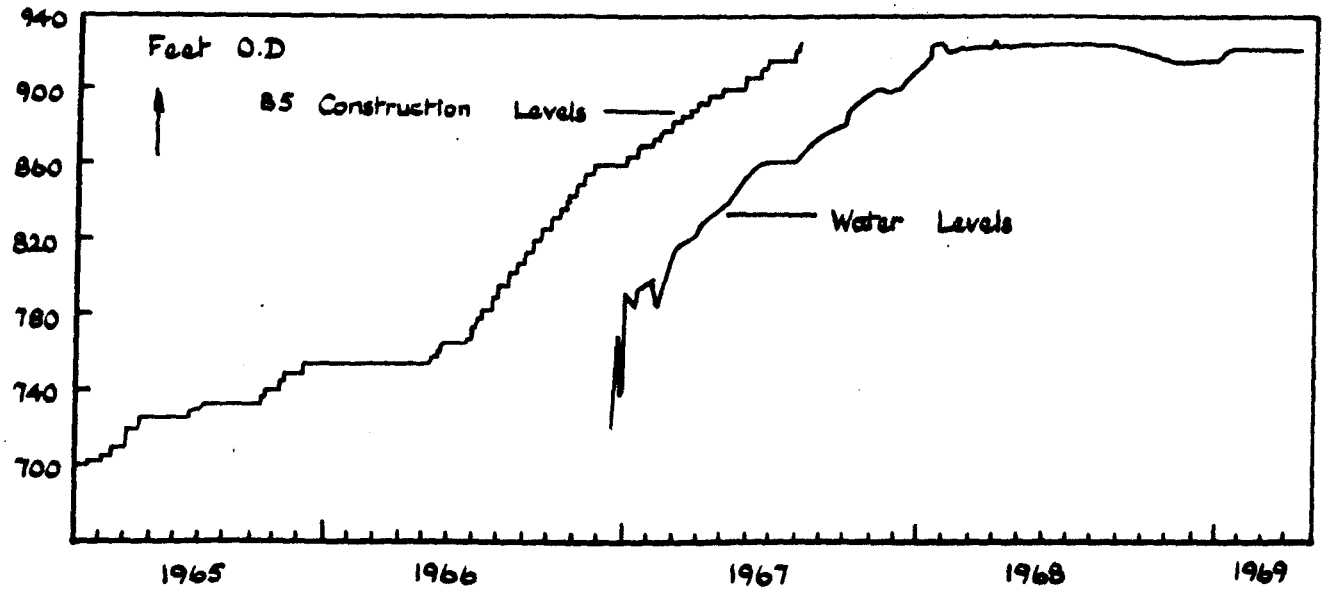

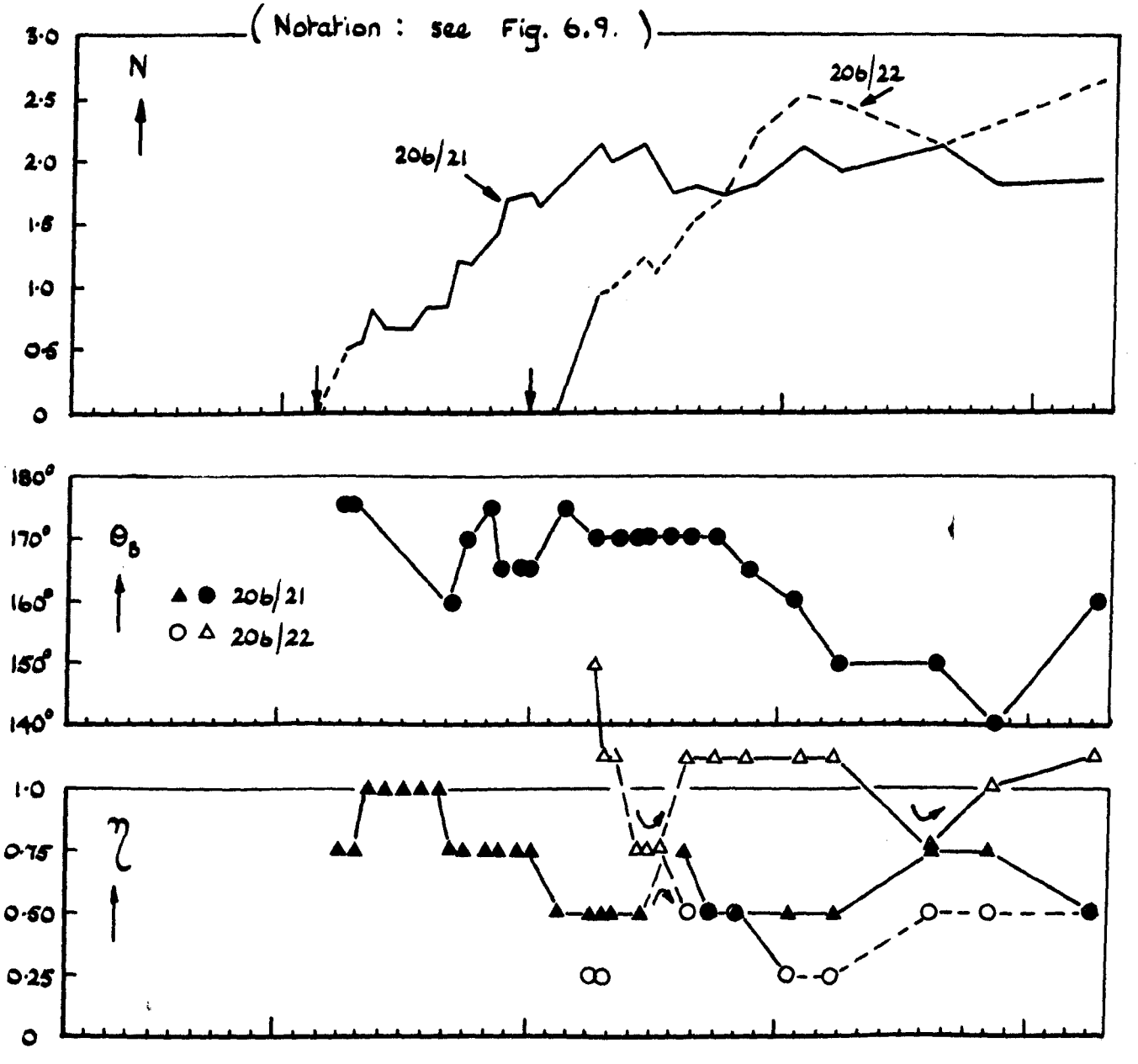

FIG. 6.10. Annular stressmeter readings, station 206

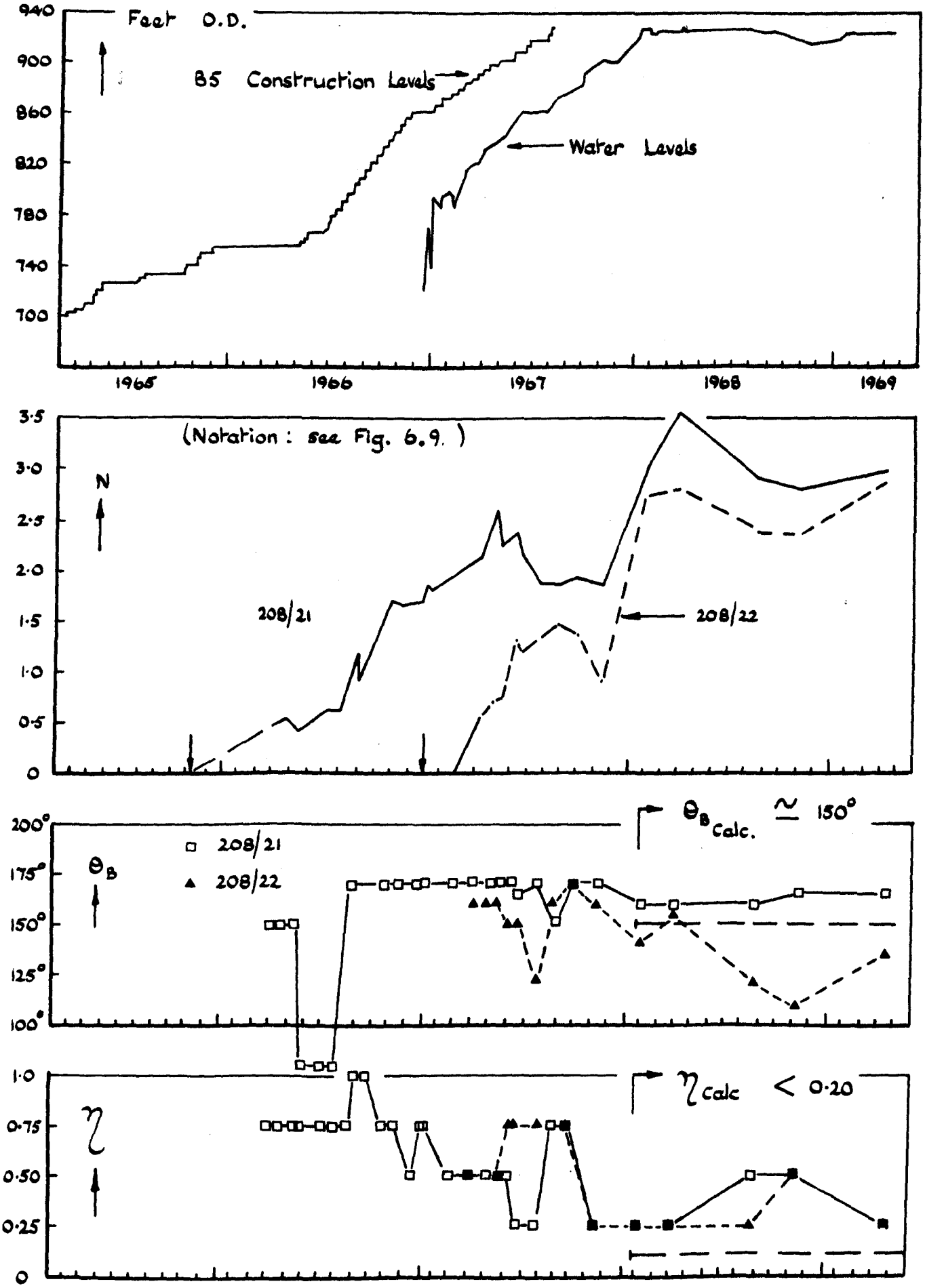

FIG. 6.11. Annular stressmeter readings, station 208.

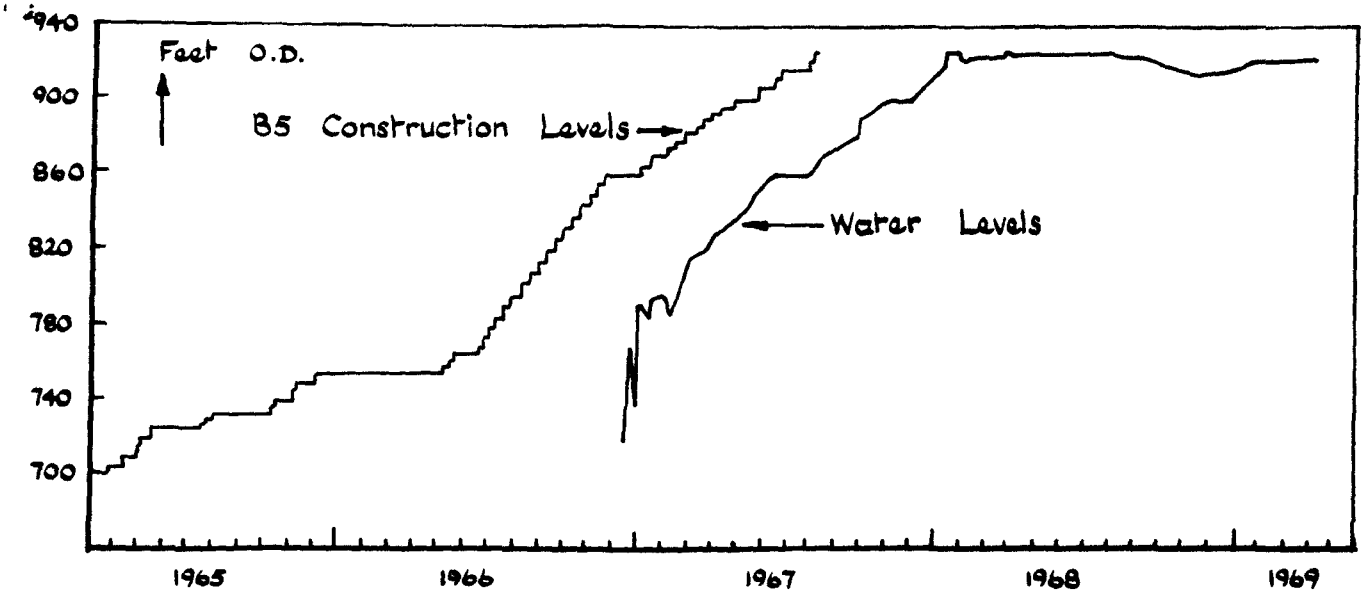

(Notation : see Fig. 6.9)

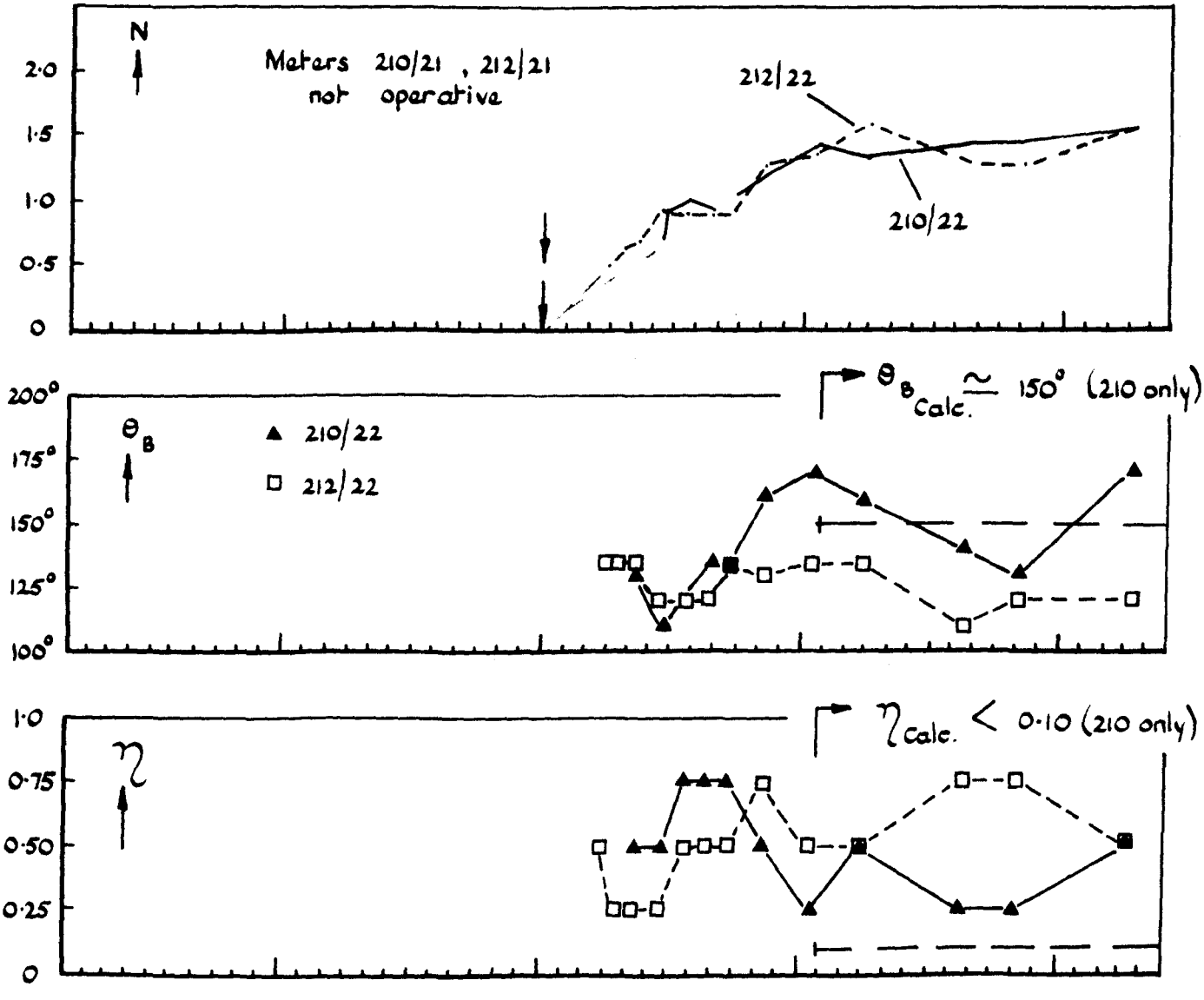

FIG. 6.12. Annular stressmeter readings , stations 210 , 212.

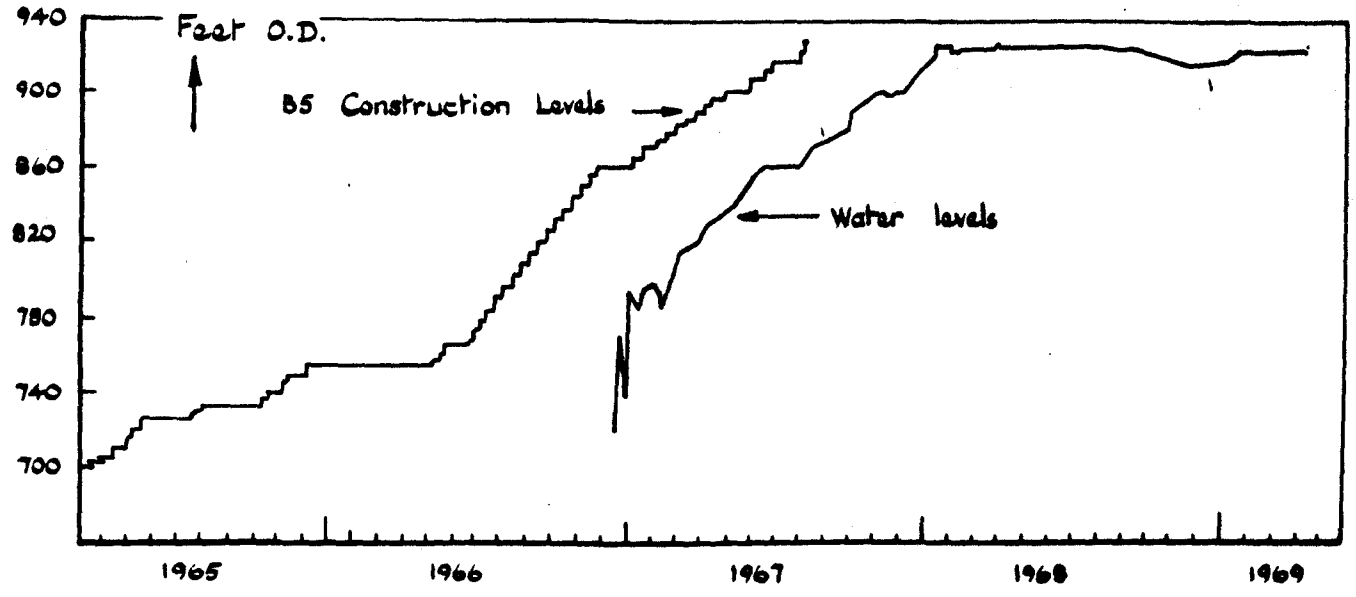

(Notation : see Fig. 6.9.)

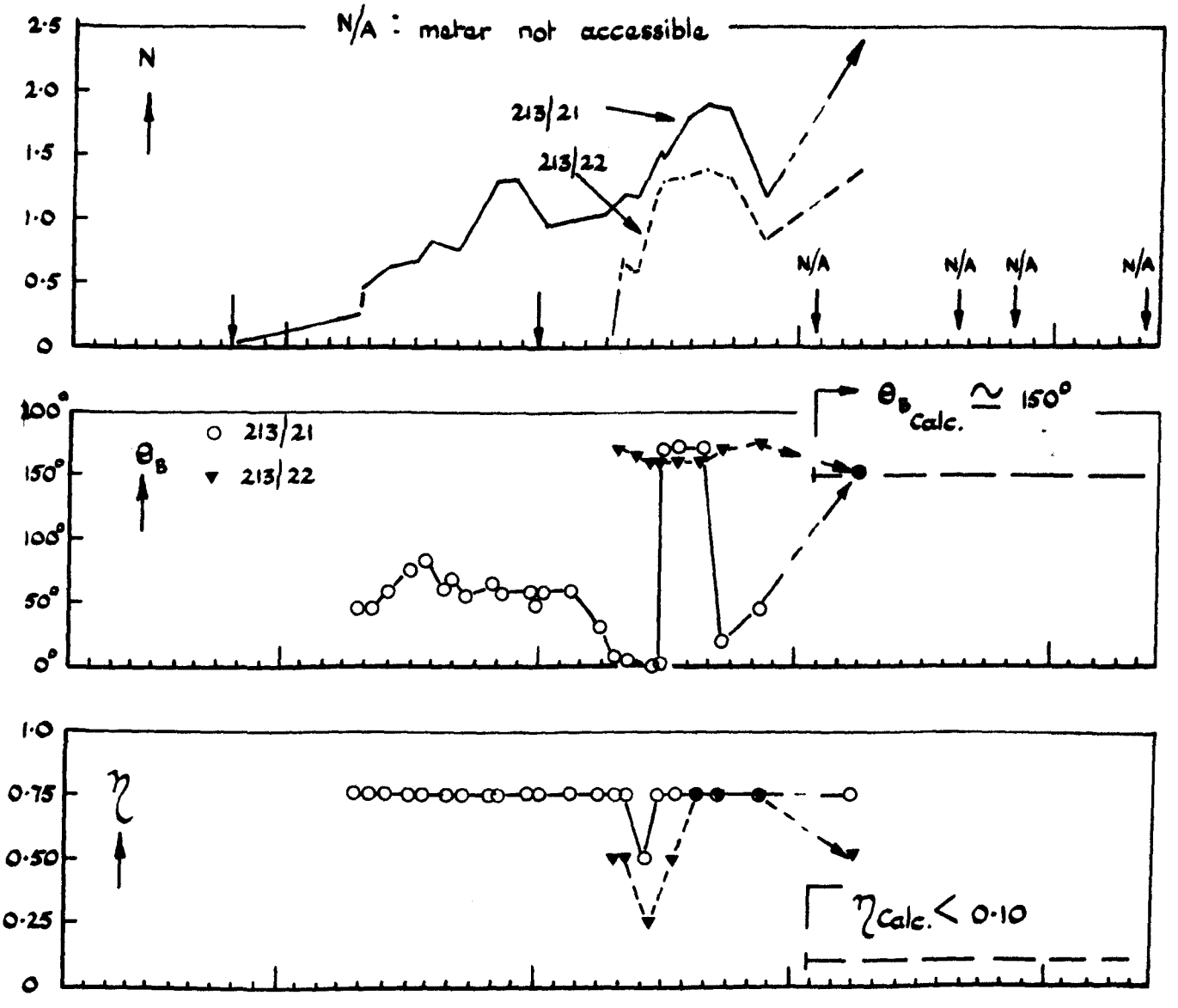

FIG. 6.13. Annular stressmeter readings, station 213.

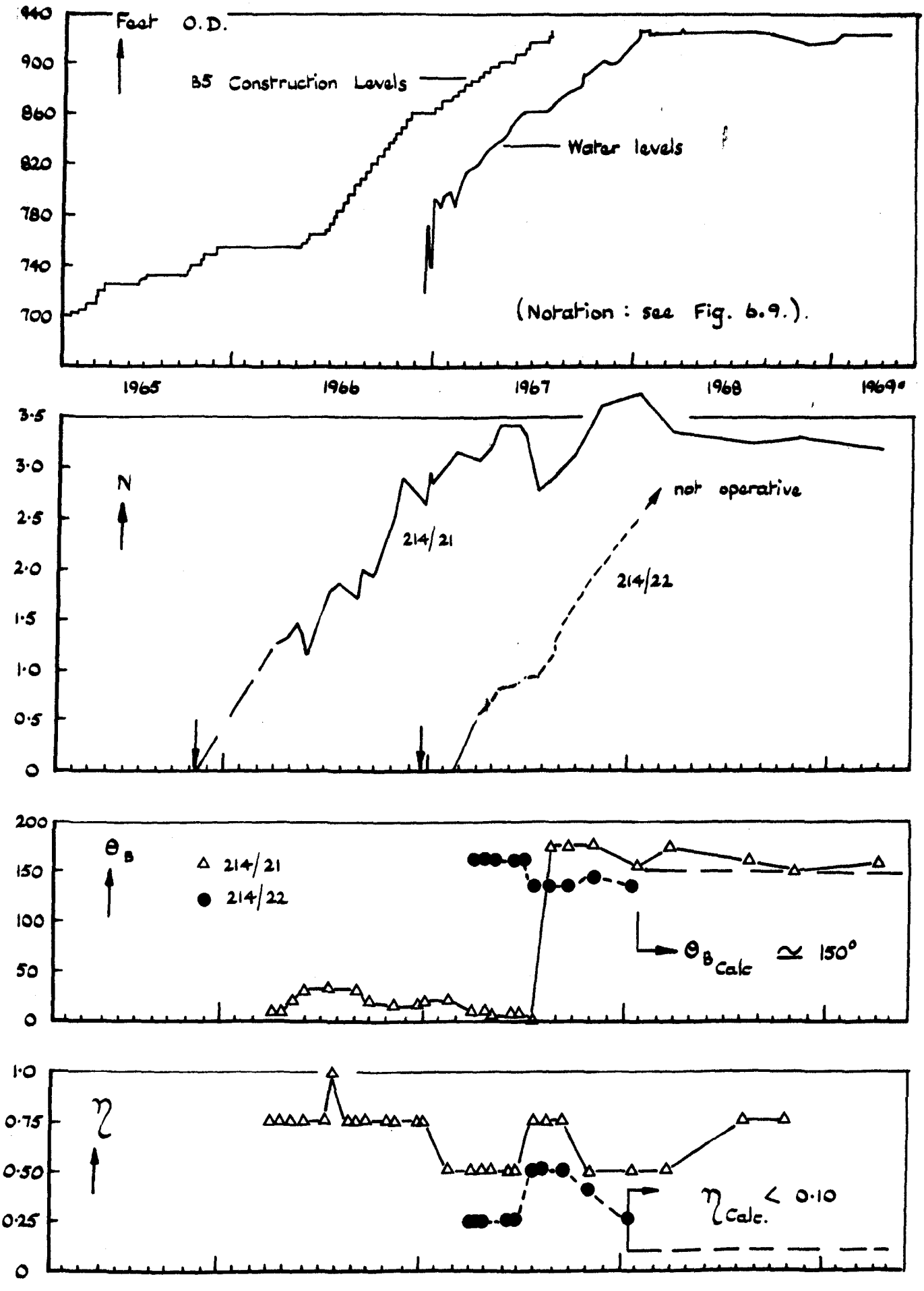

FIG. 6.14. Annular stressmeter readings, station 214.

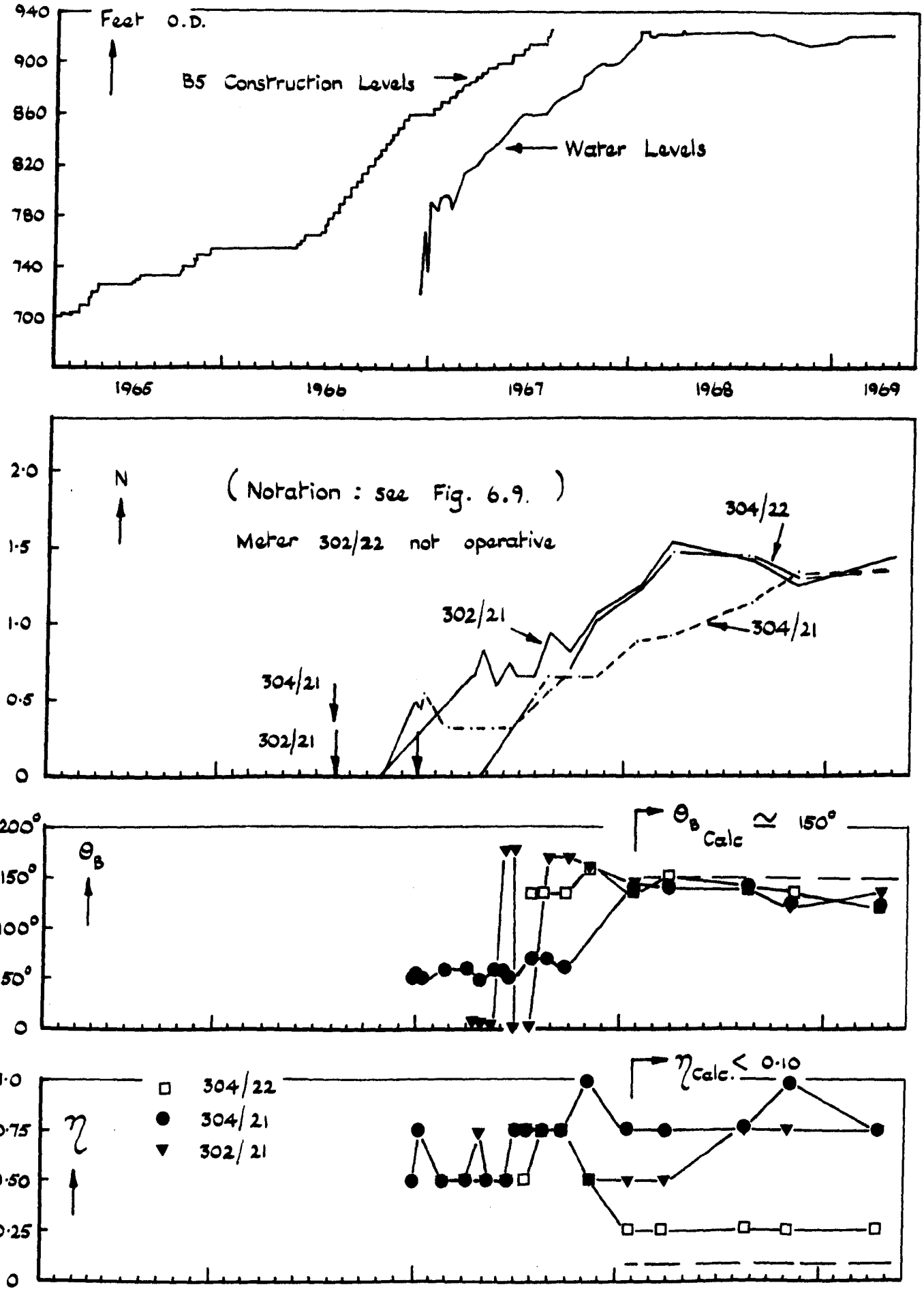

FIG. 6.15 Annular stressmeter readings , stations 302 , 304.

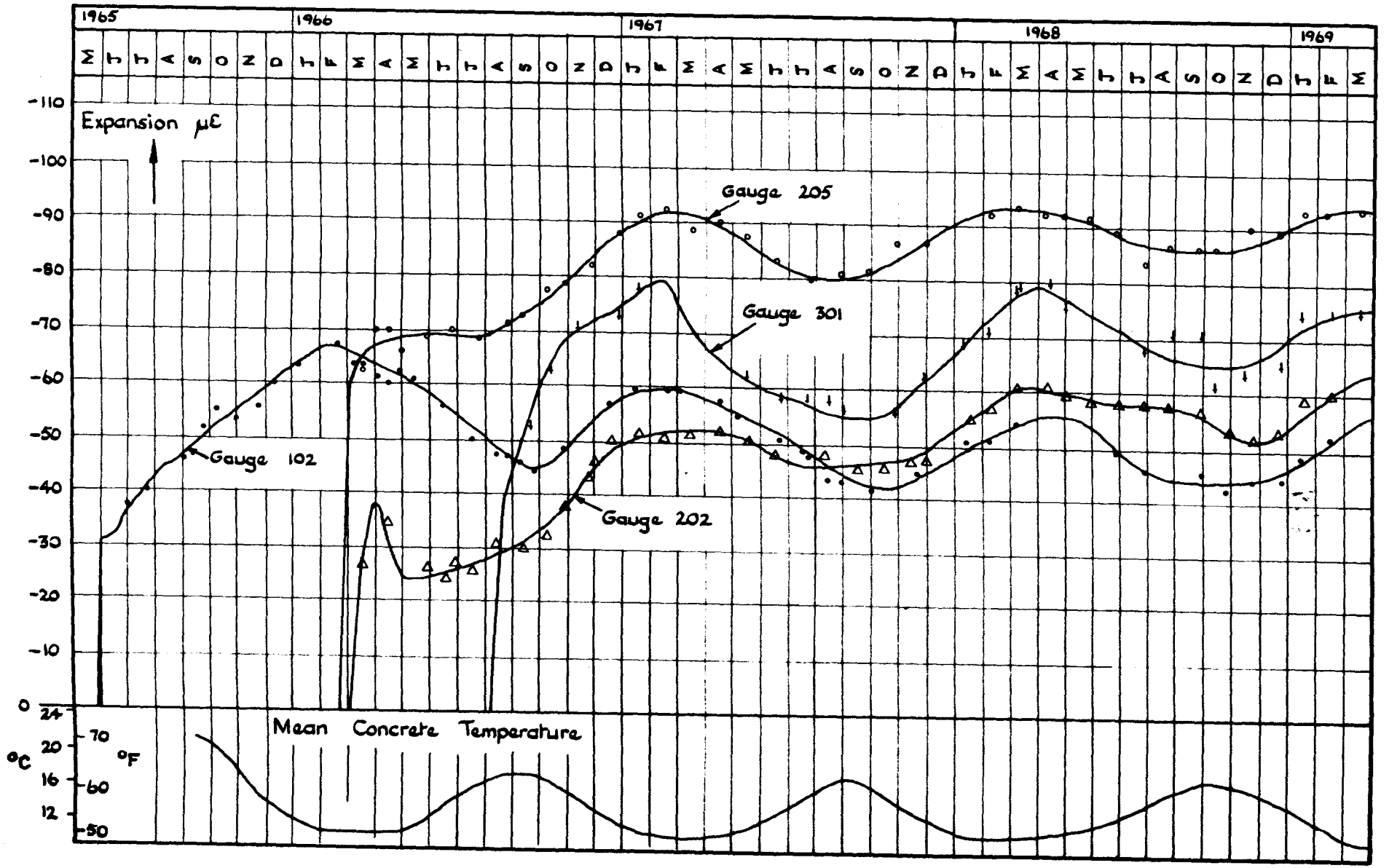

FIG. 6.16. Strains from isolated sonic gauges [after ref. (75.)]

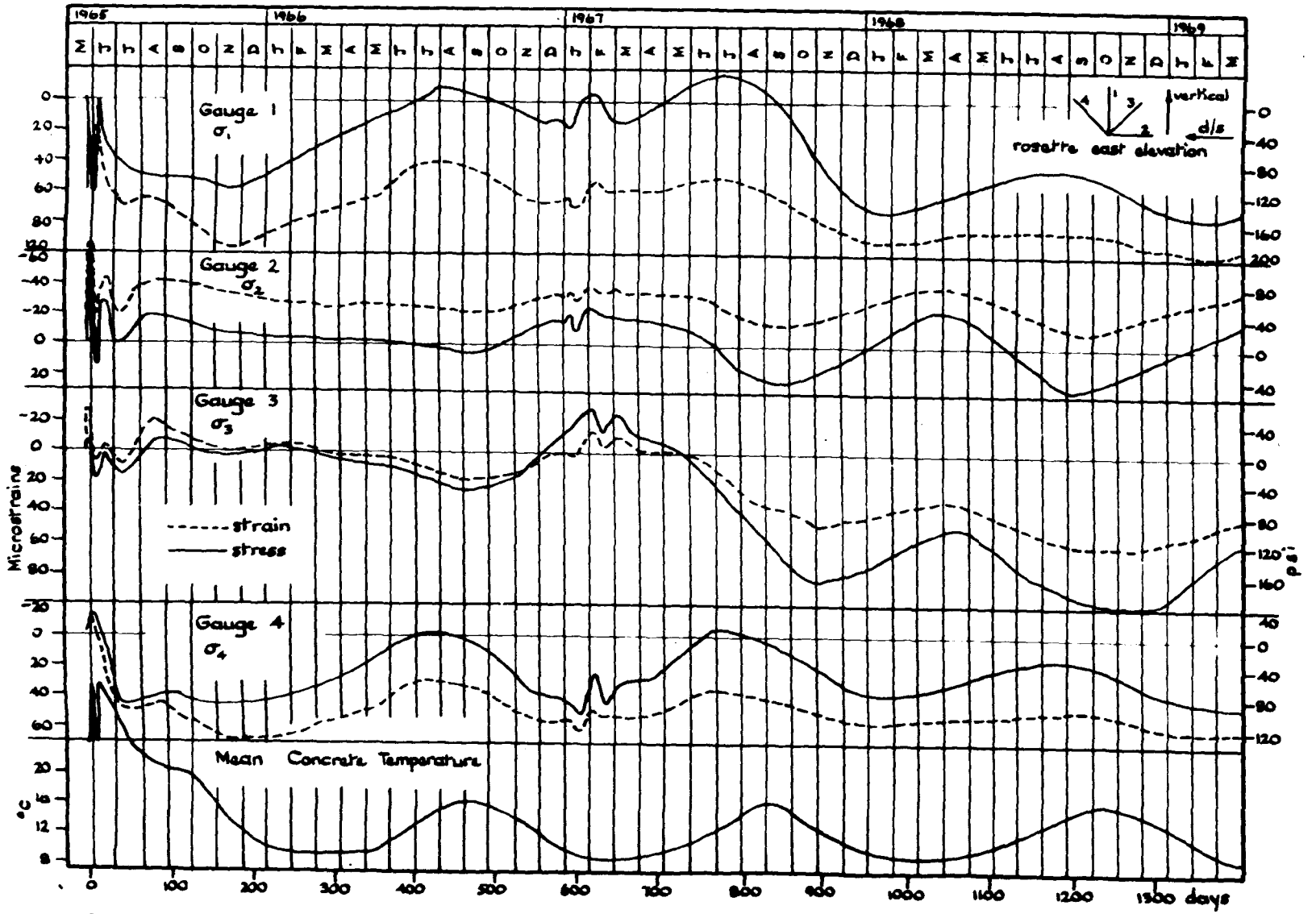

FIG. 6.17. Computed strains and stresses from sonic gauge rosette 102 [after ref (75)]

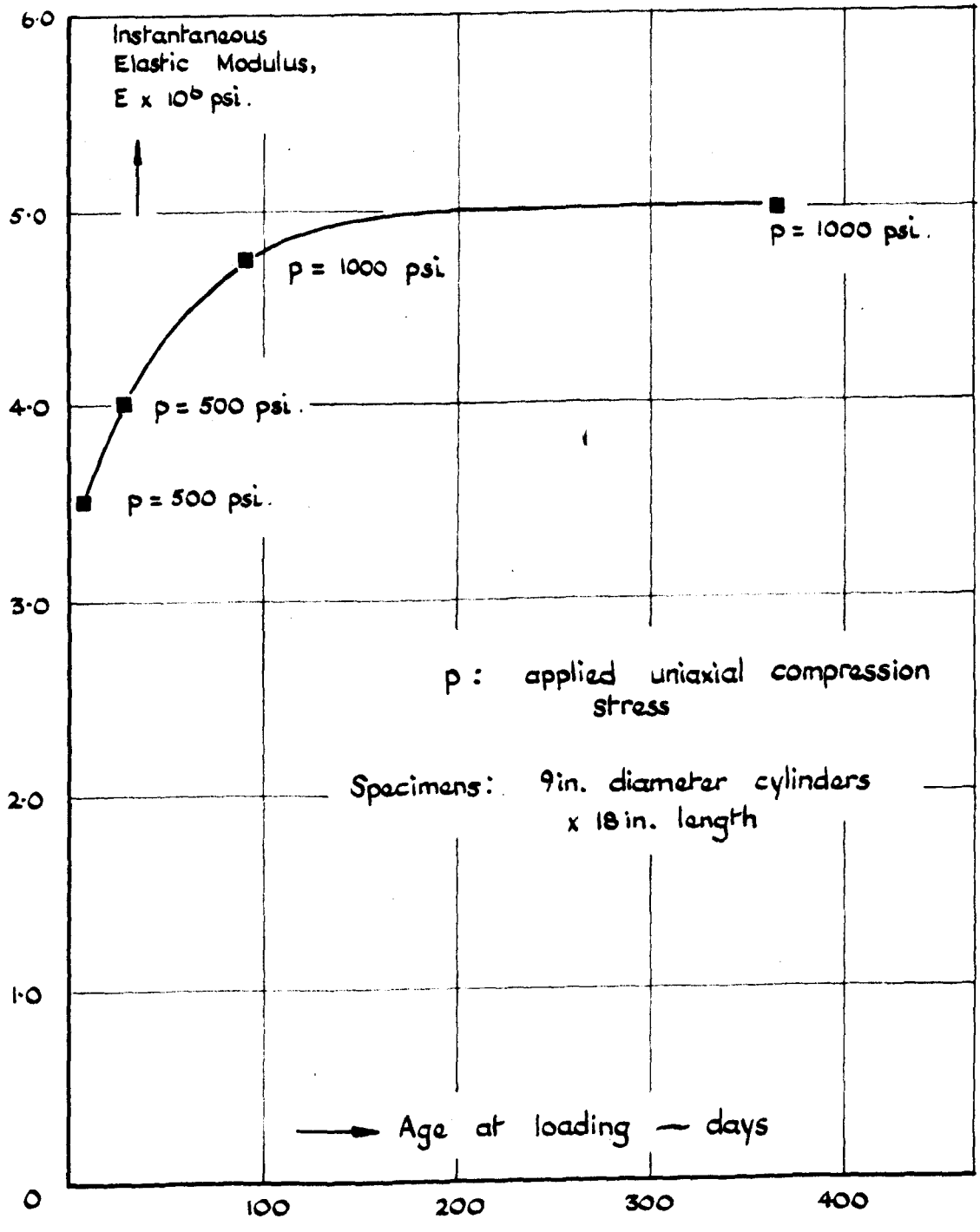

FIG. 6.18 Variation of elastic modulus with age for buttress concrete class C.
[after ref (77)]

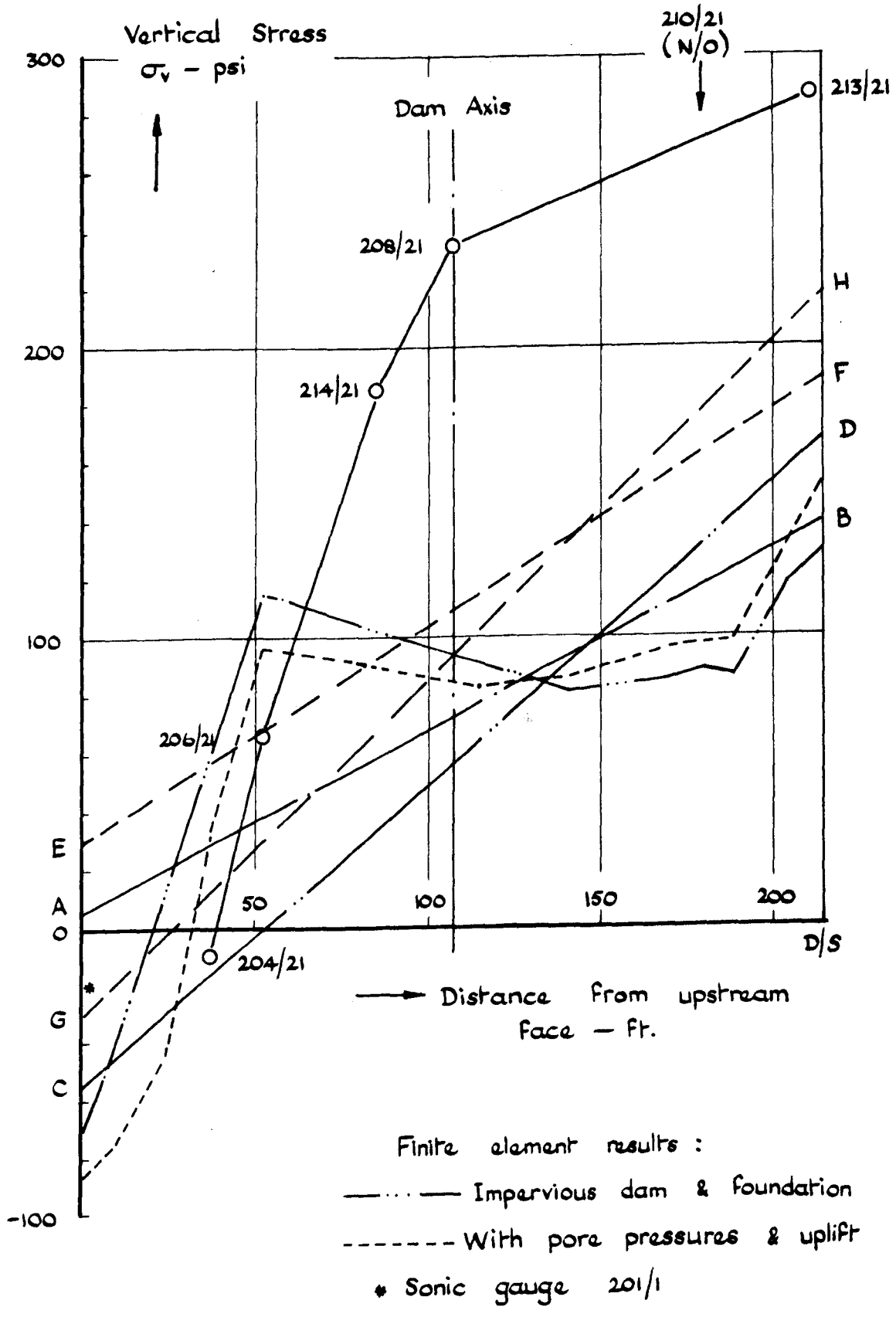

FIG. 6.19 Vertical stress distribution at 745' O.D. due to total water load

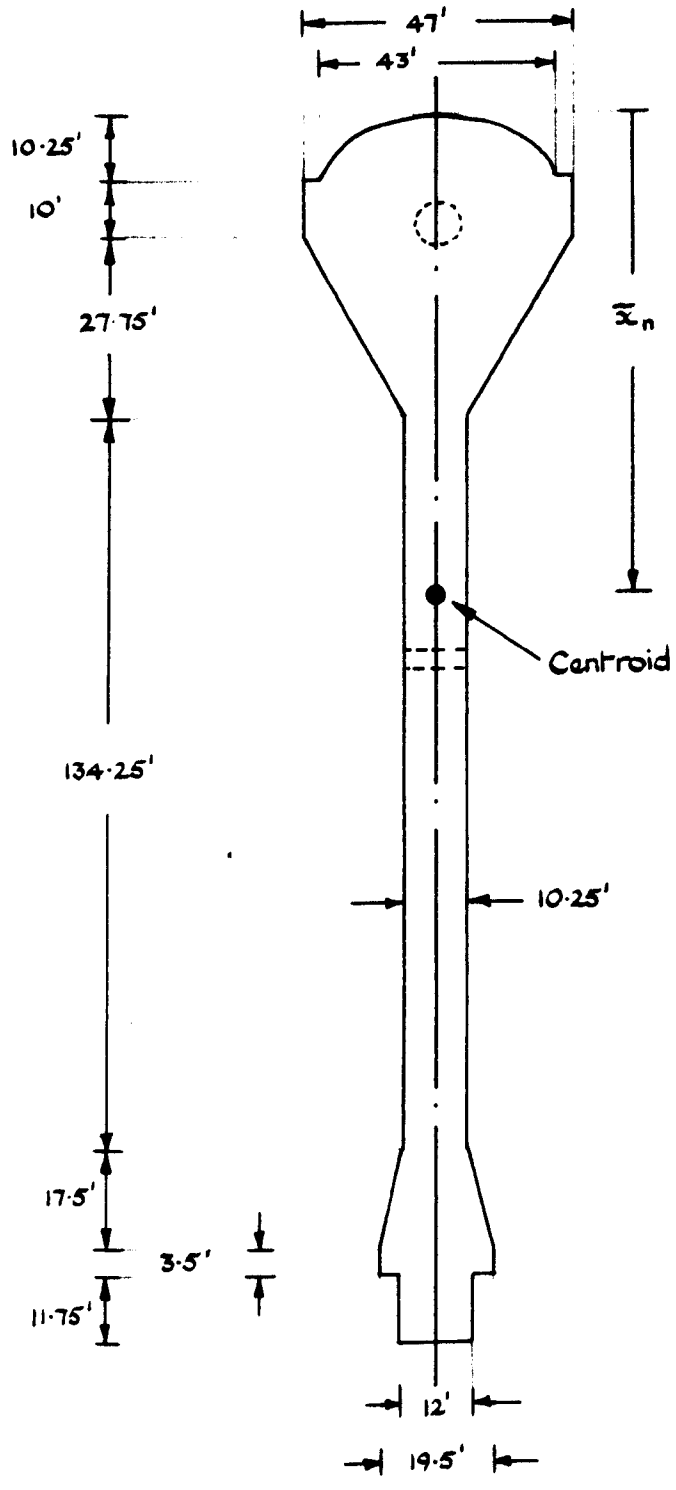

Area of cross section, A_n = 3397 ft^2

Position of centroid, $\bar{x}_n$ = 84 ft

Moment of inertia of section about centroid = $16{\cdot}08 \times 10^6$ ft^4

FIG. 6.20 Numerical terms for buttress section at 745' O.D.

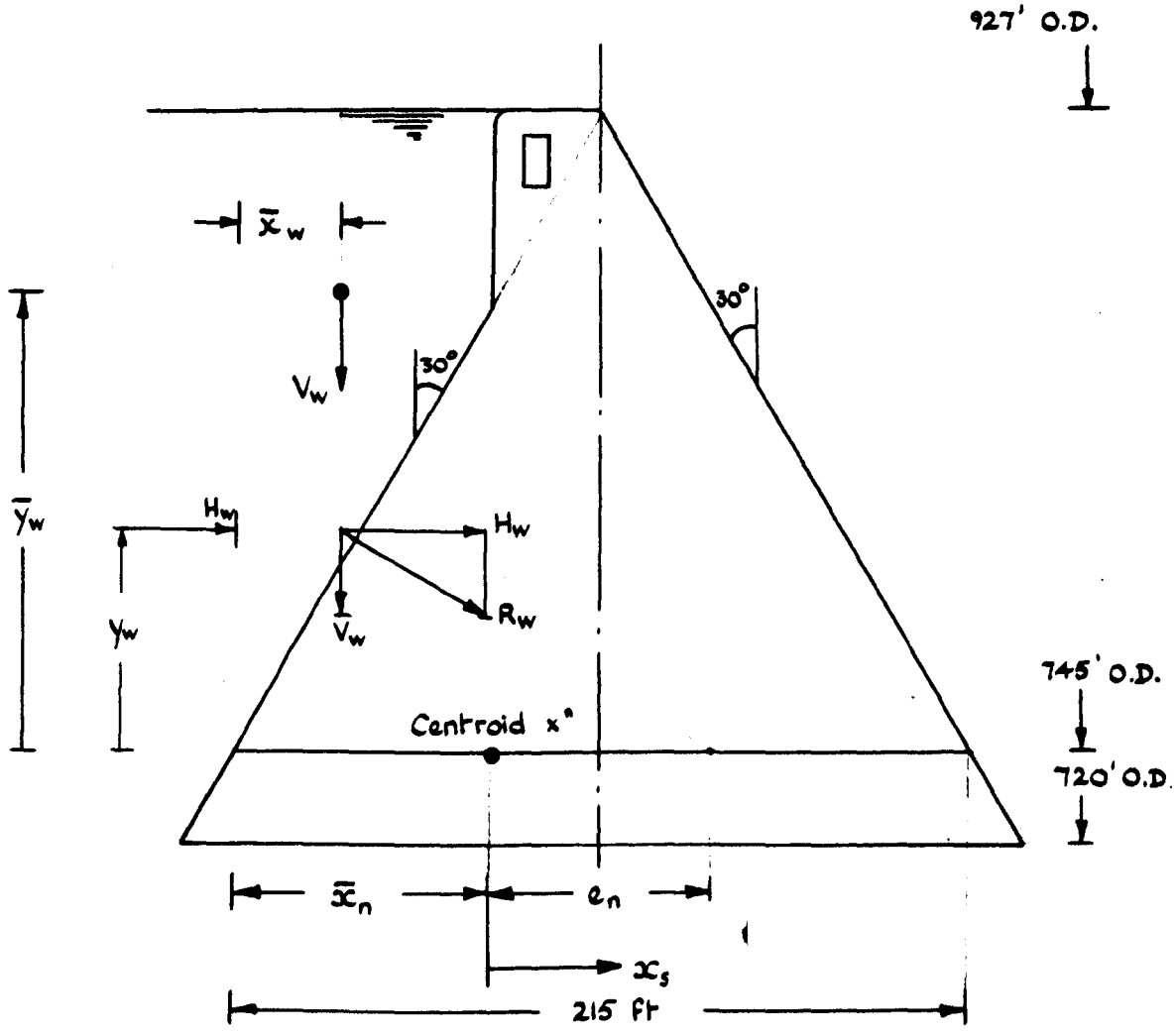

$$H_w = 48{\cdot}50 \times 10^6 \text{ lbs.}$$

$$y_w = 60{\cdot}67 \text{ ft.}$$

$$V_w = 28{\cdot}16 \times 10^6 \text{ lbs.}$$

$$(\bar{x}_w, \bar{y}_w) = (32{\cdot}3, 125{\cdot}8) \text{ ft.}$$

$$R_w = \sqrt{H_w^2 + V_w^2} \text{ lbs.}$$

$$e = 50{\cdot}8 \text{ ft.}$$

$$\bar{x}_n = 84{\cdot}0 \text{ ft.}$$

FIG. 6.21. Numerical terms for the full buttress water load (linear analysis, impervious foundation) at 745' O.D.

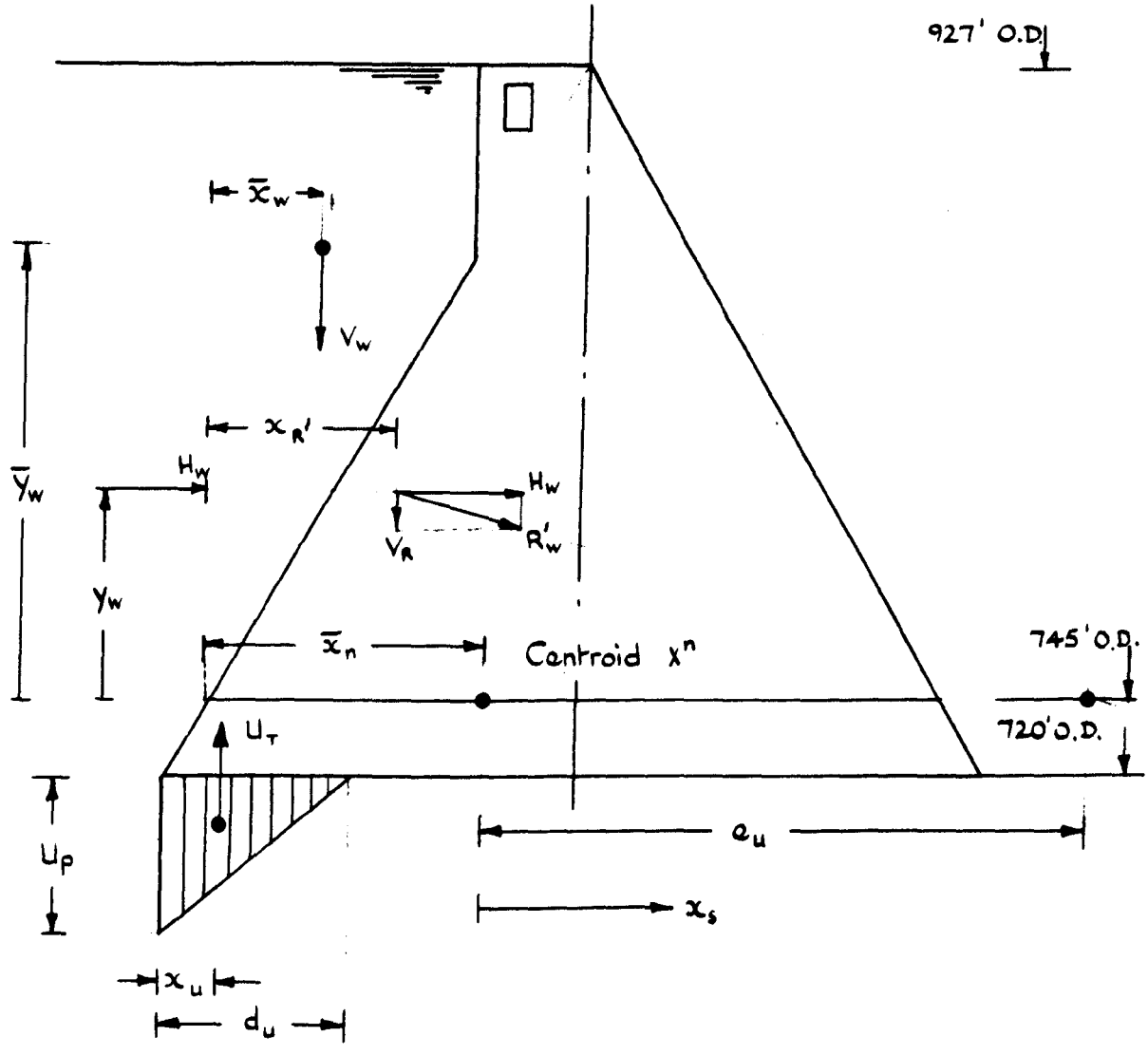

U_p = 90 psi.

U_T = 12·10 x 10^6 lbs.

d_u = 55 ft.

x_u = $d_u/3$ ft.

V_R = $(V_w - U_T)$ lbs

$x_{R'}$ = 53·8 ft

R'_w = $\sqrt{H_w^2 + V_R^2}$ lbs

e_u = 152·8 ft

All other terms — see Fig. 6.21

FIG. 6.22 Numerical terms for the full buttress water load (linear analysis, with uplift) at 745' O.D.

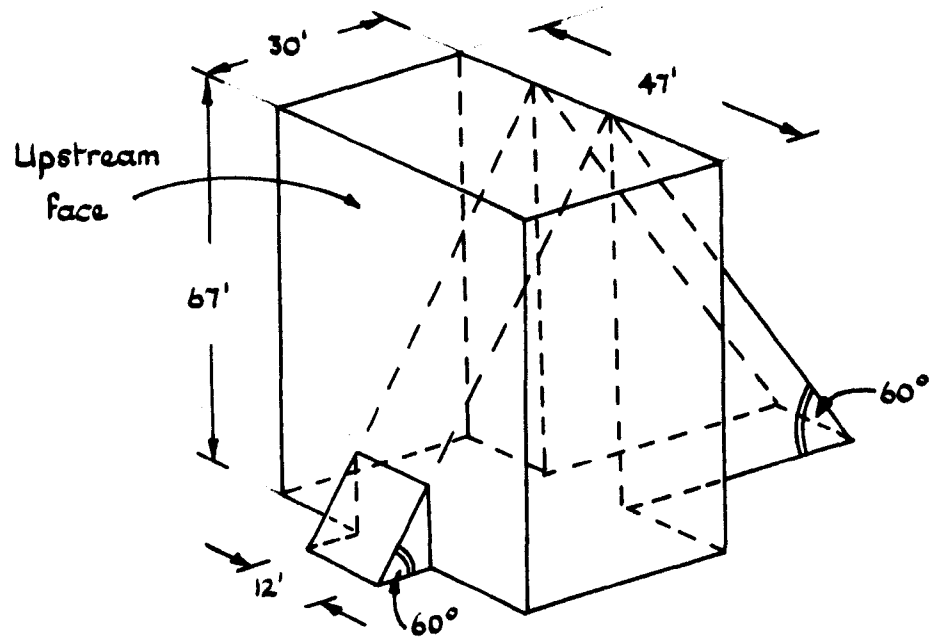

Model used for buttress cap

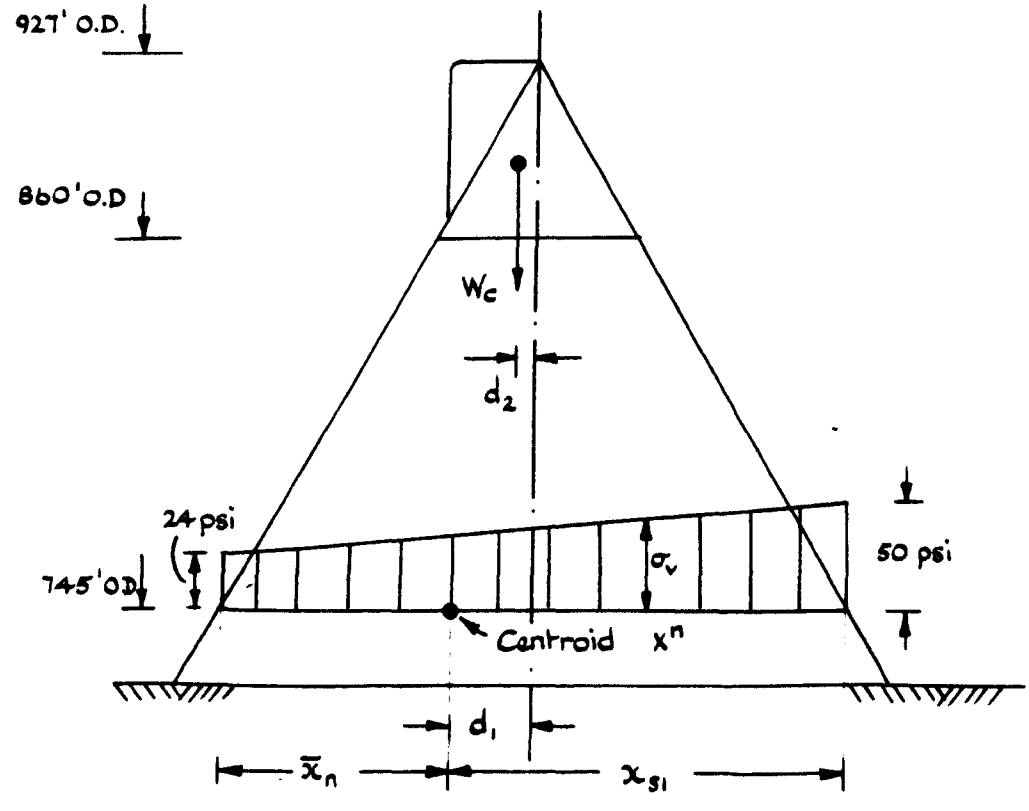

$W_c = 16{\cdot}62 \times 10^6$ lbs. $d_1 = 23{\cdot}5$ ft $d_2 = 7{\cdot}2$ ft

For parameters of cross section, see Fig. 6.20

FIG. 6.23. Vertical stresses at 745' O.D. due to buttress cap.

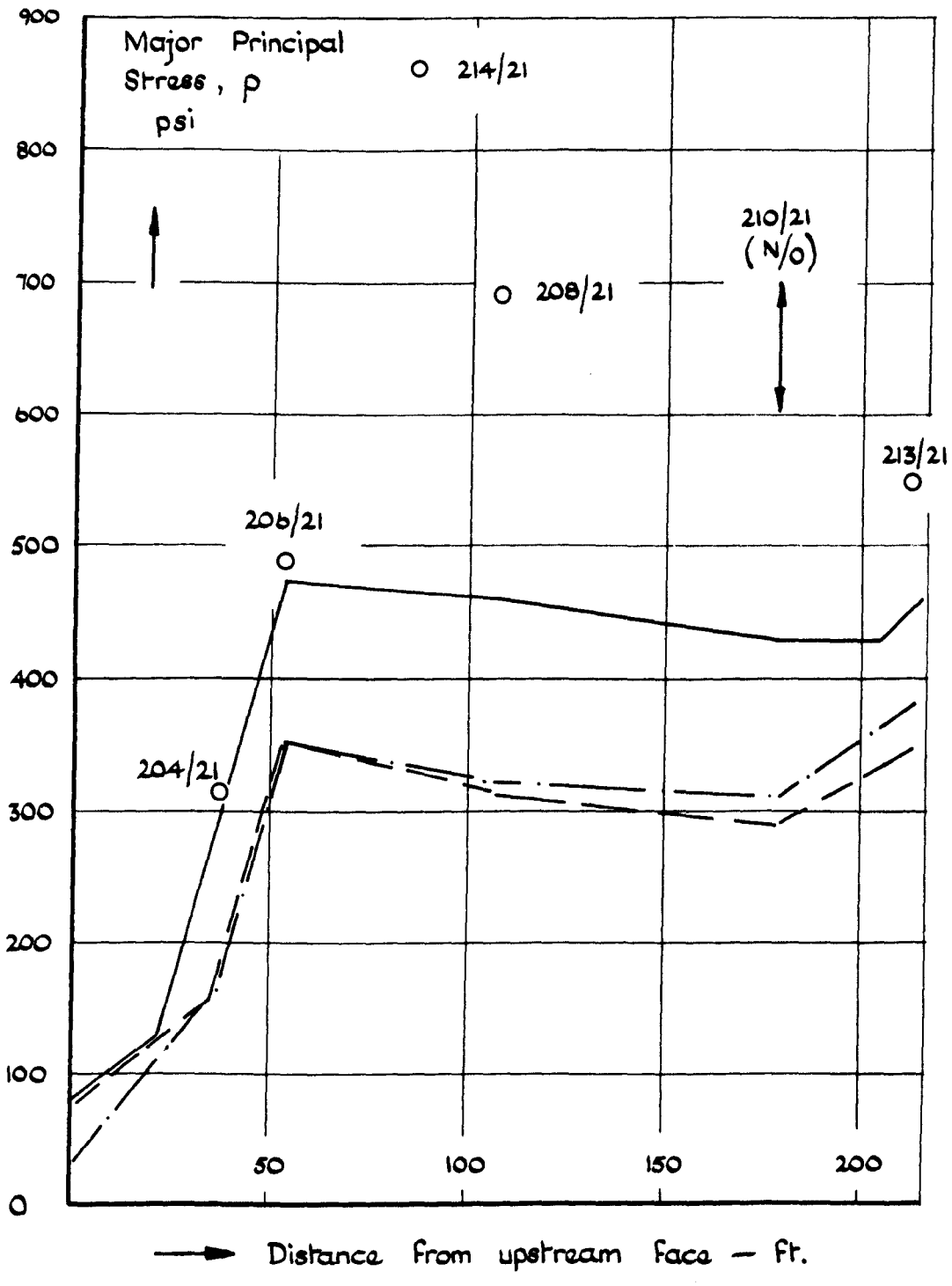

FIG. 6.24. Absolute stress comparison along level 745' OD, full dam condition.

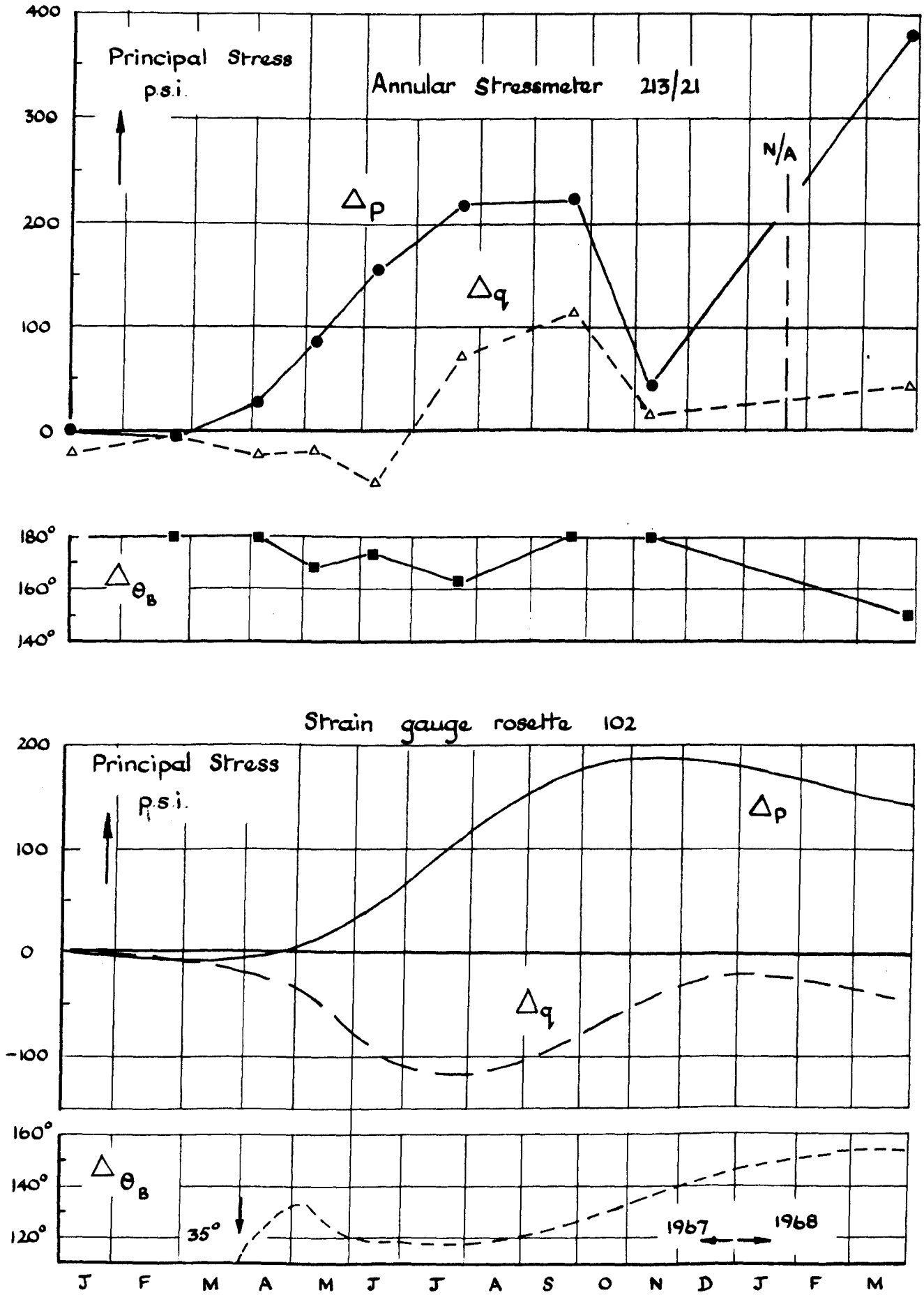

FIG. 6.25. Principal stresses, buttress toe, through 1967.

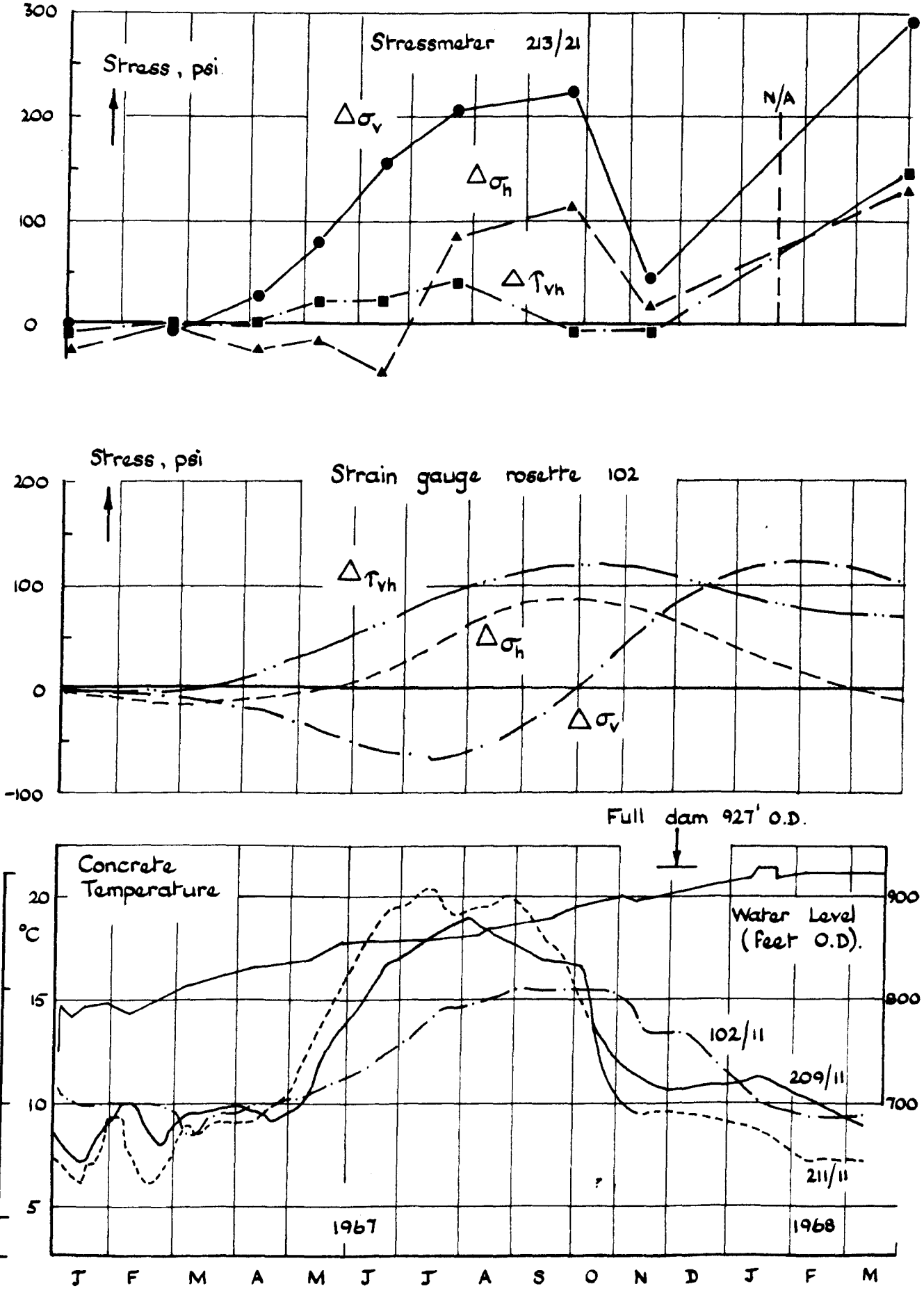

FIG. 6.26. Stress components, buttress toe, through 1967.

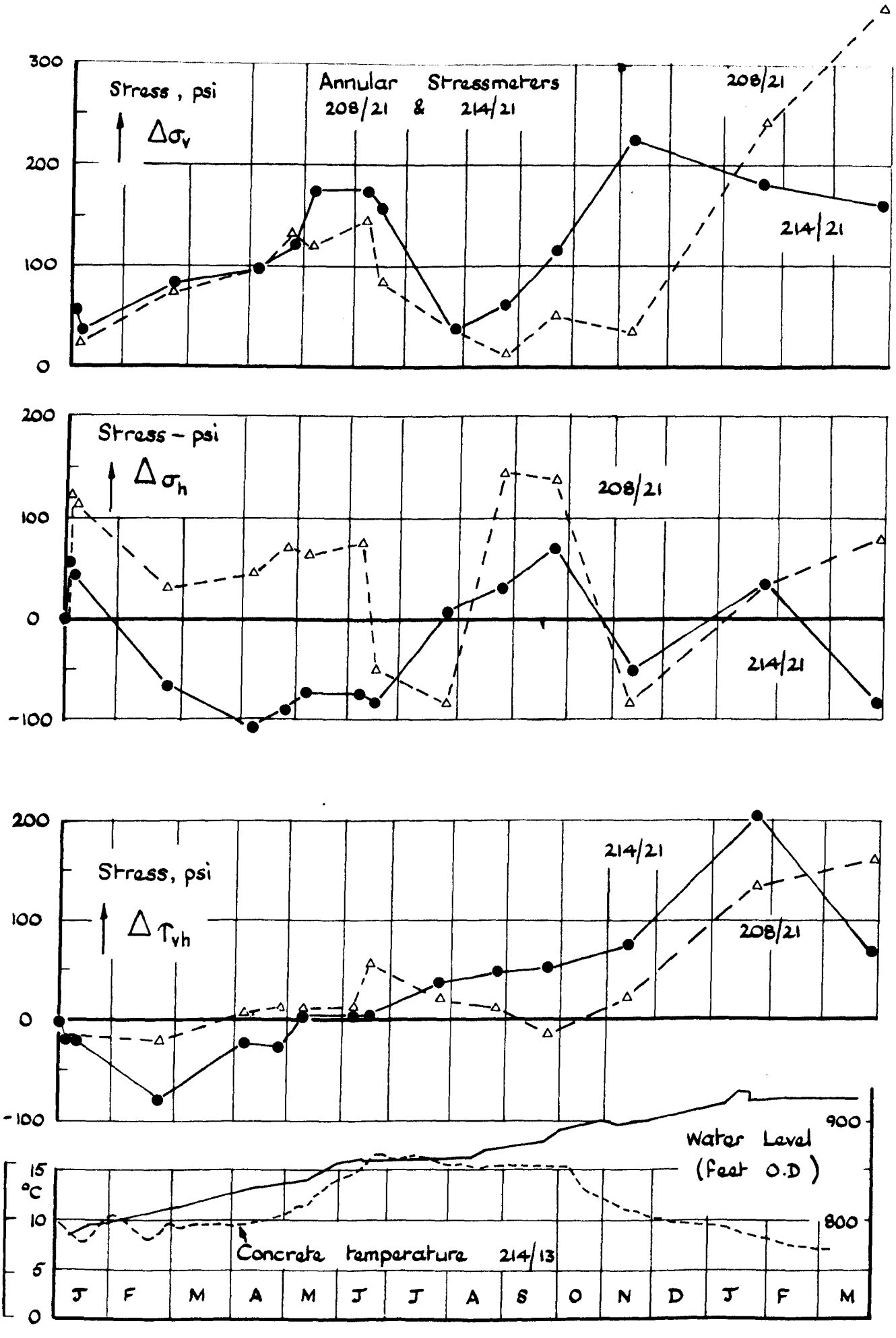

FIG. 6.27. Stress components, buttress web, through 1967.

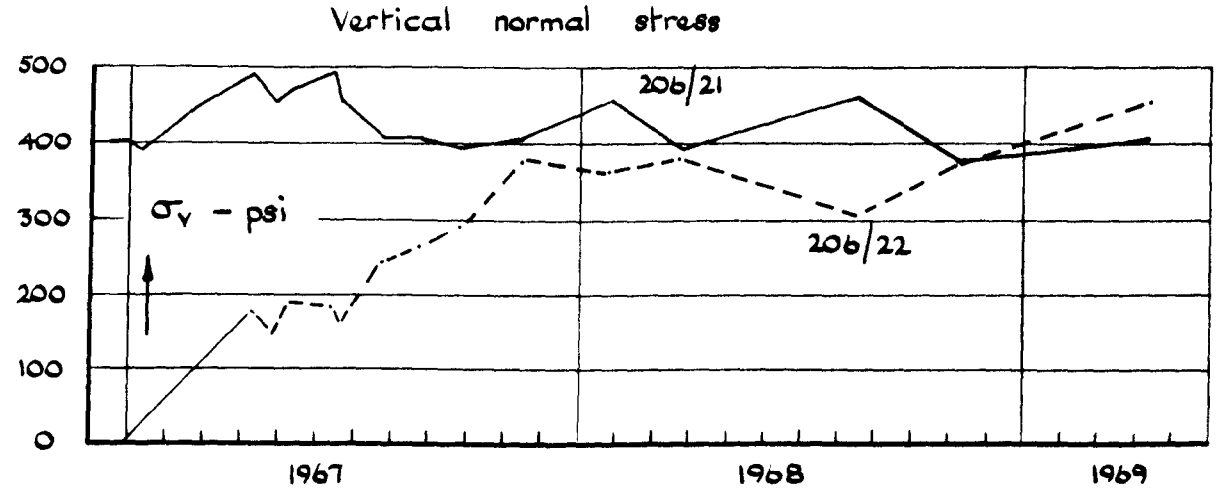

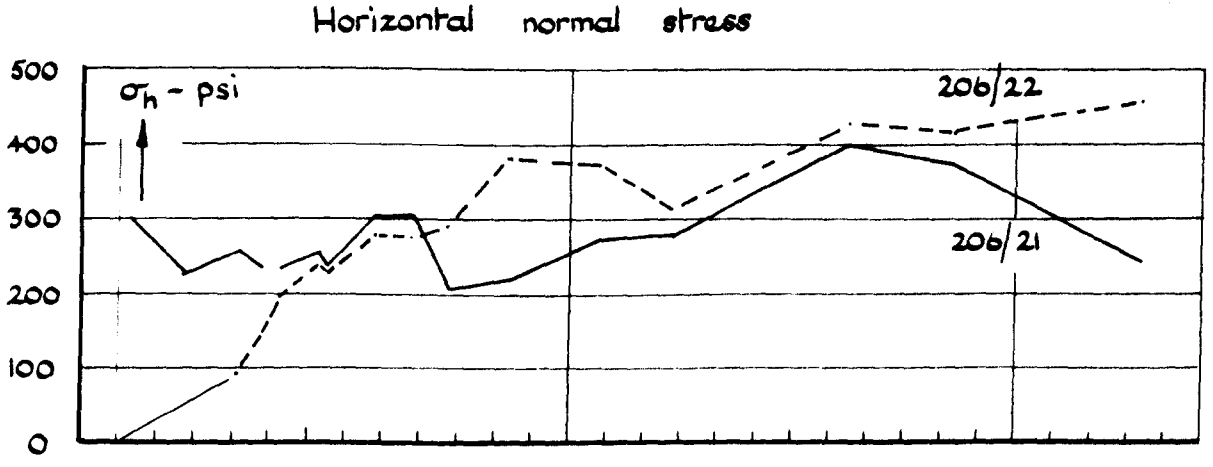

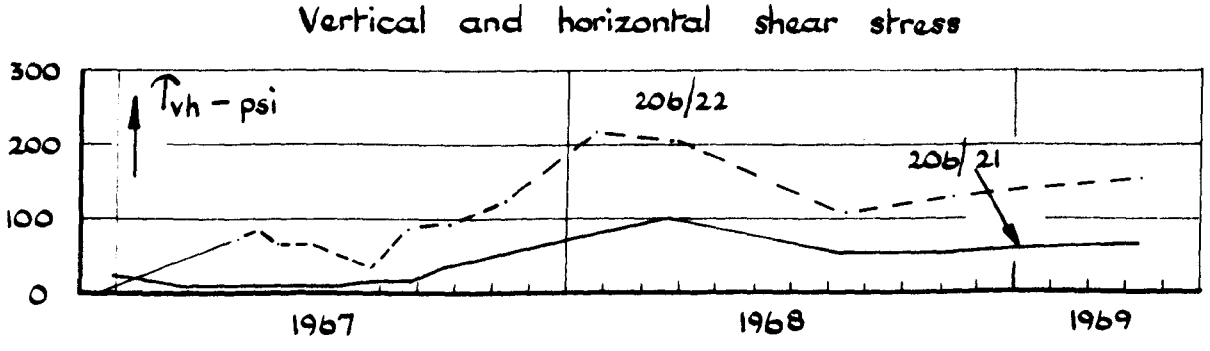

FIG. 6.28. Indicated buttress stress components station 206

APPENDIX 1

Data for Chapter 3

TABLE A.1.1.

Surface Shrinkage Readings for Concrete Mix A

Mix Details : See Tables 3.1, 3.2
Specimen Details : See Figure 3.5.

Age (Days)	Conditions		Surface Shrinkage - Microstrains							
	Temperature °F	% R.H.	Front Face Gauge Lengths				Back Face Gauge Lengths			
			1	2	3	4	1	2	3	4
7	66.5	40	0	0	0	0	0	0	0	0
8	66	40	45	35	30	20	80	100	30	30
9	66	45	105	95	50	40	100	115	60	60
12	66	45	190	180	125	105	150	170	130	135
16	66	42	255	230	180	160	195	205	175	185
20	65	40	270	255	200	175	205	210	190	195
24	70	32	315	265	240	215	250	250	240	245
29	67.5	39	325	280	245	225	260	260	255	255
36	68	38	360	310	280	255	295	295	290	295
40	66.5	38	370	330	290	260	310	300	300	305
45	69	35	375	325	300	265	315	305	310	315
50	72	38	390	335	315	280	325	315	320	325
57	68.5	51	380	330	305	270	315	325	315	320
65	70.5	40	390	335	310	280	325	330	325	325

TABLE A.1.2.

Observed Longitudinal Surface Strains and Temperature Corrections - Slab Specimen F2-2

($\alpha = 7 \times 10^{-6}/^{\circ}F$)

Age (Days)	Laboratory Conditions		Average Observed Strain με	Correction to 70°F με	Net Shrinkage at 70°F με
	Temperature °F	% R.H.			
7	69	-	0	-7	-7
7	82	51	-30	+84	+54
8	82.5	50	0	+87	+87
9	82	51	+50	+84	+134
11	82	53	+125	+84	+209
14	84	50	+200	+93	+293
17	82	50	+270	+84	+354
20	83	51	+325	+91	+416
24	82.5	55	+390	+87	+477
28	83	52	+450	+91	+541
30	84	52	+475	+98	+573
35	83	51	+545	+91	+636
35	66	35	+660	-28	+632
36	69	40	+670	-7	+663
38	70	40	+670	0	+670
42	66.5	34	+745	-25	+720
46	65.5	39	+775	-32	+743
52	65	45	+830	-35	+795
60	64	41	+870	-42	+828
65	66.5	36	+885	-25	+860
70	70.5	32	+895	+2	+897
73	69	42	+905	-7	+898
78	68	39	+930	-14	+916
84	66.5	34	+950	-25	+925
93	70.5	40	+965	+2	+967
104	70	48	+1000	0	+1000
112	71	39	+1015	+7	+1022

TABLE A.1.3.

Observed Longitudinal Surface Strains and Temperature Corrections - Slab Specimen F1-6

($\alpha = 7 \times 10^{-6}/^{o}F$)

Age (Days)	Room Temperature ^{o}F	Average Observed Strain $\mu\varepsilon$	Corrected to $70^{o}F$ $\mu\varepsilon$	Net Shrinkage at $70^{o}F$ $\mu\varepsilon$
9	71	0	+7	+7
9	82.5	-95	+87	-8
10	82	-85	+84	-1
11	82	-70	+84	+6
14	84	-75	+98	+23
17	82	-60	+84	+24
20	83	-45	+91	+46
24	82.5	-25	+87	+62
28	83	-10	+91	+81
30	84	-5	+98	+93
35	83	+20	+91	+111
35	66	+120	-28	+92
36	69	+125	-7	+118
38	70	+130	0	+130
42	66.5	+155	-25	+130
46	65.5	+170	-32	+138
52	65	+205	-35	+170
60	64	+224	-42	+182
65	66.5	+215	-25	+190
70	70.5	+200	+2	+202
73	69	+215	-7	+208
78	68	+225	-14	+211
84	66.5	+255	-25	+230
93	70.5	+245	+3.5	+249
104	70	+255	0	+255
112	71	+265	+7	+272

TABLE A.1.4.

Shrinkage Fringe Order Data

Annular Stressmeter in Specimen F3-4

Specimen Details : See Tables 3.1, 3.3, and Figure 3.7
Stressmeter Dimensions : 1.250 in. dia. x 0.265 in. dia x 2.992 in. length
f_g : 1220 p.s.i./fr./in.

Age (Days)	Conditions		Shrinkage με (Average of 6 Readings)	White Light Fringe Order Mean N_s at $\frac{r}{b} = 1.0$	
	Temperature °F	% R.H.		θ = 0°-180°	θ = 90°-270°
7	74	35	0		
10	65	35	140		
12	65	38	185		
15	68	46	245		
18	70	43	300		
22	71	42	360		
26	70	48	445		
29	71	42	490		
32	71	45	540	-0.50	-0.60
36	71	50	590		
40	72	48	640		
45	70	40	695		
51	70	40	750		
58	67	38	825	+0.80	+0.68
64	66	40	870	+1.00	+0.80
71	66	42	885	+1.30	+0.90
80	70	32	910	+1.45	+1.08
89	67	38	960	+1.72	+1.23
97	68	34	990	+1.85	+1.35
106	70	35	1010	+2.03	+1.50
116	70	48	1020		
125	70	46	1050		
133	70	42	1045	+2.08	+1.58

TABLE A.1.5.

Annular Stressmeter, Specimen F3-4

Shrinkage Fringe Orders at $\frac{r}{b}$ = 1.0 and Relative Shrinkage Changes

(Data Derived from Figure 3.12)

Specimen Details : See Tables 3.1, 3.3, and Figure 3.7
Stressmeter Dimensions : 1.250 in. dia. x 0.265 in. dia. x 2.992 in.
f_g : 1220 p.s.i./fr./in.

Age (Days)	Shrinkage με (δ) Datum: 7 days	Δδ (δ - 550) με Datum: 33 days	White Light Fringe Order at $\frac{r}{b}$ = 1.0	
			θ = 0°-180°	θ = 90°-270°
33	550	0	-0.50	-0.60
58	825	275	+0.83	+0.66
64	867	317	+1.07	+0.80
71	900	350	+1.27	+0.92
80	945	395	+1.53	+1.12
89	975	425	+1.73	+1.25
97	993	443	+1.85	+1.35
106	1013	463	+1.96	+1.46
133	1050	500	+2.10	+1.60

TABLE A.1.6.

Shrinkage Fringe Order Distribution

Annular Stressmeter of Specimen F3-4, Day 106

Specimen Details : See Tables 3.1, 3.3, and Figure 3.7
Stressmeter Dimensions : 1.250 in. dia. x 0.265 in. dia. x 2.992 in.
f_g : 1220 p.s.i./fr./in.

r inches	$\frac{r}{b}$ (for nominal $\frac{a}{b} = 5.0$)	White Light Fringe Order, $+N_s$ $+ N_s \alpha (\sigma_0' - \sigma_r')$							
		θ Value in Degrees							
		0	45	90	135	180	225	270	315
0.132	1.06	2.05	1.82	1.52	1.55	2.00	1.82	1.50	1.85
0.156	1.25	1.90	1.60	1.40	1.40	1.80	1.68	1.30	1.55
0.188	1.50	1.33	1.20	0.97	0.97	1.25	1.20	0.90	1.13
0.250	2.00	0.83	0.75	0.58	0.60	0.75	0.75	0.45	0.70
0.375	3.00	0.58	0.47	0.35	0.30	0.48	0.45	0.20	0.45
0.500	4.00	0.50	0.43	0.30	0.25	0.36	0.35	0.20	0.40
0.625	5.00	0.50	0.43	0.25	0.25	0.30	0.30	0.20	0.40

TABLE A.1.7.

Brazil Test Data - Mix F1

Mix and History : See Tables 3.1, 3.3, and Figure 3.10
Cylinder Details : Nominal length l = 4.0 in.
Diameter d = 4.0 in.
Platen Details : Flat steel platens plus paper layer
Loading rate : 4480 lbs./min.

$$\sigma_{tens} = -\frac{2P'}{\pi dl}$$

Age (Days)	Length l inches	Failure Load P' lbs.	Nominal Tensile Strength σ_{tens} p.s.i.
7	4.00	11950	475
	3.95	13550	545
	4.00	15200	605
28	3.90	12500	510
	3.90	13000	530
	4.00	14200	565
44	3.95	13650	550
	4.00	14300	570
	4.00	15700	625
70	4.05	15100	595
	3.95	15150	610
	3.95	16000	645
102	4.00	15050	600
	4.00	16200	645
	4.05	17050	670

APPENDIX 2

Data for Chapter 4

TABLE A.2.1.

Slab F3-3 Solid Stressmeter and Demec Gauge Data

(Slab Cross-Section:26.0 sq.in. f_σ = 1220 p.s.i./fr./in.
Meter length : 3 in.)

Total Load lbs.	Applied Stress p.s.i.	Meter Fringe Order (Centre Point -White Light)	Demec Gauge Readings Microstrains					
			Front			Back		
			L1	L2	L3	L1	L2	L3
0	0	0	0	0	0	0	0	0
3000	115	0.38	35	30	35	30	35	40
6000	231	0.85	65	65	70	70	75	90
9000	346	1.32	105	100	110	105	110	125
12000	462	1.78	145	135	140	140	145	160
15000	577	2.25	180	170	175	175	180	190
18000	692	2.68	215	215	205	220	220	230
21000	808	3.11	250	245	245	250	265	270
24000	924	3.52	290	285	290	295	300	305

Fringe order and strain readings have positive signs.

TABLE A.2.2.

Slab F3-4 Annular Stressmeter and Deformation Data

(Slab Cross-Section : 26.0 sq.in. f_g = 1220 p.s.i./fr./in. Meter Length : 3 in.
Fringe Orders (white light) Measured at 45° Points in Stressmeter)

Load lbs.	Applied Stress p.s.i.	Fringe Order, +N	Resistance Strain Gauge Readings - με								Demec Gauge Readings - με					
			Front				Back				Front			Back		
			G1	G2	G3	G4	G1	G2	G3	G4	L1	L2	L3	L1	L2	L3
0	0	0	0	0	0	0	0	0	0	0	0	0	0	0	0	0
3000	115	0.55	+32	0	+26	0	+40	-16	+28	-4	+40	+20	+25	+15	+40	+40
6000	230	1.22	+72	-10	+60	0	+74	-18	+70	-8	+70	+50	+50	+55	+75	+70
9000	345	1.75	+107	-23	+90	-12	+112	-20	+104	-10	+100	+90	+75	+95	+115	+100
12000	460	2.44	+138	-25	+118	-15	+150	-30	+138	-10	+130	+130	+110	+135	+150	+140
15000	575	3.04	+169	-28	+145	-16	+184	-36	+170	-24	+180	+170	+140	+185	+190	+180
18000	690	3.55	+207	-42	+175	-28	+220	-44	+208	-36	+210	+190	+170	+215	+220	+205
21000	805	4.16	+238	-48	+208	-28	+255	-48	+245	-36	+245	+220	+210	+265	+260	+250
24000	920	4.84	+268	-52	+242	-36	+292	-60	+280	-40	+280	+260	+250	+305	+295	+280

TABLE A.2.3.

Strain Gauge Rosette Data

'C' Rosettes Disc F5-2

Observed Strain Readings in Microstrains

Disc Load lbs.	Disc Orientation 1-1				Disc Orientation 2-2				Disc Orientation 4-4			
	Front		Back		Front		Back		Front		Back	
	G1	G2	G1	G2	G1	G2	G1	G2	G1	G2	G1	G2
0	0	0	0	0	0	0	0	0	0	0	0	0
3000	+22	-10	+20	-14	+6	+8	+4	+8	+8	+10	+8	+4
6000	+52	-24	+48	-28	+10	+15	+6	+10	+12	+18	+10	+6
9000	+76	-42	+70	-42	+16	+20	+10	+16	+14	+19	+14	+16
12000	+96	-52	+90	-56	+22	+23	+16	+20	+18	+25	+18	+20
15000	+120	-64	+112	-66	+26	+28	+22	+26	+27	+31	+21	+23
18000	+146	-76	+134	-80	+36	+32	+27	+30	+32	+36	+26	+30
21000	+164	-90	+160	-94	+42	+36	+30	+34	+40	+36	+33	+36

TABLE A.2.4.

Centre Element from Disc F5-2

Uniaxial Compression Test

Observed Strains in Microstrains

(Element Cross-Section Area : 26.6 sq.in.)

Total Load lbs.	Applied Stress p.s.i.	Resistance Strain Gauge Readings				Demec Gauge Readings					
		Front		Back		Front			Back		
		G1	G2	G1	G2	L1	L2	L3	L1	L2	L3
0	0	0	0	0	0	0	0	0	0	0	0
3000	113	+34	0	+34	-12	+34	+36	+36	+34	+36	+32
6000	226	+62	-21	+70	-12	+60	+66	+66	+72	+72	+76
9000	339	+93	-20	+110	-26	+90	+94	+98	+112	+116	+114
12000	452	+130	-28	+150	-32	+124	+126	+132	+139	+142	+150
15000	565	+160	-42	+181	-34	+160	+156	+157	+180	+188	+185
18000	678	+197	-46	+220	-43	+188	+191	+196	+231	+230	+216
21000	791	+231	-58	+260	-50	+220	+220	+234	+264	+265	+252
24000	904	+262	-66	+290	-58	+254	+264	+266	+298	+302	+284

TABLE A.2.5

Strain Gauge Rosette Data : 'A' Rosettes Disc F5-1

Observed Strain Readings in Microstrains

Disc Load lbs.	Disc Orientation 1-1						Disc Orientation 2-2						Disc Orientation 4-4					
	Front			Back			Front			Back			Front			Back		
	G1	G2	G3	G1	G2	G3	G1	G2	G3	G1	G2	G3	G1	G2	G3	G1	G2	G3
0	0	0	0	0	0	0	0	0	0	0	0	0	0	0	0	0	0	0
3000	+12	0	0	+8	0	0	0	0	+4	0	0	0	+24	+34	+22	+12	+40	+18
6000	+22	0	0	+14	-6	0	0	0	+8	+6	0	+2	+36	+76	+38	+28	+84	+42
9000	+32	-5	-4	+24	-8	-2	+4	-6	+10	+6	-6	+4	+66	+114	+58	+44	+126	+52
12000	+41	-9	-6	+28	-11	-4	+4	-8	+12	+10	-10	+6	+78	+154	+68	+62	+160	+70
15000	+50	-14	-8	+39	-16	-6	+8	-10	+16	+10	-10	+8	+100	+188	+84	+72	+204	+92
18000	+62	-16	-8	+44	-18	-6	+10	-16	+18	+14	-12	+8	+118	+230	+94	+82	+240	+102
21000	+70	-18	-12	+52	-21	-6	+10	-20	+18	+12	-14	+10	+136	+266	+112	+100	+280	+118

TABLE A.2.6.

Strain Gauge Rosette Data : 'B' Rosettes Disc F5-1

Observed Strain Readings in Microstrains

Disc Load lbs.	Disc Orientation 1-1						Disc Orientation 2-2						Disc Orientation 4-4					
	Front			Back			Front			Back			Front			Back		
	G1	G2	G3	G1	G2	G3	G1	G2	G3	G1	G2	G3	G1	G2	G3	G1	G2	G3
0	0	0	0	0	0	0	0	0	0	0	0	0	0	0	0	0	0	0
3000	+54	+24	-30	+66	+20	-10	0	0	+10	00	0	+10	0	+6	+14	0	+10	+4
6000	+110	+50	-40	+120	+30	-24	-6	0	+18	0	+2	+20	0	+16	+26	-6	+20	+16
9000	+150	+60	-50	+180	+46	-40	-6	0	+24	0	+2	+30	-4	+16	+30	-6	+22	+26
12000	+210	+84	-70	+240	+70	-50	-12	0	+40	-6	0	+42	-12	+28	+40	-6	+30	+32
15000	+260	+98	-84	+306	+82	-68	-18	0	+50	-8	-6	+54	-12	+38	+54	-18	+40	+46
18000	+300	+120	-104	+360	+100	-80	-18	-4	+54	-8	-6	+64	-20	+38	+60	-20	+48	+56
21000	+360	+130	-120	+440	+110	-100.	-20	-8	+56	-16	-10	+72	-20	+40	+68	-24	+54	+60

TABLE A.2.7.

Uniaxial Tension Test

Element from Disc F5-2

(Element Cross-Section : 7.42 sq.ins.)

Tensile Load lbs.	Applied Stress p.s.i.	Strain Gauge Readings Microstrains			
		Front		Back	
		G1	G2	G1	G2
0	0	0	0	0	0
180	-25	-6	0	-10	0
370	-50	-14	0	-22	-2
560	-75	-20	+2	-32	-2
740	-100	-26	+4	-40	+4
920	-125	-36	+4	-50	+4
1110	-150	-44	+4	-60	+2
1300	-175	-46	+4	-68	+6
1480	-200	-57	+9	-79	+6
1660	-225	Failure			

TABLE A.2.8.

Observed Strains on Principal Diameters of Disc F5-1

Demec Gauge Readings - Microstrains

Disc Load lbs.	Disc Orientation 1-1				Disc Orientation 2-2				Disc Orientation 4-4			
	Front		Back		Front		Back		Front		Back	
	D1	D3	D1	D3	D2	D4	D2	D4	D4	D2	D4	D2
0	0	0	0	0	0	0	0	0	0	0	0	0
3000	+25	-10	+30	+5	+25	-15	+20	-10	+30	-15	+30	-5
6000	+45	-20	+45	-10	+45	-15	+40	-20	+45	-25	+55	-20
9000	+70	-25	+65	-20	+70	-30	+65	-30	+65	-40	+90	-25
12000	+90	-35	+85	-30	+100	-40	+85	-40	+85	-50	+115	-40
15000	+120	-50	+115	-40	+125	-60	+100	-50	+105	-65	+140	-55
18000	+140	-60	+135	-55	+150	-65	+120	-65	+130	-70	+160	-65
21000	+170	-70	+165	-65	+175	-75	+150	-80	+160	-80	+190	-75

TABLE A.2.9.

Discs F5-1 and F5-3

White Light Fringe Order Data

Centre Point Stressmeters

(Meter length = 3 in, f_g = 1220 p.s.i./fr./in.)

Annular Stressmeter Disc F5-1 Fringe Orders at 45° Point				Solid Stressmeter Disc F5-3 Fringe Orders at Centre		
Disc Load lbs.	Orientation			Disc Load lbs.	Orientation	
	1-1	2-2	4-4		1B-1B	2-2
0	0	0	0	0	0	0
3000	0.50	0.48	0.53	2500	0.32	0.30
6000	0.98	1.03	1.04	5000	0.60	0.63
9000	1.58	1.54	1.57	7500	0.93	0.96
12000	2.07	2.04	2.07	10000	1.21	1.24
15000	2.52	2.56	2.53	12500	1.52	1.52
18000	3.03	3.05	3.01	15000	1.84	1.83
21000	3.55	3.54	3.57	17500	2.13	2.18
				20000	2.45	2.42
				22500	2.77	2.80

Fringe order readings have positive signs.

TABLE A.2.10

Centre Element from Disc F5-1

Uniaxial Compression Test

Annular Stressmeter and Demec Gauge Readings

(Element Cross-Section Area : 26.0 sq.in. f_g = 1220 p.s.i./fr./in
Meter Length : 3 in.)

Total Load lbs.	Applied Stress p.s.i.	Meter Fringe Order N (White Light)	Demec Gauge Readings Microstrains					
			Front			Back		
			L1	L2	L3	L1	L2	L3
0	0	0	0	0	0	0	0	0
3000	115	0.50	·40	.25	·30	35	·40	30
6000	231	1.18	.75	·70	70	65	··65	·60
9000	346	1.77	110	110	·105	·100	·100	·95
12000	462	2.48	150	145	145	135	130	135
15000	577	3.01	180	175	·170	165	165	160
18000	692	3.61	215	210	210	205	200	195
21000	808	4.23	·245	245	240	235	230	235
24000	924	4.74	290	·285	280	270	260	265

Fringe order and strain readings have positive signs

APPENDIX 3

Theoretical Isochromatic Fringe Patterns in the Annular Stressmeter

Theoretical distributions of fringe order in the annular stressmeter and stressmeter sensitivity factors have been calculated for uniaxial compression and the mixed biaxial loading conditoons discussed in Chapter 4. The calculations are based on the Hiramatsu-Barron stress solution for the inclusion; they have been carried out with the aid of a FORTRAN 1900 computer programme and an I.C.T. 1907 computer.

The programme input conditions were as follows:

(a) Pi = 3.1415925
Stressmeter external radius = 0.625 in.
Stressmeter internal radius = 0.125 in.
Glass E' value E_1 = 10×10^6 p.s.i.
Glass μ' value AMU1 = 0.24
Glass f_g value = 1230 p.s.i./fr./in.
Glass annulus length = 3.0 in.
Concrete E value E_2 = 3.5×10^6 p.s.i.
Concrete μ value AMU2 = 0.18
Loading condition P = +570 p.s.i., Q = 0.

(b) As in (a) above but with AMU1 = AMU2 = 0.20

(c) As in (a) and (b) above but with P = +520 p.s.i., Q = -173.3 p.s.i.

(d) As in (a) and (b) above but with A = 0.628 in and B = 0.132 in.

The specimen programme given below refers to cases (a) and (d) with Poisson's Ratio values of case (a). The appropriate flow diagram is also given.

It can be seen that the programme includes the computation of the constant terms in the Hiramatsu equations (3.15)-(3.17); definitions of these constants can be found in references[36], [37] or [38].

The accuracy of the programme has been confirmed by an independent hand calculation for several discrete (r,θ) positions in the case (a) condition.

```
JOB MI4STRESS,1907MI4C,ATKINSON
FORTRAN 1,CRO(MI4PRES),300,9400
****
DOCUMENT MI4PRES
       LIST(LP)
       SEND TO (ED,RUN.FILE)
       PROGRAM(MI4M1907MI4C)
       INPUT1=CRO
       OUTPUT2,(MONITOR)=LPO
       TRACE
       END
       MASTER ROSE
       E1=3.5
       E2=10
       AMU1=0.18
       AMU2=0.24
       PI=3.1415925
       A=0.625
       B=0.125
 25    AO=A**2
       BO=B**2
       AP=A**4
       BP=B**4
       ES=AO/BO
       SE=AP/BP
       TE=AO/BP
       TB=AP/BO
       TC=BP/AP
       TD=BO/AP
       TF=A/BO
       EN=E1/E2
       EP=1/A
       EQ=1/BO
 55    WRITE(2,40)
 40    OFORMAT(66H1    ALPHA1       BETA1       GAMMA1       ALPHA2       BETA2
      1    GAMMA2  ///)
       CA=3-AMU1
       DA=1+AMU1
       FA=1+AMU2
       AD=1-AMU1
       AC=3+AMU1*AMU2
       AE=3-AMU2
       AF=AMU1-AMU2
       AG=1-AMU2
       AL1=CA/E1 + FA/E2
       AL2=4*(1-ES)
       ALPHA1=AL1*AL2
       BE1=2/AO
       BE2=CA/E1
       BE3=1-SE
       BE4=FA*SE
       BE5=BE4+AE
       BE6=BE5/E2
       BE=BE2*BE3
       BET=BE-BE6
       BETA1=BET*BE1
       GAMMA1= -4/E1
       ALK= TC -4*ES +3.0
       ALK1=8*AC*ES
       ALK2=2*CA*TC
       ALK3=6*DA
       ALK4=ALK2 -ALK3
       ALK5=ALK4*FA
```

```
      ALP=ALK/E1
      ALP1=ALK1 +ALK5
      ALP2=ALP1/E2
      ALP4=-2*DA*CA
      ALP3=ALP*ALP4
      ALPHA2=ALP3+ALP2
      BT=TD-TE
      BT1=AC*TE
      BT2=FA*CA*TD
      BT3=3*AF/AO
      BT4=BT/E1
      BT5=BT1+BT2+BT3
      BT6=4*BT5/E2
      BT7=2*ALP4
      BT8= BT7*BT4
      BETA2=BT8+BT6
      GAMMA2=6*DA/E1
      GA=ALPHA1* BETA2
      GB=BETA1* ALPHA2
      G1=BETA2*GAMMA1
      G2=BETA1*GAMMA2
      G3=G1-G2
      G4=GA-GB
      C2=G3/G4
      G5=ALPHA2*GAMMA1
      G6=ALPHA1*GAMMA2
      G7=G5-G6
      G8=GB-GA
      D2=G7/G8
      V1=AG*TF
      V2=FA/A
      V3=V1+V2
      V4=V3*EN
      V5=EP-TF
      V6=DA*V5
      V7=V4-V6
      BO=-A/V7
      AK=2*C2
      AK1=D2*EQ
      AK2=AK+AK1
      A2=-AK2*EQ/3.0
      BK=2*D2*EQ
      BK1=C2+BK
      B2=-BK1*BP/3.0
      WRITE(2,45) ALPHA1,BETA1,GAMMA1,ALPHA2,BETA2,GAMMA2
45    FORMAT(3X,F8.4,3X,F8.3,3X,F8.5,3X,F8.4,3X,F8.3,3X,F8.6)
      WRITE(2,50)
50    OFORMAT(90H1  C2                D2                  BO
     1 A2                B2              ///)
      WRITE(2,60) C2,D2,BO,A2,B2
60    FORMAT(3X,F15.9,3X,F15.9,3X,F15.9,3X,F15.9,3X,F15.9)
      WRITE(2,98)
98    OFORMAT(109H1   X1          X2          X3                  SIGMA
     1          FRINGE     P          Q          R       THETAR///)
      P=-570
      Q=0
65    THETA=0.0
66    R=0.125
68    X1=2*BO/R**2
      R1=R**2
      R2=R**4
      R3=1/R1
      R4=1/R2
```

```
      W1=A2*R1
      W2=B2*R4
      W3=D2*R3
      W4=W1+W2
      W5=W1-W2
      X2=4*(3*W4+C2+W3)
      X3=4*(3*W5+C2-W3)
      PE=P+Q
      PF=P-Q
      THE=2*THETA
      SG=X1*PE
      SG1=X2*PF*COS(THE)
      SG2=X3*PF*SIN(THE)
      SG3=(SG-SG1)**2
      SG4=SG2**2
      SIGMA=SQRT(SG3+SG4)
      FRINGE=3*SIGMA/1230
      THETAR=THETA* 180/PI
      WRITE(2,100)X1,X2,X3,SIGMA,FRINGE,P,Q,R,THETAR
100   OFORMAT(3X,F10.7,3X,F10.7,3X,F10.7,3X,F20.8,3X,F8.5,3X,F6.1,3X,F6.1
     1,3X,F5.3,3X,F6.1)
      IF(R-0.375)110,120,120
110   R=R+0.025
      GO TO 68
120   R=R+0.125
      IF(R-0.625)68,68,140
140   THETA=THETA+ 5*PI/180
      IF(THETA-PI/2)66,66,190
190   A=0.628
      B=B+0.0075
      IF(B-0.136)25,25,200
200   STOP
      END
      FINISH
      ****
```

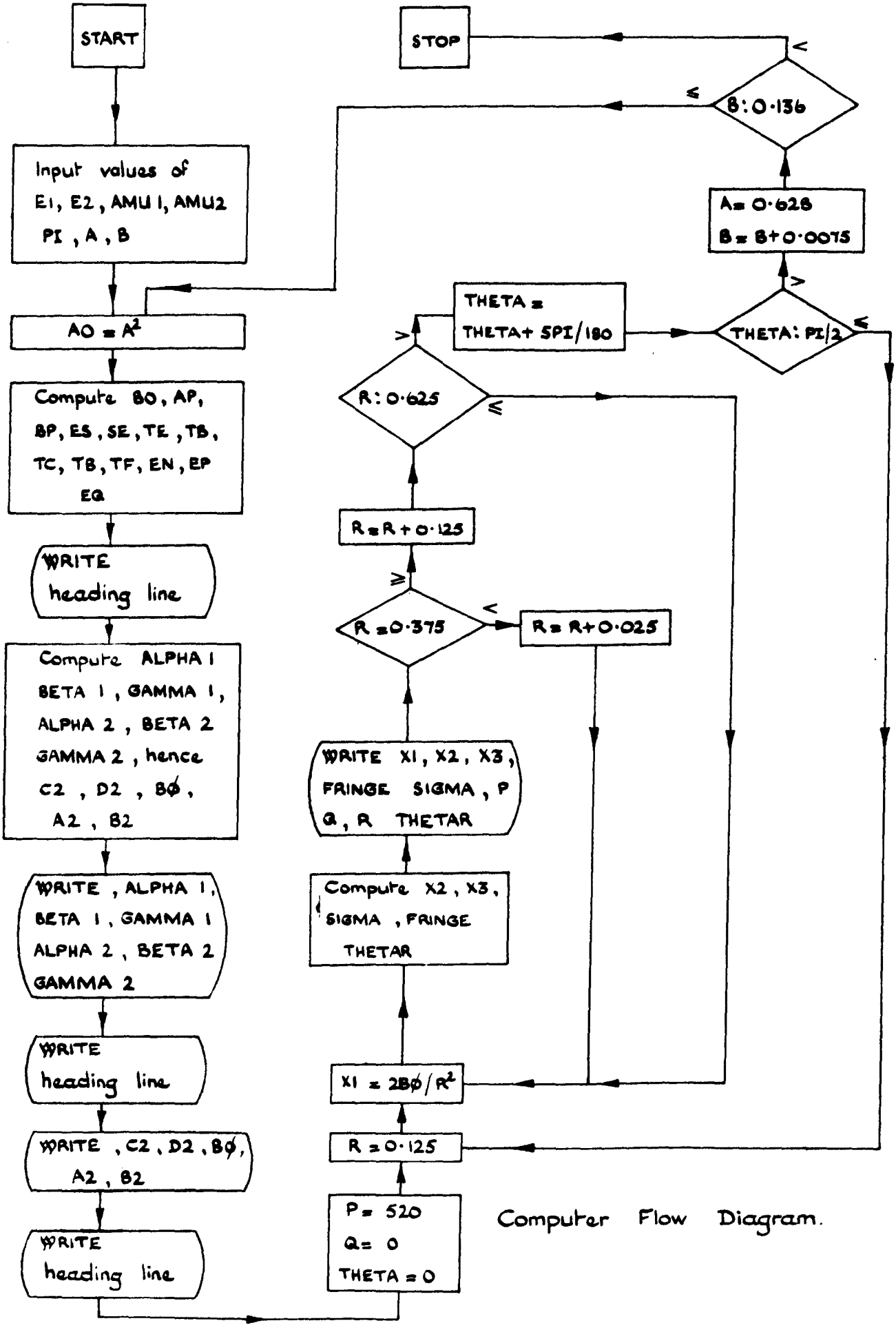

Computer Flow Diagram.

APPENDIX 4

Mechanical Loading of Inclusions in Thin Plates

(A) Solid Inclusion with a "Welded" Interface

(B) Annular Inclusion with an "Exact-Fit" Interface

(A) Solid Inclusion in a Thin Plate, Mechanical Loading - "Welded" Interface

The Hiramatsu solution[36] begins with Airey Stress functions for the domains $r \geq a$ (host material, i.e. the thin plate) and $r \leq a$ (inclusion):

For $r \geq a$:

$$\phi = Aor^2 + Bo \log r + \left(\frac{B_2}{r^2} + C_2 r^2 + D_2\right) \cos 2\theta \qquad (A.4.1)$$

This leads to equations (5.4)-(5.6) for the stress components σ_r, σ_θ, $\tau_{r\theta}$ and displacement components, u_r, u_θ given by:

$$u_r = 2(1-\mu)Aor - (1+\mu)\frac{B_o}{r} + \{2(1+\mu)\frac{B_2}{r^3}$$

$$- 2(1+\mu) C_2 r + \frac{4D_2}{r}\} \frac{\cos 2\theta}{E} \qquad (A.4.2)$$

$$u_\theta = \{2(1+\mu)\frac{B_2}{r^3} + 2(1+\mu) C_2 r - 2(1-\mu)\frac{D_2}{r}\} \frac{\sin 2\theta}{E} \qquad (A.4.3)$$

For $r \leq a$:

$$\phi' = Ao'r^2 + (A_2'r^4 + C_2'r^2) \cos 2\theta \qquad (A.4.4)$$

This leads to equations (5.1)-(5.3) for the stress components σ_r', σ_θ', $\tau_{r\theta}'$ and displacement components u_r', u_θ' given by:

$$u_r' = \left[2(1-\mu')Ao'r - \{4\mu' A_2'r^3 + 2(1+\mu')C_2'r\} \cos 2\theta\right] \frac{1}{E'} \qquad (A.4.5)$$

$$u_\theta' = \left[2(3+\mu')A_2'r^3 + 2(1+\mu')C_2'r\right] \frac{\sin 2\theta}{E'} \qquad (A.4.6)$$

In uniaxial loading the host material external boundary conditions are:

$$(\sigma_r)_{r=\infty} = \frac{P}{2}(1 + \cos 2\theta)$$

$$(\sigma_\theta)_{r=\infty} = \frac{P}{2}(1 - \cos 2\theta)$$

$$(\tau_{r\theta})_{r=\infty} = -\frac{P}{2} \sin 2\theta \qquad (A.4.7)$$

For a "welded" internal boundary equalities (5.10) also apply. Considering equations (A.4.1)-(A.4.7) and (5.1)-(5.6) all the constants A_o, B_o, B_2, C_2, D_2, A_o', A_2' can be derived as shown below:

$$A_o = \frac{P}{4}, \qquad B_o = \frac{E'(1-\mu) - E(1-\mu')}{E'(1+\mu) + E(1-\mu')} \cdot \frac{pa^2}{2},$$

$$B_2 = \frac{E'(1+\mu) - E(1+\mu')}{E'(3-\mu) + E(1+\mu')} \cdot \frac{pa^2}{4}, \qquad C_2 = -\frac{P}{4}$$

$$D_2 = \frac{E(1+\mu') - E'(1+\mu)}{E'(3-\mu) + E(1+\mu')} \cdot \frac{pa^2}{2}$$

$$A_o' = \frac{E'}{E'(1+\mu) + E(1-\mu')} \cdot \frac{P}{2}, \qquad A_2' = 0$$

$$C_2' = \frac{-E'}{E'(3-\mu) + E(1+\mu')} \cdot p.$$

The solution given above satisfies equilibrium and stated boundary conditions; it agrees with Muskhelishvili's alternative derivation[39]. The errors in Hiramatsu's paper appear in the definitions of B_2, D_2, C_2'.

(B) Annular Inclusion in a Thin Plate Mechanical Loading - "Exact-fit" Interface

For the host material, the stress and displacement components are given as before by equations (5.4)-(5.6), (A.4.2)-(A.4.3); the external boundary conditions for uniaxial loading (A.4.7.) also apply.

In the inclusion the stress components are given by equations (5.7)-(5.9) and the displacements may be written:

$$u_r' = \Big[2(1-\mu')A_o'r - (1+\mu')\frac{B_o'}{r} - \{4\mu' A_2' r^3 - 2(1+\mu')\frac{D_2'}{r^3} + 2(1+\mu')\, C_2' r - \frac{4D_2'}{r} \} \cos 2\theta \Big] \frac{1}{E'}, \qquad (A.4.8)$$

$$u_\theta' = \left[2(3+\mu')A_2'r^3 + 2(1+\mu')\frac{D_2'}{r^3} + 2(1+\mu')C_2'r - 2(1-\mu')\frac{D_2'}{r}\right]\frac{\sin 2\theta}{E'} \qquad (A.4.9)$$

Considering the new interface boundary conditions:

$$\sigma_r' = \sigma_r'_{(r=a)}, \quad \tau_{r\theta} = \tau_{r\theta}' = 0_{(r=a)} \quad u_r = u_r'(r=a) \qquad (5.11)$$

simultaneous equations for all the constants Ao, Bo, B_2, C_2, D_2, Ao', Bo', A_2', B_2', C_2', D_2' may be obtained. Their solution gives:

$$Ao = \frac{p}{4}, \quad Bo = a^2\left\{Bo'\left[\frac{b^2-a^2}{a^2b^2}\right] - \frac{p}{2}\right\}$$

$$B_2 = -\frac{pa^4}{2} - \frac{1}{3}\{C_2'(a^4-b^4) + 2D_2'(a^2-b^2)\}$$

$$C_2 = -\frac{p}{4}, \quad D_2 = \frac{1}{a^2}\{C_2'(a^4-b^4) + 2D_2'(a^2-b^2) + \frac{pa^4}{2}\}$$

$$Ao' = -\frac{Bo'}{2b^2}, \quad Bo' = -\frac{pa}{E}\left\{\frac{(1-\mu')}{Eb^2}a + \frac{(1+\mu')}{E'a} - \frac{(1+\mu)}{E}\left(\frac{1}{a} - \frac{a}{b^2}\right)\right\}^{-1}$$

$$A_2' = -\frac{1}{3b^2}\left[2C_2' + \frac{D_2'}{b^2}\right], \quad B_2' = -\frac{b^2}{3}\left[C_2'b^2 + 2D_2'\right]$$

$$C_2' = \frac{\gamma\alpha'}{\alpha\beta'-\alpha'\beta}, \quad D_2' = \frac{\gamma\beta'}{\alpha\beta'-\alpha'\beta}$$

where $\alpha = \frac{2}{b^2}\{E\left[b^4(3a^2-b^2)+\mu'(a^6-b^6)\right] - E'b^4(a^2-b^2)(5-\mu)\}$

$$\beta = \{E'b^2(a^4-b^4)(5-\mu) + Eb^2(1+\mu')(3a^4+b^4) - 4Ea^6\mu'\}$$

$$\gamma = 3E'a^4b^2.p$$

$$\alpha' = a^2(a^4 + b^4) - 2b^6$$

$$\beta' = b^2\left[b^2(a^4 + b^4) - 2a^6\right]$$

The inclusion stress components can now be written for the geometry under consideration. The principal stress difference at any point can be conveniently obtained from the relation:

$$(\sigma_1' - \sigma_2') = \sqrt{(\sigma_r' - \sigma'_\theta)^2 + 4\tau_{r\theta}'^2} \qquad (3.22)$$

APPENDIX 5

Data for Chapter 5

TABLE A.5.1.

Annular Stressmeter Data

Slab Specimens F1-2 and F1-6 in Uniaxial Compression

(Meter length : 3 in. f_g = 1220 p.s.i./fr./in
Specimen details: see Figure 3.7.)

Gauge Pressure p.s.i.	Slab Load lbs.	Applied Stress p.s.i.	White Light Fringe Orders at 45° Points									
			Specimen F1-2					Specimen F1-6 (wax coated)				
			Day 37	Day 50	Day 74	Day 94	Day 112	Day 37	Day 50	Day 74	Day 94	Day 112
0	0	0	0	0	0	0.05	0.02	0	0.10	0.20	0.28	0.30
700	3050	117	0.65	0.63	0.61	0.66	0.60	0.64	0.75	0.84	0.90	0.92
1400	6300	242	1.33	1.31	1.30	1.35	1.37	1.35	1.44	1.57	1.59	1.65
2100	9550	367	1.97	1.95	1.98	2.00	1.98	2.05	2.11	2.32	2.42	2.30
2800	12750	490	2.71	2.68	2.67	2.70	2.62	2.76	2.83	2.98	2.95	3.05
3500	15950	613	3.32	3.35	3.28	3.42	3.40	3.38	3.46	3.52	3.60	3.60
4200	19200	738	3.98	3.95	3.97	4.05	4.01	4.05	4.14	4.24	4.26	4.33
4900	22500	865	4.73	4.66	4.64	4.70	4.80	4.69	4.84	4.96	4.90	5.00
Sensitivity:p.s.i./fringe			184	186	185	185	184	182	182	181	183	184

All terms have positive signs.

TABLE A.5.2.

Longitudinal Strain Data: Slab Specimens F1-2 and F1-6 in Uniaxial Compression

(Demec Gauge (8 in.) Sensitivity: 10με/division
Specimen Details: see Figure 3.7)

Line	Slope of Line from Demec Readings - p.s.i. x 10^6									
	Specimen F1-2					Specimen F1-6 (Wax Coated)				
	Day 37	Day 50	Day 74	Day 94	Day 112	Day 37	Day 50	Day 74	Day 94	Day 112
F1	3.74	3.80	3.31	3.65	3.41	4.00	4.03	4.05	4.20	4.10
F2	3.70	3.78	3.24	3.56	3.37	3.89	3.97	3.98	4.08	4.02
F3	3.58	3.70	3.21	3.41	3.32	3.83	3.92	3.92	4.00	3.96
B1	3.45	3.54	3.71	3.54	3.55	3.68	3.73	3.74	3.83	3.81
B2	3.41	3.50	3.58	3.52	3.64	3.61	3.73	3.72	3.77	3.74
B3	3.34	3.41	3.50	3.77	3.60	3.57	3.66	3.69	3.68	3.71
Mean (E Value)	3.5	3.6	3.4	3.6	3.5	3.7	3.8	3.8	3.9	3.9

TABLE A.5.3.

Fringe Order Distribution along Principal Axes

Specimen F3-3 Solid Stressmeter - Three Uniaxial Load Levels

Glass fringe value: f_g = 1220 p.s.i./fr./in

Thickness: l_g = 3.0 in.

Ambient Temperature: 70°F

Radial Position $\frac{r}{a}$	Applied Stress p.s.i. (p)	White Light Fringe Order N				$\frac{(\sigma_\theta' - \sigma_r')}{p} = \frac{Nf_g}{l_g p}$			
		-N Major Axis		+N Minor Axis		Major Axis (Signs -ve)		Minor Axis (Signs +ve)	
		θ=0°	θ=180°	θ=90°	θ=270°	θ=0°	θ=180°	θ=90°	θ=270°
1.00	410	0.90	1.10	1.25	1.50	0.92	1.12	1.25	1.49
	640	1.55	1.56	1.86	2.15	0.98	0.99	1.18	1.37
	855	2.26	2.18	2.49	2.81	1.08	1.04	1.18	1.34
0.80	410	1.20	1.16	1.37	1.54	1.22	1.18	1.36	1.53
	640	1.85	1.87	2.04	2.25	1.18	1.19	1.30	1.43
	855	2.60	2.69	2.70	3.05	1.24	1.28	1.28	1.45
0.60	410	1.38	1.32	1.45	1.56	1.41	1.35	1.44	1.55
	640	2.16	2.13	2.21	2.33	1.37	1.35	1.41	1.48
	855	2.93	2.87	2.94	3.18	1.39	1.37	1.40	1.52
0.40	410	1.47	1.46	1.55	1.61	1.50	1.49	1.54	1.60
	640	2.30	2.32	2.31	2.43	1.46	1.48	1.47	1.55
	855	3.15	3.10	3.15	3.28	1.50	1.48	1.50	1.56
0.20	410	1.61	1.59	1.61	1.61	1.64	1.62	1.60	1.60
	640	2.44	2.49	2.43	2.51	1.55	1.58	1.55	1.60
	855	3.30	3.28	3.25	3.34	1.57	1.56	1.55	1.59
0	410	1.61	1.61	1.61	1.61	1.64	1.64	1.60	1.60
	640	2.51	2.51	2.51	2.51	1.59	1.59	1.60	1.60
	855	3.34	3.34	3.34	3.34	1.59	1.59	1.59	1.59

TABLE A.5.4.

Fringe Order Distributions along Principal Axes

Specimen F1-3 Annular Stressmeter - Three Uniaxial Load Levels

Glass fringe value: f_g = 1230 p.s.i./fr./in.
Thickness l_g = 3.0 in. Nominal $\frac{a}{b}$ ratio = 5.0
Ambient temperature = 69°F

Radial Position $\frac{r}{b}$	Applied Stress p.s.i. (p)	Sodium Light Fringe Order N				$\frac{(\sigma_\theta' - \sigma_r')}{p} = \frac{Nf_g}{l_g p}$			
		-N Major Axis		+N Minor Axis		Major Axis (Signs -ve)		Minor Axis (Signs +ve)	
		θ=0°	θ=180°	θ=90°	θ=270°	θ=0°	θ=180°	θ=90°	θ=270°
5.0	400	0.36	0.30	0.50	0.59	0.34	0.31	0.51	0.61
	490	0.39	0.31	0.55	0.60	0.33	0.26	0.46	0.50
	565	0.51	0.42	0.67	0.75	0.37	0.31	0.49	0.55
4.00	400	0.65	0.43	0.78	0.83	0.66	0.44	0.80	0.85
	490	0.76	0.55	0.85	0.95	0.64	0.46	0.71	0.80
	565	0.90	0.62	1.03	1.07	0.67	0.45	0.75	0.77
3.00	400	0.82	0.68	0.98	1.02	0.84	0.70	1.01	1.05
	490	0.95	0.81	1.16	1.18	0.80	0.68	0.97	0.99
	565	1.12	0.93	1.38	1.41	0.81	0.68	1.00	1.03
2.00	400	0.72	0.65	1.06	1.07	0.74	0.67	1.09	1.10
	490	0.82	0.72	1.35	1.27	0.69	0.60	1.13	1.06
	565	0.95	0.82	1.58	1.56	0.69	0.60	1.15	1.13
1.50	400	0.72	0.70	1.42	1.29	0.74	0.72	1.45	1.32
	490	0.82	0.72	2.12	2.00	0.69	0.60	1.76	1.67
	565	0.95	0.85	1.96	2.00	0.69	0.62	1.43	1.45
1.00	400	1.29	1.24	2.57	2.58	1.32	1.27	2.64	2.67
	490	1.56	1.47	2.95	3.05	1.31	1.23	2.47	2.55
	565	1.50	1.60	3.50	3.70	1.09	1.16	2.54	2.68

APPENDIX 6

Data for Chapter 6

TABLE A.6.1.

Annular Stressmeter Readings Station 302/21

Fringe Order Point : $\frac{r}{b} = 1.40$, $\theta = 0^{\circ}-90^{\circ}$

Glass f_g Value : $f_g = 1220$ p.s.i./fr./in.

Thickness : $l_g = 3.0$ in.

Meter Sensitivity : $S_n = 230$ p.s.i./fr.

$p = N \times S_n$ $\eta = \frac{q}{p}$

Installation Date : 30th July, 1966.

Date	Fringe Order $\pm N$	Principal Stress Ratio $\pm \eta$	Major Stress Direction $\pm \theta_D$
14.11.66	0.34	0.75	0
22.12.66	0.40	0.75	10
30.12.66	0.25	0.75	170
5.1.67	0.44	0.75	0
20.2.67	0.41	0.75	0
3.4.67	0.67	0.50	5
24.4.67	0.83	0.75	5
8.5.67	0.62	0.50	5
12.6.67	0.74	0.50	175
19.6.67	0.67	0.50	175
24.7.67	0.66	0.75	0
21.8.67	0.95	0.75	170
23.9.67	0.82	0.75	170
13.11.67	1.00	0.50	160
20.1.68	1.25	0.50	145
27.3.68	1.53	0.50	140
15.8.68	1.42	0.75	140
4.11.68	1.27	0.75	120
11.4.69	1.42	0.75	135

TABLE A.6.2.

Annular Stressmeter Readings

Station 304

Notation: see Figure 6.9 and Table A.6.1.

Installation Dates: 304/21 - 27.7.66
304/22 - 21.12.66.

Date	Fringe Order +N		Principal Stress Ratio + η		Major Stress Direction $+\theta_B$	
	304/21	304/22	304/21	304/22	304/21	304/22
14.11.66	0.24		0.50		60	
22.12.66	0.50		0.50		50	
30.12.66	0.44		0.75		60	
5.1.67	0.55		0.75		50	
20.2.67	0.32		0.50		60	
3.4.67	0.32		0.50		60	
24.4.67	0.60		0.50		45	
8.5.67	0.30		0.50		60	
12.6.67	0.30		0.50		60	
19.6.67	0.35	0.32	0.50	0.50	50	135
24.7.67	0.55	0.54	0.75	0.50	70	135
21.8.67	0.57	0.66	0.75	0.75	70	135
23.9.67	0.66	0.66	0.75	0.75	60	135
13.11.67	0.66	1.07	1.0	0.50		160
20.1.68	0.88	1.23	0.75	0.25	145	135
27.3.68	0.93	1.49	0.75	0.25	140	150
15.8.68	1.15	1.45	0.75	0.25	140	150
4.11.68	1.34	1.32	1.0	0.25		135
11.4.69	1.35	1.37	1.0	0.25		120

TABLE A.6.3.

Annular Stressmeter Readings Station 204/21

Notation: see Figure 6.9 and Table A.6.1.

Installation Date: 23.2.66

Date	Fringe Order +N	Principal Stress Ratio + η	Major Stress Direction $+\theta_B$
4.4.66	0.75	0.75	30
18.4.66	0.70	0.75	30
9.5.66	0.93	0.75	80
31.5.66	0.64	0.75	80
4.7.66	1.21	0.75	80
25.7.66	1.23	0.75	70
25.8.66	1.13	0.75	70
1.9.66	1.21	0.75	80
26.9.66	1.18	0.75	75
31.10.66	1.22	0.75	60
14.11.66	1.22	0.75	55
22.12.66	1.27	0.75	55
30.12.66	1.28	0.75	55
5.1.67	1.11	0.75	55
20.2.67	1.18	0.75	55
3.4.67	1.12	0.75	80
24.4.67	1.70	0.75	80
8.5.67	1.20	0.75	85
12.6.67	1.25	0.75	85
19.6.67	1.42	0.75	85
24.7.67	1.35	0.75	80
21.8.67	1.35	0.75	80
23.9.67	1.37	0.75	80
13.11.67	1.21	0.75	120
20.1.68	1.36	0.75	100
27.3.68	1.44	0.75	100
15.8.68	1.15	0.75	140
4.11.68	1.26	0.75	100
11.4.69	1.26	0.75	110

TABLE A.6.4.

Annular Stressmeter Readings Station 206

Notation:see Figure 6.9 and Table A.6.1

Installation Dates: 206/21: 16.2.66
206/22: 21.12.66

Date	Fringe Order +N		Principal Stress Ratio +η		Major Stress Direction $+\theta_B$	
	206/21	206/22	206/21	206/22	206/21	206/22
4.4.66	0.50		0.75		175	
18.4.66	0.56		0.75		175	
9.5.66	0.82		1.0			
31.5.66	0.68		1.0			
4.7.66	0.66		1.0			
25.7.66	0.86		1.0			
25.8.66	0.87		1.0			
1.9.66	1.23		0.75		160	
26.9.66	1.20		0.75		170	
31.10.66	1.43		0.75		175	
14.11.66	1.71		0.75		165	
22.12.66	1.75		0.75		165	
30.12.66	1.71		0.75		165	
5.1.67	1.67		0.75		165	
20.2.67	1.93	0.25	0.50	0.50	175	150
3.4.67	2.16	0.96	0.50	0.25	170	150
24.4.67	2.00	1.00	0.50	0.25	170	135
8.5.67	2.07	1.11	0.50	0.50	170	135
12.6.67	2.15	1.25	0.50	0.50	170	120
19.6.67	2.00	1.14	0.50	0.50	170	120
24.7.67	1.76	1.30	0.75	0.75	170	120
21.8.67	1.78	1.53	0.75	0.50	170	135
23.9.67	1.74	1.70	0.50	0.50	170	135
13.11.67	1.82	2.20	0.50	0.50	165	135
20.1.68	2.12	2.54	0.50	0.25	160	135
27.3.68	1.95	2.46	0.50	0.25	150	140
15.8.68	2.12	2.12	0.75	0.50	150	120
4.11.68	1.82	2.31	0.75	0.50	140	130
11.4.69	1.87	2.65	0.50	0.50	160	135

TABLE .A.6.5

Solid Stressmeter Readings 206/23

Sensitivity factor, S_n = 250 p.s.i./fr.

$(p-q) = S_n \times N$ p.s.i.

Installation date : 16.2.66

Date	Fringe Order N	Principal Stress Difference (p-q)	
		206/23	206/21
4.4.66	0	0	28
18.4.66	0	0	32
9.5.66	0	0	0
31.5.66	0.50	125	0
4.7.66	0.33	83	0
25.7.66	0.28	70	0
25.8.66	0	0	0
1.9.66	0	0	71
26.9.66	0	0	69
31.10.66	0.36	90	83
14.11.66	0.40	100	99
21.8.67	0.37	92	102
23.9.67	0.47	117	200
13.11.67	0.86	215	209
20.1.68	0.23	57	244
27.3.68	1.22	305	223
15.8.68	0.63	157	122
4.11.68	0.78	195	104
4.11.69	1.14	285	215

All terms take positive signs

TABLE A.6.6.

Annular Stressmeter Readings Station 208

Notation: see Figure 6.9 and Table A.6.1.

Installation Date: 208/21 - 5.11.65.
208/22 - 21.12.66.

Date	Fringe Order +N		Principal Stress Ratio +n		Major Stress Direction $+\theta_B$	
	208/21	208/22	208/21	208/22	208/21	208/22
4.4.66	0.45		0.75		150	
18.4.66	0.54		0.75		150	
9.5.66	0.35		0.75		150	
31.5.66	0.47		0.75		80	
4.7.66	0.62		0.75		80	
25.7.66	0.61		0.75		80	
25.8.66	1.19		0.75		170	
1.9.66	0.94		1.0			
26.9.66	1.30		1.0		170	
31.10.66	1.71		0.75		170	
14.11.66	1.66		0.75		170	
22.12.66	1.70		0.50		170	
30.12.66	1.86		0.75		170	
5.1.67	1.80		0.75		170	
20.2.67	2.00	0.20	0.50	0.50	177	170
3.4.67	2.14	0.52	0.50	0.50	170	160
24.4.67	2.30	0.70	0.50	0.50	170	160
8.5.67	2.24	0.73	0.50	0.50	170	160
12.6.67	2.35	1.30	0.50	0.75	170	150
19.6.67	2.15	1.20	0.25	0.75	165	150
24.7.67	1.89	1.34	0.25	0.75	170	120
21.8.67	1.85	1.48	0.75	0.75	150	100
23.9.67	1.92	1.30	0.75	0.75	170	170
13.11.67	1.84	0.91	0.25	0.25	170	160
20.1.68	3.00	2.73	0.25	0.25	160	140
27.3.68	3.56	2.80	0.25	0.25	160	155
15.8.68	2.89	2.36	0.50	0.25	160	120
4.11.68	2.78	2.35	0.50	0.50	165	110
11.4.69	2.98	2.86	0.25	0.25	165	135

TABLE A.6.7.

Annular Stressmeter Readings Stations 210/22, 212/22

Notation: see Figure 6.9 and Table A.6.1.
Installation Dates: 21.12.66

Date	Fringe Order +N		Principal Stress Ratio +n		Major Stress Direction $+\theta_B$	
	210/22	212/22	210/22	212/22	210/22	212/22
3.4.67		0.50		0.50		135
24.4.67		0.65		0.25		135
8.5.67	0.45	0.69	0.50	0.25	130	135
12.6.67	0.72	0.95	0.50	0.25	110	120
19.6.67	0.92	0.95	0.50	0.50	110	120
24.7.67	1.00	0.90	0.75	0.50	120	120
21.8.67	0.92	0.90	0.75	0.50	135	120
23.9.67	0.96	0.93	0.75	0.50	135	135
13.11.67	1.20	1.26	0.50	0.75	160	130
20.1.68	1.41	1.38	0.25	0.50	170	135
27.3.68	1.33	1.58	0.50	0.50	160	135
15.8.68	1.44	1.30	0.25	0.75	140	110
4.11.68	1.44	1.28	0.25	0.75	130	120
11.4.69	1.58	1.58	0.50	0.50	170	120

TABLE A.6.8.

Annular Stressmeter Readings Station 213

Notation: see Figure 6.9 and Table A.6.1.
Installation Dates: 213/21 - 15.9.65
213/22 - 21.12.66

Date	Fringe Order +N		Principal Stress Ratio +η		Major Stress Direction $+\theta_D$	
	213/21	213/22	213/21	213/22	213/21	213/22
4.4.66	0.25		0.75		45	
18.4.66	0.45		0.75		45	
9.5.66	0.56		0.75		45	
31.5.66	0.63		0.75		60	
4.7.66	0.66		0.75		75	
25.7.66	0.82		0.75		80	
25.8.66	0.76		0.75		60	
1.9.66	0.78		0.75		70	
26.9.66	0.95		0.75		55	
31.10.66	1.30		0.75		65	
14.11.66	1.30		0.75		60	
22.12.66	1.02		0.75		60	
30.12.66	0.96		0.75		45	
5.1.67	0.95		0.75		60	
20.2.67	1.00		0.75		60	
3.4.67	1.05	0.21	0.75	0.50	30	170
24.4.67	1.20	0.68	0.75	0.50	5	170
8.5.67	1.18	0.60	0.75	0.50	5	165
12.6.67	1.50	1.20	0.50	0.50	0	160
19.6.67	1.48	1.29	0.75	0.25	170	160
24.7.67	1.75	1.31	0.75	0.50	170	160
21.8.67	1.88	1.37	0.75	0.75	170	160
23.9.67	1.85	1.30	0.75	0.75	20	170
13.11.67	1.10	0.84	0.75	0.75	45	175
20.1.68	Station Inaccessible					
27.3.68	2.38	1.37	0.50	0.75	150	150
15.8.68	Station inaccessible from now on					

TABLE A.6.9.

Annular Stressmeter Readings Station 214

Notation: see Figure 6.9 and Table A.6.1.
Installation Dates: 214/21 - 11.11.65
214/22 - 21.12.66

Date	Fringe Order +N		Principal Stress Ratio +η		Major Stress Direction $+\theta_B$	
	214/21	214/22	214/21	214/22	214/21	214/22
4.4.66	1.28		0.75		10	
18.4.66	1.31		0.75		10	
9.5.66	1.47		0.75		20	
31.5.66	1.13		0.75		30	
4.7.66	1.79		0.75		30	
25.7.66	1.35		1.0			
25.8.66	1.71		0.75		30	
1.9.66	2.00		0.75		30	
26.9.66	1.95		0.75		20	
31.10.66	2.52		0.75		15	
14.11.66	2.89		0.75		15	
22.12.66	2.66		0.75		15	
30.12.66	2.95		0.75		20	
5.1.67	2.85		0.75		20	
20.2.67	3.15		0.50		20	
3.4.67	3.09	0.58	0.50	0.25	10	160
24.4.67	3.20	0.66	0.50	0.25	10	160
8.5.67	3.41	0.82	0.50	0.25	5	160
12.6.67	3.41	0.88	0.50	0.25	5	160
19.6.67	3.33	0.92	0.50	0.25	5	160
24.7.67	2.78	0.93	0.75	0.50	0	135
21.8.67	2.90	1.21	0.75	0.50	175	135
23.9.67	3.12	1.60	0.75	0.50	175	135
13.11.67	3.61	2.01	0.50	0.50	175	145
20.1.68	3.74	2.50	0.25	0.25	155	135
27.3.68	3.35	N/O	0.50	N/O	175	N/O
15.8.68	3.23	N/O	0.75	N/O	160	N/O
4.11.68	3.31	N/O	0.75	N/O	150	N/O
11.4.69	3.17	N/O	0.50	N/O	160	N/O

TABLE A.6.10

Stress Increments during Impounding for Stressmeter 213/21

Notation: see Figure 6.9 and Section 6.5.4.

Stress Units - p.s.i.

Date	Stressmeter Reading			Stress Increments during Impounding					
	+p	+q	$+\theta_B^\circ$	Δ_p	Δ_q	$\Delta\sigma_B^\circ$	$\Delta\sigma_v$	$\Delta\sigma_h$	$\Delta\tau_{vh}$
22.12.66	235	176	60						
30.12.66	221	166	45	+2	-25	0	+2	-25	-2
20.2.67	230	173	60	-2	-2	0	-2	-2	0
3.4.67	242	181	30	+28	-25	0	+28	-25	+2
8.5.67	271	204	5	+85	-21	+168	+80	-16	+21
12.6.67	345	173	0	+156	-48	+173	+154	-46	+25
24.7.67	403	302	170	+219	+71	+163	+207	+85	+41
23.9.67	425	319	20	+223	+113	0	+221	+111	-9
13.11.67	267	200	45	+44	+16	0	+43	+15	-9
27.3.68	548	274	150	+378	+43	+150	+292	+126	+145

TABLE A.6.11.

Stress Increments during Impounding from Sonic Gauge Rosette 102

Notation: see Figure 6.9 and Section 6.5.4.

Stress Units - p.s.i.

Date	Corrected Rosette Components				$\Delta\tau_{vh}$	Principal Stress Condition		
	Δ_{G1} ($\Delta\sigma_v$)	$\Delta\sigma_{G2}$ ($\Delta\sigma_h$)	$\Delta\sigma_{G3}$	$\Delta\sigma_{G4}$		Δ_p	Δ_q	$+\Delta\theta_B$
1.1.67	0	0	0	0	0	0	0	0
1.3.67	-10	-13	-20	-5	-3	-20	-5	35
1.4.67	-12	-7	+7	-28	+17	-28	+7	133
1.6.67	-50	+10	+35	-75	+55	-82	+42	120
1.7.67	-61	+29	+66	-99	+83	-111	+76	120
1.8.67	-58	+62	+63	-97	+100	+120	-114	119
1.9.67	-38	+82	+133	-87	+109	+146	-104	120
1.10.67	+2	+87	+168	-72	+113	+172	-80	125
1.11.67	+50	+80	+185	-55	+120	+185	-55	131
1.12.67	+92	+57	+178	-27	+100	+180	-28	140
1.1.68	+116	+36	+169	-16	+90	+175	-22	147
M.1.68	+122	+27	+163	-12	+88	+175	-22	149
1.2.68	+121	+16	+154	-16	+83	+170	-30	150
1.4.68	+105	-10	+120	-25	+72	+140	-45	155

TABLE A.6.12

Stress Increments during Impounding from Stressmeter 208/21

Notation: see Figure 6.9 and Section 6.5.4.

Stress Units - p.s.i.

Date	Stressmeter Reading			Stress Components			Stress Increments		
	p	q	θ_B °	σ_v	σ_h	τ_{vh}	$\Delta\sigma_v$	$\Delta\sigma_h$	$\Delta\tau_{vh}$
22.12.66	391	196	170	387	200	34	0	0	0
30.12.66	428	320	170	424	322	17	37	122	-17
5.1.67	414	310	170	410	315	17	23	115	-17
20.2.67	460	230	177	460	230	11	73	30	-23
3.4.67	492	246	170	483	244	41	96	44	7
24.4.67	530	265	170	520	272	46	133	72	12
8.5.67	515	256	170	506	265	46	119	65	12
12.6.67	540	269	170	532	276	46	145	76	12
19.6.67	495	124	165	470	150	92	83	-50	58
24.7.67	435	108	170	424	115	57	37	-85	23
21.8.67	426	320	150	398	348	46	12	147	12
23.9.67	441	331	170	437	336	18	50	136	-16
13.11.67	423	106	170	414	115	55	27	-85	22
20.1.68	690	172	160	630	232	168	243	32	134
27.3.68	820	205	160	748	276	195	361	76	161

All terms take positive signs unless otherwise stated.

TABLE A.6.13.

Stress Increments during Impounding from Stressmeter 214/21

Notation: see Figure 6.9 and Section 6.5.4.

Stress Units - p.s.i.

Date	Stressmeter Reading			Stress Components			Stress Increments		
	p	q	θ_B °	σ_v	σ_h	τ_{vh}	$\Delta\sigma_v$	$\Delta\sigma_h$	$\Delta\tau_{vh}$
22.12.66	611	460	15	602	469	-37	0	0	0
30.12.66	678	508	20	658	527	-55	56	58	-18
5.1.67	655	492	20	635	513	-53	33	44	-16
20.2.67	725	361	20	683	402	-115	81	-67	-78
3.4.67	710	354	10	702	363	-57	100	-106	-20
24.4.67	736	368	10	722	379	-64	120	-90	-27
8.5.67	785	391	5	778	395	-34	176	-74	3
12.6.67	785	391	5	778	395	-34	176	-74	3
19.6.67	765	382	5	760	386	-34	158	-83	3
24.7.67	640	478	0	640	478	0	38	9	37
21.8.67	667	499	175	665	498	14	63	29	51
23.9.67	717	538	175	717	540	16	115	71	53
13.11.67	830	414	175	828	419	39	226	-50	77
20.1.68	860	430	155	786	506	165	184	37	202
27.3.68	770	384	175	768	386	34	166	-83	71

All terms take positive signs unless otherwise stated

TABLE A.6.14.

Stress Components after Impounding from Stressmeter 206/21

Notation: see Figure 6.9 and Section 6.5.4.

Stress Units - p.s.i.

Date	Stressmeter Reading			Stress Components		
	p	q	θ_B	σ_v	σ_h	τ_{vh}
22.12.66	402	301	165	398	306	25
30.12.66	402	301	165	398	300	25
5.1.67	396	295	165	391	299	20
20.2.67	443	222	175	444	223	2
3.4.67	497	248	170	490	253	4
24.4.67	460	230	170	453	237	4
8.5.67	476	238	170	469	241	4
12.6.67	495	247	170	490	253	4
19.6.67	460	230	170	453	237	4
24.7.67	405	303	170	403	306	16
21.8.67	405	303	170	403	306	16
23.9.67	400	200	170	391	207	34
13.11.67	419	210	165	403	225	50
20.1.68	487	243	160	460	271	80
27.3.68	449	225	150	396	276	99
15.8.68	487	366	150	458	398	53
4.11.68	419	314	140	375	359	50
11.4.69	430	215	160	405	241	69

All terms have positive signs.

TABLE A.6.15.

Stress Components after Impounding from Stressmeter 206/22

Notation: see Figure 6.9 and Section 6.5.4.

Stress Units - p.s.i.

Date	Stressmeter Reading			Stress Components		
	p	q	θ_B	σ_v	σ_h	τ_{vh}
22.12.66	0	0	0	0	0	0
3.4.67	221	55	150	179	97	71
24.4.67	230	57	135	144	144	85
8.5.67	255	127	135	191	191	65
12.6.67	287	143	120	179	253	65
19.6.67	262	131	120	161	230	57
24.7.67	299	224	120	244	281	32
21.8.67	352	176	135	265	265	87
23.9.67	391	195	135	292	292	97
13.11.67	506	253	135	380	380	126
20.1.68	584	146	135	373	363	218
27.3.68	566	142	140	386	317	207
15.8.68	488	244	120	301	426	103
4.11.68	531	265	130	373	419	131
11.4.69	610	305	135	458	458	154

All terms take positive signs.